TURUN
YLIOPISTO
UNIVERSITY
OF TURKU

YBCO SUPERCONDUCTOR ON BUFFERED METALLIC TAPES FOR COATED CONDUCTOR BASED APPLICATIONS

Modifying the pinning landscape for improving the critical current densities

Mukarram Zaman Khan

TURUN YLIOPISTON JULKAISUJA – ANNALES UNIVERSITATIS TURKUENSIS
SARJA – SER. AI OSA – TOM. 651 | ASTRONOMICA – CHEMICA – PHYSICA – MATHEMATICA | TURKU 2021

TURUN
YLIOPISTO
UNIVERSITY
OF TURKU

YBCO SUPERCONDUCTOR ON BUFFERED METALLIC TAPES FOR COATED CONDUCTOR BASED APPLICATIONS

Modifying the pinning landscape for improving the critical current densities

Mukarram Zaman Khan

TURUN YLIOPISTON JULKAISUJA – ANNALES UNIVERSITATIS TURKUENSIS
SARJA – SER. AI OSA – TOM. 651 | ASTRONOMICA – CHEMICA – PHYSICA – MATHEMATICA | TURKU 2021

University of Turku

Faculty of Science
Department of Physics and Astronomy
Physics
Doctoral programme in Physical and Chemical Sciences

Supervised by

Professor, Petriina Paturi
Wihuri Physical Laboratory
Department of Physics and Astronomy
University of Turku
Finland

Dr., Hannu Huhtinen
Wihuri Physical Laboratory
Department of Physics and Astronomy
University of Turku
Finland

Doc., Jarno Järvinen
Wihuri Physical Laboratory
Department of Physics and Astronomy
University of Turku
Finland

Reviewed by

Professor, Alexey V. Pan
School of Physics and Institute for
Superconducting and Electronic Materials
University of Wollongong
Australia

Dr., Nick Strickland
Robinson Research Institute
Victoria University of Wellington
New Zealand

Opponent

Dr., Jean-Claude Grivel
Department of Energy Conversion and Storage
Technical University of Denmark
Denmark

ISBN 978-951-29-8594-4 (PRINT)
ISBN 978-951-29-8595-1 (PDF)
ISSN 0082-7002 (PRINT)
ISSN 2343-3175 (ONLINE)
Painosalama, Turku, Finland, 2021

I dedicate this thesis to my immediate family, late aunt and Prof. Ahmed Zewail. From immidiate family, my dad had a great impact on my life who dedicated his life, all with endeavoring efforts, to enlighten me with the wisdom of knowledge, honesty and hard work. In all the achievements of my life, I will ever carry the burden of kindness, protection and hard work of my parents on my shoulders.

UNIVERSITY OF TURKU
Faculty of Science
Department of Physics and Astronomy
Physics
KHAN, MUKARRAM ZAMAN: YBCO superconductor on buffered metallic tapes for coated conductor based applications
Doctoral dissertation, 156 pp.
Doctoral programme in Physical and Chemical Sciences
September 2021

ABSTRACT

High temperature $YBa_2Cu_3O_{6+x}$ superconducting films are deposited on top of differently fashioned buffered metals to enhance the critical current density and its isotropy for coated conductor applications. The improvements are achieved by engineering the defect structure within the superconducting matrix. $BaCeO_3$ and $BaZrO_3$ were used as dopants to introduce the artificial pinning landscape in $YBa_2Cu_3O_{6+x}$ matrix. It was realized that growth temperature, dopant concentration, and underlying buffer layers stack strongly affect the growth of $YBa_2Cu_3O_{6+x}$. However, these factors are already widely studied, instead, it was observed that minor changes in one of these parameters result in degrading the structural growth and superconducting properties. A new parameter is introduced in the pulsed laser deposition process, that is, reducing the target grain size from micrometer to nanometer. The effect of targets with varying grain size was tested on both single crystals and buffered metals. Far from the expectations, the natural and artificial pinning landscape was significantly enhanced as there appeared to be notable differences in the size, shape, density and distribution of created defects. Such improvements for defects led to enhanced vortex pinning phenomenon, resulting in high critical current densities and their isotropies. This approach, together with optimizing the fore mentioned parameters, can be utilized for the fabrication of microwave devices and coated conductor applications.
KEYWORDS: Superconductivity, YBCO films, coated conductor, buffered metallic substrates, target grain size, doping, nanoinclusions, critical current density

TURUN YLIOPISTO
Matemaattis-luonnontieteellinen tiedekunta
Fysiikan ja tähtitieteen laitos
Fysiikka
KHAN, MUKARRAM ZAMAN: YBCO superconductor on buffered metallic tapes for coated conductor based applications
Väitöskirja, 156 s.
Fysikaalisten ja kemiallisten tieteiden tohtoriohjelma
Syyskuu 2021

TIIVISTELMÄ

Väitöskirjatyössä tutkittiin tulevaisuuden sähkötekniikkaan soveltuvaa korkean lämpötilan suprajohdemateriaalia, $YBa_2Cu_3O_{6+x}$. Jotta materiaali olisi sovelluksiin hyödynnettävässä muodossa, laserhöyrystettiin materiaalia eri tavoin päällystetyille metallialustoille. Väitöskirjatyö koostuu useista osatutkimuksista, joissa sekä kokeellisesti että mallintamalla on pyritty ymmärtämään materiaalissa ilmeneviä fysikaalisia ilmiöitä parhaiden suprajohtavuusominaisuuksien saavuttamiseksi.

Kokeelliset päätulokset voidaan jakaa kahteen osaan. Ensimmäisessä osassa keskityttiin erilaisten magneettivuon lukkiutumiskeskusten kuten kidevirheiden tuottamiseen $YBa_2Cu_3O_{6+x}$-matriisiin. Tämän tyyppistä tutkimusta on tehty myös aiemminkin, mutta tämän työn perusteella saatiin kasvatettua ymmärrystä ohutkalvon kasvumekanismeista sekä erityisesti erilaisten lukkiutumiskeskusten vaikutuksesta kalvojen rakenteellisiin sekä suprajohtaviin ominaisuuksiin. Toinen merkittävämpi löytö oli se, missä osoitettiin laserhöyrystyksessä käytettävän kohtion raekoon vaikuttavan merkittävästi kalvon ja siihen liittyvien kidevirheiden kasvuprosesseihin ja sitä kautta muodostuneen kalvon ominaisuuksiin. Koska optimaalisiin suprajohdekalvoihin tarvittavien kidevirheiden kasvua pystyttiin kehitetyillä menetelmillä kontrolloimaan suhteellisen luotettavasti, voidaan useita väitöskirjatyön tuloksia hyödyntää tulevaisuuden mikroaaltosovelluksissa ja korkeanlämpötilan suprajohteista tehdyissä johtimissa.
ASIASANAT: Suprajohtavuus, YBCO ohutkalvo, suprajohtavat johtimet, metallinen alustamateriaali, hilayhteensopivuus, kohtion raekoko, dooppaaminen, nanokokoiset dopantit, kriittinen virtatiheys

Acknowledgements

It could not have been possible to perform this work without the guidance of my mentors and the congenial environment provided in the surroundings by University of Turku. I will ever walk slowly with silence while passing by the doors of Prof. Petriina Paturi, Dr. Hannu Huhtinen and Doc. Jarno Järvinen, may they accept all my respects. I was trapped in the circle of these mentors who, in their own ways, have a special place in my heart. Their contribution in nurturing me will be credited until my last breath. Prof. Paturi always guided me through her knowledge in understanding my work. Dr. Huhtinen was a speedy bullet train reacting fastly during experimental problems, checking my reports, thesis and manuscripts, all decorated with jokes, fruitful arguments and my improved writing. Though Prof. Paturi and Dr. Huhtinen remained reserved and gave me the work freedom during the past half a decade but my long talks with Doc. Järvinen and Prof. Kurt Gloos on all the issues, ranging from science to politics, gave me the opportunity to get a bigger picture of western world. Doc. Järvinen is solely credited for showing me the cold sea of cryogenics. I feel honored to work with a scientist like you in the field of cryogenics. All of you understood me, patiently answered my questions and thanks for tolerating my loud voice.

I thank to Dr. Yue Zhao from Shanghai Jiao Tong University, China for providing the buffered metallic substrates. Dr. Hannes Rijckaert from Ghent University is acknowledged for performing TEM measurements of my samples and also analyzing their results. His nice TEM images and analyzation skills gave me good understanding of the topic. I personnaly thank to Prof. Alexey V. Pan and Dr. Nick Strickland for reviewing my thesis. I am also grateful to Dr. Jean-Claude Grivel who acted as my opponent.

I remember my initial days at Wihuri laboratory when I encountered Ville Lahteenlähti, Dr. Jussi Tikkanen, Dr. Mika Malmivirta and Dr. Ilari Angervo. These four guys were always there for me on my first call and facilitated me in understanding my research field. Thanks Dr. Tikkanen for your long conversations in the evenings of 2016 and 2017 when I was a new comer here. Your simplicity and editorial writing style inspired me. I thank to Elmeri Rivasto and Matti Pusa who were with me during all the hard times of my studies. You both showed me the true picture of Finnish culture by taking me to your homes and I integrated well with your families thanks to Pusa for offering me tours of entire Finland and being not shy enough to

socialize with Finns everywhere. Elmeri! Again we both share the privacy of our lives, careers and we can not be unbonded and let's party hard. Thanks to both of you for your visit to Pakistan in winter of 2019 which relaxed me also by touring around the northern parts of my homeland.

I am unable to put the words for thanking my family as the members of it always did good for me by going out of their zones. Dad! I was a naughty child and you always kept a strong eye on me worrying for my studies. I wish if I could be only 1% to your level of efforts, intelligence and achievements. Mom! You faced all the hardships of life along with Dad and took care of my protection, growth and personal grooming. Time spent without both of you in a foreign land was extremely hard and I thank both of you for being patient and solving all the problems which allowed me to achieve my goal. Thanks to all my siblings for gathering around me, despite of their tightly scheduled job nature and children care, on my yearly visits to Pakistan and getting everything ready to comfort my holidays.

I am grateful to my extended family and my dad's colleagues who always welcomed me to their homes on my visits to Pakistan. Thanks to Prof. Zulqurnain Ali for being concerned about my progress in Finland and always saying Yes on my discussion calls. Gratitudes to my closest friends who used to wait for my arrival date and were next to my door early mornings. You all along with your families are close to me!

Thanks to all those funding resources of Finland which supported me financially to complete my PhD without worrying about finance. I am indebted to Finnish security forces due to whom I felt safe and remained focused on my work. I also thank to all the workforce of Finland which provided me all the necessary life resources.

September 2021
Mukarram Zaman Khan

MUKARRAM ZAMAN KHAN
MSc. Khan came to University of Turku in September 2016 for pursuing master's degree and started PhD in January 2018.
During the past five years of my higher studies, laboratory was my first home and I made sure to benefit from it in a number of ways.

Table of Contents

Abbreviations

T_{c}	Critical temperature
YBCO	$YBa_2Cu_3O_{6+x}$
BZO	$BaZrO_3$
BCO	$BaCeO_3$
BTO	$BaTiO_3$
BHO	$BaHfO_3$
BSO	$BaSnO_3$
B_{c}	Critical magnetic field
λ	Magnetic penetration depth
ξ	Coherence length
J_{c}	Critical current density
F_{L}	Lorentz force
F_{p}	Pinning force
B_{irr}	Irreversibilty field
HTS	High temperature superconductor
CSD	Chemical solution deposition
RABiTS	Rolling assisted biaxially textured substrates
IBAD	Ion beam assisted deposition
YSZ	Yttria stabilized zirconia
MgO	Magnesium oxide
PLD	Pulsed laser deposition
STO	$SrTiO_3$
T_{g}	Growth temperature
AFM	Atomic force microscopy
XRD	X-ray diffraction
TEM	Transmission electron microscopy
B^*	Accommodation field

List of Original Publications

This dissertation is based on the following original publications, which are referred to in the text by their Roman numerals:

I M. Z. Khan, Y. Zhao, X. Wu, M. Malmivirta, H. Huhtinen, and P. Paturi. Improved interface growth and enhanced flux pinning in YBCO films deposited on an advanced IBAD-MgO based template. Physica C: Superconductivity and its applications, 2018; 545: 50−57.

II M. Z. Khan, M. Malmivirta, Y. Zhao, X. Wu, R. Jha, V. P. S. Awana, H. Huhtinen, and P. Paturi. Angular and field dependent flux pinning in artificially doped YBCO films on IBAD-MgO based template. Physica C: Superconductivity and its applications, 2018; 555: 15−23.

III M. Z. Khan, Y. Zhao, X. Wu, R. Jha, V. P. S. Awana, H. Huhtinen, and P. Paturi. Improving the flux pinning with artificial BCO nanodots and correlated dislocations in YBCO films grown on IBAD-MgO based template. IEEE Transactions on Applied Superconductivity, 2019; 29: 8002105.

IV M. Z. Khan, E. Rivasto, Y. Wu, Y. Zhao, C. Chen, J. Zhu, H. Palonen, J. Tikkanen, H. Huhtinen, and P. Paturi. Modifying the critical current anisotropy of YBCO films via buffering layers on IBAD-MgO based templates. Journal of Physics: Conference Series, 2020; 1559: 012037.

V M. Z. Khan, E. Rivasto, J. Tikkanen, H. Rijckaert, M. Malmivirta, M. O. Liedke, M. Butterling, A. Wagner, H. Huhtinen, I. Van Driessche, and P. Paturi. Enhanced flux pinning isotropy by tuned nanosized defect network in superconducting $YBa_2Cu_3O_{7-\delta}$ films, Scientific Reports, 2019; 9: 15425.

VI M. Z. Khan, E. Rivasto, H. Rijckaert, M. O. Liedke, Y. Zhao, M. Butterling, A. Wagner, I. Van Driessche, H. Huhtinen, and P. Paturi. Strongly enhanced critical current densities in YBCO superconductor on buffered metal for coated conductor applications, (Submitted to ACS Applied Electronic Materials).

Articles relevant to this work but not included in this thesis

VII M. M. Aye, M. Z. Khan, E. Rivasto, J. Tikkanen, H. Huhtinen, and P. Paturi. Role of columnar defect size in angular dependent flux pinning properties of YBCO thin films. IEEE Transactions on Applied Superconductivity, 2019; 29: 8000805.

VIII J. Chu, Y. Zhao, M. Z. Khan, X. Tang, W. Wu, J. Shi, Y. Wu, H. Huhtinen, H. Suo, and Z. Jin. Insight into the interfacial nucleation and competitive growth of $YBa_2Cu_3O_{6+x}$ films as high-performance coated conductors by a fluorine-free metal−organic decomposition route. ACS Crystal Growth & Design, 2019; 19: 6752−6762.

IX J. Díez-Sierra, P. López-Domínguez, H. Rijckaert, M. Rikel, J. Hänisch, M. Z. Khan, M. Falter, J. Bennewitz, H. Huhtinen, S. Schäfer, R. Müller, S. A. Schunk, P. Paturi, M. Bäcker, K. De Buysser, and I. Van Driessche. High critical current density and enhanced pinning in superconducting films of $YBa_2Cu_3O_{7-\delta}$ nanocomposites with embedded $BaZrO_3$, $BaHfO_3$, $BaTiO_3$, and $SrZrO_3$ nanocrystals. ACS Applied Nano Materials, 2020; 3: 5542−55543.

X E. Rivasto, M. Z. Khan, M. Malmivirta, H. Rijckaert, M. M. Aye, T. Hynninen, H. Huhtinen, I. Van Driessche, and P. Paturi. Self-assembled nanorods in YBCO matrix− a computational study of their effects on critical current anisotropy. Scientific Reports, 2020; 10: 3169.

XI E. Rivasto, M. Z. Khan, Y. Wu, Y. Zhao, C. Chen, J. Zhu, H. Huhtinen, and P. Paturi. Lattice defect induced nanorod growth in YBCO films deposited on an advanced IBAD-MgO template. Superconductor Science and Technology, 2020; 33: 075008.

XII M. M. Aye, E. Rivasto, M. Z. Khan, H. Rijckaert, E. Salojärvi, C. Haalisto, E. Mäkilä, H. Palonen, H. Huhtinen, I. Van Driessche, and P. Paturi. Control of the nanosized defect network in superconducting thin films by target grain size. Scientific Reports, 2021; 11: 6010.

XIII Y. Wu, Y. Zhao, X. Han, G. Jiang, J. Shi, P. Liu, M. Z. Khan, H. Huhtinen, J. Zhu, Z. Jin, and Y. Yamada, Ultra-fast growth of cuprate superconducting films: Dual-phase liquid assisted epitaxy and strong flux pinning. Materials Today Physics, 2021; 18: 100400.

1 Introduction

Superconductors are renowned for their exciting property of exhibiting zero resistance when cooled down to critical temperature (T_c). Heike Kamerlingh Onnes discovered this phenomenon for the very first time by dipping mercury wire in liquid He back in 1911. Since then, sufficient progress has been made to practically implement superconducting materials for various applications. Superconductors can be used as magnets in magnetic resonance imaging for producing large and homogeneous magnetic fields, and as large scale wires in the electrical power systems to pass through extremely high currents [1]. Different superconducting materials are used both in research and commercial based mega projects like large hadron collider, NASA, Google and IBM quantum computer, magnetically levitated trains, metropolitan grids, ultra-high-speed supercomputers, super efficient generators and fusion energy [2; 3; 4; 5].

This thesis delves into the specific class of superconductivity, that is, high temperature superconductor (HTS) $YBa_2Cu_3O_{6+x}$ (YBCO), which was discovered more than three decades ago and is now used in large electrical power systems. It is a cuprate and ceramic material which, in our case, was deposited on single crystals for better understanding of the growth mechanism and on metallic templates for large scale bendable wires.

Manufacturing lengthy, cheap and efficient superconducting wires good enough to pass through huge currents at high magnetic fields is the main goal of HTS community. There are many factors which are crucial to fabrication of HTS wirings, such as, the underlying buffered metal, growth temperature, created flux pinning landscape and thickness of YBCO films. This thesis mainly focuses on improving the flux pinning landscape within HTS films for further enhancement of critical current density J_c. In this regard, several buffered metals have been used to optimize the better growth of YBCO superconductor deposited at different temperatures. The growth temperature of undoped and doped YBCO films grown on specific buffered metals has been optimized. The critical thicknesses of YBCO films were also optimized on one of the metallic substrate. Furthermore, different kinds of substrate buffer stacks were compared. The effect of dopant concentration was also investigated and it has been realized that low dopant concentration is optimal for enhancing J_c. The artificial pinning landscapes were created by using $BaZrO_3$ and $BaCeO_3$ dopants and a new approach of reducing the target grain size has been introduced in

engineering better growth of natural and artificial pinning defects within the YBCO matrix to tackle and restrict the movement of Abrikosov vortices when the magnetic field is applied. The effect of reduced target grain size was investigated both on single crystal and buffered metal substrates. The results showed improved pinning landscape within YBCO and improved the J_c and its isotropy by several folds when deposited on buffered metal which is important for coated conductor applications.

2 Basics

2.1 Properties of superconductors

One of the most fascinating and well-known property of the superconductors is the complete diminishing of resistance when they are cooled down below T_{c}. Another property is the expulsion of the magnetic field below T_{c}, where no magnetic field is present inside the superconductor thus referring to their diamagnetic state with negative (-1) susceptibility. This phenomenon is called the Meissner effect [6].

The two main types of superconductors are: type I and type II. As shown in Figure 1 that both types of superconductors are classified according to their critical magnetic field (B_{c}), where type I has only one B_{c} and type II with two B_{c}s, named as, B_{c1} and B_{c2}. In type I superconductor, the superconductivity breaks down if the applied magnetic field is above the B_{c}, whereas in type II, the superconductor is in the Meissner state below B_{c1} and, in between B_{c1} and B_{c2}, the magnetic field starts penetrating inside the superconductor in the form of Abrikosov vortices. But if the magnetic field is applied above the B_{c2}, then the superconductor turns into its normal state. The type I superconductors are pure elements and their B_{c} is very low, that is, below 1 T [6], whereas type II superconductors are alloys or ceramics which can have B_{c2} easily above 100 T [7; 8].

Type I and type II superconductors can also be differentiated based on characteristic parameters, such as, magnetic penetration depth (λ) and coherence length (ξ). λ describes the length that magnetic field can penetrate inside the superconductor, where it decays exponentially from surface to deep inside the superconductor as

$$B(x) = B_o e^{-x/\lambda}, \tag{1}$$

where B_o is the magnetic field at the surface and x the distance.

ξ is the parameter corresponding to the distance within which the density of Cooper pairs can change. The Cooper pairs are formed when the nearby positive ions are attracted by travelling electrons and the slight movement of these ions forms phonons. This concentration of positive charge then attracts the second electron and as a result both the electrons interact with each other. This process is known as the phonon-mediated pairing of electrons, where Cooper pairs travel without any dissipation in low temperature superconductors (LTS) when the temperature is below 30 K. The occurrence of Cooper pairs in LTS via electron-phonon interaction is the

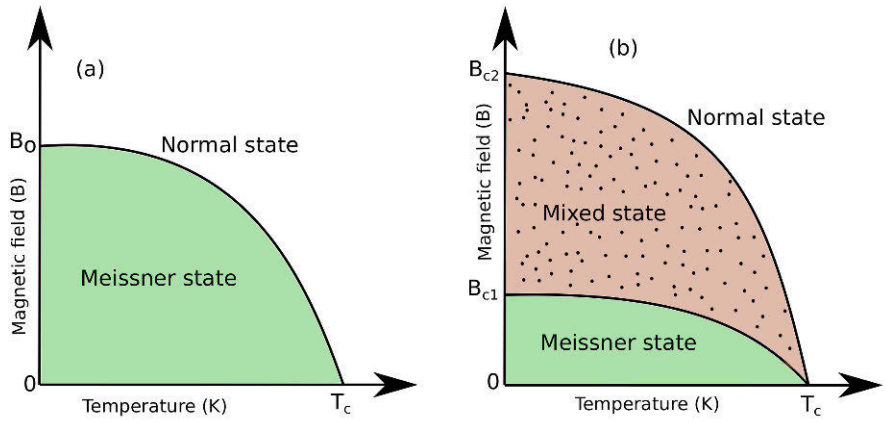

Figure 1. Phase diagrams of (a) type I and (b) type II superconductors.

fundamental of BCS theory [9]. The pairing up of electrons in high temperature superconductors is not due to phonons but can be due to magnetic interactions [10; 11]. The Cooper pairs have weak interaction energy, 10^{-3} eV, and break down when thermal energy is high. The formation of Cooper pairs forms the energy gap at the fermi surface and therefore the excitation of electrons requires extra energy.

In order to differentiate between type I and type II superconductor, Ginzburg–Landau parameter κ can also be used, where $\kappa = \lambda/\xi$. If $\kappa > 1/\sqrt{2}$ then superconductor will be type II, otherwise type I. Moreover, λ is always greater than ξ for type II superconductors which means that magnetic field can penetrate inside the superconductor in form of vortices.

2.1.1 Vortex

A vortex is a magnetic flux tube created within the superconductor in the presence of magnetic field. λ and ξ characterize the vortex, that is, the former measures the radial distance up to which the supercurrent circulates and the latter corresponds to the size of normal or non-superconducting core. λ and ξ for cuprates are $\approx$150 nm and $\approx$1.5 nm, respectively. Figure 2 depicts the confinement of magnetic field lines to the vortex region due to circulating supercurrents. Each vortex has only one magnetic flux quantum with $\Phi = 2.07 \times 10^{-15}$ Tm^2. The vortices coming closer to each other face repulsion. As a result, a proper periodic arrangement is formed, which is called as Abrikosov vortex lattice. This type of lattice only occurs in defect free superconductor, where there are no dislocations or voids to interrupt the periodic arrangement. The average distance d between the vortices can be calculated by the applied magnetic field as $d = \sqrt{\Phi / B}$. If the applied field is 1 T then d corresponds

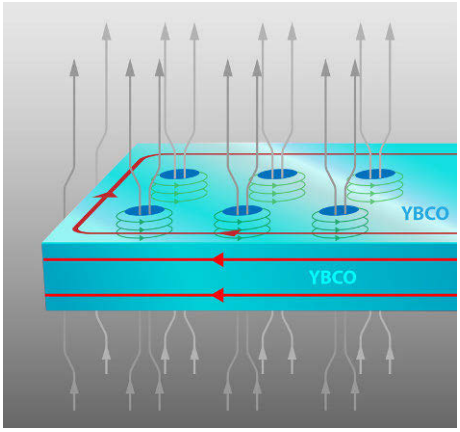

Figure 2. Schematic of magnetic field penetrating inside the YBCO superconductor in the form of swirling tubes to what is called as vortices. The supercurrents formed by cooper pairs can also be visualized around the non-superconducting vortex core [13].

to 45 nm. The distance between the vortices decreases with the increasing field and when d is equal to the size of vortex core, the superconductor turns into a normal conductor. [12].

2.1.2 Vortex phases and disorder

The structure of the vortex lattice depends on the magnetic field and temperature and can be divided into three distinct phases; 1) Vortex lattice, 2) Glassy Vortex state, and 3) Vortex liquid phase. The vortex lattice forms when the vortex-vortex distances are fairly large and there are plenty of pinning sites around. On the other hand, the glassy vortex state occurs due to the interactions between the vortices and the structural defects. The defects within the superconductor pin the vortices, which as a result breaks the order of the vortex lattice. Finally, the vortex liquid phase is governed by the thermal energies where the vortices are allowed to move freely, thus causing resistance. This means that the pinning is reduced and vortices are mobile in the vicinity of defects [12].

The vortex order is associated with the interplay of three main energy scales related to vortices, that are, 1) the repulsive energy between the vortices, 2) the attractive energy between the vortices and defects, also known as pinning energy, and 3) the thermal energy, characterized by the temperature, which causes the vortex to vibrate around its lattice position. These three energies determine the phase of the vortex at a specific temperature and magnetic field as shown in Figure 3.

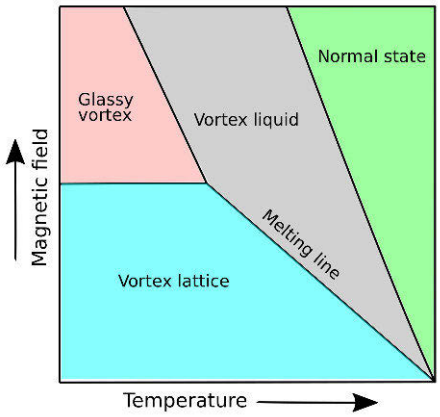

Figure 3. The vortex phase diagram for a HTS [12].

2.1.3 Vortex pinning

As mentioned above, flux pinning is a phenomenon which is totally related to the type II superconductors, where the magnetic field start penetrating inside the superconductor. The movement of the vortices causes resistance in the superconductor. The vortices experience a Lorentz force (F_{L}) upon the flow of the electrical current [14; 15; 16]. $F_{\mathrm{L}} = \Phi \times J$, where Φ is the magnetic flux quantum and J the current density (see Figure 4(a)). The direction of F_{L} is always perpendicular to that of applied current and vortices. Superconductors with structural defects have the potential to pin the vortices, resulting in the minimization of superconducting energy. This phenomenon of pinning the vortices into structural defects is called ”vortex pinning” and is the foundation for electrical applications of superconductors. With the defected structure of superconductor, the vortices experience pinning force (F_{p}), which pins them into the defects. If the applied current exceeds the limit, that is, when $F_{\mathrm{L}} > F_{\mathrm{p}}$, the vortices will be depinned and can move freely. These vortices will cause resistance since the non-superconducting core of the vortex drags through the superconductor. When F_{L}=F_{p}, then the J_{c} is achieved.

Significant progress has been made to introduce the pinning centers or defects within the superconducting film for vortex pinning. The pinning centers differ from each other based on dimensionality (0D$-$3D), size and orientation. The sizes can range from 2$-$3 nm to 40$-$50 nm [17; 18]. 0D pinning defects are nanoparticles and are also known as point defects (Figure 4(b)). The 1D pinning structures are linear in shape, for example, columnar defects (see Figure 4(c)). The 2D pinning centers are twin boundaries, stacking faults or grain boundaries located in planes. Finally, the 3D pinning defects are pores, voids or impurities and their impact is less in vortex pinning but rather they reduce the mechanical properties of superconductor. The

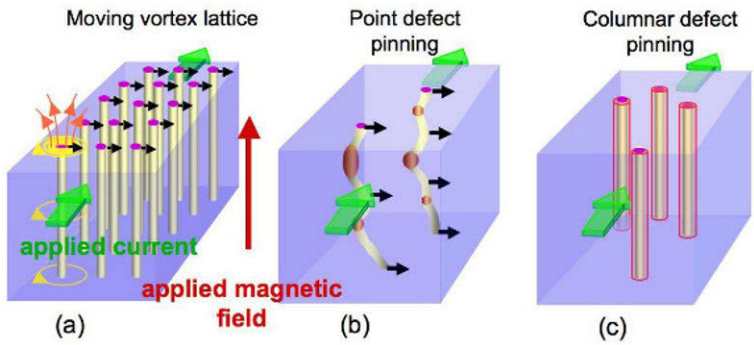

Figure 4. Schematic of (a) the vortices experiencing the F_{L} (black arrows) under applied current and magnetic field in a defect free sample, (b) 0D defects created within the superconductor, which can be oxygen vacancies or precipitates-sections of pinned vortices can be seen, and (c) the 1D defects induced within the superconductor for vortex pinning [12].

1D pinning structures are efficient for high temperatures and their direction is very important as the cuprate superconductors are highly anisotropic [18; 19; 20]. The 1D pinning also has a geometric match with the vortices, thus pinning the vortices most effectively. In ideal cases, the radius of the pinning centers must be the same order than ξ of the specific superconductor [18]. Pinning sites with small size can not accommodate the entire vortex core, whereas large size pinning centers can pin several vortices simultaneously but, on the other hand, they also waste the area of superconducting body [12].

The thermal energies, especially at high temperatures, can supress the vortex pinning phenomenon since the vortices can depin and jump between different pinning sites. This phenomenon is well explained by a vortex path model [21]. The model predicts that each vortex bends itself and wants to be in its ground state by pinning itself in different pinning sites with short intervals. A vortex can be in several defects at the same time since it bends itself and can be pinned both at ab-plane and c-axis oriented defects [21]. Moreover, the model also says that a vortex jumping around different pinning centers can be pinned in one site and, with increasing thermal energies, it gets depinned and see the next pinning site as the potential to be pinned and minimize its energy.

Several methods can be used to introduce pinning centers inside the superconducting films. The conventional one has been through the irradiation of particles, such as, protons [22], neutrons [23], electrons [24] or ions [25]. But these irradiation methods are rarely used now due to their high cost, radioactivity issues and also the pinning centers start disappearing with the passage of time due to thermal instability [26]. Therefore, other methods like chemical reactions are utilized, which prove to

be simple and cheap. In such methods, non-superconducting phases are introduced in the superconducting matrix, which results in the randomly oriented precipitates [27]. Numerous metal oxides, for example, $BaZrO_3$ [28], $BaTiO_3$ [29] or ZnO [30] etc. can be used as non-superconducting phases to act as pinning centers in rare earth based superconductors. The shape of the pinning centers can be 1D columns or 0D spheres, depending on the used dopant and methodology.

2.1.4 YBCO

YBCO discovered in 1987 has a high T_c of 92 K and falls in the category of HTS [31]. YBCO is the first HTS to work above 77 K which is the temperature of liquid nitrogen. Before the discovery of HTS in 1986 [32] by J. Georg Bednorz and K. Alex Müller, all the superconductors had T_c below 30 K.

Figure 5 depicts the unit cell structure of YBCO with lattice parameters a = 3.82 Å, b = 3.89 Åand c = 11.68 Å. The layer structure is: CuO–BaO–CuO_2–Y–CuO_2–BaO. In the CuO_2 plane, the O atoms are bridged between the square lattice of Cu atoms. Y atom is located between CuO planes and Ba atoms are sandwitched between the CuO_2 planes and CuO chains [33]. The supercurrent passes through the CuO_2 planes.

YBCO is intrinsically anisotropic which is related to its crystal structure, where the difference between the parameters of ab-axis and c-axis is quite large [34]. The anisotropy between the a-b planes is quite small and can be neglected. The electronic mass anisotropy corresponds to the intrinsic anisotropy and is defined by the ratio as: $\gamma = \sqrt{m_c/m_{ab}}$, where m_c and m_{ab} are the effective masses in c and ab-axis, respectively. The γ can vary from $2-7$ [35; 36; 37; 38], where lower values correspond to more isotropic behaviour of J_c. The same anisotropic behaviour is seen in the B_{c2} of YBCO, where B_{c2} is six times larger in the in-plane than in the out-of-plane axis [38]. Pure YBCO would have an anisotropic $J_c(\theta)$ curve, similar to the BCO doped $J_c(\theta)$ curve (Figure 7(b)), which is due to the electron mass anisotropy, but with sharper a/b-peaks.

The structure of YBCO is highly dependent on the oxygen content, that is, when oxygen is less than 6.4 the material is tetragonal and non-superconducting because of lack of O atoms in CuO chains [33; 39; 40]. By increasing the O content, the CuO chains are filled with more O and transition from the tetragonal to orthorhombic phase occurs. The transition from the tetragonal to orthorhombic phase occurs during the thin film deposition process where additional O is added at atmospheric pressure [40; 41].

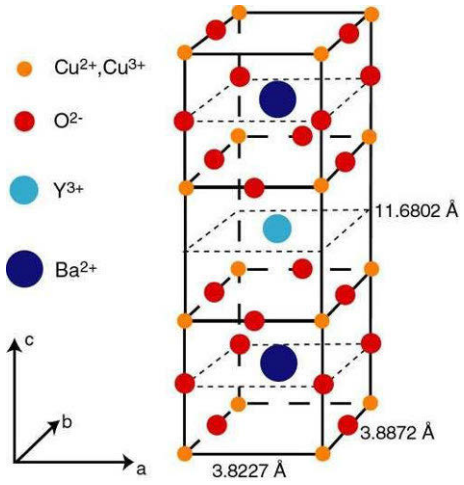

Figure 5. Orthorhombic structure of YBCO [42].

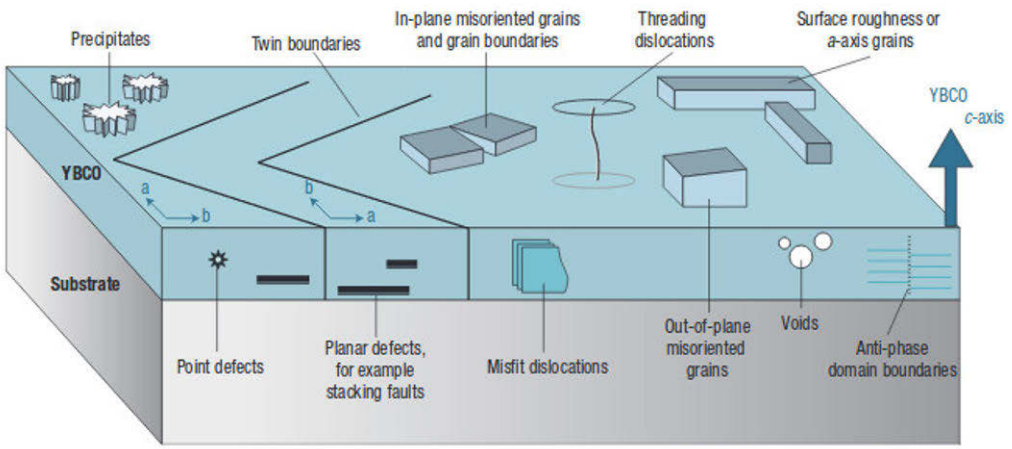

Figure 6. Different types of naturally occuring defects in YBCO matrix during growth process which can be effective for vortex pinning [43].

2.1.5 Defects in YBCO

The defects within YBCO films can be categorized as natural and artificial. The natural defects are formed during the film growth process, where twin boundaries are the common ones due to the transition from tetragonal to orthorhombic phase. Twin boundaries are the result of swapping of a and b axis. The stacking faults also arise within YBCO films which occur when the layered structure is perturbed. A schematic of natural defects, which may arise in YBCO films, is presented in Figure 6.

The artificial defects are introduced within the YBCO films via dopants or irradiation methods (explained earlier). Different dopants can induce artificial pinning defects with varying size, shape or orientation thus strongly enhancing the superconducting properties [28]. Preference is given to those dopants which can induce nanorods within YBCO matrix, for example, $BaZrO_3$ (BZO), $BaHfO_3$ (BHO) and $BaSnO_3$ (BSO) structurally growing as nanorods by the physical method [44; 45; 46; 47; 48]. However, these induced nanorods differ from each other in terms of their sizes [48]. Contrary to these nanorods producing dopants, $BaCeO_3$ (BCO) grows in the form of nanosized spherical particles [49].

The most commonly used dopant has been cubic perovskite BZO due to its relatively low lattice mismatch with YBCO, that is, 9% in-plane lattice mismatch [50; 51]. The diameter of BZO nanorods range from $5-10$ nm and their density depends on the doping concentration [52], for example, 1300 $1/\mu m^2$ for 2.9 wt.$\%$ BZO in YBCO [53].

Strain is induced in YBCO upon doping and the dopant growth is highly dependent on growth conditions. The YBCO c-axis lengthens when strain arises and the T_c slightly decreases [54; 55]. The length of nanorods can easily vary depending on the growth temperature T_g [56]. Moreover, the dopant growth also depends on the methodology, for example, nanorods are formed by pulsed laser deposition and nanodots by chemical solution deposition [57; 58; 59]. Furthermore, the density of stacking faults can also be increased by growing YBCO at high temperature but there is a limit to that too [60].

If the critical current of the sample is measured by applying magnetic field in different orientations, it is found to vary with respect to the direction and strength of the applied field. In short, such measurements are known as angular dependent critical current density ($J_c(\theta)$). Generally, the undoped YBCO films show more anisotropic $J_c(\theta)$ curves than doped YBCO [61]. The dopant orientation, along the c-axis gives rise to a c-peak in $J_c(\theta)$ curves when the field is applied parallel to c-axis of YBCO film. On the other hand, the vortex pinning by in-plane defects usually give rise to ab-peaks in the $J_c(\theta)$ curves when the magnetic field is applied parallel to the plane of sample. The $J_c(\theta)$ of our BZO doped YBCO films is isotropic at low fields but starts getting more anisotropic with increasing magnetic field [47; 62; 36].

But even this depends on the method used to deposit the films, that is, more isotropic behaviours are observed both at low and high applied magnetic fields by utilizing PLD [44; 45; 47; 52; 63; 64; 65; 66], as highly anisotropic $J_c(\theta)$ is achieved by any other chemical method [59; 67; 68]. However, pinning enhancements by other methods have been already achieved and several groups are still working for further improvements [69; 70; 71; 72; 73; 74; 75]. Both chemical and physical methods have their own advantages, that are, the former is fast and films with large areas can be deposited, whereas in the latter with better control on the thickness of films one can achieve high and isotropic J_c via growing and controlling the size, shape and density of pinning centers during the deposition process [76; 77].

Figure 7 displays the schematics of vortices trapped in different pinning landscapes thus resulting in varying shapes of $J_c(\theta)$ curves. With an undoped YBCO film, there occurs a network of natural pinning landscape, such as, threading dislocations, voids or pores. The pinning phenomenon by in-plane defects gives rise to ab-peaks, whereas the c-axis oriented threading dislocations pin the vortices thus producing c-peak in $J_c(\theta)$ curve. The intensity of this c-peak is very small and usually a large network of threading dislocations occurs on buffered metal where the low angle angle grain boundaries channel the growth of YBCO [62]. The schematic of vortices pinned in these threading dislcoations in undoped YBCO is illustrated in Figure 7(a)). Spherical particles pin the vortices in several pinning sites since the vortices can not fit themselves in a single defect, as depicted in Figure 7(b). Finally, the induced nanorods within the YBCO film are most effective for achieving the highest J_c and reducing the anisotropy of $J_c(\theta)$ as a vortex can be pinned in a single nanorod and, in some cases, can also be in two nanorods simultaneously thus giving pronounced c-peak (Figure 7(c)).

The diameter, length and splay of nanorods are important parameters since they affect the pinning phenomenon. Large diameter of nanorods can pin more vortices at a time and the c-peaks are observed to be highly pronounced for YBCO films with large defect diameters [46]. On the other hand, the shorter length of nanorods are less effective for vortex pinning than the long sized nanorods, which reduces the pinning along c-axis, thus diminishing the intensity of c-peak [47]. Moreover, large splay of nanorods lead to wide c-peak but there is still less variation in $J_c(\theta)$. The J_c is decreased when magnetic field is inclined away from c-axis which reduces the length of trapped vortex [78; 79]. At sufficient inclination, the vortex region gets untrapped where $J_c(\theta)$ reaches the minimum. All these factors affect the shape of $J_c(\theta)$ and are shown by results in the discussion section. Furthermore, the ab-peaks in all the $J_c(\theta)$ curves of Figure 7 arise mainly due to pinning by in-plane defects, such as, stacking faults etc. but the wide ab-peaks with shoulders can arise due to pinning together by in-plane and out-of-plane defects [78].

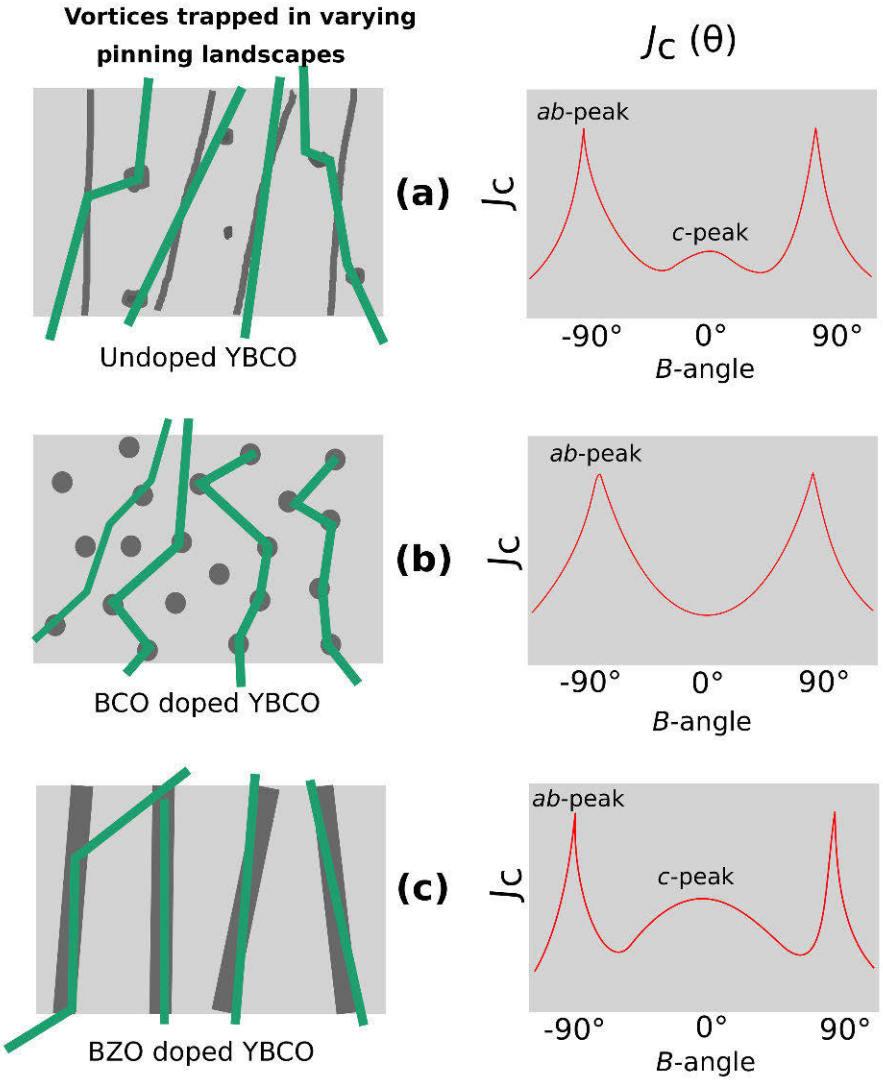

Figure 7. An illustration of vortex trapping in varying pinning landscapes corresponding to different $J_c(\theta)$ curves. Dark grey colour represent several kind of defects, whereas vortices are displayed in dark green colour. (a) Vortex pinned in natural defects like threading dislocations (long threads) or voids where slight c-peak is seen, (b) Vortex pinning by spherical nanoparticles which enhances the $J_c(\theta)$ values, and (c) vortices pinned by nanorods with pronounced c-peaks.

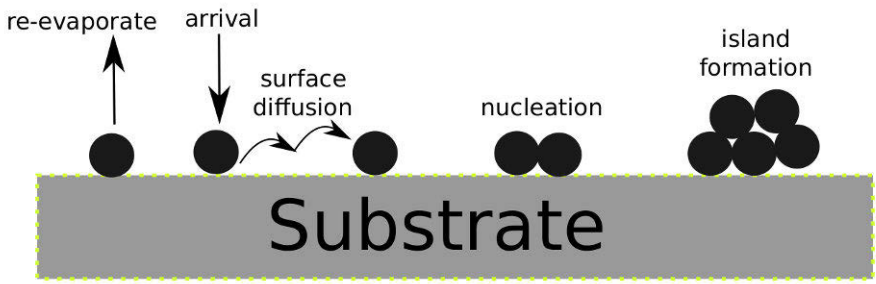

Figure 8. Schematic of atomic level of growth mechanism for YBCO films grown by PLD process. The black circles are atoms and their mergence for island formation is shown.

2.1.6 YBCO growth mechanism

The YBCO growth in pulsed laser deposition (PLD) process occurs by the Volmer-Weber growth model [80; 81]. The first atom deposited diffuses across the surface of substrate and, with the arrival of second atom, makes bonds with other atoms thus forming an island. This island formation leads to higher mass and less mobility on the substrate. With the ever increasing number of atoms reaching the substrate, more and more islands are formed which are 3D in shape and have greater size and stability. Several islands merge together and form larger sized particles where the size can be in the range of micrometer. The stability of islands depends on their size, that is, smaller islands can break easily and the remains can bond with larger sized islands. On the other hand, islands with larger size are more stable, hard to break and less mobile. The schematic of this growth process is presented in Figure 8.

In the YBCO growth process, the substrate temperature is crucial since low T_{g} leads to small diffusion lengths for atoms which forms islands with smaller size, thus having the higher probability of their break down. The density and size of structural defects also depend on the T_{g} [47; 60]. The shape of artificial defects also changes with different methods, that is, the BZO dopant grows as nanorods and particles with PLD and CSD processes, respectively [59; 57; 58].

2.2 Coated conductors

Superconductors deposited on lengthy buffered tapes are referred to coated conductors. There are mainly two methods by which the buffered tapes are manufactured: Rolling assisted biaxially textured substrates (RABiTS) and ion beam assisted deposition (IBAD).

2.2.1 RABiTS and IBAD

The presence of weak links in grain boundaries of YBCO conductors on metal substrates is the chief obstacle in manufacturing as it halts the flow of current in non-superconducting regions. This can be overcome by aligning the grains of the underlying substrate which excludes high angle grain boundaries and allows more current to flow. By applying RABiTS, nearly perfect biaxial texture is achieved of the substrate which is followed by the buffer layers and superconducting material deposited on the top of it. In RABiTS, nickel or its alloy (often NiW) is used as the base metal. In the first phase of this process, Ni alloy is biaxially textured through thermomechanical process of rolling deformation and then heat treated. As a result, a face-centered cubic texture of the metal is formed. Then the buffer layers are deposited, via sputtering or electron beam, to combat the diffusion of metal into the superconducting layer grown on the top of cap-layer [82].

Unlike in RABiTS, the metal base (hastelloy) is untextured in the IBAD method but rather the subsequent buffer layers provide the textured base for the growth of YBCO. There are two main types of IBAD texturing, that are, Yttria stabilized zirconia (YSZ) [83] and magnesium oxide (MgO) [84]. IBAD, if applied with YSZ layer, is a slow process but if extended with MgO the process is quick as compared with conventional YSZ buffer layer [84; 85]. So IBAD-MgO has replaced YSZ layer due to its less thickness of only few nm in a time span of only a second [86].

In the IBAD method, MgO is grown on the amorphous layer and it is simultaneously etched by Ar^+ ions bombarding on MgO layer at an angle of 45°. The energy of Ar^+ ions can range from $600-1000$ eV. In this way, MgO grows with (001) out-of-plane orientation [87]. Through this method a uniform biaxially textured MgO layer is produced which acts as a seed layer to grow epitaxially textured layers on the top of it. The YBCO grows heteroepitaxially on the top of cap-layer, where strain occurs on the interface and then the growth is relaxed with increasing thickness.

Conclusively, the buffer layers in both RABiTS and IBAD processes act as a texture base and the reaction barrier between the YBCO and base metal. Both the RABiTS and IBAD-MgO produce qualitatively similar results but some other factors like cost, thickness and processing time can cause differences [88]. All the work in this thesis was carried out on the IBAD-MgO based buffered metal.

2.2.2 Substrates

The substrates are highly important for the deposition of HTS films. Small lattice mismatch, similar thermal expansion and zero chemical interaction between HTS and substrate are desired. Furthermore, the substrates for coated conductor applications must have good textured surface on the top, be mechanically strong and abundant which makes them cost effective. Out of many, the following substrates

Table 1. Examples of buffer layers deposited on different buffered substrates with resulting textures on top layer [101; 102; 103; 104].

Buffer layer configuration	Texture
$SrTiO_3$/YSZ	Polycrystalline [101]
$SrTiO_3$/$LaAlO_3$	Biaxial [101]
$LaAlO_3$/CeO_2/YSZ	Amorphous [101]
CeO_2/YSZ/CeO_2/Ni	Biaxial [105]
CeO_2/$LaMnO_3$/IBAD-MgO/Y_2O_3/Al_2O_3/C276	Biaxial [36]
$LaMnO_3$/IBAD-MgO/Y_2O_3/Al_2O_3/C276	Biaxial [36; 106]
$LaMnO_3$/MgO/IBAD-MgO/Y_2O_3/Al_2O_3/C276	Biaxial [36; 106]

have been used as base materials for the growth of HTS films in the past: $LaAlO_3$, $SrTiO_3$, MgO, YSZ, $LaGaO_3$, $NdGaO_3$ and Si etc. [89; 90; 91; 92; 93; 94]. The structure of these substrates vary and are applied for different HTS materials, where the afore-mentioned parameters are taken into account to better match the HTS and substrate [95]. Typically, HTS films have been grown on $LaAlO_3$, $SrTiO_3$ and MgO substrates. YBCO films grown on $LaAlO_3$, $SrTiO_3$ have lattice mismatch from 1% to 2% and high J_c is achieved [96], but the main drawback of these substrates are the inflexibility and high cost. MgO and YSZ substrates with lattice mismatch to that of YBCO is 9% and 6%, respectively, but the problem lies in the instability of MgO in air and if YBCO is grown on YSZ, the formation of $BaZrO_3$ occurs [96; 97; 98]. The reaction between Si and YBCO film is even more serious than that of YSZ. So to tackle these reaction, inflexibilty and cost problems, buffer layers are used on the top of flexible metals.

2.2.3 Buffer layers

As discussed above, the buffer layers are to enable the better growth of YBCO by stopping the diffusion from metal and also to get the texturized cap-layer. Many different configurations of buffer layers have been used to improve the growth of YBCO. Some of the buffer layers deposited on single crystals along with achieved texture are presented in Table 1. As can be seen from Table 1, differently fashioned buffer layer stacks lead to varying textures, that are, biaxial, polycrystalline and amorphous. Usually for the growth of YBCO, a biaxial texture is required for the cap layer. Depending on the buffered material used, there can be differences in the average grain misorientations coming from the underlying cap-layer [99]. This misorintation angle can range from 2° to 10° depending on the substrate. It is observed that the YBCO grain misorientation is less when hastelloy C276 was used as compared with NiW [78; 100].

Significant progress has been made for the better growth of YBCO supercon-

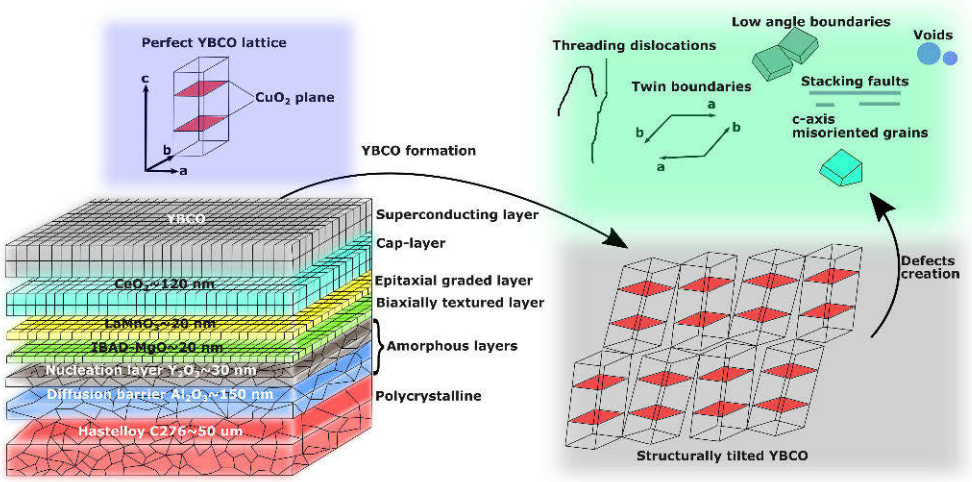

Figure 9. Schematic of buffered metallic template and the growth of YBCO on the top of it. It can be seen that the YBCO lattice grows tilted on such a metal with many naturally occuring defects.

ductor on buffered metallic templates. The Hastelloy C276 tapes used in this work are easy to handle and flexible. Different buffer layer stacks have been used in this work for achieving better superconducting properties. As in IBAD process, a biaxial texture is produced on the cap-layer and a grain misorientation of 2° to 3° can be achieved for YBCO which is comparable to that when grown on single crystal [99].

A schematic example of one of the buffered metal (used in this work) and how the YBCO grows on a typical metal is shown in Figure 9. This stack was manufactured by IBAD method. The first two layers on top of hastelloy C276 are amorphous, where Al_2O_3 is a diffusion barrier to prohibit the diffusion of material from C276, and Y_2O_3 act as a nucleation layer for the growth of textured layers. The biaxially textured MgO layer is fabricated through IBAD on nucleation layer and then $LaMnO_3$ layer is epitaxially grown on the top of this IBAD-MgO layer. Once a great texture is achieved, the cap layer of CeO_2 is fabricated with the purpose of having low lattice mismatch between YBCO and the buffer layer stack underneath.

All the buffered metallic substrates utilized in this work were manufactured and provided by our collaborator Dr. Yue Zhao affiliated with Shanghai Jiao Tong University and Schanghai Superconductor Technology Co. Ltd., China. With the passage of time, some advancements were made in provided substrates with respect to varying thicknesses and moficiations of buffer layers. In general, the used substrates were not completely novel but were named as advanced due to certain modifications. Since the YBCO films were grown directly on provided substrates, so expertise on technical substrates is out of the scope of this thesis.

3 Experimental

3.1 Target synthesis

In this thesis, the YBCO targets were synthesized by two different methodologies, that are, 1) solid-state ceramic reaction, and 2) sol-gel process. The first method leads to the target grain size in micrometer range, whereas the second one gives us the target with nanometer grain size (ca. 60 nm) **[V]**. The dopants were also added in both the processes to understand the differences in sizes of induced defects within produced films. The recipies of both the processes can be found in [107; 108; 109; 110]. The undoped and BZO doped targets used in **[V, VI]** had densities of 76 %, 80 %, 86 % and 75 % for μ-YBCO, μ-YBCO+BZO, n-YBCO and n-YBCO+BZO, respectively **[V]**. All targets used for depositing the films were synthesized by my colleagues Dr. Jussi Tikkanen, Dr. Veer P. S. Awana and Dr. Rajveer Jha.

3.2 PLD

PLD is a technique used to grow the films of various thicknesses on different substrates. It is a suitable method to homogeneously grow the films of complex oxide materials as it has an advantage of stoichiometrically transferring the material in gas flow. The schematic of PLD process is illustrated in Figure 10. The laser beam of UV wavelength is directed towards the target material (pellet) through an optical window. The laser beam firstly hits the target, then heats and ablates off the material thus transferring it to the substrate in the form of a plume. The material then recondensates on the surface of the substrate via merging of atoms, ions or formation of islands. The substrate is heated with an infrared laser and the film is deposited at an optimized T_{g}.

Substrates are chosen based on two facts: 1) small lattice mismatch between the substrate and the target material and 2) the intended application of the film, for example, YBCO is grown on $SrTiO_3$ (STO) to comprehensively understand the growth mechanism, and on buffered metal for the large scale coated conductors. On the other hand, MgO can be used due to its suitable dielectric constant for microwave applications [111]. In this work, thin films were deposited on STO and differently buffered metallic substrates.

Depending on the structure of the metallic substrate and the wanted growth of

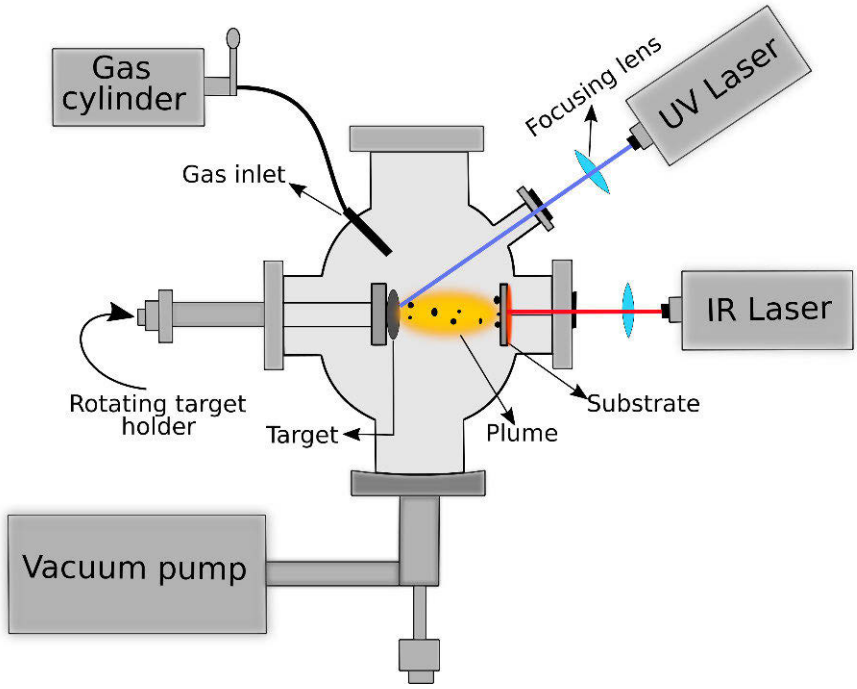

Figure 10. The schematic of PLD process used in this work.

artificial pinning sites, T_gs were tuned while the rest of parameters were kept constant except the number of pulses for achieving films of varying thicknesses. All the substrates were attached to the sample holder with silver paste for better thermal conductivity.

Firstly, the PLD chamber was pumped with scroll and turbo pumps to reach high vacuums while oxygen was also introduced to avoid the reduction of oxygen from the substrate and target. The substrates were heated up to desired T_gs (700 °C−775 °C) with 25 °C/min heating rate and constant flow of oxygen under the pressure (1.75×10^{-4} torr). Then the excimer XeCl laser pulses were shot (5 Hz frequency, 1.3 J/cm^2 energy and wavelength, λ = 308 nm) on the target to deposit the films. After the deposition, oxygenation and post-annealing were done at temperature which is 25 °C lower than the T_g, usually 700 °C to 750 °C, since the introduction of oxygen leads to the phase transition of YBCO from tetragonal to orthorhombic phase at this temperature [112]. The post-annealing treatment was done for 10 minutes and after that the film was cooled back to room temperature at 25 °C/min rate.

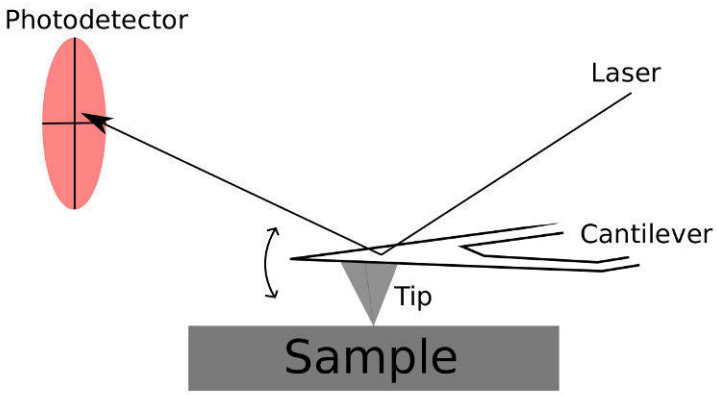

Figure 11. The schematic of basic operation of AFM.

3.3 AFM

The surface microstructure of films can be accurately measured by atomic force microscopy (AFM). In this method, the probe or triangular tip is attached to the cantilever and upon pressing down the tip with constant force, it interacts with the surface of film and scans over surface area where the probe senses the variation of interaction force thus creating deflections in the cantilever. The deflections in the cantilever are measured by a photodetector thus compiling the topographic image of the surface [113].

The two main operational modes of AFM are: contact and non-contact. In the contact or repulsive mode, the tip touches and scans the surface of the sample. The force interacting between the tip and the sample is repulsive. In the non-contact or attractive mode, the tip is brought closer to the sample and the long-range attractive force is sensed by the tip. The cantilever is oscillated at high or resonant frequency in non-contact mode. The sensitivity of AFM decreases with increasing vibrations produced at high frequencies. Therefore, relatively stiff material, for example, silicon or silicon nitride are used to manufacture the cantilever so that high resonant frequencies can be ensured. The resonant frequencies can be in the range of $10-100$ kHz [114].

In this work, AFM was used in contact mode to measure the surface topography, roughness and thickness of films after etching. Depending on the films grown from different grain sized or modified targets and at varying temperatures, the surface roughness and the size of the particles vary. The image sizes were in the range of 2×2 μm^2 to 50×50 μm^2.

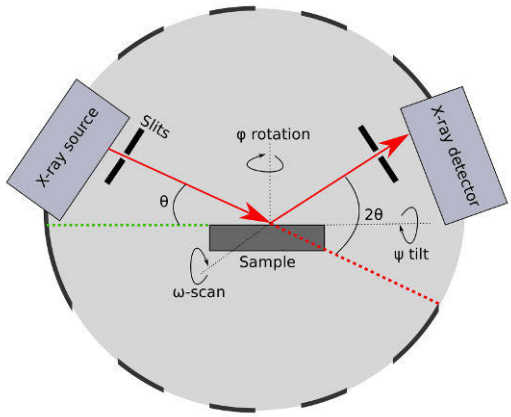

Figure 12. The schematic of a typical XRD measurement set-up.

3.4 XRD

The structural analysis of the samples can be done by using x-ray diffraction (XRD). The main principal of XRD lies in the Bragg's formula [115]

$$n\lambda = 2dsin\theta, \tag{2}$$

where λ is the wavelength of x-ray source, d the spacing between the atomic planes and θ is the angle between the incident and scattered x-ray. Upon exposing the sample with x-rays, all electrons of the atoms participate in the scattering of the x-rays. The re-emitted x-rays are then recorded by the detector functioning opposite to x-ray source. In order to obtain the diffracted peaks, the scattered waves must be in-phase. Deeper in the planes, the x-rays travel more so to get the constructive interference, the path difference must be equal to integer number of wavelengths. This integer is denoted by n in above equation [115].

Figure 12 depicts a basic XRD set-up which is used for measuring different samples. The diffractometer consists of two main axis, that are, 2θ and ω. The 2θ angle refers to the detector axis, whereas ω for sample's axis. The soller slits are used to reduce the noise, angular dispersion and also for improving beam's resolution on the detector side. The sample can be rotated and tilted at different angles by utilizing ϕ and ψ scans, respectively [115]. ψ is the angle when the sample is tilted, whereas ϕ is the angle when the film is only rotated.

An Empyrean XRD was used to structurally measure all the samples, where Cu K_α source producing x-rays with a wavelength of 1.54 Å. The Cu K_α radiation was filtered by an x-ray mirror (the Bragg-Brentano HD) in front of the source. The soller slits of 0.04 rad. were used to cut-off the non-parallel rays. Since, unlike

powder samples, thin films do not necessarily have all the crystal orientations and positioning the films is very important.

In this work, $\theta - 2\theta$ scans were performed to know the phase purity in the films and also for determining the c-parameter by using the (004), (005) and (006) peaks. The oxygenation level in the films was also determined by intensity ratios: $I(005)/I(004)$. For more detailed analysis, the (102) ϕ (2θ = 27.8°, ψ = 56° and 31°) and (005) ω (2θ = 38.6°, ψ = 0°) scans were also done to reveal the in-plane variations and out-of-plane crystallographic ordering. Moreover, the oxygen level for YBCO films was also calculated by taking the intensity ratio of (005) and (004) peaks.

3.5 TEM

In transmission electron microscopy (TEM), a beam of electrons is used to probe the sample. The electrons are produced by the tungsten filament and are then accelerated by an electron gun towards the focussed lenses. In this way, the TEM consists of an electron source, lenses and a detector. Firstly, the sample is positioned in front of the electron beam. Then the beam is accelerated and focused onto the sample by lenses. The lenses are simply coils which can be moved to adjust the electron beam. The beam, after passing through the focusing lens, then hits, transmits through the sample and is magnified by the magnification lens thus finally imprinting the image on fluorescent screen.

One type of TEM is the scanning transmission electron microscope (STEM), which takes the image from a specific part of sample, not the whole sample. The scanning of surface here again allows to visualize the magnified image of the sample. TEM can take both bright and dark field images. The bright field (BF) images provide dark or light contrast between different parts of taken images. The BF images refer the crystalline or heavy mass density areas to be dark, whereas vice versa for dark field images. In BF imaging, the transmitted electrons are passed through the aperture but the scattered electrons are blocked, which is opposite to that of the dark field. The entire setup of TEM is enclosed in a vacuum chamber to avoid the dirt and energy losses of the electron beam.

In this thesis, bright field image of TEM were produced by utilizing BF-TEM option. The BF-TEM was carried out by utilizing a Cs-corrected JEOL JEM 2200FS instrument operating at 200 kV. The samples were prepared by cutting a cross-sectional lamella via the Focused Ion Beam (FIB) technique in a FEI Nova 600 Nanolab Dual Beam FIB-SEM. The lamella were extracted using the *in-situ* lift out procedure with an Omniprobe extraction needle. All the TEM work was done by the facility staff of Ghent University, Belgium.

3.6 Magnetic measurements

A Quantum Design Physical property measurement system (PPMS) was utilized to measure the magnetic moments of superconducting films via AC measurement system (ACMS). The system can be used in DC or AC mode. While using DC mode, the system acts as a vibrating sample magnetometer where the applied magnetic field is firstly applied to the sample which induces magnetic moments in it. The sample is then vibrated and in response the change in flux, proportional to magnetic moment, is detected in the pick up coils thus giving the DC magnetization. On the other hand, in AC mode, the sample is excited by applying AC magnetic field and as a result AC magnetization is measured. This AC signal induces a change in the magnetic moments of the sample which is recorded as another signal, which is proportional to $dM/dH$where M is magnetization and H is the excitation field.

T_{c} of all the samples were measured by utilizing AC mode of PPMS, whereas DC measurements for calculating the J_{c}. The AC magnetization for all the samples was performed from 100 K down to 10 K by scanning 0.1 mT AC field with 113 Hz frequency. The onset T_{c} is the temperature where the real part of the magnetization curve deviates from that of the imaginary part. The deviation point is where the transition starts from the normal to superconducting state. The DC magnetization curves were measured at 10 K and 77 K under the magnetic field from -8 T$-$8 T. The magnetic field dependent J_{c} can be easily determined from the measured hysteresis loops of samples by using Bean critical state model for rectangular films. The Bean model for thin films measured by applying magnetic field perpendicular to the film is

$$J_{\mathrm{c}} = 2\Delta m/[a(1 - a/3b)V], \tag{3}$$

where a is the width and b the length of the sample with $b \geq a$, V is the volume of the film and Δm is the opening of the hysteresis loop [116]. Δm is equal to $m_{-}(B) - m_{+}(B)$ and subscripts +,- describe the increasing and decreasing magnetic field.

The Bean critical state model assumes that the flowing current within the sample is either J_{c} or zero. The J_{c} is dependent on the vortex density which increases and decreases with the increasing and decreasing magnetic field, respectively. Upon increasing the field, the vortices start to enter from the sides of the sample and leave when the magnetic field is decreased. Thus the slope of magnetic field within the sample is realised. This is proportional to J_{c}.

3.7 Transport measurements

For measuring the angular dependent $J_{\mathrm{c}}(\theta)$, the samples were etched for performing the four-probe measurements. After spin coating the photoresist on the samples,

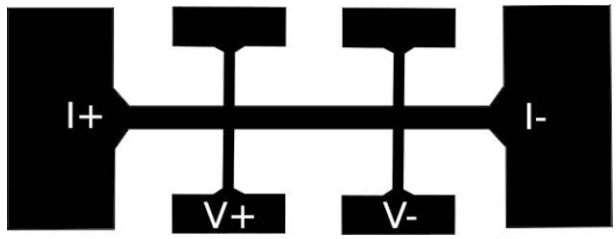

Figure 13. Stripes developed by wet chemical etching to carry out the transport measurements.

they were dried at 80°C and then exposed by UV light. The as-exposed samples were developed by rinsing in NaOH solution and finally etched in H_3PO_4 solution.

The schematic of etched pattern is shown in Figure 13, where the stripe width is 50 μm and 200 μm for films on STO and metallic substrates, respectively. For performing the transport measurements, contacts were made on the current and voltage pads of samples and pucks by using Al wire in TPT wire bonder. Then the current was ramped through the electrical circuit, in zero magnetic field, and once a threshold voltage is reached the maximum critical current I_c is measured. This I_c is the limit for measurements under applied magnetic fields. Of course, the I_c varies from sample to sample but the voltage limit was set to 215 μV/cm to protect the samples. The measurements were done from 0° to 360° under applied magnetic fields ranging from 0 T to 8 T and at different temperatures (usually 40 K). The field was parallel to sample at 0° and then the sample rotated with 3° of steps, once each data point has been measured. Finally, the $J_c(\theta)$ was calculated by using formula: $J_c = I_c/A$, where A was measured with AFM. The typical maximum currents achieved with our patterned films were from 200 mA to 300 mA at 10 K, varying among different samples. The current ramp was 240 mA/s for each measured data point. Since the critical currents were quite low, that is, in mA range so the heating is not expected during the measurements.

4 Results and Discussion

4.1 YBCO layer optimization

4.1.1 Growth temperature optimizations

On a typical buffered metal substrate as shown in Figure 14, we optimized the T_g for undoped and doped YBCO **[I, II]**. The structural and superconducting properties showed that T_g is highly important for better applications of coated conductors. The T_gs were optimized in view of obtaining homogeneous films with better pinning landscape resulting in high J_c under wide magnetic field and temperature range.

YBCO films with varying T_g were grown on the buffered metal (Figure 14) with 1600 pulses. The basic structural and magnetic properties showed that T_g = 725 °C is optimal for the thickness dependent series **[I]**, which is discussed in the next section.

The T_g was also optimized for the doped films where two types of dopants were introduced within the YBCO matrix, that are, BCO and BZO **[II]**. For comparison, the structural parameters of all the deposited films are tabulated in Table 2. As can be seen, the T_g affects the in-plane and out-of-plane growth of doped YBCO films which in return has an impact on superconducting properties. The YBCO grown at 700 °C, 750 °C and 800 °C show slightly higher values of c-parameter than the nominal value of YBCO c-axis, as measured elsewhere [117]. Contrary to BCO dopant, all the BZO doped YBCO films have slightly elongated c-axis. However, for both cases, the YBCO films grown at 650 °C show large deviation from the nominal value in c

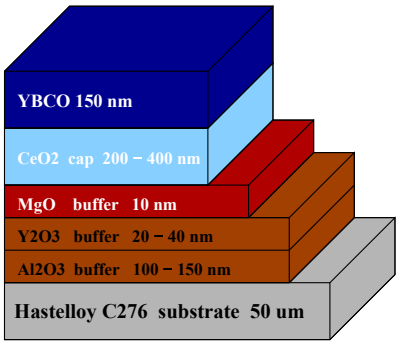

Fig. 14. The schematic of buffered metal on which the undoped and BCO, BZO doped YBCO films with various thicknesses were grown **[I]**.

Table 2. Comparison of structural parameters for undoped, BCO and BZO doped YBCO films grown at different temperatures **[II]**..

T_g(°C)	YBCO lattice c (Å)	$\Delta 2\theta$ (005) (°)	$\Delta\phi$ (102) (°)	$\Delta\omega$ (005) (°)	I(005)/ I(004)
YBCO + BCO					
650	11.78	0.62	4.13	2.25	16.06
700	11.71	0.44	4.04	1.62	15.24
750	11.71	0.37	3.86	2.30	13.98
800	11.70	0.26	4.12	1.95	16.23
750 (STO)	11.68	0.23	1.35	0.47	14.97
YBCO + BZO					
650	11.79	0.58	4.45	2.43	16.34
700	11.73	0.34	4.30	2.66	11.38
750	11.72	0.22	4.40	1.64	12.25
800	11.74	0.21	4.28	2.15	13.97
750 (STO)	11.72	0.22	1.06	0.29	12.94

lattice parameter. Moreover, the $\Delta 2\theta$ values for doped samples, extracted from (005) peaks, reveal that the variation of unit cells is smaller with increasing T_g. The films deposited at 800 °C showed half the $\Delta 2\theta$ values to that of films deposited at 650 °C. The BCO doped film at 750 °C revealed similar $\Delta 2\theta$ value to that when grown on STO [49]. Furthermore, the in-plane $\Delta\phi$ values stay about the same for both the BCO and BZO doped films. $\Delta\omega$ values, showing the crystallographic orientation along c-axis, revealed less values as compared to that of YBCO films deposited on NiW substrate [89]. As can be seen from Table 2, $\Delta\phi$ and $\Delta\omega$ values for films on STO are four times smaller than those on our buffered template, which shows that these peak widths of ϕ and ω are solely because of metallic template which does not allow fully epitaxial growth of YBCO layer. The oxygen deficiency for both the BCO and BZO doped films, seen from intensity ratio I(005)/I(004) peaks, was well in range of $\delta < 0.1$ [55].

Figures 15(a,b) depict the performed T_c measurements for BCO and BZO doped YBCO films. In both the cases, the T_c is noticed to be the highest for the films grown at high temperature and it decreases with decreasing T_g. It was observed that BCO and BZO doped films deposited at intermediate temperatures have the highest J_c (Figure 16 (a,b)). This is related to the change of dopant morphology with respect to T_g. Similar results were also reported in previous work [56], where the intermediate temperature range works best for dopant growth. In our case, it was 750 °C. BZO growth as elongated nanorods within YBCO can easily turn into shortened and highly splayed nanocolumns when films are grown at very low or too high temperatures [56]. The insets of Figures 16(a,b) reveal the effect of T_g on the accommodation field B^*, which is defined as the end point of the low field plateau of

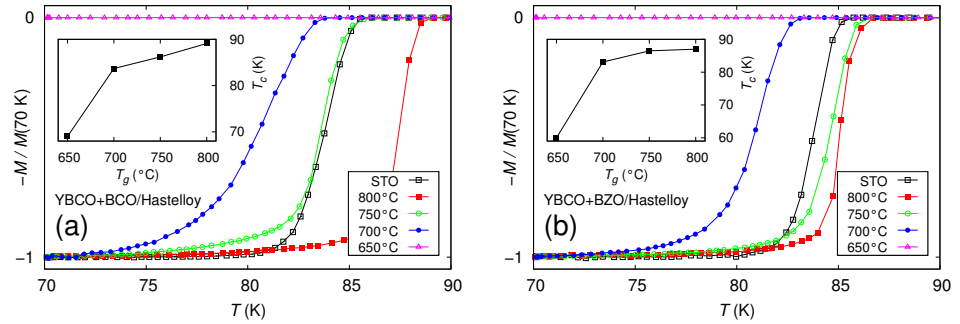

Fig. 15. Ac magnetization curves as a function of temperature for (a) BCO doped and (b) BZO doped YBCO films deposited on buffered metal at different T_{g}s. The films on STO are given for comparison. The insets show the T_{g} dependence of T_{c} in different set of samples **[II]**.

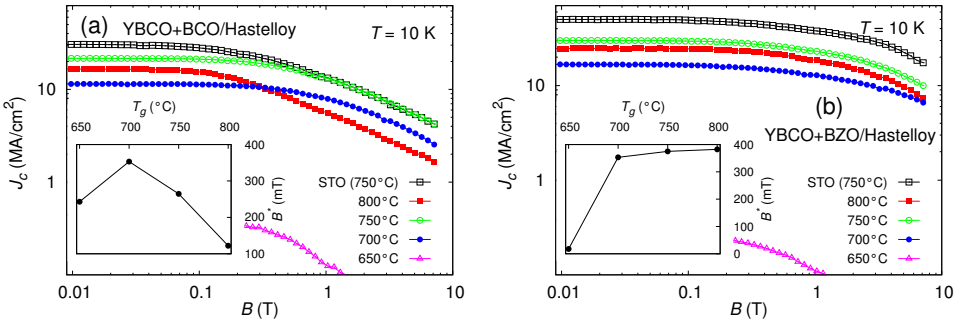

Fig. 16. J_{c} curves as a function of applied magnetic field at 10 K for (a) BCO doped and (b) BZO doped YBCO films, grown at varying T_{g}s on buffered metal and at 750 °C on STO. The insets show the dependence of the B^* on T_{g} **[II]**.

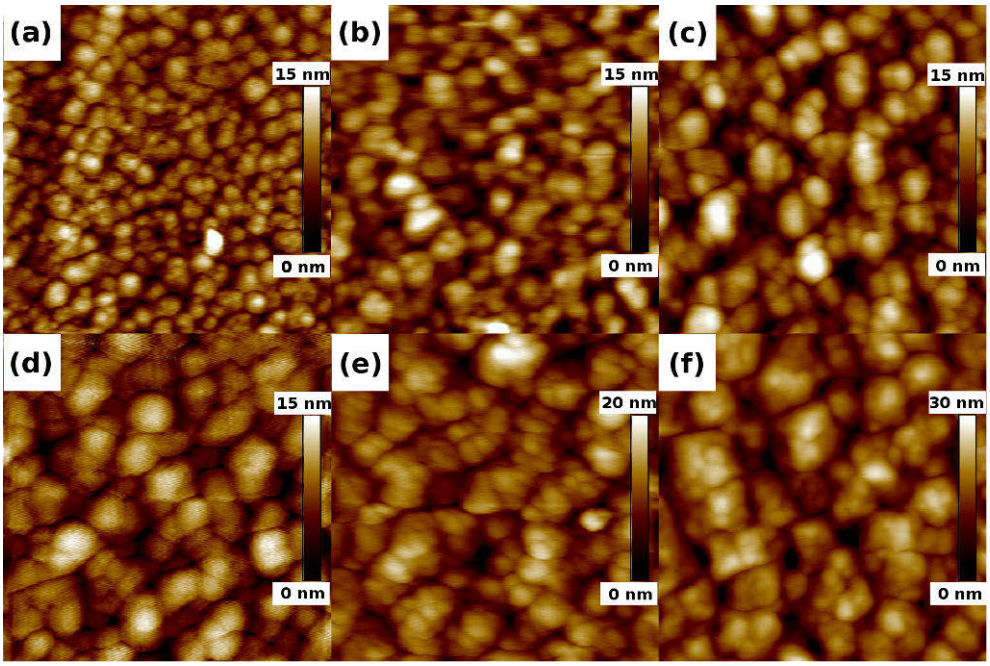

Figure 17. (a)−(f) AFM images (2×2 μm^2) of the YBCO films with varying thicknesses of 60, 115, 205, 295, 480 and 670 nm, respectively. The values for height scale bars are mentioned in each subfigure **[I]**.

J_c, which in this work is J_c = 0.9 $J_c(0)$ [118]. The single vortex pinning dominates below the B^* but the interactions between vortices are significant above B^* [119]. In BCO doped films, with the initial increase of B^*, it starts decreasing with increasing T_g. Contrary to this, the B^* jumps at 700 °C and is approximately the same above that with increasing T_g.

4.1.2 Optimization of film thickness

Thicker films are desired in coated conductors to pass through high currents. Films with 500, 1000, 2000, 3000, 5000 and 8000 laser pulses were deposited at T_g = 725 °C, which resulted in thicknesses of 60, 115, 205, 295, 480 and 670 nm **[I]**. The 2×2 μm^2 surface images (Figure 17) scanned through AFM revealed the merging of particles leading to the formation of larger islands with the increasing number of laser pulses. The thinnest film had only on an average 25 nm particle diameter compared with the thickest ones (480 nm and 670 nm), with 100−200 nm particle diameter. The surface roughness, RMS values, for all the films are presented in Figure 18(a). The surface roughness increases moderately up to films with 300 nm thickness, but above that a rapid increase is observed. On the other hand, the 20×20 μm^2 surface image

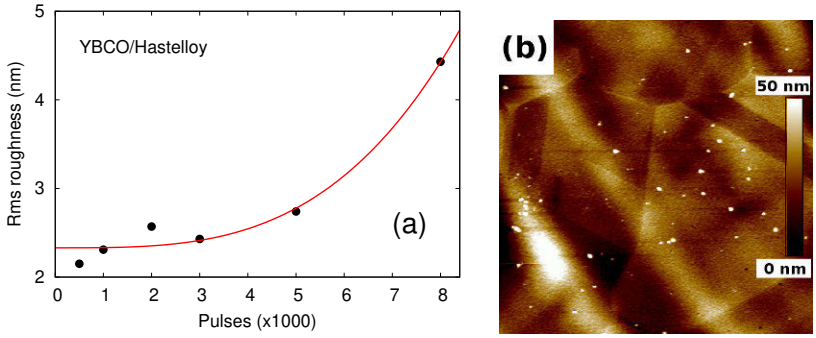

Figure 18. (a) RMS roughness values as function of films with different thicknesses and (b) the surface image of the 60 nm YBCO film using 20×20 μm^2 scan area **[I]**.

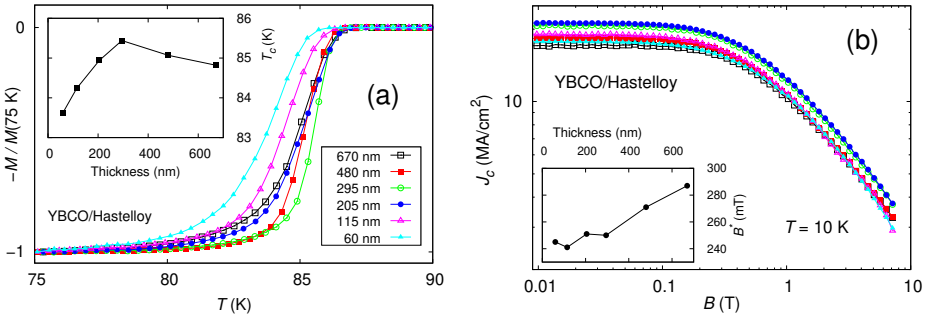

Figure 19. (a) Normalized ac magnetization as a function of temperature for undoped YBCO films grown with different thicknesses. Inset shows the thickness dependence of T_{c} and (b) J_{c} dependence of films with varying thicknesses **[I]**.

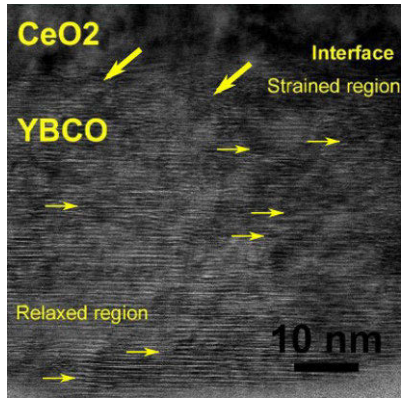

Figure 20. Cross-sectional TEM image of 60 nm YBCO film grown on buffered metal. Thick arrows show the disordered regions and indicate the strained layer just next to the interface of CeO_2 and YBCO. Above strained region the ordered arrows depict the stacking faults and dislocations **[I]**.

is shown in Figure 18(b) for 60 nm thick film. Clearly the grain diameter of ≈ 10 μm can be observed. In thicker films, such a grain structure was not observed which indicates improved interface growth of YBCO on hastelloy as compared with NiW buffered substrate [100].

The T_cs measured for all the films are presented in Figure 19(a). It can be seen that the T_c is lowest (below 84 K) for the thinnest film and it gradually increases as the film thickness increases. The highest T_c is found to be 85.5 K for 300 nm thick film and above that it again starts decreasing. Lowest T_cs for the thinnest film is related to the unrelaxed growth of YBCO unit cells [120]. Above 60 nm, the structural growth starts to relax and improves up to 300 nm. In thicker films (more than 300 nm), a thin surface layer arises that contains more crystalline defects or other disorders which degrades the structure, thus lowering the T_c.

Figure 19(b) depicts the J_c for as measured films where one realizes that J_c is the highest for $200-300$ nm thick films. Below and above this thickness range, the J_c is lower but has a moderate tendency. In thinnest films, the lower J_c can be attributed to the worst crystalline quality and also weak pinning cites which are important for vortex pinning. On the other hand, the crystalline quality for thickest films is also degraded and is related to the retarted growth rate above a certian limit when particles start forming agglomerates. These results are in agreement with the films on NiW buffered substrate, where the intermediate thicknesses produced the best results [100].

The TEM was conducted on the 60 nm film in order to understand the interface growth and structural relaxation (Figure 20). The TEM image showed that YBCO grows epitaxially in $(00l)$ direction. The high defect density is realized around the

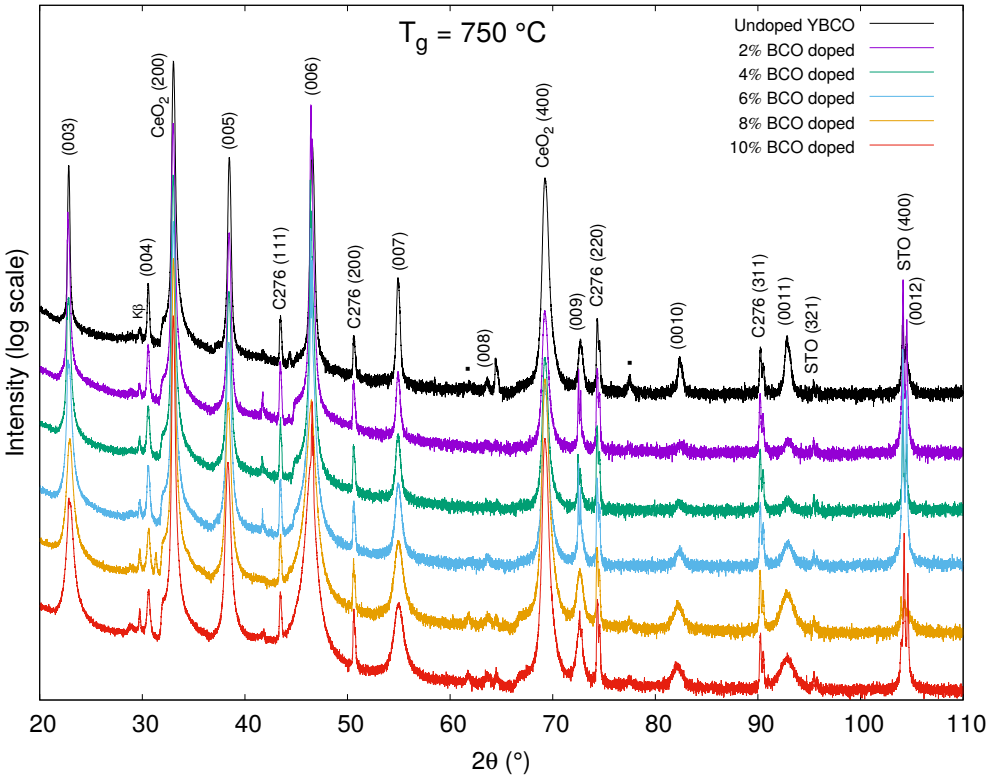

Fig. 21. XRD diffractogram of YBCO films doped with varying BCO concentration. Labelled peaks, CeO_2 from cap-layer, '·' peaks are from the buffer layers and C276 peaks arose from the metal itself. STO peak is also observed because the hastelloy tape was glued on it **[III]**.

interface which is due to the strain caused by underlying cap-layer and is labelled by thick and randomly oriented arrows in Figure 20. Above the small region (less than 10 nm) next to the interface, the YBCO starts relaxing and the crystal quality improves above this strained layer. Although there are still some defects in the top region as labelled by thin and unidirectional arrows, it is believed that such stacking faults and dislocations are highly beneficial for vortex pinning phenomenon which in return increases the J_c.

4.1.3 BCO concentration optimization

Experiments were made by growing films with varying BCO concentration in YBCO **[III]**. The BCO dopant concentration was varied from 0% to 10% with 2 vol% step size. All the films were again deposited at 750 °C on the buffered metal (Figure 14) with 1500 laser pulses thus giving the film thickness of approximately 150 nm. The XRD was firstly measured to check the purity of samples (Figure 21). Despite the buffered metal, all the films were phase pure, epitaxially textured and c-axis oriented

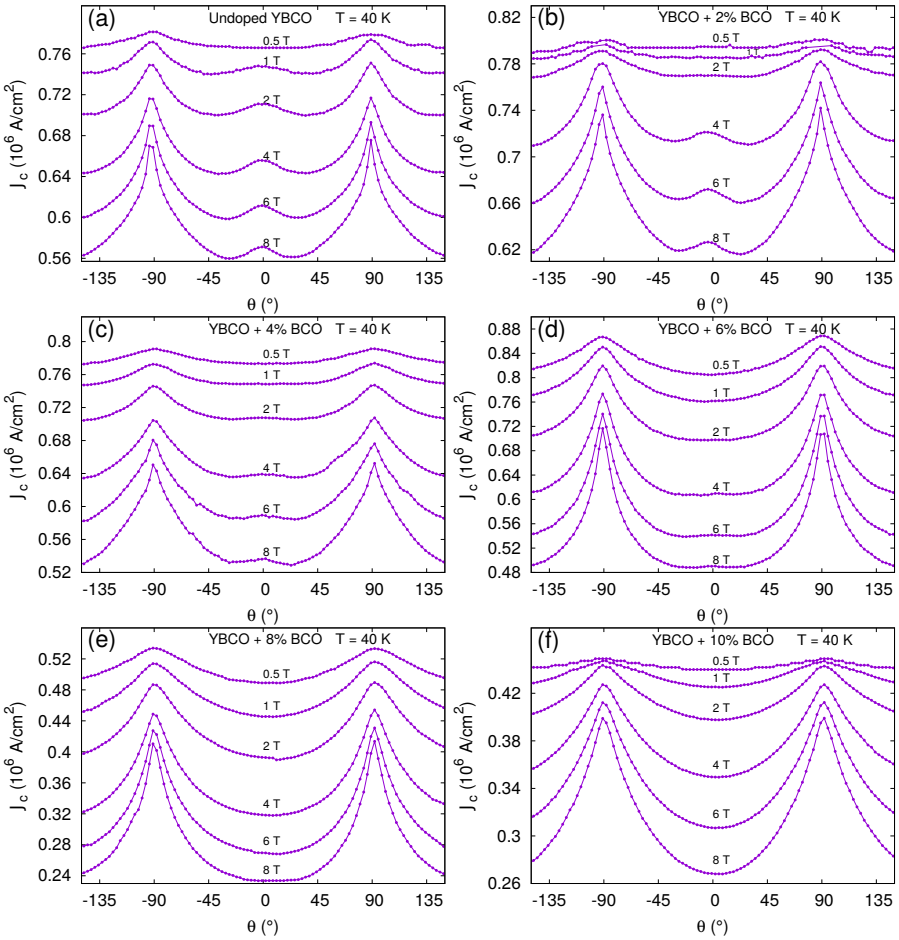

Figure 22. (a)−(f) The $J_c(\theta)$ graphs for undoped and BCO doped YBCO films grown on buffered metal measured at 40 K and 0.5 T−8 T. All the curves were shifted so that 0° refers to the direction of c-axis, while -90° and 90° for ab-planes of YBCO **[III]**.

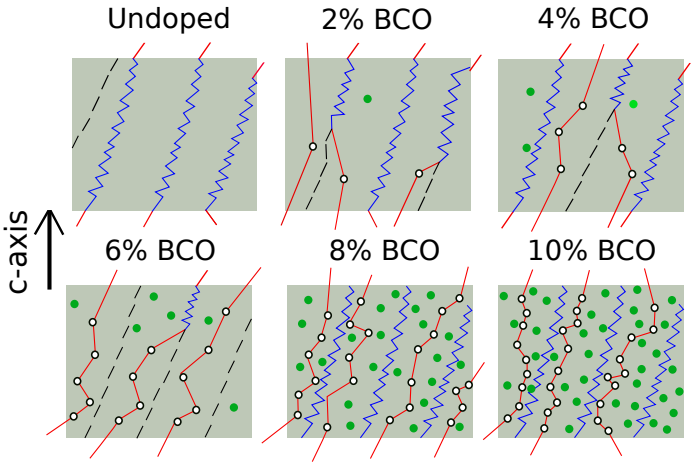

Fig. 23. The schematic of vortex pinning in 0% to 10% BCO doped YBCO films grown on buffered metal. Black dashed lines are threading dislocations where no vortex pinning occurs, whereas blue zig-zag lines depict the pinned vortices within threads. The green and open circles are BCO nanodots where the vortices (red lines) are unpinned and pinned, respectively **[III]**.

which showed no inter-diffusion between the underlying metal to superconducting layer. It was revealed that the T_c tends to decrease with increasing BCO concentration, which has also been observed previously [121]. The dopant concentration causes the non-uniform strain which structurally deforms YBCO [49; 122]. Both the magnetic and angular dependent resistivity data revealed that films with 2% and 4% BCO concentration had the best J_c **[III]**.

The angular dependent J_c results are presented in Figure 22. YBCO films doped with 2% and 4% BCO concentrations showed the highest $J_c(\theta)$ in entire magnetic field and angular range. Such BCO content in YBCO matrix is effective for trapping the vortices both at low and high magnetic fields. The occurence of c-peak in undoped and 2% BCO doped films reveal the presence of threading dislocations which also helps in pinning the vortices. But no c-peak is seen in $J_c(\theta)$ curves for films doped with high BCO concentration. This can be explained by the vortex path model, where high density of point particles affects the paths of vortices, resulting in less vortex pinning by threading dislocations. A schematic of vortex pinning by BCO nanoparticles and threading dislocations is presented in Figure 23. The vortices are mostly mobile in the undoped case and are only pinned by threading dislocations, whereas vortices are caught by BCO nanodots and their path deviates with respect to neighbouring nanodots sitting next to each other. Therefore, BCO nanoparticles improve the flux pinning phenomenon in YBCO films grown on buffered metallic substrates. However, this schematic is just a general illustration and the vortex pinning can be modified depending on the strength and orientation of applied magnetic field with respect to the measurement temperature, for example, at low temperatures

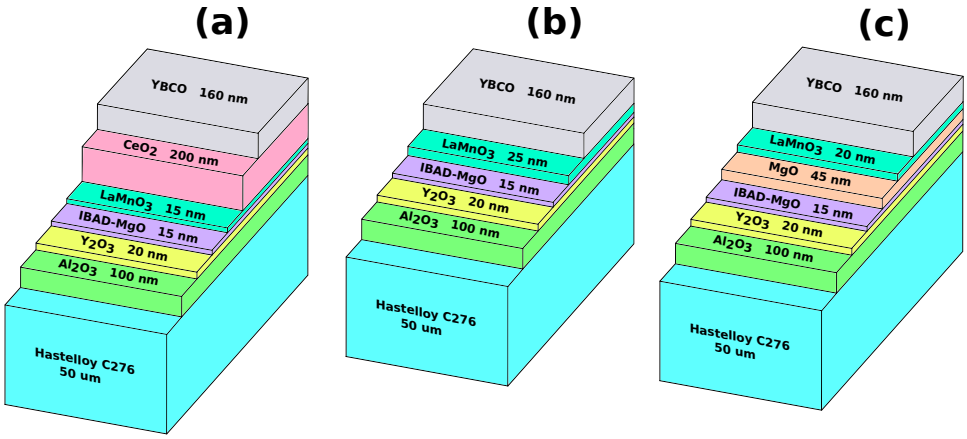

Figure 24. (a)−(c) Schematics of used IBAD-MgO based substrates for growing YBCO films. The three templates, (a) CeO_2, (b) LMO-MgO, and (c) LMO-Epi-MgO, differ from each other in thicknesses and buffer layer stacks **[IV]**.

and weak magnetic fields, the vortices might be pinned in a smooth fashion within a single nanodot or dislocation. On the other hand, at high temperatures and strong magnetic fields, where the thermal fluctuations are obvious to arise, can disrupt the pinning phenomenon thus allowing the jumping of vortices across different pinning sites.

4.2 Effect of modified buffer layer stack

Extending work towards the effect of buffer layers, three differently architectured substrates were exploited in pursuit of high J_c with small anisotropy **[IV]**. The substrates are presented in Figure 24. Firstly, the T_g was optimized by growing undoped YBCO on all of the three substrates and, by premilinary measurements, the optimized T_g turned out to be 775 °C **[IV]**. Both undoped and 4 wt.% BZO doped YBCO films were grown on 5×5 mm^2 substrates and their measured structural parameters are shown in Table 3. The c-axis lengths for undoped films on all the substrates are closer to the nominal value of YBCO c-axis as compared with lengthy c -axis of BZO doped films. This means that BZO is causing strain along c-axis. It can also be observed that the CeO_2 buffer layer has a good impact on the growth of both undoped and doped YBCO since it has the least variation along c-axis as revealed by $\Delta 2\theta$ values, which are quite small as compared with our previously used templates [62; 100; 123; 124]. Moreover, the $\Delta\phi$ values between the differently buffered substrates is half of that reported earlier for NiW buffered substrate [100]. The $\Delta\phi$ (102)

Table 3. Structural parameters calculated for undoped and BZO doped YBCO films grown on three different buffered substrates **[IV]**.

Template	YBCO lattice c (Å)	$\Delta 2\theta$ (004) (°)	$\Delta\phi$ (102) (°)	I(005)/ I(004)
undoped YBCO				
CeO_2	11.69	0.12	3.40	14.0
LMO-MgO	11.70	0.15	4.36	13.7
LMO-Epi-MgO	11.70	0.14	3.77	13.5
YBCO + BZO				
CeO_2	11.74	0.19	3.37	13.9
LMO-MgO	11.75	0.21	4.42	12.5
LMO-Epi-MgO	11.73	0.20	4.75	12.9

values are critical since they are related to low-angle grain boundaries, arising from the underlying substrate, which channel the YBCO growth along c-axis and forms threading dislocation. Furthermore, the T_c for BZO doped films was reported to be lower than that of undoped films which is related to the strain occuring due to 8% of lattice mismatch between YBCO and BZO, and also possibly the oxygen deficiency occuring around BZO induced nanorods [89; 123; 125]. Among the templates, the CeO_2 based YBCO film showed the highest T_c, which can be related to the less strain on the interface due to the least lattice mismatch between YBCO and CeO_2.

The $J_c(\theta)$ measured for all the films presented in Figure 25 depict the effect of underlying buffer structure on as grown undoped and BZO doped YBCO films. It can be seen that the aniosotropic levels shift for both undoped and doped films at low (0.5 T$-$ 2 T) and high (4 T$-$ 8 T) magnetic fields. The CeO_2 cap-layer proved to be the most effective for undoped films measured at low magnetic fields since it gives highly isotropic results with the appearance of c-peak (Figure 25(a)). The broad and intense ab-peaks for LMO-Epi-MgO substrate tells us that pinning sites are more populated along ab-direction than c-axis in such a YBCO film, which is a general case in undoped YBCO films [21]. At high magnetic fields, LMO-Epi-MgO turns out to be anisotropic, than LMO-MgO and CeO_2, with the appearance of sharp and narrow ab-peaks along with shoulders. The shouldering occurs because of interplay of in-plane and out-of-plane pinning [126]. However, LMO-MgO and CeO_2 based templates do not show much of the differences in isotropic behaviours even at 8 T. These $J_c(\theta)$ results reveal that the network of natural pinning sites can easily vary in size depending on buffer layers [36].

Concerning the BZO doped films, the $J_c(\theta)$ curves for LMO-Epi-MgO revealed to be more isotropic at low fields for doped films as shown in Figure 25(c). The strong c-peaks rising above 1 T for LMO-MgO and CeO_2 indicates strong vortex pinning by BZO induced nanorods along c-direction. Figure 25(d) depicting the $J_c(\theta)$ mea-

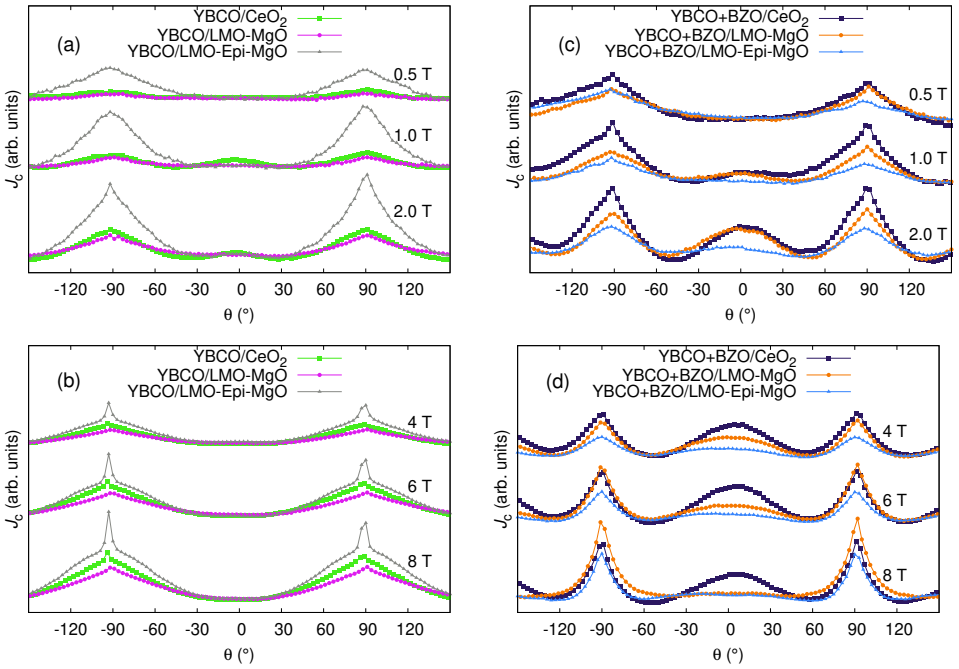

Fig. 25. $J_c(\theta)$ curves for (a)−(b) undoped and (c)−(d) BZO doped YBCO films grown on CeO_2, LMO-MgO and LMO-Epi-MgO templates measured at 40 K and at different B **[IV]**. The data for each constant magnetic field was firstly separated and then shifted in such a way that the lowest point of every curve falls at the same level.

sured at high fields reveal that CeO_2 based buffer stack is the best performer for the nanorods growth as pronounced and strong c-peaks are observed even at very high magnetic fields. This scales up to the highly isotropic behaviour of such BZO doped film grown on CeO_2, which again means that the least lattice mismatch between the cap-layer and YBCO is the backbone for enhanced growth of superconducting films. To be noted, the LMO-MgO and LMO-Epi-MgO did show the c-peaks but not as pronounced as CeO_2, especially at 8 T. Therefore, CeO_2 based buffer template was optimized in this work.

4.3 Control of defect size through target grain size

4.3.1 On single crystal

To improve the natural and artificial pinning landscape within YBCO matrix, the targets used in the PLD process were modified by downscaling their grain size from micron to nanometer [109; 110]. Both the undoped (n-YBCO and μ-YBCO) and 4% BZO doped YBCO (n-YBCO+BZO and μ-YBCO+BZO) films were firstly deposited on single crystalline STO substrates for testing and understanding better the growth mechanism **[V]**. By AFM images it was revealed that the average in-plane diameter for n-YBCO is smaller compared with μ-YBCO, thus indicating more number of nucleation sites and small island size in n-films. Such growth enhances the flux pinning phenomenon by defects localized on the surroundings of merged single particles. A detailed microstructural analysis of both undoped and BZO doped films was performed by TEM and is presented in Figure 26. The TEM images depicted the enhanced pinning landscape in undoped and BZO doped films grown by utilizing nano grain sized targets. As realized by Figure 26(a,b), that the n-YBCO has long stacking faults in the entire film, as opposed by short stacking faults in μ-film. In case of BZO doped films (Figure 26(c,d)), the self-assembled BZO nanorods are at least four times longer in n-YBCO+BZO than in μ-YBCO+BZO, that is, $85-203$ nm for the former and $21-45$ nm for latter. Moreover, their diameters were observed to be 7.5 nm and 6.5 nm with an average estimated spacing of 9 nm and 12 nm for n-YBCO+BZO and μ-YBCO+BZO, respectively. On average, the films grown from nanosized targets were $\approx$ 15 nm thicker than those deposited by micro grain sized targets. The compilation of the TEM results are shown in Table 4.

The transport measurements for all the films were carried out and the results are presented in Figure 27. Comparing the undoped cases (Figure 27(a,b)), it can be seen that the n-YBCO has clearly higher $J_c(\theta)$ than μ-YBCO under the entire magnetic field range. In extension to this, the $J_c(\theta)$ are highly isotropic, especially below 4 T, in n-YBCO thus revealing improved vortex pinning by natural defects within n-YBCO.

This is in agreement with our structural results where the smaller island size

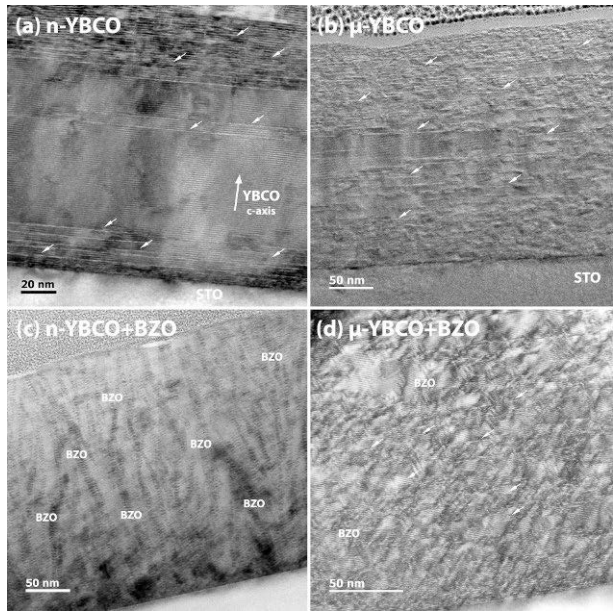

Figure 26. (a)−(d) TEM images of both undoped and BZO doped YBCO films deposited from nano and micron grain sized targets. Stacking faults are labelled by bright arrows. Nanocolumns are labeled by BZO in doped films **[V]**.

Table 4. A compilation of parameters for undoped and BZO doped n- and μ-YBCO films, taken from TEM results **[V]**.

Sample	Stacking faults	Splay of nanorods (°)	Twin boundaries
n-YBCO	Bottom layer with long stacking faults	-	In bottom layer
μ-YBCO	Randomly distributed short stacking faults	-	Visible (see SI)
n-YBCO+BZO	Few in number	5-15 (unbroken)	Not visible
μ-YBCO+BZO	Randomly distributed short stacking faults	20-25 (often broken)	Not visible

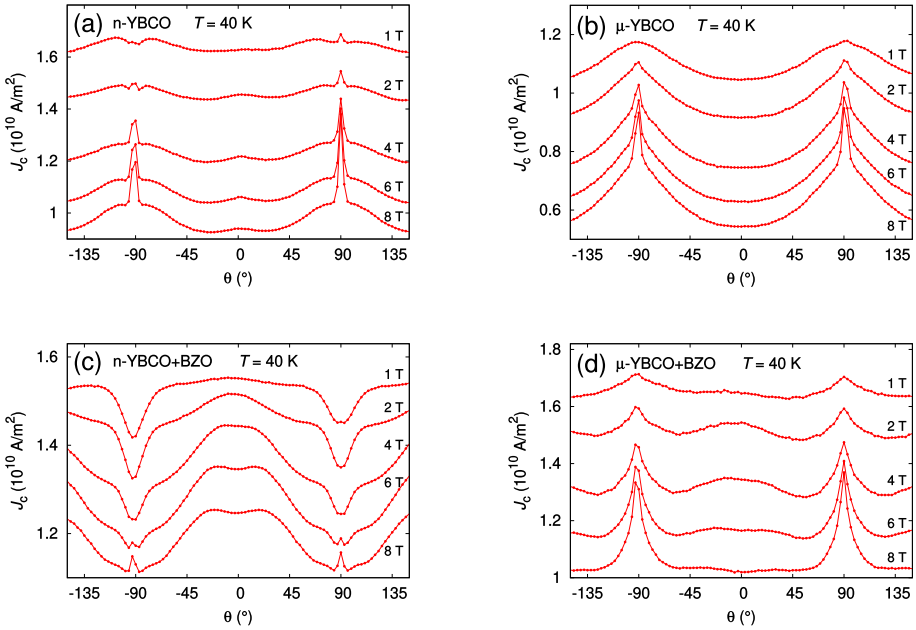

Figure 27. The $J_c(\theta)$ measured at 40 K and different magnetic fields for (a) n-YBCO, (b) μ-YBCO, (c) n-YBCO+BZO and (d) μ-YBCO+BZO **[V]**.

produces greater number of strain relaxed defects within n-YBCO. Furthermore, we previously noticed that the twin domain size is also small in n-YBCO, which means that there are more number of twin boundaries in the c direction [120]. The vortex path model tells us that due to the occurence of short stacking faults in μ-YBCO the vortices will be pinned more along ab-planes, which is in line with disappearance of c-peak in μ-YBCO [61; 127]. The sharp and intense ab-peaks in n-YBCO occur due to long stacking faults responsible for effective vortex pinning along ab-planes. It is noted that shoulders occur around these ab-peaks both at low and high fields, which is an indication of mixed vortex pinning by the in-plane and out-of-plane defects [126]. The small c-peak in n-YBCO is the direct evidence of presence of a large number of c-axis oriented threading dislocations, which also contribute in flux pinning. Contrary to this, in μ-YBCO, broad ab-peaks occur at low fields which get stronger at high fields. The short stacking faults are responsible for most of the vortex pinning with the increasing magnetic field in such a case. The non-existence of c-peak in μ-YBCO does not refer to lack of pinning along c-axis since the c-peak only occurs when the total F_p has a local maximum along the c-axis [128].

The $J_c(\theta)$ curves for BZO doped films presented in Figure 27(c,d) revealed huge differences between n-YBCO+BZO and μ-YBCO+BZO. Firstly, the $J_c(\theta)$ is observed to be higher in low field ($B \leq 2$ T) in μ-YBCO+BZO but a cross over is soon realized by strong c-peaks in n-YBCO+BZO above 2 T. These effects are only due

to the strong vortex pinning by lengthy and less splayed grown nanorods with larger diameters within n-YBCO+BZO, which is opposite in the case for μ-YBCO+BZO. The shortened BZO rods in μ-YBCO+BZO allow the stacking faults to effectively pin the vortices along ab-direction, thus giving rise to pronounced ab-peaks and weakened c-peaks. Such $J_{\mathrm{c}}(\theta)$ features were also observed when BZO doped films were grown at very high temperatures which lead to shortened growth of nanorods and densily populated stacking faults along ab-direction [56]. The dips of ab-peaks in n-YBCO+BZO are likely related to the dominance of pinning by elongated and well ordered nanorods, which suppress the vortex pinning along ab-direction [129]. At 6 T, the small ab-peaks starts to rise, which get more pronounced at 8 T. This means that when applied field is too high, then even the strong c-axis oriented nanorods can not pin all the vortices thus giving freedom to defects sitting around ab-planes. On the other hand, the random stacking faults in μ-YBCO+BZO can deteriorate the growth of BZO nanorods along c-direction, which reduces the vortex pinning along c-axis at low and high magnetic fields.

Based on the TEM images, a schematic of the as-grown defects within all the films was produced as shown in Figure 28. The schematic shows us the long stacking faults right next from the interface to the top of film in n-YBCO, whereas the short stacking faults were visible in μ-YBCO. Moreover, the threading dislocations are also greater in number in n-YBCO as compared to its μ-YBCO counterpart, revealed by the appearance of c-peaks in Figure 27(a). This is related to the smaller island size, which leads to enhanced natural pinning landscape in n-YBCO. The random growth of stacking faults not only contributes in the broad ab-peaks but also hinders the c-peaks (Figure 27(b)). Considering the BZO doped samples, the enhanced growth of BZO induced nanorods in n-YBCO+BZO can be related to the better local conditions for YBCO$-$BZO interfaces to occur by high diffusion of oxygen through great number of grain boundaries and other defects occuring around growth islands. It was revealed by AFM images, that the n-films have smaller in-plane surface particle diameter which indicates small sized growth islands and higher number of nucleation sites **[V]**, thus increasing the density of grain boundaries within n-films. On the other hand, the fragmented and small nanorods (Figure 28(d)) occuring in μ-YBCO+BZO may occur from similar origins as in n-YBCO+BZO but is possible from the low local availability of BZO during the deposition process **[V]**. However, the occurrence of short stacking faults may also halt the growth of BZO in μ-YBCO+BZO. The double c-peaks occur under different magnetic fields due to the growth of highly elongated and dense network of splayed nanorods in n-YBCO+BZO 27(c). Moreover, the pass through of elongated BZO nanords from the interface to film surface effectively pins the vortices producing broad c-peaks at 6 T and 8 T Figure 27(c). On the other hand, the short stacking faults in μ-YBCO+BZO can perturb the growth of BZO nanorods. This may result in shorter and splayed growth of nanorods. This in return weakens the pinning along c-direction, where vortices can take several steps

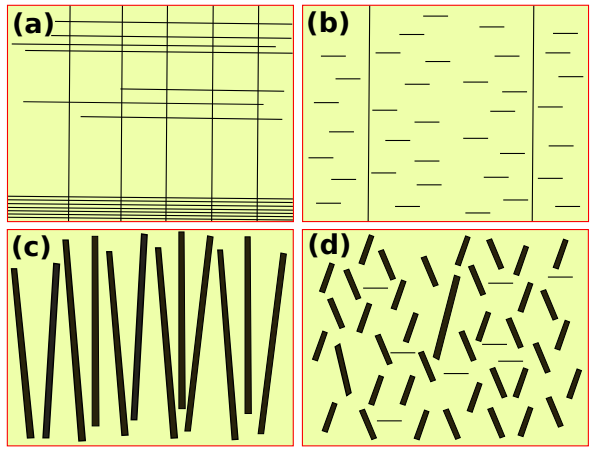

Figure 28. The schematic diagram of created defects in (a) n-YBCO, (b) μ-YBCO, (c) n-YBCO+BZO and (d) μ-YBCO+BZO films. Long vertical lines are threading dislocations. The short and long horizontal lines refer to stacking faults. The short and extended vertical columns represent the BZO induced nanorods **[V]**. The stacking faults are long and greater in number in n-YBCO and vice versa for μ-YBCO, whereas the nanocolumns are elongated and pass through the entire film thickness in n-YBCO+BZO but are highly fragmented in μ-YBCO+BZO along with short stacking faults.

to be pinned and can be untrapped while the field orientation is changed. Especially, when the field is quite high (above 4 T), the weak vortex pinning phenomenon occurs which tells that the shortened nanorods are only effective at low fields (see Figure 27(d)).

Molecular dynamics (MD)-simulations were performed to comprehensively understand the flux pinning mechanism and work was done by my colleague Elmeri Rivasto **[V, VI]**. The pinning structure for these simulations was taken by TEM measurements, where the length and splay of BZO induced nanorods is given. The effect of columnar defects on $J_{\mathrm{c}}(\theta)$ was studied using pinning site configurations presented in Figure 29. The model used for simulations [130] was a layer structure which keeps every particle in the same ab-plane. The angular limit of layer structure is $\pm 60^{\circ}$, around the YBCO c-axis.

The simulated $J_{\mathrm{c}}(\theta)$ graphs are presented in Figure 30(a). It can be seen from Figure 30(a) that the width of $J_{\mathrm{c}}(\theta)$ c-peaks is not dependent on the splay of BZO nanorods but the peak intensities are observed to decrease with increasing splay of nanorods. A double c-peak, where the local maxima of c-peak lies at an angle of $\pm 20^{\circ}$. The c-peak maxima at an angle of 20° instead of 0° is due to the dominance of F_{p} of nanorods over vortex magnetic force which aligns and pins the vortices strongly. Also the vortices are splayed enough to come across different pinning sites and are then pinned into several nanorods, simultaneously **[V]**. As the splay

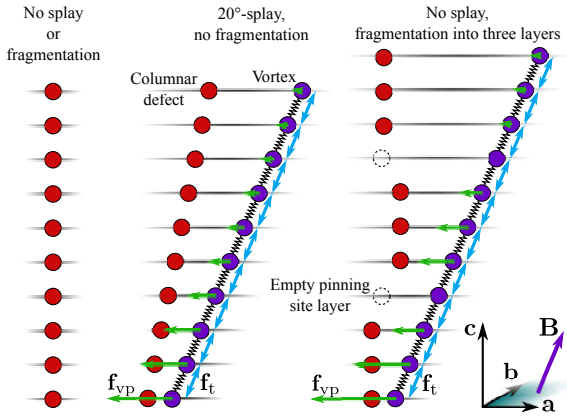

Figure 29. The pinning site configuration used for MD-simulations. Red circles illustrate the pinning defect and vortices are displayed in purple color. Each red circle represent one immobile pinning site corresponding to a single layer, whereas each purple circle corresponding to a mobile vortex. Left−the columnar pinning sites without any splay and fragmentation, Middle−splayed but not fragmented pinning sites interacting with vortex, Right−Not splayed but fragmented pinning sites intecation with vortex. The F_p experienced between vortex and columnar pinning defects with vortex line tension F_t is also presented **[V]**.

of nanorods is increased, the magnetic force dominates the F_{p}, thus partly depinning the vortices which results in reducing the $J_{\mathrm{c}}(\theta)$ along c-axis.

The effect of fragmentation of nanorods on $J_{\mathrm{c}}(\theta)$ is displayed in Figure 30(b). It is seen that the fragmented nanorods widen the c-peaks and a double c-axis peak is only observed when the nanorods are unfragmented. The fragmented layer structure of pinning sites or nanorods diminishes the double c-peak since vortices then bend themselves to be pinned in these fragmented layers. However, this fragmented structure does not seem to signficantly reduce the $J_{\mathrm{c}}(\theta)$ but instead decreases the anisotropy.

In order to compare our experimental results to the simulated ones, the $J_{\mathrm{c}}(\theta)$ curve measured at 4 T was chosen **[V]**. This simulation was made with both the splay and fragmentation of nanorods, where 20 nm long columnar defect with 10° of splay was modelled for n-YBCO+BZO, whereas μ-YBCO+BZO column was fragmented into four small pieces with 22.5° of splay. Figure 31 shows the simulated and experimentally measured c-peak. As can be seen, at $\theta \leq 30°$, the experimental and simulated data fits quite well. But, on the other hand, above $\theta \geq 30°$ the simulated c-peaks for both the μ-YBCO+BZO and n-YBCO+BZO start to deviate, which is due to the limitation of simulation model. In conclusion, the differences in parameters of BZO nanorods explain the differences in shapes of $J_{\mathrm{c}}(\theta)$ curves.

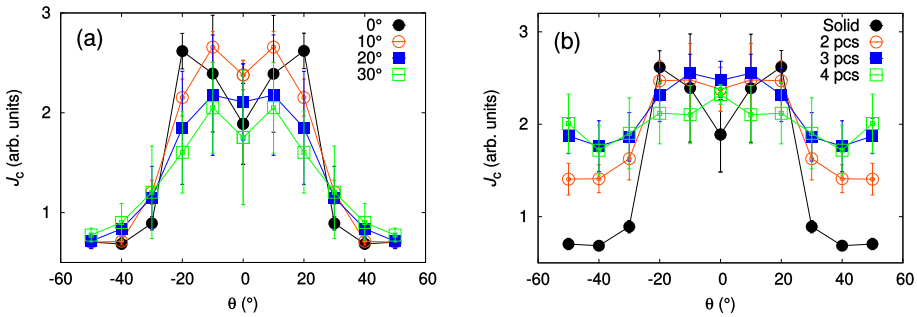

Figure 30. The $J_c(\theta)$ curves for (a) non-fragmented and splayed nanords with 0°, 10°, 20° and 30°, (b) fragmented nanorods into 1, 2, 3 and 4 pieces with 0° splay **[V]**.

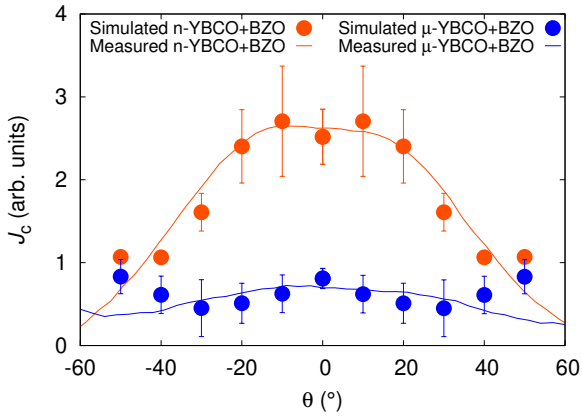

Figure 31. The experimental and simulated $J_c(\theta)$ curves for both μ-YBCO+BZO and n-YBCO+BZO determined from measurement at 4 T and 40 K. **[V]**.

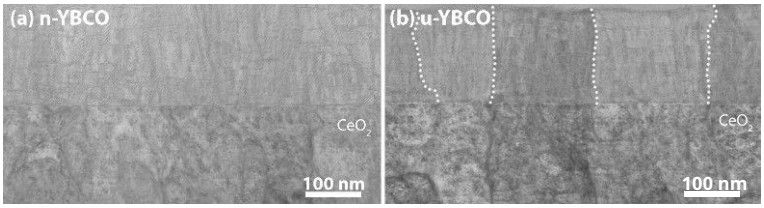

Figure 32. TEM images of, (a) n-YBCO+BZO and (b) μ-YBCO+BZO, films where the effect of texture is depicted **[VI]**.

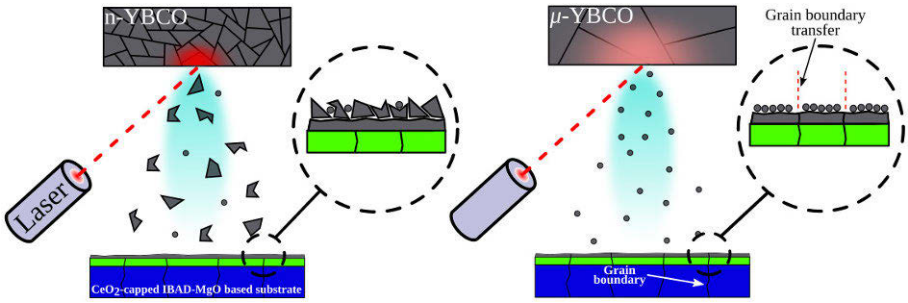

Figure 33. Schematic illustration of PLD growth process on technical substrate when nano and microcrystalline targets are used **[VI]**.

4.3.2 On buffered metal

In motivation from the improved results of films grown on STO, the doped films were also grown on buffered metal by utilizing the same targets only differing with respect to crystalline grain size. The schematic of the used buffered metal is presented in Figure 9. Two 4% BZO doped the films were deposited at 775 °C with 1500 pulses.

Figure 32 depicts TEM images for both BZO doped, n-YBCO and μ-YBCO, films. It is seen that the grain boundaries from the CeO_2 cap-layer are replicated in the μ-YBCO+BZO, whereas there is no such texture transfer in n-YBCO+BZO. Despite this lack of texture transfer in n-YBCO+BZO, the density and size of intrinsic defects is higher than in μ-YBCO+BZO. From our TEM measurements, we schematically deduced the growth mechanism as depicted in Figure 33. Our previous studies [131] showed that the n-YBCO+BZO target with small grains has excessive oxygen on grain boundaries. The laser pulse will not be able to penetrate deep inside the target due to oxygen acting as thermal insulator, thus cleaving-off mainly the clusters from n-YBCO+BZO target as opposed by the atomic level transfer in μ-YBCO+BZO [131]. The larger sized clusters limit the movement of smaller atoms on the substrate surface, which in return hinders the grain boundaries transfer in n-YBCO+BZO. However, this schematic is just an illutsration based on our experi-

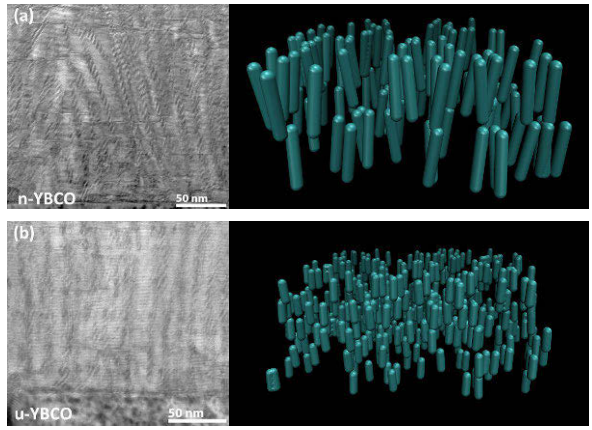

Figure 34. TEM images along with their 3D simulations of both the YBCO films grown by utilizing (a) n-YBCO+BZO and (b) μ-YBCO+BZO targets **[VI]**.

Table 5. A compilation of microscopic results measured by BF-STEM for BZO doped YBCO grown by different grain sized targets **[VI]**.

	n-YBCO+BZO	μ-YBCO+BZO
Film thickness (nm)	200–210	160–170
Stacking fault length (nm)	22.8±8.5	21.9±5.0
Nanorod diameter (nm)	7.8±1.4	6.1±1.0
Nanorod length (nm)	75–150	25–45
Nanorod spacing (nm)	12.3±3.6	10.3±2.8
Nanorod splay (°)	15.2±3.3	7.5±1.7

mental results, where the growth process can possibly change if the PLD parameters are tuned [132]. These parameters include target-substrate distance, laser frequency, repetition rate, substrate temperature and growth temperature.

The TEM measurements revealed an improved growth of BZO induced nanorods within n-YBCO matrix compared with μ-YBCO+BZO (Figure 34). The detailed results of TEM measurements are compiled in Table 5. Firstly, the nanorods are again three times longer in n-YBCO+BZO than in μ-YBCO+BZO, which sums up the improved growth of BZO nanorods when using a nano grain sized target. This is in line with the results when films were grown on STO **[V]**. The μ-YBCO+BZO has two times greater splay of nanorods than n-YBCO+BZO. In addition, we again observed an increased film growth rate when deposited by nano sized target, that is, n-YBCO+BZO has 25% faster growth rate than μ-YBCO+BZO, quite similarly to the STO case **[V]**. However, unlike for similar doped films grown on STO, the stacking faults are present in n-YBCO+BZO and are of approximately the same lengths

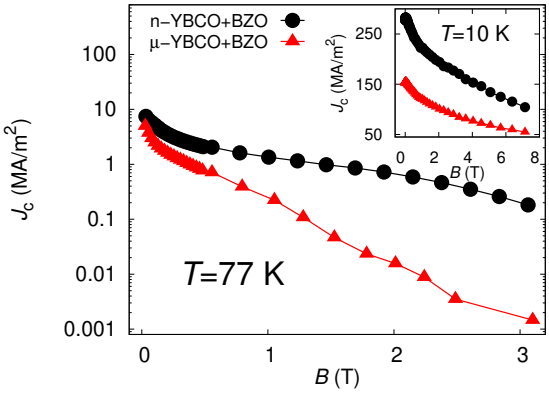

Figure 35. The magnetically measured J_c of both (a) n-YBCO+BZO and (b) μ-YBCO+BZO films at 77 K (main) and 10 K (inset) **[VI]**.

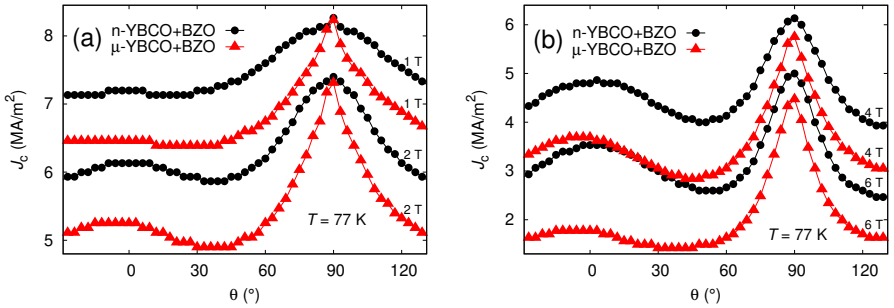

Figure 36. The angular dependent J_c of n-YBCO+BZO and μ-YBCO+BZO films measured at 77 K and under magnetic fields of (a) 1 T−2 T and (b) 4 T−6 T **[VI]**.

as in μ-YBCO+BZO.

The films were magnetically measured at 10 K and 77 K under zero and applied magnetic fields. The results are displayed is Figure 35. It can be seen that at 10 K the n-YBCO+BZO has 1.7 times higher J_c than μ-YBCO+BZO in the entire field range of 0 T−8 T. At 77 K, this difference is observed to be 100 times larger when the field is increased above 2 T. This overwhelming improvement demonstrates the effectiveness of the grain boundary network in resisting the flow of Cooper pairs at high temperatures. We conclude that the different grains in μ-YBCO+BZO can act as individual superconducting regions, separated by grain boundaries acting as insulators, thus giving very low J_c calculated by Bean model. But at low temperatures, the Cooper pairs easily surpass through the channels of grain boundaries and allows reliable values in this case.

The angular dependent $J_c(\theta)$ measurements were done at 77 K and in wide magnetic field range to support the capability of this work in coated conductor applica-

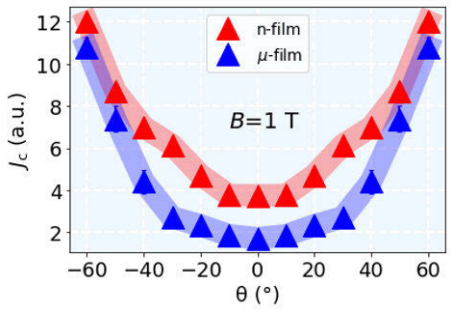

Figure 37. The simulated $J_c(\theta)$ curves for both μ-YBCO+BZO and n-YBCO+BZO under 1 T magnetic field with different orientations **[VI]**.

tions. The obtained $J_c(\theta)$ curves at 1 T and 2 T are displayed in Figure 36(a). It is realized that the n-YBCO+BZO has higher J_c both at 1 T and 2 T and is also less anisotropic than μ-YBCO+BZO. This is attributed to the enhanced flux pinning by lengthy nanorods within the YBCO matrix. However, the ab-peaks in μ-YBCO+BZO are observed to be sharp and intense, which is related to the strong dominance of pinning by in-plane defects, like stacking faults, in this case. Taking into account the measurements at 4 T and 6 T (see Figure 36(b)), an upward shift in the relative height of c-peak is clearly observed in n-YBCO+BZO. This striking result gives us an impressive 40% improvement in n-YBCO+BZO as compared to its counterpart. Such enhancements in $J_c(\theta)$ values are due to the improved growth of BZO induced nanorods in n-YBCO+BZO as we already visualized and discussed in TEM analysis.

To understand that how much the formation of nanorods affects the shape of $J_c(\theta)$ of μ-YBCO+BZO and n-YBCO+BZO, simulations were performed for 1 T magnetic field. The used pinning landscape for these simulations is illustrated in Figure 34 and the simulated results are displayed in Figure 37. The results are clearly in line with the experimental ones, since the c-peak is absent for both the samples at 1 T and the $J_c(\theta)$ is observed to decrease at higher angles. The simulations also revealed that $J_c(\theta)$ around c-axis is higher for n-YBCO+BZO than for the μ-YBCO+BZO which fits nicely with the experimental $J_c(\theta)$.

By just modifying the target itself via downscaling its grain size, high improvements are obtained on the laboratory scale, which can be tested and then implemented on the industrial scale. As a final note, the tuning of PLD parameters for growing the films from micron and nano grain sized targets is another interesting issue to study and it is possible that the results can be degraded or enhanced. So these results are specific with respect to our PLD growth conditions and substrate sizes which can not be fully generalized for all the PLD processes operated globally. However, with our specific conditions implemented, the results can be tested for industrial scale.

5 Conclusions

In this thesis, different methodologies have been performed to modify and enhance J_c of YBCO layers on buffered metal substrates. Experiments were made on films grown on both the single crystals and IBAD-MgO based metallic templates to investigate the natural and artificial pinning structure formed within the YBCO layer. To create an artificial pinning landscape within YBCO matrix, BZO and BCO were used as dopants which produce nanorods and nanodots, respectively. On buffered metals, T_gs were optimized for undoped and doped YBCO films, where T_gs were found to be in the range of 725 °C to 775 °C. T_g out of this range detoriates the structural growth and in return worsens the superconducting properties. The thicknesses of YBCO films were also optimized on the buffered metal. It was concluded that the films with intermediate thicknesses (200−300 nm) on a specific buffered metal have the highest J_c on the laboratory scale.

The BCO doped YBCO films were also optimized on buffered metal with respect to dopant concentration. It was revealed that the BCO with lower dopant concentration perform better superconducting properties and reduce the anisotropic behavior. Dopant concentration, over 4%, degrades the structural growth of YBCO thus detoriating the superconducting properties.

Three differnently fashioned IBAD-MgO based templates were used and it was found that the template having cap-layer with least lattice mismatch to that of YBCO works the best, ensuring the better growth of artificial nanorods within YBCO matrix thus giving less anisotropy in $J_c(\theta)$ curves. This works impressively considering the BZO doped films where strong c-peaks of $J_c(\theta)$ were observed for films on CeO_2 cap-layer, especially at high magnetic fields.

Effect of reducing the target grain size from micrometer to nanometer is the novelty produced from this thesis into the field of coated conductors. The effect was investigated both on single crystal and buffered metal substrates. The natural and artificial pinning landscape was greatly enhanced in this regard. The length of nanorods within the YBCO matrix was enhanced 3 to 4 times when films deposited from nano grain sized target to that of generally used micron grain sized target. Moreover, the diameters of these nanords were also observed to be larger in films grown from target with nanosized grains. Such improvements of the defects resulted in higher J_c and isotropic behaviors at wide temperature, magnetic field and angular ranges. Together with other enhancements in defect structures, the growth rate was also improved by

25% both on single crystal and buffered metal. Such improvements on single crystals can be utilized for microwave applications, and on buffered metals for coated conductors.

Conclusively, the YBCO growth on buffered metal is complex and various factors must be taken into account to counter the problems faced in coated conductor applications. One has to take a broad picture for tackling the problems and together with all the optimizations, the field remains active to be explored in mega-projects. The work performed in this thesis helped the Shanghai Superconductor Technology Ltd. to better understand the growth mechanisms which resulted in improvements for their superconducting wire fabrication.

List of References

[1] S. Nishijima, S. Eckroad, A. Marian, K. Choi, W. S. Kim, M. Terai, Z. Deng, J. Zheng, J. Wang, K. Umemoto, et al. Superconductivity and the environment: A roadmap. *Superconductor Science and Technology*, 26(11):113001, 2013.

[2] L. Rossi. Superconductivity: its role, its success and its setbacks in the Large Hadron Collider of CERN. *Superconductor Science and Technology*, 23(3):034001, 2010.

[3] H. Huang, D. Wu, D. Fan, and X. Zhu. Superconducting quantum computing: a review. *Science China Information Sciences*, 63(8):1–32, 2020.

[4] V. O. Heinen, M. M. Sokoloski, P. R. Aron, K. B. Bhasin, E. G. Wintucky, and D. J. Connolly. NASA space applications of high-temperature superconductors. In *Advances in Superconductivity IV*, pages 11–15. Springer, 1992.

[5] H. Thomas, A. Marian, A. Chervyakov, S. Stückrad, D. Salmieri, and C. Rubbia. Superconducting transmission lines–Sustainable electric energy transfer with higher public acceptance? *Renewable and Sustainable Energy Reviews*, 55:59–72, 2016.

[6] C. Kittel. Introduction to solid state physics. 2005.

[7] J. L. Smith, J. S. Brooks, C. M. Fowler, B. L. Freeman, J. D. Goettee, W. L. Hults, J. C. King, P. M. Mankiewich, E. I. De Obaldia, M. L. O'Malley, et al. Low-temperature critical field of YBCO. *Journal of Superconductivity*, 7(2):269–270, 1994.

[8] G. Grissonnanche, O. Cyr-Choinière, Fs. Laliberté, S. De Cotret, A. Juneau-Fecteau, S. Dufour-Beauséjour, M-E. Delage, D. LeBoeuf, J. Chang, B. J. Ramshaw, et al. Direct measurement of the upper critical field in cuprate superconductors. *Nature Communications*, 5(1):1–8, 2014.

[9] J. Bardeen, L. N. Cooper, and J. R. Schrieffer. Theory of superconductivity. *Physical Review*, 108(5):1175, 1957.

[10] B. Dalla Piazza, M. Mourigal, N. B. Christensen, G. J. Nilsen, P. Tregenna-Piggott, T. G. Perring, M. Enderle, D. F. McMorrow, D. A. Ivanov, and H. M. Rønnow. Fractional excitations in the square-lattice quantum antiferromagnet. *Nature physics*, 11(1):62–68, 2015.

[11] M. Inui, S. Doniach, P. J. Hirschfeld, and A. E. Ruckenstein. Coexistence of antiferromagnetism and superconductivity in a mean-field theory of high-T_c superconductors. *Physical Review B*, 37(4):2320, 1988.

[12] J. Sarrao, W. K. Kwok, I. Bozovic, I. Mazin, J. C. Seamus, L. Civale, D. Christen, J. Horwitz, G. Kellogg, D. Finnemore, et al. Basic Research Needs for Superconductivity. Report of the Basic Energy Sciences Workshop on Superconductivity, May 8-11, 2006. Technical report, DOESC (USDOE Office of Science (SC)), 2006.

[13] C-L. Song and Q-K. Xue. Cuprate superconductors may be conventional after all. *Physics*, 10: 129, 2017.

[14] Y. B. Kim, C. F. Hempstead, and A. R. Strnad. Flux-flow resistance in type-II superconductors. *Physical Review*, 139(4A):A1163, 1965.

[15] T. Maniv, V. Zhuravlev, I. Vagner, and P. Wyder. Vortex states and quantum magnetic oscillations in conventional type-II superconductors. *Reviews of Modern Physics*, 73(4):867, 2001.

[16] A. A. Abrikosov. On the magnetic properties of superconductors of the second group. *Sov. Phys. JETP*, 5:1174–1182, 1957.

[17] C. H. Cheng, Y. Zhao, Y. Feng, H. Zhang, M. Nishiyama, N. Koshizuka, and M. Murakami. Superconductors with nanoscale pinning centers. *Frontiers in Superconducting Materials, ed. AV Narlikar, Springer*, pages 619–647, 2005.

[18] J. Horvat. Nanopinning in high-temperature superconductors. In *Encyclopedia of nanoscience and nanotechnology*, volume 7, pages 207–218. American Scientific Publishers, 2004.

[19] P. Kummeth, H-W. Neumüller, G. Ries, M. Kraus, S. Klaumünzer, and G. Saemann-Ischenko. Enhancement of critical current density j_{cm} and pinning energy U in melt textured $Bi_2Sr_2CaCu_2O_{8+\delta}$ on Ag-tape by heavy ion irradiation. *Journal of Alloys and Compounds*, 195: 403–406, 1993.

[20] P. Yang and C. M. Lieber. Nanostructured high-temperature superconductors: Creation of strong-pinning columnar defects in nanorod/superconductor composites. *Journal of Materials Research*, 12(11):2981–2996, 1997.

[21] N. J. Long, N. M. Strickland, and E. F. Talantsev. Modeling of vortex paths in HTS. *IEEE Transactions on Applied Superconductivity*, 17(2):3684–3687, 2007.

[22] H. Safar, J. H. Cho, S. Fleshler, M. P. Maley, J. O. Willis, J. Y. Coulter, J. L. Ullmann, P. W. Lisowski, G. N. Riley Jr, M. W. Rupich, et al. Enhancement of transport critical current densities at 75 K in $(Bi, Pb)_2Sr_2Ca_2Cu_3O$ Y/Ag tapes by means of fission tracks from irradiation by 0.8 GeV protons. *Applied Physics Letters*, 67(1):130–132, 1995.

[23] H. W. Weber, H. P. Wiesinger, W. Kritscha, F. Sauerzopf, G. W. Crabtree, J. Z. Liu, Y. C. Chang, and P. Z. Jiang. Critical currents in neutron irradiated YBCO and BiSCCO single crystals. *Superconductor Science and Technology*, 4(1S):S103, 1991.

[24] J. Giapintzakis, W. C. Lee, J. P. Rice, D. M. Ginsberg, I. M. Robertson, R. Wheeler, M. A. Kirk, and M-O. Ruault. Production and identification of flux-pinning defects by electron irradiation in $YBa_2Cu_3O_{7-\delta}$ single crystals. *Physical Review B*, 45(18):10677, 1992.

[25] A. Wahl, M. Hervieu, G. Van Tendeloo, V. Hardy, J. Provost, D. Groult, C. Simon, and B. Raveau. Columnar defects and irreversibility lines in Tl-based superconductors. *Radiation Effects and Defects in Solids*, 133(4):293–310, 1995.

[26] J. R. Thompson, D. Paul, Z. L. Wang, D. M. Kroeger, and D. K. Christen. Thermal stability and annealing of columnar defects in $Bi_2Sr_2Ca_1Cu_2O_8$/Ag superconductor. *Applied Physics Letters*, 67(7):1007–1009, 1995.

[27] R. Weinstein and R. Sawh. A class of chemical pinning centers including two elements foreign to HTS. *Physica C: Superconductivity*, 383(4):438–444, 2003.

[28] J. L. MacManus-Driscoll, S. R. Foltyn, Q. X. Jia, H. Wang, A. Serquis, L. Civale, B. Maiorov, M. E. Hawley, M. P. Maley, and D. E. Peterson. Strongly enhanced current densities in superconducting coated conductors of $YBa_2Cu_3O_{7-\delta}$+$BaZrO_3$. *Nature Materials*, 3(7):439–443, 2004.

[29] G. Li, S. Wang, J. Li, and W. Yang. Introducing multi-source pinning centers into Y–Ba–Cu–O superconductor through addition of $BiFeO_3$ nano-particles. *Scripta Materialia*, 132:22–24, 2017.

[30] B. Latha, H. Ikuta, and U. Mizutani. Enhancement of critical currents and trapped fields of melt textured ZnO doped Dy–Ba–Cu–O bulk superconductors. *Physica C: Superconductivity*, 412: 566–570, 2004.

[31] M. Wu, J. R. Ashburn, C. J. Torng, P. H. Hor, R. L. Meng, L. Gao, Z. J. Huang, Y. Q. Wang, and A. Chu. Superconductivity at 93 K in a new mixed-phase Y-Ba-Cu-O compound system at ambient pressure. *Physical Review Letters*, 58(9):908, 1987.

[32] J. G. Bednorz and K. A. Müller. Possible high T_c superconductivity in the Ba-La-Cu-O system. *Zeitschrift für Physik B Condensed Matter*, 64(2):189–193, 1986.

[33] J. M. Tranquada, S. M. Heald, A. R. Moodenbaugh, and Y. Xu. Mixed valency, hole concentration, and T_c in $YBa_2Cu_3O_{6+x}$. *Physical Review B*.

[34] E. Bartolome, F. Valles, A. Palau, V. Rouco, N. Pompeo, F. F. Balakirev, B. Maiorov, L. Civale, T. Puig, X. Obradors, et al. Intrinsic anisotropy versus effective pinning anisotropy in $YBa_2Cu_3O_7$ thin films and nanocomposites. *Physical Review B*, 100(5):054502, 2019.

[35] J. Chu, Y. Zhao, M. Z. Khan, X. Tang, W. Wu, J. Shi, Y. Wu, H. Huhtinen, H. Suo, and Z. Jin. Insight into the interfacial nucleation and competitive growth of $YBa_2Cu_3O_{7-\delta}$ films as high-performance coated conductors by a fluorine-free metal–organic decomposition route. *Crystal Growth & Design*, 19(11):6752–6762, 2019.

[36] M. Z. Khan, E. Rivasto, Y. Wu, Y. Zhao, C. Chen, J. Zhu, H. Palonen, J. Tikkanen, H. Huhtinen, and P. Paturi. Modifying the critical current anisotropy of YBCO films via buffering layers on IBAD-MgO based templates. In *Journal of Physics: Conference Series*, volume 1559, page 012037. IOP Publishing, 2020.

[37] M. Malmivirta, H. Palonen, S. Inkinen, L. D. Yao, J. Tikkanen, H. Huhtinen, R. Jha, V. P. S. Awana, S. Van Dijken, and P. Paturi. Dirty limit scattering behind the decreased anisotropy of doped $YBa_2Cu_3O_{7-\delta}$ thin films. *Journal of Physics: Condensed Matter*, 28(17):175702, 2016.

[38] H. Palonen, H. Huhtinen, M. A. Shakhov, and P. Paturi. Electron mass anisotropy of $BaZrO_3$ doped YBCO thin films in pulsed magnetic fields up to 30 T. *Superconductor Science and Technology*, 26(4):045003, 2013.

[39] R. J. Cava, A. W. Hewat, E. A. Hewat, B. Batlogg, M. Marezio, K. M. Rabe, J. J. Krajewski, W. F. Peck Jr, and L. W. Rupp Jr. Structural anomalies, oxygen ordering and superconductivity in oxygen deficient $Ba_2YCu_3O_x$. *Physica C: Superconductivity*, 165(5-6):419–433, 1990.

[40] J. D. Jorgensen, M. A. Beno, D. G. Hinks, L. Soderholm, K. J. Volin, R. L. Hitterman, J. D. Grace, I. K. Schuller, C. U. Segre, K. Zhang, et al. Oxygen ordering and the orthorhombic-to-tetragonal phase transition in $YBa_2Cu_3O_{7-\delta}$. *Physical Review B*, 36(7):3608, 1987.

[41] E. D. Specht, C. J. Sparks, A. G. Dhere, J. Brynestad, O. B. Cavin, D. M. Kroeger, and H. A. Oye. Effect of oxygen pressure on the orthorhombic-tetragonal transition in the high-temperature superconductor $YBa_2Cu_3O_{6+x}$. *Physical Review B*, 37(13):7426, 1988.

[42] M. D. Ainslie. *Transport AC loss in high temperature superconducting coils*. PhD thesis, University of Cambridge, 2012.

[43] S. R. Foltyn, L. Civale, J. L. MacManus-Driscoll, Q. X. Jia, B. Maiorov, H. Wang, and M. Maley. Materials science challenges for high-temperature superconducting wire. *Nature Materials*, 6(9): 631–642, 2007.

[44] B. Maiorov, S. A. Baily, H. Zhou, O. Ugurlu, J. A. Kennison, P. C. Dowden, T. G. Holesinger, S. R. Foltyn, and L. Civale. Synergetic combination of different types of defect to optimize pinning landscape using $BaZrO_3$-doped $YBa_2Cu_3O_7$. *Nature materials*, 8(5):398–404, 2009.

[45] M. Miura, B. Maiorov, M. Sato, M. Kanai, T. Kato, T. Kato, T. Izumi, S. Awaji, P. Mele, M. Kiuchi, et al. Tuning nanoparticle size for enhanced functionality in perovskite thin films deposited by metal organic deposition. *NPG Asia Materials*, 9(11):e447–e447, 2017.

[46] M. M. Aye, M. Z. Khan, E. Rivasto, J. Tikkanen, H. Huhtinen, and P. Paturi. Role of columnar defect size in angular dependent flux pinning properties of YBCO thin films. *IEEE Transactions on Applied Superconductivity*, 29(5):1–5, 2019.

[47] M. Z. Khan, E. Rivasto, J. Tikkanen, H. Rijckaert, M. Malmivirta, M. O. Liedke, M. Butterling, A. Wagner, H. Huhtinen, I. Van Driessche, et al. Enhanced flux pinning isotropy by tuned nanosized defect network in superconducting $YBa_2Cu_3O_{6+x}$ films. *Scientific Reports*, 9(1): 1–12, 2019.

[48] E. Rivasto, M. Z. Khan, M. Malmivirta, H. Rijckaert, M. M. Aye, T. Hynninen, H. Huhtinen, I. Van Driessche, and P. Paturi. Self-assembled nanorods in YBCO matrix–a computational study of their effects on critical current anisotropy. *Scientific Reports*, 10(1):1–14, 2020.

[49] M. Malmivirta, L. D. Yao, S. Inkinen, H. Huhtinen, H. Palonen, R. Jha, V. P. S. Awana, S. van Dijken, and P. Paturi. The Angular Dependence of the Critical Current of $BaCeO_3$ doped $YBa_2Cu_3O_{6+x}$ Thin Films. *IEEE Transactions on Applied Superconductivity*, 25(3):1–5, 2014.

[50] I. Levin, T. G. Amos, S. M. Bell, L. Farber, T. A. Vanderah, R. S. Roth, and B. H. Toby. Phase equilibria, crystal structures, and dielectric anomaly in the $BaZrO_3$–$CaZrO_3$ system. *Journal of Solid State Chemistry*, 175(2):170–181, 2003.

[51] A. Erb, E. Walker, and R. Flükiger. $BaZrO_3$: the solution for the crucible corrosion problem during the single crystal growth of high-Tc superconductors $REBa_2Cu_3O_{7-\delta}$; RE=Y, Pr. *Physica C: Superconductivity*, 245(3-4):245–251, 1995.

[52] J. Z. Wu, J. J. Shi, J. F. Baca, R. Emergo, T. J. Haugan, B. Maiorov, and T. Holesinger. The effect of lattice strain on the diameter of $BaZrO_3$ nanorods in epitaxial $YBa_2Cu_3O_{7-\delta}$ films. *Superconductor Science and Technology*, 27(4):044010, 2014.

[53] K. Traito, M. Peurla, H. Huhtinen, Y. P. Stepanov, M. Safonchik, Y. Y. Tse, P. Paturi, and R. Laiho. Magnetic field dependence of the critical current and the flux pinning mechanism in $YBa_2Cu_3O_{6+x}$ films doped with $BaZrO_3$. *Physical Review B*, 73(22):224522, 2006.

[54] R. Liang, D. A. Bonn, and W. N. Hardy. Evaluation of CuO_2 plane hole doping in $YBa_2Cu_3O_{6+x}$ single crystals. *Physical Review B*, 73(18):180505, 2006.

[55] J. Ye and K. Nakamura. Quantitative structure analyses of $YBa_2Cu_3O_{7-\delta}$ thin films: Determination of oxygen content from x-ray-diffraction patterns. *Physical Review B*, 48(10):7554, 1993.

[56] M. Malmivirta, L. D. Yao, H. Huhtinen, H. Palonen, S. van Dijken, and P. Paturi. Three ranges of the angular dependence of critical current of $BaZrO_3$ doped $YBa_2Cu_3O_{7-\delta}$ thin films grown at different temperatures. *Thin Solid Films*, 562:554–560, 2014.

[57] A. Llordes, A. Palau, J. Gázquez, M. Coll, R. Vlad, A. Pomar, J. Arbiol, R. Guzman, S. Ye, V. Rouco, et al. Nanoscale strain-induced pair suppression as a vortex-pinning mechanism in high-temperature superconductors. *Nature Materials*, 11(4):329–336, 2012.

[58] T. Puig, J. Gutiérrez, A. Pomar, A. Llordés, J. Gazquez, S. Ricart, F. Sandiumenge, and X. Obradors. Vortex pinning in chemical solution nanostructured YBCO films. *Superconductor Science and Technology*, 21(3):034008, 2008.

[59] J. Gutierrez, A. Llordes, J. Gazquez, M. Gibert, N. Roma, S. Ricart, A. Pomar, F. Sandiumenge, N. Mestres, T. Puig, et al. Strong isotropic flux pinning in solution-derived $YBa_2Cu_3O_{7-\delta}$ nanocomposite superconductor films. *Nature Materials*, 6(5):367–373, 2007.

[60] J. Wang, J. H. Kwon, J. Yoon, H. Wang, T. J. Haugan, F. J. Baca, N. A. Pierce, and P. N. Barnes. Flux pinning in $YBa_2Cu_3O_{7-\delta}$ thin film samples linked to stacking fault density. *Applied Physics Letters*, 92(8):082507, 2008.

[61] M. Malmivirta, H. Rijckaert, V. Paasonen, H. Huhtinen, T. Hynninen, R. Jha, V. S. Awana, I. Van Driessche, and P. Paturi. Enhanced flux pinning in YBCO multilayer films with BCO nanodots and segmented BZO nanorods. *Scientific Reports*, 7(1):1–8, 2017.

[62] M. Z. Khan, Y. Zhao, X. Wu, R. Jha, V. P. S. Awana, H. Huhtinen, and P. Paturi. Improving the Flux Pinning With Artificial BCO Nanodots and Correlated Dislocations in YBCO Films Grown on IBAD-MgO based template. *IEEE Transactions on Applied Superconductivity*, 29(5): 1–5, 2019.

[63] R. L. S. Emergo. *Enhancing J_c (B, theta) in $YBa_2Cu_3O_{7-\delta}$ via nano-engineering of pinning structures*. PhD thesis, University of Kansas, 2009.

[64] W. Hirata, S. Muto, Y. Adachi, T. Yoshida, S. Fujita, K. Kakimoto, Y. Iijima, M. Daibo, and S. Awaji. Artificial pinning centers-doped RE-based coated conductors. *Fujikura Technical Review*, page 23, 2019.

[65] M. Igarashi, K. Kakimoto, S. Hanyu, R. Kikutake, Y. Sutoh, R. Suzuki, M. Daibo, H. Fuji, H. Kutami, Y. Iijima, et al. Advanced development of IBAD/PLD coated conductors at FUJIKURA. *Physics Procedia*, 36:1412–1416, 2012.

[66] H. Kutami, T. Hayashida, S. Hanyu, C. Tashita, M. Igarashi, H. Fuji, Y. Hanada, K. Kakimoto, Y. Iijima, and T. Saitoh. Progress in research and development on long length coated conductors in Fujikura. *Physica C: Superconductivity*, 469(15-20):1290–1293, 2009.

[67] F. Vallès, A. Palau, V. Rouco, B. Mundet, X. Obradors, and T. Puig. Angular flux creep contributions in $YBa_2Cu_3O_{7-\delta}$ nanocomposites from electrical transport measurements. *Scientific reports*, 8(1):1–7, 2018.

[68] J. Diez-Sierra, P. Lopez-Dominguez, H. Rijckaert, M. Rikel, J. Hanisch, M. Z. Khan, M. Falter, J. Bennewitz, H. Huhtinen, S. Schafer, et al. High critical current density and enhanced pinning

in superconducting films of $YBa_2Cu_3O_{7-\delta}$ nanocomposites with embedded $BaZrO_3$, $BaHfO_3$, $BaTiO_3$, and $SrZrO_3$ nanocrystals. *ACS Applied Nano Materials*, 3(6):5542–5553, 2020.

[69] M. Paidpilli, R. Pratap, M. Kochat, E. Galstyan, C. Goel, G. Majkic, and V. Selvamanickam. Growth of high-performance 4-5 μm thick film REBCO tapes doped with hafnium using advanced MOCVD. *IEEE Transactions on Applied Superconductivity*, 31(5):1–5, 2021.

[70] G. Majkic, R. Pratap, M. Paidpilli, E. Galstyan, M. Kochat, C. Goel, S. Kar, J. Jaroszynski, D. Abraimov, and V. Selvamanickam. In-field critical current performance of 4.0 μm thick film REBCO conductor with Hf addition at 4.2 K and fields up to 31.2 T. *Superconductor Science and Technology*, 33(7):07LT03, 2020.

[71] S. Kar, J. S. Sandra, W. Luo, M. Kochat, J. Jaroszynski, D. Abraimov, G. Majkic, and V. Selvamanickam. Next-generation highly flexible round REBCO STAR wires with over 580 A mm-^{2} at 4.2 K, 20 T for future compact magnets. *Superconductor Science and Technology*, 32(10): 10LT01, 2019.

[72] M. W. Rupich, X. Li, S. Sathyamurthy, C. L. H. Thieme, K. DeMoranville, J. Gannon, and S. Fleshler. Second generation wire development at AMSC. *IEEE transactions on applied superconductivity*, 23(3):6601205–6601205, 2012.

[73] M. W. Rupich, X. Li, S. Sathyamurthy, C. Thieme, and S. Fleshler. Advanced development of TFA-MOD coated conductors. *Physica C: Superconductivity and its Applications*, 471(21-22): 919–923, 2011.

[74] W. M. W. R. Zhang, M. W. Rupich, U. Schoop, D. T. Verebelyi, C. L. H. Thieme, X. Li, T. Kodenkandath, Y. Huang, E. Siegal, D. Buczek, et al. Progress in AMSC scale-up of second generation HTS wire. *Physica C: Superconductivity and its applications*, 463:505–509, 2007.

[75] M. Erbe, J. Hänisch, R. Hühne, T. Freudenberg, A. Kirchner, L. Molina-Luna, C. Damm, G. Van Tendeloo, S. Kaskel, L. Schultz, et al. $BaHfO_3$ artificial pinning centres in TFA-MOD-derived YBCO and GdBCO thin films. *Superconductor Science and Technology*, 28(11):114002, 2015.

[76] H. Rijckaert, J. De Roo, M. Van Zele, S. Banerjee, H. Huhtinen, P. Paturi, J. Bennewitz, S. J. L. Billinge, M. Bäcker, K. De Buysser, et al. Pair distribution function analysis of ZrO_2 nanocrystals and insights in the formation of ZrO_2-$YBa_2Cu_3O_7$ nanocomposites. *Materials*, 11(7):1066, 2018.

[77] A. Gabovich. *Superconductors: New Developments*. InTech, 2015.

[78] M. Z. Khan, M. Malmivirta, Y. Zhao, X. Wu, R. Jha, V. P. S. Awana, H. Huhtinen, and P. Paturi. Angular and field dependent flux pinning in artificially doped YBCO films on IBAD-MgO based template. *Physica C: Superconductivity and its Applications*, 555:15–23, 2018.

[79] L. M. Paulius, J. A. Fendrich, W-K. Kwok, A. E. Koshelev, V. M. Vinokur, G. W. Crabtree, and B. G. Glagola. Effects of 1-GeV uranium ion irradiation on vortex pinning in single crystals of the high-temperature superconductor $YBa_2Cu_3O_{7-\delta}$. *Physical Review B*, 56(2):913, 1997.

[80] B. Dam, N. J. Koeman, J. H. Rector, B. Stäuble-Pümpin, U. Poppe, and R. Griessen. Growth and etching phenomena observed by stm/afm on pulsed-laser deposited $YBa_2Cu_3O_{7-\delta}$ films. *Physica C: Superconductivity*, 261(1-2):1–11, 1996.

[81] K. Oura, V. G. Lifshits, A. A. Saranin, A. V. Zotov, and M. Katayama. *Surface Science: An Introduction*. Springer Science & Business Media, 2003.

[82] Y. L. Xu and D. Shi. A review of coated conductor development. *Tsinghua Sience and Technology*, 8(3):342–369, 2003.

[83] Y. Iijima, N. Tanabe, Y. Ikeno, and O. Kohno. Biaxially aligned $YBa_2Cu_3O_{7-\delta}$ thin film tapes. *Physica C: Superconductivity*, 185:1959–1960, 1991.

[84] C. P. Wang, K. B. Do, M. R. Beasley, T. H. Geballe, and R. H. Hammond. Deposition of in-plane textured MgO on amorphous Si_3N_4 substrates by ion-beam-assisted deposition and comparisons with ion-beam-assisted deposited yttria-stabilized-zirconia. *Applied Physics Letters*, 71 (20):2955–2957, 1997.

[85] J. R. Groves, P. N. Arendt, S. R. Foltyn, R. F. DePaula, E. J. Peterson, T. G. Holesinger, J. Y. Coulter, R. W. Springer, C. P. Wang, and R. H. Hammond. Ion-beam assisted deposition of biaxially aligned MgO template films for YBCO coated conductors. *IEEE Transactions on Applied Superconductivity*, 9(2):1964–1966, 1999.

[86] V. Matias, J. Hänisch, E. J. Rowley, and K. Güth. Very fast biaxial texture evolution using high rate ion-beam-assisted deposition of MgO. *Journal of Materials Research*, 24(1):125–129, 2009.

[87] S. Wang, C. Antonakos, C. Bordel, D. S. Bouma, P. Fischer, and F. Hellman. Ultrathin IBAD MgO films for epitaxial growth on amorphous substrates and sub-50 nm membranes. *Applied Physics Letters*, 109(19):191603, 2016.

[88] V. Matias and R. H. Hammond. YBCO superconductor wire based on IBAD-textured templates and RCE of YBCO: Process economics. *Physics Procedia*, 36:1440–1444, 2012.

[89] H. Huhtinen, M. Irjala, P. Paturi, and M. Falter. Optimal BZO doping in YBCO films grown on single crystal STO and buffered NiW substrates. *IEEE Transactions on Applied Superconductivity*, 21(3):2753–2757, 2011.

[90] M. Bruanescu, A. Vailionis, J. Huh, A. Moldovan, and G. Socol. AFM and complementary XRD measurements of in situ grown YBCO films obtained by pulsed laser deposition. *Applied surface science*, 253(19):8179–8183, 2007.

[91] X. M. Cui, B. W. Tao, J. Xiong, X. Z. Liu, and Y. R. Li. YBCO superconducting film coated on $LaAlO_3$ substrate by TFA-MOD process. *Journal of superconductivity*, 18(2):291–294, 2005.

[92] E. Celik, Y. Yamada, I. Hirabayashi, and Y. Shiohara. Nb-doped $SrTiO_3$ buffer layers on $LaAlO_3$ substrates by metalorganic deposition for YBCO superconducting films. *Materials Science and Engineering: B*, 110(1):94–102, 2004.

[93] D. K. Fork, F. A. Ponce, J. C. Tramontana, and T. H. Geballe. Epitaxial MgO on Si (001) for Y-Ba-Cu-O thin-film growth by pulsed laser deposition. *Applied Physics Letters*, 58(20): 2294–2296, 1991.

[94] T. Nurgaliev, T. Donchev, E. Mateev, S. Miteva, P. B. Mozhaev, and J. E. Mozhaeva. Properties of HTS YBCO thin films deposited on tilted $NdGaO_3$ substrates. *Physica C: Superconductivity and its applications*, 420(1-2):61–67, 2005.

[95] M. Leskelä, H. Mölsä, and L. Niinistö. Chemical vapour deposition of high-T_c superconducting thin films. *Superconductor Science and Technology*, 6(9):627, 1993.

[96] R Gross, P Chaudhari, M Kawasaki, MB Ketchen, and A Gupta. Low noise $YBa_2Cu_3O_{7-\delta}$ grain boundary junction dc SQUIDs. *Applied physics letters*, 57(7):727–729, 1990.

[97] J. Geerk, G. Linker, and O. Meyer. Epitaxial growth and properties of YBaCuO thin films. *Materials Science Reports*, 4(4):193–260, 1989.

[98] D. M. Hwang, T. S. Ravi, R. Ramesh, Siu-Wai Chan, C. Y. Chen, L. Nazar, X. D. Wu, A. Inam, and T. Venkatesan. Application of a near coincidence site lattice theory to the orientations of $YBa_2Cu_3O_{7-\delta}$ grains on (001) MgO substrates. *Applied physics letters*, 57(16):1690–1692, 1990.

[99] J. L. MacManus-Driscoll and S. C. Wimbush. Processing and application of high-temperature superconducting coated conductors. *Nature Reviews Materials*, pages 1–18, 2021.

[100] M. Malmivirta, H. Huhtinen, Y. Zhao, J-C. Grivel, and P. Paturi. Thickness-dependent properties of YBCO films grown on GZO/CLO-buffered NiW substrates. *Journal of Low Temperature Physics*, 186(1):74–83, 2017.

[101] D. Shi. Buffer layers for YBCO superconducting films on single crystal YSZ substrates and cubic textured Ni substrates. 2002.

[102] Y. Uzun, O. Kuran, and I. Avci. Fabrication of superconducting $YBa_2Cu_3O_{7-\delta}$ thin films on Si wafer via YSZ/CeO_2 buffer layers. *Journal of Superconductivity and Novel Magnetism*, 30(8): 2335–2340, 2017.

[103] J-K. Chung, R-K. Ko, D-Q. Shi, H-S. Ha, H. Kim, K-J. Song, C. Park, S-H. Moon, and S-I. Yoo. Use of $SrTiO_3$ as a single buffer layer for RABiTS YBCO coated conductor. *IEEE transactions on applied superconductivity*, 15(2):3020–3023, 2005.

[104] E. Baruch-El, M. Baziljevich, T. H. Johansen, and Y. Yeshurun. Substrate influence on dendritic flux instability in YBCO thin films. *Journal of Superconductivity and Novel Magnetism*, 28(2): 379–382, 2015.

[105] T. Aytug, M. Paranthaman, S. Kang, H. Y. Zhai, K. J. Leonard, C. E. Vallet, S. Sathyamurthy, H. M. Christen, A. Goyal, and D. K. Christen. $Lamno_3$: a single oxide buffer layer for high-J_c $YBa_2Cu_3O_{7-\delta}$ coated conductors. *IEEE Transactions on Applied Superconductivity*, 13(2): 2661–2664, 2003.

[106] X. Xiong, K. P. Lenseth, J. L. Reeves, A. Rar, Y. Qiao, R. M. Schmidt, Y. Chen, Y. Li, Y-Y. Xie, and V. Selvamanickam. High throughput processing of long-length IBAD MgO and epi-buffer templates at SuperPower. *IEEE transactions on applied superconductivity*, 17(2):3375–3378, 2007.

[107] C.N.R. Rao, R. Nagarajan, and R. Vijayaraghaven. Synthesis of cuprate superconductors. *Superconductor Science and Technology*, 6(1):1, 1993.

[108] M. Kakihana. Invited review "sol-gel" preparation of high temperature superconducting oxides. *Journal of sol-gel science and technology*, 6(1):7–55, 1996.

[109] J. Raittila, H. Huhtinen, P. Paturi, and Yu P. Stepanov. Preparation of superconducting $YBa_2Cu_3O_{7-\delta}$ nanopowder by deoxydation in Ar before final oxygenation. *Physica C: Superconductivity*, 371(2):90–96, 2002.

[110] P. Paturi, K. Schlesier, and H. Huhtinen. Effect of target density on YBCO thin films deposited from nanograined targets. *Physica C: Superconductivity*, 469(14):839–842, 2009.

[111] R. Wördenweber. Growth of high-T_c thin films. *Superconductor Science and Technology*, 12 (6):R86, 1999.

[112] E. D. Specht, C. J. Sparks, A. G. Dhere, and J. Brynestad. Effect of oxygen pressure on the orthorhombic-tetragonal transition in the high-temperature superconductor $YBa_2Cu_3O_{6+x}$. *Phys. Rev. B*, 37:7426, 1988.

[113] Peter Eaton and Paul West. *Atomic force microscopy*. Oxford university press, 2010.

[114] J. C. Vickerman and I. S. Gilmore. *Surface analysis: the principal techniques*. John Wiley & Sons, 1997.

[115] Y. Waseda, E. Matsubara, and K. Shinoda. *X-ray diffraction crystallography: introduction, examples and solved problems*. Springer Science & Business Media, 2011.

[116] H. P. Wiesinger, F. M. Sauerzopf, and H. W. Weber. On the calculation of J_c from magnetization measurements on superconductors. *Physica C: Superconductivity*, 203(1-2):121–128, 1992.

[117] P. Schweiss, W. Reichardt, M. Braden, G. Collin, G. Heger, H. Claus, and A. Erb. Static and dynamic displacements in $RBa_2Cu_3O_{7-\delta}$ (R=Y, H_o; delta =0.05, 0.5): A neutron-diffraction study on single crystals. *Physical Review B*, 49(2):1387, 1994.

[118] P. Paturi, M. Irjala, A. B. Abrahamsen, and H. Huhtinen. Defining B_c, B^* and ϕ for YBCO Thin Films. *IEEE Transactions on Applied Superconductivity*, 19(3):3431–3434, 2009.

[119] L. Krusin-Elbaum, L. Civale, J. R. Thompson, and C. Feild. Accommodation of vortices to columnar defects: Evidence for large entropic reduction of vortex localization. *Physical Review B*, 53(17):11744, 1996.

[120] M. Peurla, H. Huhtinen, Y. Y. Tse, J. Raittila, and P. Paturi. Structural properties of YBCO thin films deposited from different kinds of targets. *IEEE Transactions on Applied Superconductivity*, 17(2):3608–3611, 2007.

[121] M. Irjala, H. Huhtinen, R. Jha, V. P. S. Awana, and P. Paturi. Optimization of the $BaCeO_3$ Concentration in YBCO Films Prepared by Pulsed Laser Deposition. *IEEE Transactions on Applied Superconductivity*, 21(3):2762–2766, 2011.

[122] M. Peurla, P. Paturi, Y. P. Stepanov, H. Huhtinen, Y. Y. Tse, A. C. Bódi, J. Raittila, and R. Laiho. Optimization of the $BaZrO_3$ concentration in YBCO films prepared by pulsed laser deposition. *Superconductor Science and Technology*, 19(8):767, 2006.

[123] H. Huhtinen, M. Irjala, P. Paturi, and M. Falter. The effect of BZO doping concentration and thickness dependent properties of YBCO films grown by PLD on buffered NiW substrates. *Physica C: Superconductivity*, 472(1):66–74, 2012.

[124] M. Z. Khan, Y. Zhao, X. Wu, M. Malmivirta, H. Huhtinen, and P. Paturi. Improved interface growth and enhanced flux pinning in YBCO films deposited on an advanced IBAD-MgO based template. *Physica C: Superconductivity and its Applications*, 545:50–57, 2018.

[125] S. H. Wee, Y. L. Zuev, C. Cantoni, and A. Goyal. Engineering nanocolumnar defect configurations for optimized vortex pinning in high temperature superconducting nanocomposite wires. *Scientific Reports*, 3(1):1–9, 2013.

[126] S. C. Wimbush and N. J. Long. The interpretation of the field angle dependence of the critical current in defect-engineered superconductors. *New Journal of Physics*, 14(8):083017, 2012.

[127] P. Paturi. The vortex path model and angular dependence of J_c in thin YBCO films deposited from undoped and $BaZrO_3$-doped targets. *Superconductor Science and Technology*, 23(2): 025030, 2010.

[128] L. Civale, B. Maiorov, A. Serquis, J. O. Willis, J. Y. Coulter, H. Wang, Q. X. Jia, P. N. Arendt, J. L. MacManus-Driscoll, M. Maley, et al. Angular-dependent vortex pinning mechanisms in $YBa_2Cu_3O_7$ coated conductors and thin films. *Applied Physics Letters*, 84(12):2121–2123, 2004.

[129] X. Wang, F. J. Baca, R. L. S. Emergo, J. Z. Wu, T. J. Haugan, and P. N. Barnes. Eliminating thickness dependence of critical current density in $YBa_2Cu_3O_7$ films with aligned $BaZrO_3$ nanorods. *Journal of Applied Physics*, 108(11):113911, 2010.

[130] P. Paturi, M. Malmivirta, T. Hynninen, and H. Huhtinen. Angle dependent molecular dynamics simulation of flux pinning in YBCO superconductors with artificial pinning sites. *Journal of Physics: Condensed Matter*, 30(31):315902, 2018.

[131] M. M. Aye, E. Rivasto, M. Z. Khan, H. Rijckaert, E. Salojärvi, C. Haalisto, E. Mäkilä, H. Palonen, H. Huhtinen, I. Van Driessche, et al. Control of the nanosized defect network in superconducting thin films by target grain size. *Scientific Reports*, 11(1):1–11, 2021.

[132] S. V. Pysarenko, A. V. Pan, and S. X Dou. Origin of surface morphology variation during pulsed laser deposition of $YBa_2Cu_3O_7$ superconducting films. *IEEE transactions on applied superconductivity*, 21(3):3179–3183, 2010.

Original Publications

M. Z. Khan & Y. Zhao & X. Wu & M. Malmivirta & H. Huhtinen & P. Paturi
Improved interface growth and enhanced flux pinning in YBCO films deposited on an advanced IBAD-MgO based template

Physica C: Superconductivity and its applications, 545, 2018, 50−57

I

Physica C: Superconductivity and its applications 545 (2018) 50–57

Contents lists available at ScienceDirect

Physica C: Superconductivity and its applications

journal homepage: www.elsevier.com/locate/physc

Improved interface growth and enhanced flux pinning in YBCO films deposited on an advanced IBAD-MgO based template

M.Z. Khan [a], Y. Zhao [b], X. Wu [c], M. Malmivirta [a,d], H. Huhtinen [a,*], P. Paturi [a]

[a] Wihuri Physical Laboratory, Department of Physics and Astronomy, University of Turku, Turku FI-20014, Finland
[b] Department of Electrical Engineering, Shanghai Jiao Tong University, Shanghai 200240, People's Republic of China
[c] Shanghai Superconductor Technology Co. Ltd., Shanghai 200240, People's Republic of China
[d] University of Turku Graduate School (UTUGS), University of Turku, Turku FI-20014 , Finland

ARTICLE INFO

Article history:
Received 9 June 2017
Revised 27 October 2017
Accepted 26 November 2017
Available online 28 November 2017

Keywords:
YBCO
Pulsed laser deposition
Buffer layers
Hastelloy substrate

ABSTRACT

The growth mechanism is studied from the flux pinning point of view in small-scale $YBa_2Cu_3O_{6+x}$ (YBCO) thin films deposited on a polycrystalline hastelloy with advanced IBAD-MgO based buffer layer architecture. When compared the situation with YBCO films grown on single crystal substrates, the most critical issues that affect the suitable defect formation and thus the optimal vortex pinning landscape, have been studied as a function of the growth temperature and the film thickness evolution. We can conclude that the best critical current property in a wide applied magnetic field range is observed in films grown at relatively low temperature and having intermediate thickness. These phenomena are linked to the combination of the improved interface growth, to the film thickness related crystalline relaxation and to the formation of linear array of edge dislocations that forms the low-angle grain boundaries through the entire film thickness and thus improve the vortex pinning properties. Hence, the optimized buffer layer structure proved to be particularly suitable for new coated conductor solutions.

1. Introduction

The manufacturing of high-temperature superconducting (HTS) coated conductors for electric power systems has still numerous fundamental challenges that need to be solved [1–3]. Already the understanding of the limiting factors for the applications, such as weak intragrain pinning and intergrain coupling [4,5], have led to suitable material choices and to increasing development work on metallic substrate and buffer layer architectures [6–10]. However, the growth mechanisms, especially the early interface growth, of superconducting (SC) layer have got too little attention in this development activity [11]. This is true especially, when thinking about envisioned high-current carrying applications, that require strong intrinsic flux pinning capability, operating at relatively high temperatures in strong magnetic fields [12,13].

Significant attention has been drawn to the materials issues, such as the HTS compound $YBa_2Cu_3O_{6+x}$ (YBCO) grown on the textured or untextured metallic substrates with a suitable reaction barrier and epitaxially compatible buffer layer [3]. In this development work, the textured template is carried out by either texturing the buffer layer structure on Hastelloy with ion-beam assisted deposition (IBAD) or by deformation-texturing the metal substrate, typically NiW allow, by the rolling assisted biaxially textured substrate approach (RABiTS^{TM}) [14–16]. However, one of the most critical objectives has been to avoid grain boundaries that propagate through the buffer layer structure and originate from the underlying substrate [17,18]. This effect is extremely crucial especially in relatively thin superconducting films, where the misorientation of the grains produces a barrier to current flow in films grown by pulsed laser deposition. Therefore, it is important to concentrate on the development of the high-quality, highly biaxially textured substrate with optimized buffer layer combinations and thicknesses and, on the other hand, improve the properties of the low-angle grain boundaries and thus the current-carrying capability of the YBCO layers.

In terms of complex nucleation and growth of YBCO films, the size of the single growth islands [11,19] and particularly the nanoscale structural defects within the YBCO lattice [2] have a key role when optimizing these materials for future applications. Especially, the performance of the film, either in self-field or at the high magnetic field of several teslas, is fully dependent on the nature of the defects, such as their size, shape, dimensionality and orientation [11]. If the strong, artificially produced and self-assembled pinning centers, isotropic or anisotropic, [2,20] are not introduced in the YBCO matrix, in addition to intrinsic pinning along the

* Corresponding author.
E-mail address: hannu.huhtinen@utu.fi (H. Huhtinen).

https://doi.org/10.1016/j.physc.2017.11.016
0921-4534/

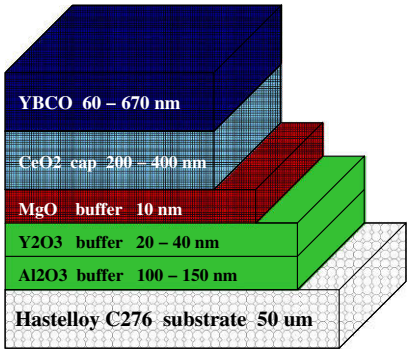

Fig. 1. Schematic layer structure with average thickness values of the epitaxially grown YBCO films deposited on a polycrystalline hastelloy with IBAD-MgO based buffer layer architecture.

direction of the CuO_2 planes, the randomly distributed and localized structural defects are only capable of producing weak, albeit directionally uniform pinning, at relatively low magnetic field range. On the other hand, the anisotropic correlated pinning centers, including an array of extended linear or planar defects that function against thermal activation and vortex depinning, are strongest at high applied magnetic fields aligned along them [2]. Therefore, the most important naturally present defects in YBCO films are the threading dislocations, including basal and edge dislocations along the *c*-axis [21]. Since these pinning mechanisms and their coupling is strongly dependent on the applied temperature and magnetic field, the defect engineering for improving the flux pinning should be based on the demands of the applications.

In the present work, we have first optimized the growth temperature T_g in order to produce small-scale YBCO films on IBAD-MgO based template with the best possible in-field superconducting properties. Secondly, using optimized T_g, the detailed YBCO thickness dependent analysis was implemented in order to obtain the optimal YBCO growth and layer thicknesses for a variety of applications.

2. Experimental details and methods

Two sets of YBCO films were grown by pulsed laser deposition (PLD) using an excimer XeCl ($\lambda = 308$ nm) laser with a pulse duration of 25 ns and a repetition rate of 5 Hz with a laser fluence of 1.3 Jcm^{-2}. The details of the PLD system with the typical deposition parameters have been given elsewhere [22]. The films were deposited on buffered metallic hastelloy substrates with a configuration of Hastelloy C276/Al_2O_3/Y_2O_3/MgO/CeO_2 [23]. Based on previous measurements, the rms roughness of the topmost CeO_2 cap layer varies between 1.5 and 3.0 nm. Also the in-plane texture quality is suitable for the growth of following layers, having FWHM of CeO_2 (111) reflection in ϕ-direction 4–6 degrees [23]. The schematic architecture of the film structures with layer thicknesses is given in Fig. 1. For the growth and measurements, the whole structure was mounted on the top of a $SrTiO_3$ (STO) substrate by conductive silver paint. In the growth temperature optimization, we used 1500 laser pulses for every film which again produced a film thickness of $\approx$160 nm. In thickness dependent analysis, the number of applied laser pulses used were 500, 1000, 2000, 3000, 5000 and 8000 producing the average thicknesses of 60, 115, 205, 295, 480 and 670 nm, respectively, as calculated by using linear interpolation for our films measured earlier [9].

The crystallographic properties of the films were determined by X-ray diffraction (XRD) measurements with a Philips X'Pert Pro-MPD system (Cu K_α radiation). To determine the phase purity of the films, $\theta - 2\theta$ scans in the (00*l*) direction were made. The out-of-plane crystallographic texture was determined by XRD rocking curves (RC) of the YBCO (005) peaks (ω scans). The oxygen stoichiometries of the films were estimated from the intensity ratios of the YBCO (005)/(004) peaks [24,25]. The surface microstructure was studied with an atomic force microscopy (AFM) provided by Bruker Innova®. A specimen for cross-sectional TEM observations was prepared by conventional route including cutting, gluing, grinding, polishing and finally ion polishing. TEM studies were performed using a Technai G2 F20 S-Twin operating at 200 kV. Magnetic measurements were made with a Quantum Design PPMS system, and the critical temperatures, T_c, were determined with ac magnetization measurements in the range of 10–100 K (in an ac field of 0.1 mT). The critical current densities, J_c, at 10 K were determined from the hysteresis loops using the Bean model for rectangular films: $J_c = 2\Delta m/[a(1 - a/3b)V]$, where a and b ($b \geq a$) are the width and the length of the sample, V is the sample volume and Δm is the opening of the hysteresis loop [26].

3. Optimization of the growth temperature

As can be observed from Fig. 2(a), the critical temperature, T_c, of the YBCO film increases with increasing T_g up to 775 °C where the onset $T_c \approx 88$ K. At temperatures $T_g < 725$ °C, T_c starts to decrease dramatically producing also clearly broader superconducting transitions. It is worth noticing that the transition of YBCO film grown at $T_g = 750$ °C on buffered hastelloy is exactly similar to the YBCO films grown on single crystal $SrTiO_3$ (STO) substrate at the same temperature. When comparing these magnetically measured T_c values with those of we earlier deposited on NiW substrates with a wide variety of buffer layer structures [9,27,28], we can conclude that the SC transitions are clearly sharper in the films with T_g of 725 °C and 750 °C although the onset T_c is slightly decreased. However, from the application point of view, the critical current density, and especially its magnetic field dependence, is a more important factor when optimizing the T_g. From Fig. 2(b), we can see that the zero field $J_c(0)$ is slightly decreased in all our films with different T_g, when compared with film grown on STO. The J_c of the film grown at 725 °C is clearly the best at high external magnetic field range above 200 mT, being comparable to the properties of YBCO on STO in the magnetic field range between 1 T and 3 T. As shown in the inset of Fig. 2(b), the accommodation field B^* at 10 K, defined as $J_c(B^*) = 0.9J_c(0)$, has clearly the highest value of $\approx$450 mT in YBCO deposited at 700 °C, while in the film grown at 725 °C, B^* is already decreased to the level of 250 mT. Because the high B^* is usually linked to high number of correlated defects [29], we can conclude that the growth temperature has a great importance in the formation of the proper structural defects for vortex pinning.

Since the superconducting properties of the YBCO films start to deteriorate rapidly below $T_g = 700$ °C, we decided to apply the detailed structural analysis only for temperatures $T_g \geq 700$ °C. The XRD $\theta - 2\theta$ scans (Fig. 3) and detailed 2D (ϕ, 2θ) scans revealed that all the films deposited at temperatures 700 °C $\leq T_g \leq$ 775 °C are phase pure, epitaxially textured and *c*-axis oriented. The most important structural parameters are presented in Table 1. Regardless of the growth temperature, the *c* lattice parameter values, calculated using the Nelson-Riley method [30], are relatively close to the nominal values of YBCO [31]. In addition, the YBCO 2θ peaks are in its entirety extremely narrow (FWHM) although a decreasing tendency with increasing T_g can be observed. The FWHM of 2θ peaks (hereafter $\Delta 2\theta$ and for FWHM of ϕ as $\Delta\phi$) is clearly smaller than earlier observed in YBCO films grown on buffered NiW substrates [7,9,28], indicating only marginal variation in unit cell volume through the film in these samples. Although the $\Delta\phi$

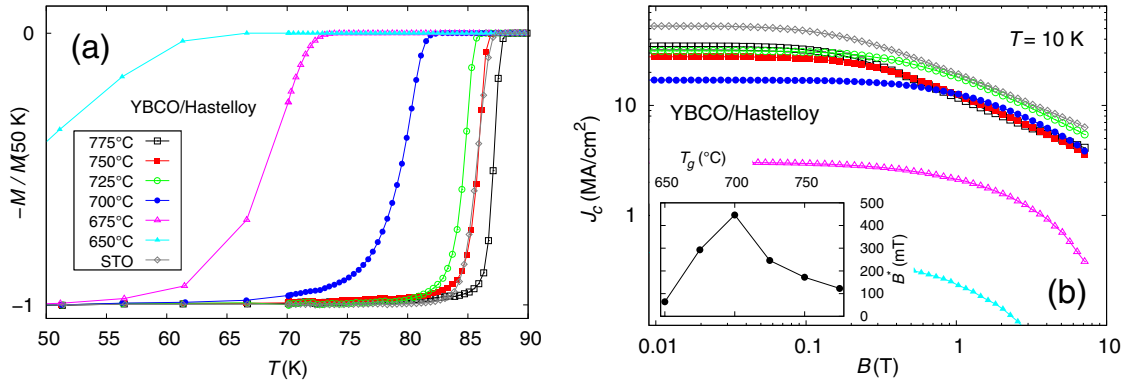

Fig. 2. The normalized ac magnetizations as functions of temperature (a) and the magnetic field dependencies of J_c determined from the hysteresis loops at 10 K (b) for YBCO films deposited at different temperatures T_g on IBAD-MgO based template. The inset of (b) shows the T_g dependence of the accommodation field B^*.

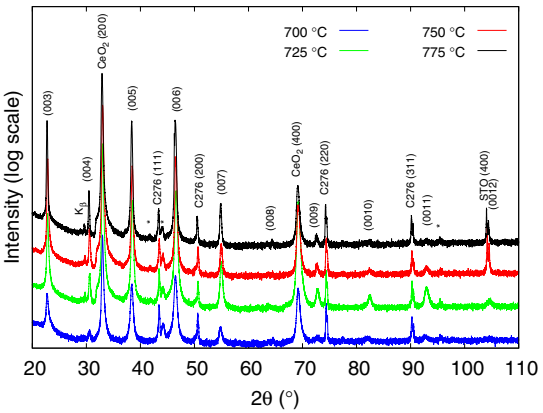

Fig. 3. XRD $\theta - 2\theta$ scans of the YBCO thin films grown on IBAD-MgO based template at different deposition temperatures. The YBCO (00l) peaks are indexed along with the most intense peaks from the substrate and buffer layers. The peaks marked with asterisk arise from the sample holder. The intensities are given in logarithmic scale and the diffractograms are shifted for clarity. In the two upper diffractograms the STO substrate beneath of the sample is visible for the x-ray beam at high 2θ. Thus the STO (400) peak is observed.

Table 1
Structural parameters determined from XRD measurements for YBCO films deposited on buffered hastelloy using different growth temperatures T_g.

T_g (°C)	YBCO lattice c (Å)	FWHM 2θ (005) (°)	FWHM ϕ (102) (°)	FWHM ω (005) (°)	I(005)/ I(004)	ε_{WH} (%)
700	11.71	0.38	4.3	2.2	17.3	0.49
725	11.69	0.26	3.9	1.5	15.8	0.62
750	11.69	0.26	4.2	1.7	9.8	0.67
775	11.69	0.20	4.0	2.8	11.1	0.43

values are greater than observed earlier for YBCO films grown on single crystalline STO substrate, the widths of the peaks in ϕ direction are only half on the values measured for films deposited on buffered NiW and, therefore, $\Delta\phi$ values illustrate the improved structural in-plane quality in the whole measured T_g range [28,32,33]. The out-of-plane crystallographic texture is determined from the FWHM of the rocking curve ω (005) (hereafter $\Delta\omega$) peaks and especially in films deposited at 725 °C and 750 °C, $\Delta\omega$ values are relatively small, almost in the level of values observed earlier in YBCO films grown on STO substrates [7]. This means that the YBCO long range coherence is clearly longer than earlier observed for films deposited on buffered NiW substrates. In addition, the intensity ratio I(005)/I(004) varies between $\approx 10 - 17$ in all the films grown at different T_g, which indicates that the oxygen deficiency is $\delta < 0.1$ [24]. However, the intensity ratio is even smaller in films with $T_g \geq 750$ °C, indicating that higher *in situ* post-annealing temperature leads to even better oxidation of the film.

In more detailed structural analysis of the films, the microstrain in c direction was determined with the Williamson-Hall method [34]. The FWHM of the (00l) peaks was used to determine the microstrain, ε_{WH}, which in this case describes the variation of the c parameter throughout the whole film thickness. As can be seen in Table 1, ε_{WH} is relatively constant in films grown at low T_g, but slightly lower in film grown at 775 °C. This is in line with the obtained SC properties, where increased T_g improves the crystalline quality with increased T_c although, the in-field J_c is decreased most in films grown with high T_g.

Based on the above explained structural and especially on the magnetic results, we decided to choose the growth temperature $T_g = 725$ °C for detailed thickness dependent analysis, as will be discussed in the following section. It is good to note that the optimized substrate temperature of 725 °C for films grown on IBAD-MgO based template is slightly lower than that for YBCO films grown on STO, ≈750 °C.

4. Film thickness optimization

4.1. Structural growth

As in the growth temperature dependence analysis, all the films with different thicknesses are also phase pure, epitaxially textured and c-axis oriented (Fig. 4). The most important structural parameters are collected in Table 2. The c-axis lattice parameters are in practise unchanged as a function of the film thickness although they are slightly longer than the nominal value of 1.167 nm for powders and single crystals. However, we can assume that the unit cell volume stays constant, at least within the used thickness range. The widths of the 2θ peaks are relatively small, almost at the level of that in YBCO films grown on the top of the STO substrate [7,28]. However, the slight decrease in $\Delta 2\theta$ with increasing thickness could indicate the improved unit cell structure caused by the increased relaxation time and therefore a subtle modification

Table 2
Structural parameters determined from XRD measurements for YBCO films deposited on buffered hastelloy with different thicknesses (number of laser pulses).

Thickness (nm)	YBCO lattice c (Å)	FWHM 2θ (005) (°)	FWHM ϕ (102) (°)	FWHM ω (005) (°)	I(005)/ I(004)	ε_{WH} (%)
60	11.69	0.33	3.8	2.8	14.9	0.39
115	11.70	0.32	3.4	1.6	15.6	0.60
205	11.69	0.32	4.1	2.6	15.1	0.78
295	11.69	0.31	4.0	2.3	13.8	0.75
480	11.69	0.31	3.4	2.2	15.2	0.58
670	11.69	0.28	3.2	1.5	15.4	0.60

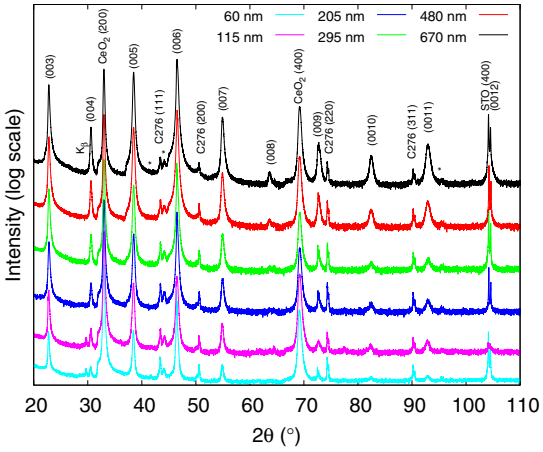

Fig. 4. XRD $\theta - 2\theta$ scans of the YBCO thin films with different thicknesses deposited on IBAD-MgO based template. The YBCO (00l) peaks are indexed along with the most intense peaks from the substrate and buffer layers. The peaks marked with asterisk arise from the sample holder. The intensities are given in logarithmic scale and the diffractograms are shifted for clarity. Here the STO (400) peak (see Fig. 3 caption for the explanation of the STO (400) peak).

in the thicknesses of the uppermost buffer layers could be feasible. When looking at the ε_{WH} values, one can observe the highest ε_{WH} in films with thicknesses $\approx 200 - 300$ nm. Since the microstrain is induced by different types of structural defects such as vacancies, dislocations, interstitials, fault layers etc. which, on the other hand, broaden the XRD peaks [34], this suggests increased amount of threading dislocations along the YBCO c-axis in films with intermediate thicknesses.

Also, the widths of the XRD peaks in ϕ- and ω-directions are, within the error limits, constant and thus independent of the film thickness. The absolute values of $\Delta\phi$ and $\Delta\omega$ are approximately half of the values observed earlier for the YBCO films pulsed laser deposited on buffered NiW substrates [7,28] and, on the other hand, $\Delta\phi$ is four times greater than in films deposited on single crystal STO substrate [7]. This means that the films in this work with the whole thickness range have more pronounced low-angle grain boundaries and thus a greater number of dislocations which are capable of pinning vortices in the c direction [2,35,36]. Also, these films have better long range lattice ordering, where the atomic positions are correlated along the YBCO c-axis [37,38]. In addition, based on the peaks intensity ratios of I(005)/I(004), all the films with different thicknesses are relatively well-oxygenized, being in line with high T_c values close to 90 K.

According to the $2 \times 2\,\mu m^2$ AFM images seen in Fig. 5, the in-plane surface particle size is relatively small, on average 25 nm in diameter in the thinnest YBCO film deposited with 500 pulses. When increasing the number of pulses, according to the island growth model, the particles start to grow together forming larger islands with increased particle size. In the two thickest films with 5000 and 8000 pulses, producing thicknesses of 480 and 670 nm, the average in-plane particle diameter varies between 100 nm and 200 nm, but clearly smaller subparticles, as a part of the base structure, can be observed. The height of the growth islands increases similarly with increasing thickness and this is reflected in the calculated surface RMS roughness values, as shown in Fig. 6(a). However, the surface roughness increases moderately up to the thickness of 300 nm, above which the surface roughness starts to increase rapidly. This gives the kind of limit for the optimal film thickness, especially if thinking about the applications, where the surface smoothness has a crucial role.

In Fig. 6(b), the larger area scan of $20 \times 20\,\mu m^2$ is shown for the thinnest YBCO film deposited with 500 pulses. In spite of the multilayer buffer structure, the grain diameter of $\approx 10\,\mu m$ that probably originates from the morphology of the Hastelloy tape is still visible on the surface of the CeO_2 layer (not shown here) as well as relatively weakly on the thinnest YBCO film of 60 nm (Fig. 6(b)). In thicker films, above 100 nm, the grain structure is no more visible, indicating clearly improved interface growth of YBCO, especially when compared with the YBCO films grown on buffered NiW substrate [28]. However, on the surface of relatively thick CeO_2 cap layer, we can observe the surface particles with the diameter of $20 - 30$ nm. If this value indicates the size of the CeO_2 growth islands, we can conclude that the island size in the thinnest YBCO layer is roughly on the same level. On the other hand, the island size in the thickest YBCO film of 670 nm is already $5 - 10$ times larger than that in the CeO_2 layer.

In the cross-sectional TEM image (Fig. 7), we observed that the YBCO grows along the c-axis, the [001] direction, onto the CeO_2 cap layer. The absence of commonly observed secondary phase $BaCeO_3$ at YBCO-CeO_2 interface indicate negligible reactions during the YBCO film deposition, which could be related to low growth temperature of YBCO and high stability of the CeO_2 layer. The possibility using a relatively low growth temperature is a clear step forward, since the complete interfacial reaction in YBCO films on CeO_2 layer has been observed at as low temperature 740 °C in chemical solution deposited films [39] as well as in the pulsed laser deposited films at around 800 °C [40]. Although the YBCO matrix generally shows pure phase, based on the contrasts in the TEM image, we observed a high defect density which indicate a strained region, especially close to the interface below thickness of a few tens of nanometers, as indicated by the thick arrows in Fig. 7. The YBCO structure relaxes and crystallinity improves above this strained layer, but a minor amount of stacking faults and dislocations are still discerned through the whole thickness, as indicated by the horizontal arrows. It is believed that those defects introduced by low-temperature growth conditions of YBCO are beneficial for J_c enhancement at high magnetic fields, as will be discussed below.

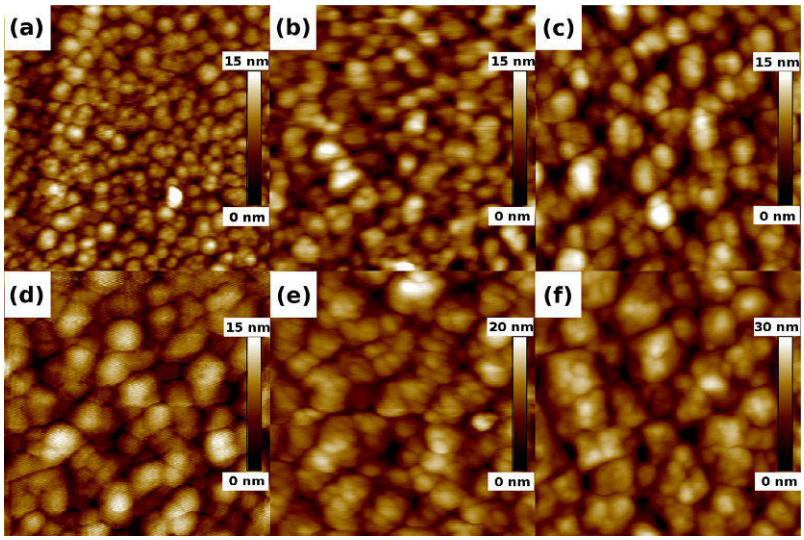

Fig. 5. (a)–(f) AFM images of the YBCO films deposited at $T_g = 725$ °C on IBAD-MgO based template having different thicknesses of 60, 115, 205, 295, 480 and 670 nm, respectively. The scan sizes of the images are $2 \times 2\,\mu m^2$ and the values of the height scale bars are given in each subfigure.

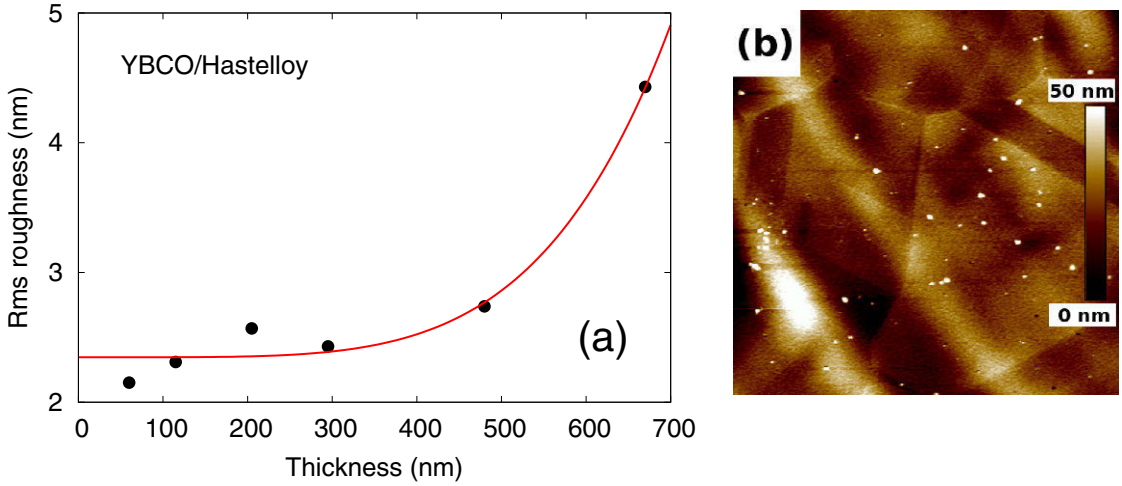

Fig. 6. (a) RMS roughness values as functions of film thickness, which is modified by varying the number of laser pulses during deposition. The red line in the figure is drawn to guide the eye. (b) The AFM image of the thinnest 60 nm YBCO film surface using relatively large $20 \times 20\,\mu m^2$ scan area. (For interpretation of the references to colour in this figure legend, the reader is referred to the web version of this article.)

4.2. Thickness dependent superconducting properties

As can be seen from Fig. 8(a), T_c is slightly lower, below 84 K, in the thinnest film deposited with 500 pulses. When more pulses are applied and the film thickness increases, T_c also increases and it reaches the highest value of 85.5 K with thickness of ≈300 nm. The T_c is exactly the same as in the samples of the growth temperature optimization, but above 300 nm, T_c starts to decrease slowly again. As can be seen in Fig. 8(a), when compared to the T_c defined by the midpoint of the SC transition, the onset T_c values are slightly higher and the differences between the samples with different thicknesses are even smaller. Together with the thickness dependent structural data, we can conclude that lower T_c with the broadest transition in the thinnest film indicate that the growth and thus the unit cell is not yet completely relaxed [41]. Above 60 nm, the structure improves up to the thickness of 300 nm, having more time for crystalline relaxation. In films with thickness over 300 nm, above the relaxed layer there appears a thin surface layer that includes more crystalline defects or other disordering. This is in line with the almost unchanged onset T_c albeit the mid-T_c is clearly decreased, at least up to the thickest film in this set of samples. This is also qualitatively in agreement with the XRD results, where $\Delta 2\theta$ decreases with increasing thickness and $\Delta\phi$ as well as $\Delta\omega$ are approximately constant within this thickness range.

According to the J_c curves in Fig. 8(b), the zero field $J_c(0)$ has the highest value in the films with intermediate thicknesses

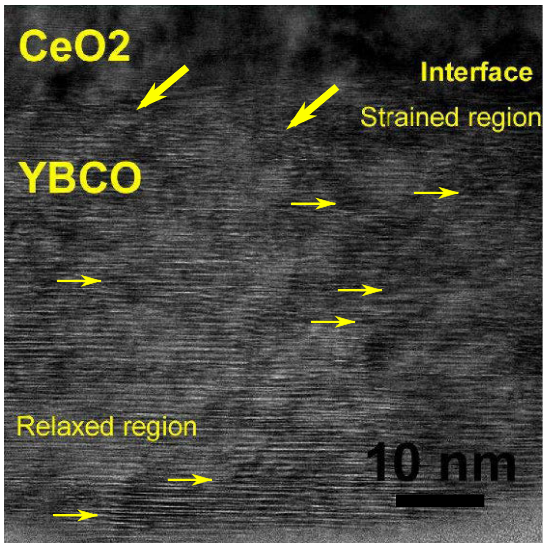

Fig. 7. TEM image of a cross-section of YBCO/CeO_2/IBAD-MgO/Y_2O_3/Al_2O_3 stack. The image shows the interface between the topmost CeO_2 buffer cap and the 60 nm thick YBCO film on the top. The disordered regions (thick arrows), indicating strained layer next to the interface and mostly relaxed layer with occasional stacking faults and dislocations (horizontal arrows) are indicated in the image.

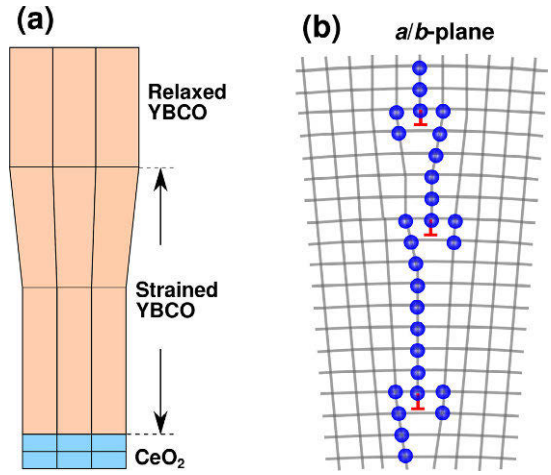

Fig. 9. A schematic illustration of the YBCO growth on the top of IBAD-MgO based template. (a) The CeO_2/YBCO interface without the reaction layer and the relaxation of YBCO film below the critical thickness of a few tens of nanometers under a subtle compressive strain (not in scale) and (b) the connection between the edge dislocations and the observed low-angle grain boundaries that positively affect the out-of-plane vortex pinning properties.

200 – 300 nm, above which there is a decreasing but still moderate tendency in $J_c(0)$ when the number of laser pulses is increased. In two thinnest films, the decreased $J_c(0)$ and T_c can be explained by the decreased crystalline quality as well as by the less amount of relatively weak random pinning centers that are important in the self-field range [21]. In thicker films, besides the worsened crystalline structure, the decreased $J_c(0)$ could be at least partly related to the even more retarded growth rate than used in the thickness extrapolation for the thickest films. In the high external magnetic field range between 1 T and 3 T, $J_c(B)$ values are approximately similar in all the other films except the films with thicknesses between 200 and 300 nm, where slightly improved in-field J_c properties can be observed. This is in agreement with our earlier results for YBCO films grown on buffered NiW substrates, where the films with intermediate thicknesses produced the best vortex pinning behavior [28]. Since we observed also clearly increased microstrain ε_{WH} values for these films, we can collectively describe the improvement in in-field J_c with the increased number of edge dislocations formed through the entire film.

To summarize, our structural and magnetic analysis showed that the improved critical current density in a wide magnetic field range is observed in YBCO films with intermediate thickness of 200–300 nm and which are deposited at lower temperature than similar films grown on single crystal substrates. These findings can be qualitatively explained by the following mechanisms as schematically illustrated in Fig. 9. First, based on the TEM and XRD results, the advanced IBAD-MgO based buffer layer structure induced favorable interface growth. That is to say, there are no

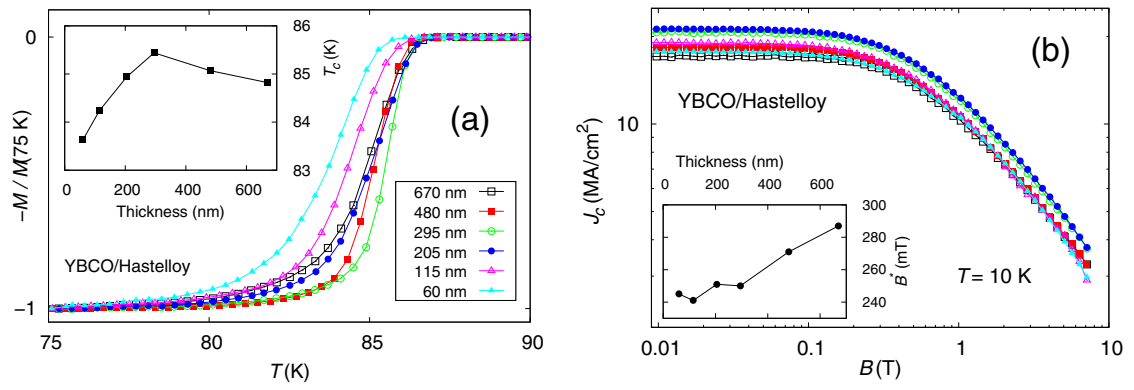

Fig. 8. (a) The normalized ac magnetizations as functions of temperature (main panel) and the thickness dependence of the critical temperature T_c determined from the middle of the transition (inset). (b) The magnetic field dependencies of J_c determined from the hysteresis loops at 10 K. The inset of (b) shows the film thickness dependence of the accommodation field B^*. All the measurements were made for YBCO films deposited at $T_g = 725$ °C on buffered hastelloy with varying number of pulses, producing different film thicknesses.

reaction layer at the YBCO/CeO_2 interface and the relaxation of the YBCO crystalline structure occurs at early growth thickness level, where the critical thickness for the primary strain relaxation is below a few tens of nanometers. This, on the other hand, improves the crystalline quality of the films. In addition, based on the detailed XRD analysis in ϕ direction, the linear array of edge dislocations, that forms the low-angle grain boundaries in the YBCO matrix, positively affects the magnetic flux pinning properties thus increasing the high-field J_c value, in this case especially along the out-of-plane YBCO *c*-axis [42]. When looking at the thickness dependent B^* values (inset of Fig. 8(b)), we can obtain relatively constant B^* but, above the thickness of 300 nm, slightly increasing B^* which, on the other hand, indicates similar flux pinning within the whole thickness range. However, in thicker films the relaxation time also for the YBCO interface layer increases, which could further promote the reorganization of the YBCO matrix during the growth process [41]. Therefore, even better and more compatible buffer layer structure would assist the early growth of YBCO and minimize the effect of CeO_2 grain boundaries, which still affects the granular structure of YBCO although only next to the cap layer interface.

5. Conclusions

In this work, we have investigated the role of growth temperature and film thickness in small-scale YBCO films grown on an advanced IBAD-MgO based buffer layer structure. This is done by concentrating on structural and superconducting properties that are important when trying to understand the growth process, structural defect formation and, on the other hand, the effective magnetic flux pinning in relatively high external magnetic fields. When thinking about the growth of YBCO on the metallic substrates that are suitable for coated conductor applications, it turns out that, the lower growth temperature than in films grown on single crystal substrates and the intermediate film thickness of 200–300 nm seem to be optimal. Based on the thickness dependent structural and superconducting properties minutely shown in this study, it can be concluded that the existing IBAD-MgO based buffer layer structure with hastelloy C276 substrate works better than all the other small scale combinations we have tried to optimize earlier by pulsed laser deposition. Therefore, we suggest that this buffer layer structure is a valuable alternative when optimizing and improving the novel buffer layer structures for future coated conductor technologies.

Acknowledgments

The Jenny and Antti Wihuri Foundation is acknowledged for financial support.

References

[1] D. Finnemore, K. Gray, M. Maley, D. Welch, D. Christen, D. Kroeger, Coated conductor development an assessment, Physica C 320 (1999) 1.
[2] S.R. Foltyn, L. Civale, J.L. MacManus-Driscoll, Q.X. Jia, B. Maiorov, H. Wang, M. Maley, Materials science challenges for high-temperature superconducting wire, Nat. Mater. 6 (2007) 631.
[3] X. Obradors, T. Puig, Coated conductors for power applications: materials challenges, Supercond. Sci. Technol. 27 (2014) 044003.
[4] D.M. Feldmann, D.C. Larbalestier, D.T. Verebelyi, W. Zhang, Q. Li, G.N. Rilay, R. Feenstra, A. Goyal, D.F. Lee, M. Paranthaman, D.M. Kroeger, D.K. Christen, Inter- and intragrain transport measurements in YBCO deformation textured coated conductors, Appl. Phys. Lett. 79 (2001) 3998.
[5] Y. Xu, D. Shi, A review of coated conductor development, Tsinghua Sci. Technol. 8 (2003) 342.
[6] J.K. Chung, R.K. Ko, D.Q. Shi, H.S. Ha, H. Kim, K.J. Song, C. Park, S.H. Moon, S.I. Yoo, Use of $SrTiO_3$ as a single buffer layer for RABiTS YBCO coated conductor, IEEE T. Appl. Supercond. 15 (2005) 3020.
[7] H. Huhtinen, M. Irjala, P. Paturi, J.C. Grivel, Y.Y. Tse, M. Falter, J. Eickemeyer, Y. Zhao, Growth and BZO-doping of the nanostructured YBCO thin films on buffered metal substrates, Physica C 470 (2010) S1013.
[8] J. Kunert, M. Bäcker, O. Brunkahl, D. Wesolowski, C. Edney, P. Clem, N. Thomas, A. Liersch, Advanced titania buffer layer architectures prepared by chemical solution deposition, Supercond. Sci. Technol. 24 (2011) 085018.
[9] H. Huhtinen, M. Irjala, P. Paturi, M. Falter, The effect of BZO doping concentration and thickness dependent properties of YBCO films grown by PLD on buffered NiW substrates, Physica C 472 (2012) 66.
[10] D. Xu, Y. Wang, L. Liu, Y. Li, Dependences of microstructure and critical current density on the thickness of $YBa_2Cu_3O_{7-x}$ film prepared by pulsed laser deposition on buffered NiW tape, Thin Solid Films 529 (10) (2013).
[11] X. Obradors, T. Puig, S. Ricart, M. Coll, J. Gazquez, A. Palau, X. Granados, Growth, nanostructure and vortex pinning in superconducting $YBa_2Cu_3O_7$ thin films based on trifluoroacetate solutions, Supercond. Sci. Technol. 25 (2012) 123001.
[12] D. Larbalestier, A. Gurevich, D.M. Feldmann, A. Polyanskii, High-t_c superconducting materials for electric power applications, Nature 414 (2001) 368.
[13] Y. Shiohara, Y. Aoki, Activity of R&D for coated conductors in Japan, Physica C 426–431 (2005) 1.
[14] Y. Iijima, K. Kakimoto, M. Kimura, K. Takeda, T. Saitoh, Reel to reel continous formation of Y-123 coated conductors by IBAD and PLD method, IEEE T. Appl. Supercond. 11 (2001) 2816.
[15] A. Goyal, D. Norton, J. Budai, M. Paranthaman, E. Specht, D. Kroeger, High critical current density superconducting tapes by epitaxial deposition of $YBa_2Cu_3O_x$ thick films on biaxially textured metals, Appl. Phys. Lett. 69 (1996) 1795.
[16] A. Goyal, D.F. Lee, F.A. List, E.D. Specht, R. Feenstra, M. Paranthaman, X. Cui, S.W. Lu, P.M. Martin, D.M. Kroeger, D.K. Christen, B.W. Kang, D.P. Norton, C. Park, D.T. Verebelyi, J.R. Thompson, R.K. Williams, T. Aytug, C. Cantoni, Recent progress in the fabrication of high-J_c tapes by epitaxial deposition of YBCO on RABiTS, Physica C 357–360 (2001) 903.
[17] D.M. Feldmann, J.L. Reeves, A.A. Polyanskii, G. Kozlowski, R.R. Biggers, R.M. Nekkanti, I. Maartense, M. Tomsic, P. Barnes, C.E. Oberly, T.L. Peterson, S.E. Babcock, D.C. Larbalestier, Influence of nickel substrate grain structure on $YBa_2Cu_3O_{7-x}$ supercurrent connectivity in deformation-textured coated conductors, Appl. Phys. Lett. 77 (2000) 2906.
[18] Y. Zhao, L. Ma, W. Wu, H.-L. Suo, J.-C. Grivel, Study on advanced $Ce_{0.9}La_{0.1}O_2/Gd_2Zr_2O_7$ buffer layers architecture towards all chemical solution processed coated conductors, J. Mater. Chem. A 3 (2015) 13275.
[19] H. Huhtinen, J. Järvinen, R. Laiho, P. Paturi, J. Raittila, Laser deposition from a nanostructured YBaCuO target: Analysis of the plume and growth kinetics of particles on $SrTiO_3$, J. Appl. Phys. 90 (2001) 1521.
[20] S.H. Wee, Y.L. Zuev, C. Cantoni, A. Goyal, Engineering nanocolumnar defect configurations for optimized vortex pinning in high temperature superconducting nanocomposite wires, Sci. Rep. 3 (2013) 2310.
[21] T.G. Holesinger, L. Civale, B. Maiorov, D.M. Feldmann, J.Y. Coulter, D.J. Miller, V.A. Maroni, Z. Chen, D.C. Larbalestier, R. Feenstra, X. Li, Y. Huang, T. Kodenkandath, W. Zhang, M.W. Rupich, A.P. Malozemoff, Progress in nanoengineered microstructures for tunable high-current, high-temperature superconducting wires, Adv. Mater. 20 (2008) 391.
[22] H. Palonen, H. Huhtinen, M.A. Shakhov, P. Paturi, Electron mass anisotropy of $BaZrO_3$ doped YBCO thin films in pulsed magnetic fields up to 30 T, Supercond. Sci. Technol. 26 (2013) 045003.
[23] Q.-Q. Mu, L.-F. Liu, Y.-J. Li, Fabrication of IBAD-MgO and PLD CeO_2 layers for YBCO coated conductors, Chin. Phys. Lett. 32 (2015) 078102.
[24] J. Ye, K. Nakamura, Quantitative structure analyses of YBCO thin films: Determination of oxygen content from x-ray-diffraction patterns, Phys. Rev. B 48 (1993) 7554.
[25] J. Ye, K. Nakamura, Systematic study of the growth-temperature dependence of structural disorder and superconductivity in $YBa_2 Cu_3 O_{7-\delta}$ thin films, Phys. Rev. B 50 (1994) 7099.
[26] H.P. Wiesinger, F.M. Sauerzopf, H.W. Weber, On the calculation of J_c from magnetization measurements on superconductors, Physica C 203 (1992) 121.
[27] H. Huhtinen, M. Irjala, P. Paturi, M. Falter, Optimal BZO doping in YBCO films grown on single crystal STO and buffered NiW substrates, IEEE T. Appl. Supercond. 21 (2011) 2753.
[28] M. Malmivirta, H. Huhtinen, Y. Zhao, J.-C. Grivel, P. Paturi, Thickness-dependent properties of YBCO films grown on GZO/CLO-buffered NiW substrates, J. Low Temp. Phys. 186 (2017) 74.
[29] F.C. Klaassen, G. Doornbos, J.M. Huijbregtse, R.C.F. van der Geest, B. Dam, R. Griessen, Vortex pinning by natural linear defects in thin films of $YBa_2Cu_3O_{7-\delta}$, Phys. Rev. B 64 (2001) 184523.
[30] J.B. Nelson, D.P. Riley, An experimental investigation of extrapolation methods in the derivation of accurate unit-cell dimensions of crystals, Proc. Phys. Soc. 57 (1945) 160.
[31] P. Schweiss, W. Reichardt, M. Braden, G. Collin, G. Heger, H. Claus, A. Erb, Static and dynamic displacements in $RBa_2Cu_3O_{7-\delta}$ (R =Y, Ho; δ = 0.05, 0.5): A neutron-diffraction study on single crystals, Phys. Rev. B 49 (1994) 1387.
[32] R. Kromann, J.B. Bilde-Sørensen, R. de Reus, N.H. Andersen, P. Vase, T. Freltoft, Relation between critical current densities and epitaxy of YBCO thin films on MgO and $SrTiO_3$, J. Appl. Phys. 71 (1992) 3419.
[33] V. Svetchnikov, V. Pan, C. Træholt, H. Zandbergen, Formation of edge dislocations in thin epitaxial YBCO films, IEEE T. Appl. Supercond. 7 (1997) 1396.
[34] M. Birkholz, Thin Film Analysis by X-ray Scattering, Wiley-VCH, 2006.
[35] N.F. Heinig, R.D. Redwing, J.E. Nordman, D.C. Larbalestier, Strong to weak coupling transition in low misorientation angle thin film $YBa_2Cu_3O_{7-x}$ bicrystals, Phys. Rev. B 60 (1999) 1409.

[36] M. Irjala, H. Huhtinen, V.P.S. Awana, M. Falter, P. Paturi, Increased grain boundary critical current density J_c^{gb} by Pr-doping in pulsed laser deposited $Y_{1-x}Pr_x$ BCO thin films, J. Appl. Phys. 110 (2011) 113905.
[37] A. Gauzzi, D. Pavuna, Quantitative analysis of growth-induced reduction of long range lattice order in ion-beam sputtered $YBa_2Cu_3O_{6.9}$ films, Appl. Phys. Lett. 66 (1995) 1836.
[38] H. Huhtinen, K. Schlesier, P. Paturi, Growth and *c*-axis flux pinning of nanostructured YBCO/BZO multilayers, Supercond. Sci. Technol. 22 (2009) 075019.
[39] Y. Zhao, W. Wui, X. Tang, N.H. Andersen, Z. Han, J.-C. Grivel, Epitaxial growth of $YBa_2Cu_3O_{7-x}$ films on $Ce_{0.9}La_{0.1}O_{2-y}$ buffered yttria-stabilized zirconia substrates by an all-chemical-solution route, CrystEngComm 16 (2014) 4369.
[40] Y.A. Boikov, T. Claeson, D. Erts, F. Bridges, Z. Kvitky, Ceo_2 compatibility with $YBa_2Cu_3O_{7-\delta}$ in superdonducting-film multilayers, Phys. Rev. B 56 (1997) 11312.
[41] M. Peurla, H. Huhtinen, Y.Y. Tse, J. Raittila, P. Paturi, Structural properties of YBCO thin films deposited from different kinds of targets, IEEE T. Appl. Supercond. 17 (2007) 3608.
[42] G. Kästner, D. Hesse, R. Scholtz, H. Koch, F. Ludwig, M. Lorenz, H. Kittel, Microstructure defects in YBCO thin films – a TEM study to discuss their influence in device properties, Physica C 243 (1995) 281.

M. Z. Khan & M. Malmivirta & Y. Zhao & X. Wu & R. Jha & V.P.S. Awana & H. Huhtinen & P. Paturi
Angular and field dependent flux pinning in artificially doped YBCO films on IBAD-MgO based template

Physica C: Superconductivity and its applications, 555, 2018, 15−23

II

Physica C: Superconductivity and its applications 555 (2018) 15–23

Contents lists available at ScienceDirect

Physica C: Superconductivity and its applications

journal homepage: www.elsevier.com/locate/physc

Angular and field dependent flux pinning in artificially doped YBCO films on IBAD-MgO based template

M.Z. Khan*,[a,b], M. Malmivirta[a], Y. Zhao[c], X. Wu[d], R. Jha[e], V.P.S. Awana[e], H. Huhtinen[a], P. Paturi[a]

[a] Wihuri Physical Laboratory, Department of Physics and Astronomy, University of Turku, Turku FI-20014, Finland
[b] University of Turku Graduate School (UTUGS), University of Turku, Turku FI-20014, Finland
[c] Department of Electrical Engineering, Shanghai Jiao Tong University, Shanghai 200240, People's Republic of China
[d] Shanghai Superconductor Technology Co. Ltd., Shanghai 200240, People's Republic of China
[e] Superconductivity Division, National Physical Laboratory (CSIR), New Delhi 11012, India

ARTICLE INFO

Keywords:
YBCO
BCO and BZO
IBAD-MgO based template
Vortex pinning

ABSTRACT

The self-organized artificial pinning structure in superconducting thin films of $YBa_2Cu_3O_{6+x}$ (YBCO) is optimized on a new type of IBAD-MgO based template by doping YBCO with non-superconducting $BaCeO_3$ (BCO) and $BaZrO_3$ (BZO). In these films, the YBCO is well ordered, no large angle grain boundaries are seen and the isotropic BCO particles are randomly distributed while the BZO grows as unidirectionally splayed and shortened nanorods. Additionally, the low-angle grain boundaries formed during the growth process have an impact on the flux pinning. The flux pinning behaviour can be explained by the vortex path model, where the pinning paths are shorter in BZO doped than in BCO doped films. In BZO doped films, the vortices are pinned with greater pinning force and thus the critical current density J_c is higher than in BCO doped films, especially in high magnetic fields, where the wide peaks in $J_c(\theta)$ were seen along the YBCO *c*-direction. This direction dependent pinning can be explained by the nearly similar diameters of BZO nanorods with those of vortices, thus efficiently increasing the vortex pinning in the vicinity of YBCO *c*-axis.

1. Introduction

The electrical efficiency with high power density is one of the fascinating properties that makes the high temperature superconductor (HTS) interesting for the applications in electrical power systems [1]. In order to apply superconductors in wire applications, single crystalline substrates have limitations as they can not be bent and thus flexible metal substrates are a substitute in this regard. HTS material as $YBa_2Cu_3O_{6+x}$ (YBCO) with a high critical magnetic field and temperature has shown its potential in electrical applications when coated on metallic substrates [2]. As the motion of vortices causes resistance and at a high applied magnetic field more vortices come into the structure, the directional pinning architecture plays a vital role in improving the properties of superconductors [3].

Besides naturally created defects during the growth process of HTS, artificially implemented non-superconducting defects have also been produced within the YBCO structure to enhance the in-field pinning performance, leading to higher critical current density, J_c, especially at high magnetic fields [3–5]. Among the other dopant materials, $BaCeO_3$ (BCO) and $BaZrO_3$ (BZO) have been successfully doped to YBCO in order to induce isotropic spherical nanoparticles and correlated nanocolumns formed through the entire film, respectively [6–8]. From the application point of view, the spatial distribution of the pinning centres and thus the impact on the anisotropy of the intrinsic YBCO behaviour is an extremely critical factor when optimizing the vortex pinning landscape in YBCO matrix [3,9].

The industrial based research, which concentrates mainly on the product development of long-length tapes, has not sufficiently focused on the comprehensive vortex pinning behaviour in HTS materials, since the properties can vary in lengthy tapes ($>$ 2 cm) due to the high probability of presence of unwanted defects that lead to non-homogeneity at different sites of the material. Therefore, the complex laboratory work for small-scale samples where mechanisms in vortex pinning can be investigated at wide external magnetic fields with various temperature ranges, could be as a stepping stone for the modern understanding about critical problematics for future HTS coated conductors. Especially, the interface growth of YBCO as well as the formation of self-assembled dopants within the YBCO matrix are in an extremely important role when optimizing these materials on polycrystalline hastelloy with an advanced ion beam assisted deposition-

* Corresponding author.
E-mail address: mukarram.z.khan@utu.fi (M.Z. Khan).

https://doi.org/10.1016/j.physc.2018.10.006
Received 1 August 2018; Received in revised form 9 October 2018; Accepted 11 October 2018
Available online 11 October 2018
0921-4534/

magnesium oxide (IBAD-MgO) based buffer layer structure. As shown previously [10], large-angle grain boundaries were not present in films grown on an IBAD-MgO based template but instead, the observed low-angle grain boundaries based on threading dislocations along the *c*-axis would considerably channel the growth and distribution of strong artificial pinning centres.

In this work, we investigated the small-scale BCO and BZO doped YBCO thin films with the same thicknesses prepared at different temperatures on an advanced IBAD-MgO based template. Furthermore, the structural, magnetic and transport properties were compared for both set of samples prepared with different dopants. In order to get the complete picture of superconducting properties in different magnetic field strengths and orientations, we concentrated more on the angular dependent properties.

2. Experimental details

YBCO targets doped with 4 % non-superconducting BCO and BZO were used to prepare two different sets of *in situ* YBCO films by pulsed laser deposition (PLD) method. The targets were synthesized by the solid state ceramic method and the details of this method can be found in Ref. [11]. Both BCO and BZO were doped with a ratio of 4 % to the total weight of YBCO which has proved to be the optimal doping concentration for flux pinning in high field range in case of single crystal substrates, when grown with our PLD system [12–14]. In each set, four films were grown at growth temperature (T_g) range from 650 °C to 800 °C with a step difference of 50 °C. The T_g was measured with a thermocouple placed behind the substrate inside the Inconel plate substrate holder. Excimer XeCl laser with the deposition parameters of wavelength $\lambda = 308$ nm, pulse duration 25 ns and pulse repetition rate 5 Hz with 1.3 Jcm^{-2} laser fluence was used to deposit all the films. The details of the PLD system along with the optimized deposition parameters can be found elsewhere [15]. Buffered metallic tape with the configuration of Hastelloy C276/Al_2O_3/Y_2O_3/MgO/CeO_2 as shown in Fig. 1 was manufactured according to Ref. [16] and was used as a substrate for depositing YBCO. The IBAD-MgO layer forms in-plane grain alignment and has biaxial texture. Finally, the topmost CeO_2 cap layer has the thermal expansion coefficient close to YBCO, good chemical compatibility and small lattice mismatch to that of deposited YBCO [16]. The $5 \times 5\,mm^2$ sized IBAD-MgO based templates were fixed on $SrTiO_3$ (STO) with conductive silver paste for growth processes and measurements. Each film was deposited by applying 1600 laser pulses with a growth rate of 0.1 nm/pulse, producing the 160 nm thick layer of YBCO. As a comparison, we prepared the reference films on STO substrates using earlier optimized growth temperature of 750 °C. However, based on our temperature calibrations by Cryclops portable infrared thermometer, the surface temperature at the beginning of the growth was ≈ 50 °C higher in films grown on IBAD-MgO based templates than in STO.

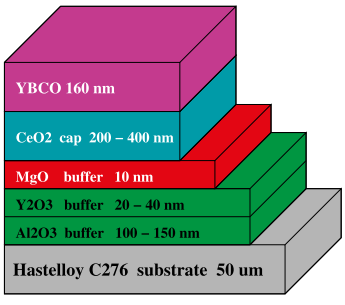

Fig. 1. Schematic structure of IBAD-MgO based polycrystalline metallic substrate, different buffer layers and their thicknesses. 160 nm thick layer of YBCO doped with BCO and BZO were deposited on top of it.

X-ray diffractometry (XRD) with Philips X'Pert Pro MPD was used for determining the crystallographic properties of the films and the (00*l*) directional $\theta - 2\theta$ scans were done to check the phase purity. The in-plane and out-of-plane crystallographic textures were calculated by using ϕ and rocking curves (RC) of YBCO (102) (ϕ scans) and (005) (ω scans) peaks, respectively. Intensity ratios of YBCO (005) / (004) peaks were used to determine the oxygen stoichiometry within all the films. The surface microstructure was studied with atomic force microscope (AFM) provided by Bruker Innova®. Magnetic measurements were done by a Quantum Design physical property measurement system (PPMS). Ac magnetization measurements ranging from 10–100 K were made in 0.1 mT ac field for determination of critical temperatures T_c of all the films. Critical current densities, J_c, were calculated by applying the Bean model for the magnetic hysteresis loops [17].

The transport properties of all the films were measured by using the horizontal rotator option available in PPMS. The measurements were done at 0.5 T, 1 T, 2 T, 4 T, 6 T and 8 T fields and at temperatures from 10 K–50 K in 10 K steps and at 77 K with 0° to 360° angular range using 3° steps. For this purpose, all the films were patterned by wet chemical etching. The etched patterns were 200 μm wide current stripes on each film. The contacts on the films were made by aluminium wire using TPT HBO5 Wire Bonder. Only samples deposited at 700 °C and 750 °C were chosen for angular dependent measurements. The films grown at 650 °C were not measured because already from basic J_c measurements, these films showed the worst properties among all the films. On the other hand, the films prepared at 800 °C were not measured either because it was impossible to bond the Al wire contacts on their surfaces. This is likely due to much rougher surfaces of these films as discussed in detail in the surface microstructure section. After angular dependent measurements with complete set of temperatures, only 40 K data is shown here because at this temperature, T_c variation between samples is not significant and because 40 K is also the intermediate temperature from the entire temperature range showing the similar type of results as in the other measurement temperatures.

3. Basic characterizations

3.1. Crystallographical properties

The θ-2θ diffractograms with (003), (004), (005), (006), (007), (008), (009), (0010), (0011) and (0012) reflections are measured for BCO and BZO doped YBCO films, as shown in Fig. 2. From these graphs, we can conclude that no signs of misorientations were observed in these measurements. The presence of only (00*l*) peaks, within the XRD detection limit, reveals that all the samples are fully *c*-axis textured.

Table 1shows the structural parameters for both BCO and BZO doped YBCO films. The YBCO *c*-axis for BCO doped films grown at 700 °C, 750 °C and 800 °C is only slightly longer than the nominal value of 11.68 Å, as experimentally measured elsewhere [18]. However, the BZO doped films have slightly more elongated *c*-axis than in the BCO doped ones. When the films were grown at 650 °C, in both BCO and BZO cases, the length of the *c*-axis got highly extended i.e. a difference of ≈ 0.10 Å in comparison to the nominal value. Furthermore, the relatively narrow 2θ peaks for both BCO and BZO doped films suggest only subtle variation in *c*-axis parameter. It can be seen from Table 1 that the peaks become narrower and the variation in unit cells decreases as the T_g increases. For example the value of $\Delta 2\theta$ at 800 °C is less than half of that obtained in the film grown at the lowest T_g of 650 °C. The film prepared at 750 °C has similar $\Delta 2\theta$ to that of YBCO + 4 % BCO film grown at the same temperature on STO substrate [12]. In addition, we can conclude that the YBCO films prepared at 700 °C on IBAD-MgO based template revealed smaller $\Delta 2\theta$ than that in film grown earlier on NiW substrate [19].

The variation in the in-plane orientations, shown by the $\Delta\phi$ data, is approximately the same regardless of the T_g*s* for all BCO and BZO

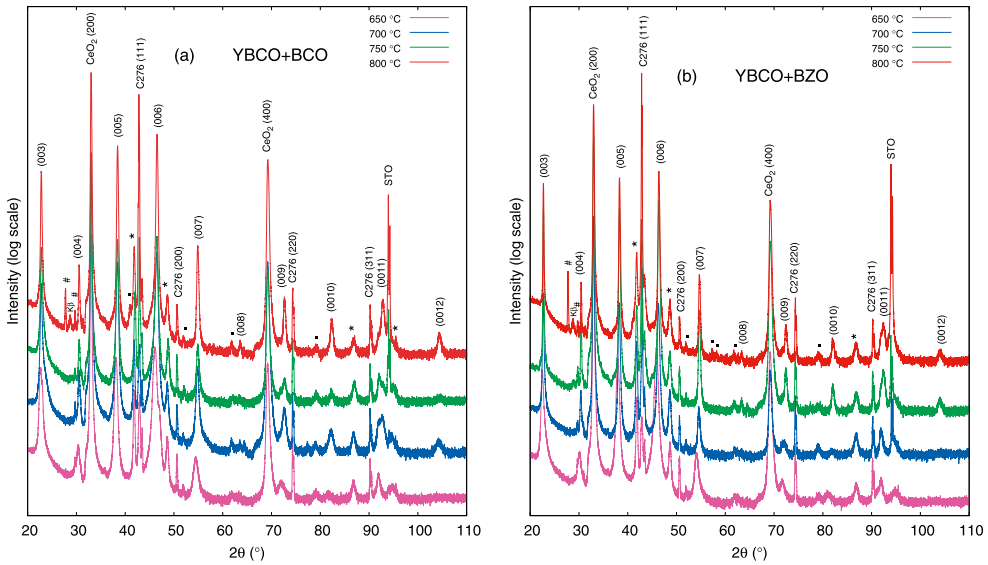

Fig. 2. X-ray diffractograms of YBCO films doped with 4 % (a) BCO and (b) 4% BZO grown at 650 °C - 800 °C range. Labelled peaks, CeO_2 are from the cap layer, K_β is the X-ray source peak, peaks marked with '#' are due to interplay of hastelloy C276 and buffer layers, '·' peaks arose from buffer layers, '*' peaks came from the sample holder during XRD measurements, C276 peaks reflecting from the metal itself. STO peak is also seen due to tape glued on it.

Table 1
Structural parameters determined from XRD measurements for undoped, 4 % BCO and 4 % BZO doped YBCO thin films grown on IBAD-MgO based template at different temperatures. The values for undoped YBCO were taken from our previous work [10].

T_g(°C)	YBCO lattice c (Å)	$\Delta 2\theta$ (005) (°)	$\Delta\phi$ (102) (°)	$\Delta\omega$ (005) (°)	$I(005)/I(004)$
		Undoped YBCO			
750	11.69	0.26	4.2	1.7	9.8
		YBCO + BCO			
650	11.78	0.62	4.13	2.25	16.06
700	11.71	0.44	4.04	1.62	15.24
750	11.71	0.37	3.86	2.30	13.98
800	11.70	0.26	4.12	1.95	16.23
750 (STO)	11.68	0.23	1.35	0.47	14.97
		YBCO + BZO			
650	11.79	0.58	4.45	2.43	16.34
700	11.73	0.34	4.30	2.66	11.38
750	11.72	0.22	4.40	1.64	12.25
800	11.74	0.21	4.28	2.15	13.97
750 (STO)	11.72	0.22	1.06	0.29	12.94

doped YBCO films. Moreover, the out-of-plane $\Delta\omega$ values revealed less variation in the orientation of *c*-axis for all the films grown on an IBAD-MgO based template than on buffered NiW substrate [20]. The $\Delta\omega$ values show only slight variation in crystallographic ordering in *c*-direction i.e. orthorhombic unit cells are similarly tilted from the vertical direction in all the films grown on IBAD-MgO template. However, this tilting is much larger when comparing with the films grown on single crystalline STO substrates, because the buffer layers play an important role in perturbing the structure [12]. Both BCO and BZO doped films grown on STO showed four times smaller values of $\Delta\phi$ and $\Delta\omega$. Therefore, we can conclude that the peak widths in ϕ and ω directions are mainly due to the metal substrate. The data of $\Delta 2\theta$, $\Delta\phi$ and $\Delta\omega$ is quite similar, as earlier observed for the undoped YBCO films grown on the same IBAD-MgO based template at different T_gs [10]. However, slightly shorter *c*-axis in undoped YBCO is in agreement with smaller oxygen deficiency as indicated by the intensity ratio. This means that the doping does not affect the crystallographic structure, in terms of structural tilting along *a*/*b* and *c*-axis. The intensity ratio $I(005)/I(004)$ varies between $\approx 13 - 17$ in BCO doped films and $\approx 11 - 17$ in BZO doped films, and this reveals that the oxygen deficiency is in the range of standard $\delta < 0.1$ [21].

3.2. Surface microstructure

As shown in Figs. 3(a) and (e), the BCO doped film prepared at 650 °C has a relatively smooth surface, especially when compared with the BZO doped film which has large particles on its surface. When the T_g increases, unlike in the BCO doped case, more particles appear on the surface in BZO doped films and the particles seem to coalesce together, thus making the surface clearly rougher than in the BCO case. The similar tendency can be observed between the films grown at 700 °C and 750 °C, as depicted by Figs. 3(f) and (g). When T_g increases up to 800 °C, porous structure was seen in the BCO doped film due to the growth of large islands which makes the surface of the film uneven as shown in Fig. 3(d). The roughest surface in BZO doped films can be observed in film grown at 800 °C with a great number of large coalesced particles on the surface (Fig. 3(h)). The change in the height scale bar values with increasing T_g also indicate the modification in the surface out-of-plane features.

Table 2shows the RMS roughness values of all the BCO and BZO doped films. In both BCO and BZO dopant cases, the RMS roughness is roughly 2–4 nm for films grown at 650 °C and 700 °C, while for films grown at 750 °C and 800 °C, the surfaces are slightly rougher, giving the RMS roughness in the range of 4−6 nm. It is obvious that when larger particulates appear on the surface, the roughness value will be larger, matching exactly with the visual impression from the entire AFM images. By looking at the AFM images in Fig. 3, we can see that both BCO and BZO doped films have similar type of surface structure on the

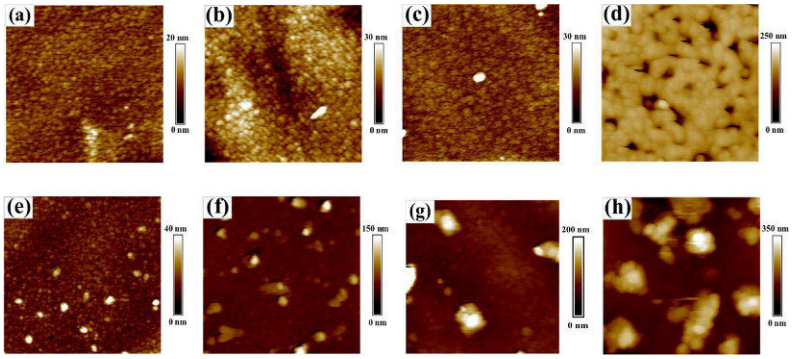

Fig. 3. (a)–(h) The surface microstructure measured by AFM using 5 × 5 μm^2 scan area images with proper height scale bar values for films grown on IBAD-MgO based template. (a) to (d) images are of BCO doped films grown at 650 °C, 700 °C, 750 °C and 800 °C respectively, while (e) to (h) are images of BZO doped films grown at same temperatures, respectively.

Table 2
Calculated surface roughness values of 4 % BCO and 4 % BZO doped YBCO films grown at different T_gs on IBAD-MgO based templates and STO substrates. All the values were determined from 5 × 5 μm^2 scan area images, but only from the base level regions having no merged surface particulates.

Sample	RMS roughness (nm)	
(T_g (°C))	YBCO + BCO	YBCO + BZO
650	2.3	3.4
700	3.6	4.0
750	4.3	6.1
800	6.9	4.7
750 (STO)	4.1	4.3

base level which, on the other hand, is in line with the roughness values shown in Table 2. In addition, both BCO and BZO doped films grown on STO show similar roughness values with each other and the values are not different what we observed for films grown on the IBAD-MgO template.

3.3. Magnetic properties

Temperature dependent magnetization curves in Figs. 4(a) and (b) show that the T_c increases with increasing T_g. The films grown at 800 °C have the highest T_c i.e. onset T_c is ≈ 88 K and ≈ 86 K for BCO and BZO doped films, respectively. The BCO doped film prepared on an IBAD-MgO based template at 750 °C has almost the same T_c as the film grown on STO substrate. However, the BZO doped film deposited at 750 °C on IBAD-MgO based template shows ≈ 1 K higher T_c than the film deposited on STO. The difference in T_c for BCO doped films grown at 750 °C and 800 °C is quite large. Especially, when compared with the BZO doped film deposited at the same T_gs, where T_c is almost the same, as depicted in Fig. 4(b). T_c for both BCO and BZO doped films grown at T_g of 700 °C is clearly lower, i.e. 83 K. In addition, when compared with the films deposited at higher temperatures, the BCO and BZO doped films prepared at 700 °C have clearly broader superconducting transition, even more pronounced in the BCO doped film. On the other hand, the transition is relatively sharp for the films prepared at 750 °C and 800 °C, in both BCO and BZO doped cases.

In films grown at 650 °C, T_c decreases dramatically and the superconducting transition is extremely broad, showing very low T_c, of around 65 K, in both BCO and BZO doped YBCO. The low T_c of ≈ 65 K means that at least the threshold temperature in between 650 °C and 700 °C is needed for growing the YBCO films with reasonable superconducting properties. The onset T_c in the insets of Figs. 4(a) and (b) shows the high jumps from 60 K to 85 K when T_g is increased from 650 °C to 700 °C. For the BCO doped films deposited between 700 °C and 800 °C, T_c increases linearly whereas for BZO doped films, T_c increases from 700 °C to 750 °C, above which it stays almost constant for film deposited at 800 °C. The increase in T_c with increasing T_g, for both BCO and BZO doped films, can be compared with our structural data, where 2θ peaks become narrower when T_g is increased. The $\Delta 2\theta$ value of the film grown at 650 °C is more than twice of the value for film grown at 800 °C, which confirms that the high crystallographic quality leads to high T_c. Since, we are optimizing J_c and thus the pinning properties in high magnetic field range, we have not focused on the highest T_c but on the T_g which produced the best J_c properties.

The J_c curves calculated from the hysteresis loops using the Bean model for both BCO and BZO doped films are shown in Figs. 5(a) and (b), respectively. As an ideal case, the YBCO grown on STO showed the highest J_c (0) for both BCO and BZO doped YBCO films. However, the highest J_c in films on an IBAD-MgO based template was with T_g of 750 °C for both BCO and BZO doped YBCO. The J_c analysis of BCO doped films shown in Fig. 5(a) shows that the zero field J_c for film on

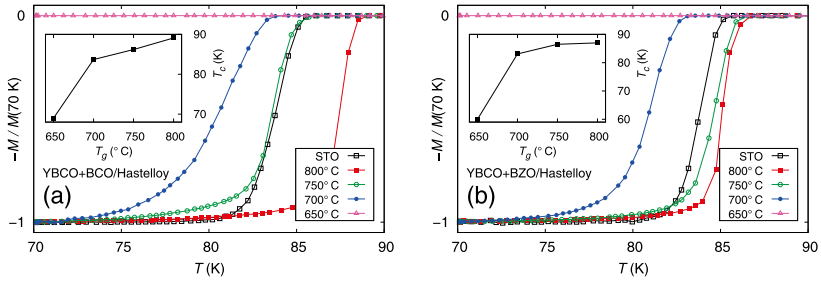

Fig. 4. Ac magnetization curves as a function of temperature for (a) BCO doped and (b) BZO doped YBCO films grown on IBAD-MgO based template at different T_gs. The films grown on STO at 750 °C are given as a comparison. The insets show the T_g dependence of T_c in both set of samples.

STO is greater than that in film grown on buffered metal substrate grown at 750 °C, but in fields from ≈ 0.7 T to 9 T, the J_c is equal in both of them. In addition, $J_c(0)$ is greater for film grown at 800 °C than at 700 °C but, in high external magnetic fields, the case becomes only reverse as J_c starts to decrease earlier for film prepared at 800 °C, whereas a slight decrease in J_c occurs for film with 700 °C, even at 9 T field. Both in the zero and applied magnetic field, the BZO doped YBCO deposited on STO substrate clearly showed higher J_c than that in all the films grown on buffered metal substrate, as depicted in Fig. 5(b). On the other hand, for films on IBAD-MgO based templates, J_c for film deposited at 750 °C is the highest whereas the film prepared at 800 °C has slightly smaller J_c. The film with T_g of 700 °C has already a decreased J_c and for 650 °C film, the decrease is phenomenal as also in the case of BCO doped YBCO. This is due to the weakened crystalline properties, as shown by our structural data.

The insets of Figs. 5(a) and (b) represent the T_g dependent accommodation field B^*, defined as an end point of the low field plateau of J_c [22]. Single vortex pinning dominates below B^* but above it, the vortex-vortex interaction becomes significant [23]. Experimentally, B^* is the magnetic field where J_c value drops to 90 % of its value at the zero magnetic field [14,24]. As seen in the inset of Fig. 5(a), the BCO doped film with T_g of 700 °C has the highest B^* of approximately 350 mT. With increasing T_g from 700 °C upwards, B^* decreases to the value of 120 mT for the film with T_g = 800 °C while the films deposited at 650 °C and 750 °C have approximately the same B^*. When comparing T_c with J_c in our samples, we can conclude that the film deposited at the highest temperature has the highest T_c, while it has lower J_c than in the film grown at 750 °C. The BZO doped films (inset of Fig. 5(b)) firstly shows a high jump in B^* as T_g is increased from 650 °C to 700 °C i.e. almost from 0 mT to 350 mT, and then B^* increases smoothly up to 390 mT for the film with T_g of 750 °C and stays approximately the same for film grown at 800 °C.

In order to investigate the shape of the $J_c(B)$ curve above B^* and thus the size of the pinning centres and their effect on vortex lattice, we have calculated the scaled pinning force function for fitting pinning force F_p. The F_p values were determined by using the formula $F_p(B) = BJ_c(B)$. For fitting $F_p(B)$, the data was firstly scaled by maximum pinning force $F_{p,\,max}$ and maximum field B_{max} in order to get the maximum of $F_p(B)$ plot at (1,1). The function used for fitting in its simplified form can be expressed as [25]

$$\frac{F_p(B)}{F_{p,max}} = \left(\frac{p}{q}\right)^q \left(\frac{B}{B_{max}}\right)^p \left(\frac{p+q}{p} - \frac{B}{B_{max}}\right)^q \quad (1)$$

Fig. 6shows the fittings for BCO and BZO doped samples with isotropic nanoparticles and correlated nanorods as pinning sites, respectively. The Eq. (1) fits quite nicely above B^* and the fitting explains the field dependence of J_c above B^*. Also B^* was the lower limit for fitting [25]. In Table 3, the p parameter is smaller for BCO doped films and is approximately the same for all the BZO doped films. This fitted p parameter gives an estimation for BCO and BZO diameters in *ab*-plane. From the analysis, the BCO dopant produced smaller sized pinning sites than BZO. With increasing diameter of the pinning sites, the vortex lattice smoothly breaks [26] as in our case the p parameter changes in between the values 0.5−1. The smooth breaking of the vortex lattice means that with small pinning sites the vortex lattice stays intact (hexagonal) but, with large pinning sites there is no organized lattice and the change between these happens smoothly. On the other hand, the q parameter is same for all the films or fits with the value 1.1 as obtained in [25]. This is in between to that given by most of the theories [27,28]. B_{max} varies with T_g in both BCO and BZO doped films. It is notable that BCO doped film grown at 750 °C on IBAD-MgO based

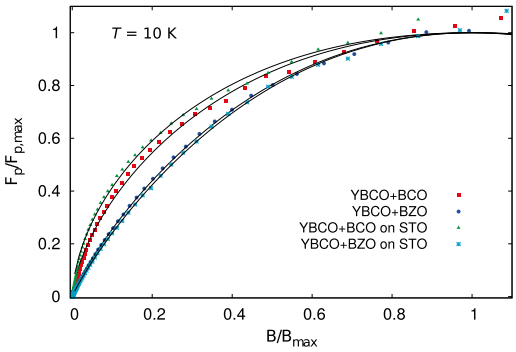

Fig. 6. Fitting of Eq. (1) to F_p data of both BCO and BZO doped films grown at 750 °C on IBAD-MgO based templates and STO substrates. The curves are plotted from the data of Fig. 5.

Table 3
The calculated fitting parameters at 10 K p, q, B_{max} and $F_{p,\,max}$ for both BCO and BZO doped films grown at certain temperatures on IBAD-MgO based templates and STO substrates.

T_g(°C)	p	q	B_{max} (T)	$F_{p,\,max}$ (GN/m^3)
		YBCO + BCO		
700	0.70	1.1	6.30	174.8
750	0.59	1.1	8.71	302.8
800	0.50	1.1	8.34	110.9
750 (STO)	0.58	1.1	8.55	304.2
		YBCO + BZO		
700	0.82	1.1	10.73	505.8
750	0.81	1.1	7.97	715.7
800	0.81	1.1	7.15	524.8
750 (STO)	0.82	1.1	8.94	1313.8

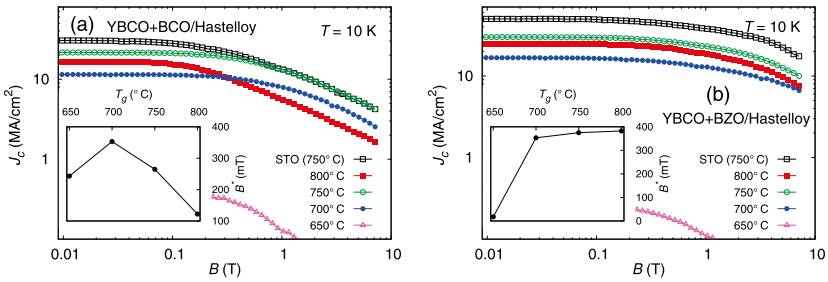

Fig. 5. J_c curves as a function of zero and applied magnetic fields measured at 10 K for (a) BCO doped and (b) BZO doped YBCO films with different T_gs deposited on IBAD-MgO based templates and also for films grown on STO at 750 °C. The insets show the dependence of the accommodation field on T_g.

template has approximately the same B_{max} than in the film grown on STO. This shows that F_p reaches its maximum value at the same B_{max} in both the deposition cases of BCO doped YBCO on STO and our IBAD-MgO based template at T_g = 750 °C, having also the nearly similar $F_{p,max}$. The BZO doped film grown at 750 °C on IBAD-MgO based template has the highest $F_{p,max}$ and it is half of that to the BZO doped film grown on STO.

Here, the films prepared at 750 °C on IBAD-MgO based templates showed the highest $F_{p,max}$, and thus it is better to compare only these for the analysis of pinning site diameters. The $F_p(B)$ of 309.13 GN/m^3 for BCO doped film grown on STO at 750 °C has been reported [25], and it is very close to the value of our films grown on IBAD-MgO based template at the same T_g. In addition, the diameter of BCO nanoparticles calculated earlier in [25] is ≈ 2.5 nm for 4 % BCO doped film grown on STO at 750 °C and has p parameter of 0.60. This p value is very close to the p value of our BCO doped YBCO grown on IBAD-MgO based template. The diameter of correlated nanorods is ≈ 5 nm for the 4 % BZO doped film grown at 750 °C on STO [25], which has the same p value to our BZO doped film deposited on IBAD-MgO based template with same T_g. Both the BCO and BZO doped films grown on our IBAD-MgO based template at 750 °C showed the highest $F_{p,max}$ when compared with the films deposited at 700 °C and 800 °C. Because the p values in films grown at 750 °C on STO and IBAD-MgO substrates are roughly the same with respect to the dopants, so we can conclude that both BCO and BZO grow similarly in terms of diameter, regardless of the substrate. In conclusion, the BZO nanorods are larger in diameter in *ab*-directions than BCO particles as shown by clearly enhanced $F_{p,max}$ values, and therefore the BZO rods can more effectively pin the vortices along *c*-axis.

4. Angular dependent transport properties

In transport measurements, BZO doped films grown on buffered metallic substrates have higher absolute J_c at both low and high magnetic fields than those in films doped with BCO, as shown in Figs. 7(a)–(d). In Figs. 7(a) and (b), the BCO and BZO doped films prepared at 700 °C show smaller $J_c(\theta)$ than films prepared at 750 °C, as presented in Figs. 7(c) and (d). In Fig. 7(b), BZO doped YBCO deposited at 700 °C did not show *c*-axis peak in any field, but the film prepared at 750 °C exhibits strong *c*-axis peak at high fields, as shown in Fig. 7(d). Earlier reports have also shown no *c*-axis peak for BZO doped YBCO film deposited on STO substrate at low T_g i.e. below 725 °C, but at higher T_g, the behaviour was similar to our case [29,30]. The appearance of the *c*-axis peak is usually linked to the network of BZO nanorods formed in YBCO films, and they have been reported being continuous and elongated at high T_g [31]. In films with lower T_g, the columns are typically short, discontinuous and splayed, and thus less effective as pinning centres [29,31–33]. As the rods become shorter at low T_g, there is a critical limit where they are no longer correlated rods but the spherical type pinning centres [33], leading to the disappearance of the *c*-axis peak. Moreover, based on the vortex path model [34], if rods are shrinked as isotropic particles and they are randomly situated, they will not produce any *c*-peak as the vortex takes different short sized steps. However, these shortened BZO rods are still stronger pinning centres than the isotropic BCO particles as well as the naturally formed structural defects [32].

The field dependent $J_c(\theta)$ data reveals that there is no *c*-axis peak at 0.5 T for the BZO doped film grown at 750 °C but, at higher fields ≥ 1 T, there is a clear peak along the YBCO *c*-axis, being in line with the data reported for the 2 % BZO doped YBCO grown on STO substrate and measured at 1 T and 77 K [31]. The shape of all the $J_c(\theta)$ curves for BZO doped film grown at 700 °C (Fig. 7(b)) are approximately independent of the applied field, but the situation is clearly different in the film prepared at 750 °C, where the *ab*-plane peaks are higher and narrower at high fields. In our case, at high T_g, pinning along *ab*-direction is enhanced as the intense *ab*-peaks occur in films grown at 750 °C (Figs. 7(c) and (d)). The sharp *ab*-peaks in BZO doped films suggest the presence of in-plane pinning centres such as stacking faults within the YBCO lattice [29], while the presence of spherical nano-sized particles broadens the *ab*-peaks in BCO doped films [12].

The comparison with our reference samples deposited on STO substrate, the films prepared on IBAD-MgO based templates have lower J_c in the whole angular range. In Fig. 7(e), showing the BCO doped film on STO, the broadened *ab*-peaks at low fields tend to sharpen at higher fields. However, the shoulders along the sharp *ab*-peaks appear whereas no significant *c*-axis peak can be seen. At low fields, a quite high *c*-axis peak in BZO doped film on STO (750 °C) can be observed, as shown in Fig. 7(f) and there are dips in the *ab*-peaks which is not the case for any of the films deposited on IBAD-MgO based templates. These dips can be due to highly effective pinning along *c*-axis resulting in quite broad *c*-axis peak, thus hiding the *ab*-peak. When the field increases up to 6 T, the *ab*-peak starts to occur again and this behaviour is seen even more pronounced at 8 T. This effect can be due to weaker *c*-axis pinning at high fields which narrows the *c*-peaks and allows the *ab*-peaks to appear [30].

5. Flux pinning mechanism

From the graphs of Fig. 7, the most important data measured at the fields of 2 T and 6 T was selected for the more detailed shape and anisotropy analysis. To make the comparison easier, the curves in Fig. 8 were shifted in such a way that the lowest point is at the same level for both the data measured at 2 T and 6 T. Fig. 8(a) shows that the data is not completely symmetric in the vicinity of 0° in neither BCO nor BZO doped films prepared at 700 °C. The asymmetry of the $J_c(\theta)$ curve is typically visible in films grown on IBAD-MgO templates and this can be due to the inclined or tilted growth of the buffer layer during the IBAD process [35–37]. The absence of *c*-axis peak at 2 T does not mean that there is no pinning along the *c*-axis but a *c*-axis peak occurs only if the total $F_p(\theta)$ has a local maximum in the *c*-direction [38]. Based on our results at the high fields, the *ab*-peaks sharpen and become narrower for both BCO and BZO doped films when compared with the curves measured at low fields. Regardless of the external magnetic field, the *ab*-peaks in BZO doped films are broader when compared with the BCO ones. The narrow *ab*-peaks for BCO doped films can be due to the interaction of point type defects or this could be related to the growth of BCO nanoparticles within the *ab*-planes [38]. On the other hand, the broader *ab*-peaks in BZO doped films can be due to the interplay between the *ab*-planes and high density of *c*-axis correlated defects such as edge dislocations and *c*-axis oriented nanorods [38,39].

The angular dependent data of BZO doped film grown at 750 °C, shown in Fig. 8(b), reveals that the *c*-axis peak at both low and high fields tells about the effective pinning of vortices in *c*-direction. On the other hand, the *ab*-peaks were quite small at 2 T field, approximately half of the *ab*-plane peaks measured at 6 T. This can be explained that more vortices are pinned in the CuO_2 planes and stacking faults in the *ab*-direction at high fields [30]. Above 4 T, the *c*-axis peak starts to decrease since the nanorods are not able to accommodate more vortices [40]. The matching field for 4 % doped BZO film is around 5 T [14]. The appearance of the sharp *ab*-peaks at high fields can be explained by the relatively strong in-plane pinning due to the stacking faults [10] and, in the BCO doped cases that the particles are more concentrated in the *ab*-planes [12].

The angular dependent curves for our reference films deposited on STO, as presented in Fig. 8(c), show huge dips along the *ab*-axis at 2 T field, but the small *ab*-peaks starts to appear at 6 T for the BZO doped film. An earlier report [29] suggests that greater number of ordered rods, due to high T_g, distort the *ab*-planes and worsen the pinning properties in this direction. Instead, a strong *c*-axis peak here refers to elongated columns in the YBCO structure along the *c*-direction. The broad *c*-axis peaks also reveal that the BZO nanorods are slightly splayed [34,39]. In addition to the BZO induced nanocolumns, this

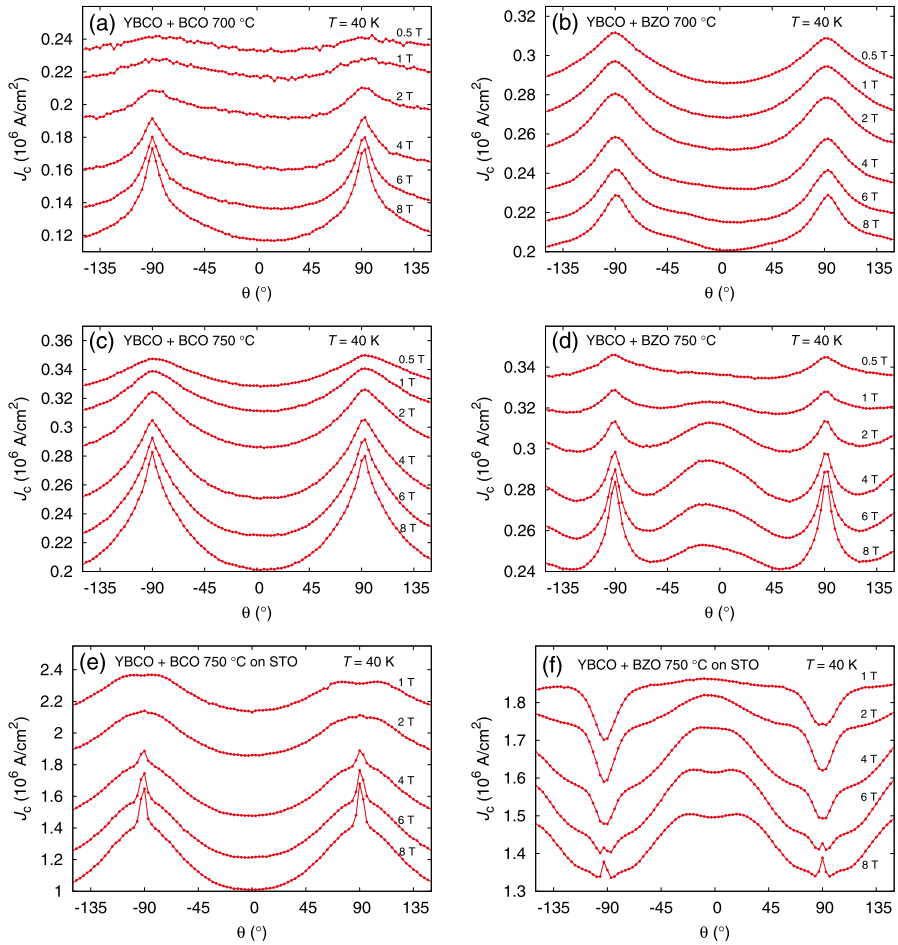

Fig. 7. (a)–(f) The angular dependent J_c plots for BCO doped and BZO doped YBCO films prepared at different temperatures on IBAD-MgO based templates and at 750 °C on STO, measured at 40 K in field range of 0.5 T - 8 T and 1 T - 8 T respectively. 0° always shows the direction of *c*-axis while -90° and 90° refer to *ab*-planes in the YBCO structure.

significant *c*-axis oriented pinning in the films on STO is basically provided by the array of well-known structural defects which result from the island growth during the deposition [3]. In BCO doped case at low fields, the point-like and correlated particles at low fields proved to show widened *ab*-peaks, but very sharp peaks at 6 T. The shoulders in between *ab*- and *c*-axis peaks observed at high fields in BCO doped film grown on STO can be explained by the interplay of in-plane and out-of-plane correlated pinning which is a natural result and not a symbol of any unorthodox pinning at some angle [39].

As explained in the vortex path model [34,39], the anisotropy of all the curves seen in Fig. 8 is dependent on the density of the available pinning paths along both *ab*- and *c*-axis. In undoped films, the *ab*-planes have more pinning paths than along the *c*-axis [34]. This is in agreement with our previous results [10], where the undoped YBCO was grown on this newly fashioned IBAD-MgO based template, producing the naturally created edge-type of threading dislocations, that act as an important source of vortex pinning. However, a strong anisotropy is seen only when the population of pinning paths in one direction is larger than in the other direction [34]. Therefore, the extra artificial defects have a great impact on the density of pinning paths, thus decreasing the anisotropy and increasing the overall vortex pinning.

Fig. 9shows the schematic illustration of the difference in the distribution of artificial defects within the YBCO lattice grown on IBAD-MgO based templates and STO substrates. As shown earlier [10], the threading dislocations through the entire film are significant due to low-angle grain boundaries arising from the underlying IBAD-MgO based template (Fig. 9(a)). In agreement with the $J_c(\theta)$ data, the BCO nanodots seem to be randomly distributed and some of them also grow along the dislocations whereas the BZO nanorods are broken and slightly tilted in one direction which causes the asymmetry of the *c*-axis peaks in the BZO doped films grown on IBAD-MgO based template. In BZO doped film, the vortex strongly takes smaller steps in entire angular range as vortices are pinned by rods, which again trap the large part of the entire vortex. On the other hand, the vortex takes the greater number of steps along the pinning path in BCO doped film. This could be due to the isolated particles with small cross-sectional area, thus pinning only small portion of a vortex. The BZO nanorods are more effective in flux pinning than the BCO nanodots, due to their greater

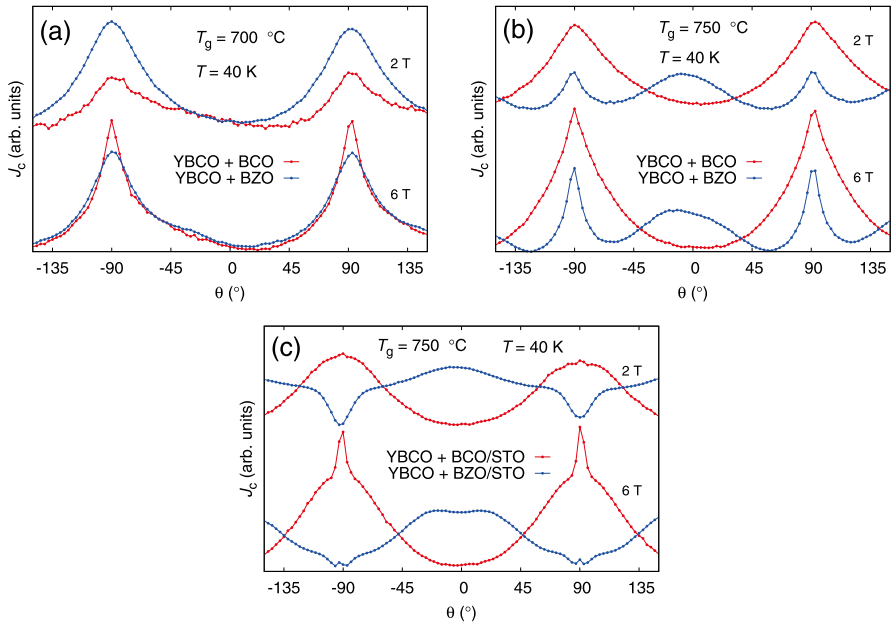

Fig. 8. The shape comparison of the angular dependent J_c (40 K: 2 and 6 T field) in films prepared on (a) and (b) IBAD-MgO based templates at different temperatures and on (c) STO substrate.

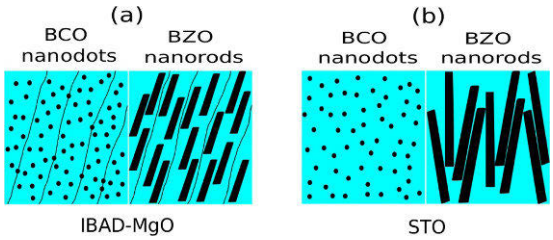

Fig. 9. Schematic diagram showing the growth and distribution of induced dopants within the YBCO lattice in films grown at 750 °C on IBAD-MgO based template (a) and on single crystal STO substrate (b). The extended black lines in (a) illustrates the significant appearance of edge-type threading dislocations that are formed in films grown on IBAD-MgO based templates.

size and similarity in shape with the vortices. As the vortex density increases and their interaction becomes notable at high fields, the vortices can get looser from the nanosized particles or nanocolumns. On the other hand, when the nanorods are passing through the entire thickness of the film, vortices are trapped even at high applied fields and in wide angular range which is the case when the films are grown on our reference STO substrates, as depicted in Fig. 9(b). In the films on STO substrates, the elongated BZO nanocolumns are tilted in different directions, leading to the double *c*-axis peaks at high fields as shown in Figs. 7(f) and 8(c). In BCO doped films on STO, the size and the distribution of BCO nanoparticles are the same as in films grown on IBAD-MgO based templates.

According to the model presented by Paulius et al. [41], J_c is reduced with increasing the inclination of the applied field with respect to *c*-axis, decreasing the length of trapped vortex portion. At the sufficient inclined field, none of the vortex region is trapped and subsequently $J_c(\theta)$ becomes to its minimum. In our case, even though the vortices can become free from the artificial pinning sites of BCO and BZO in the intermediate angular regime (between *ab*- and *c*-axis peaks), the threading dislocations in YBCO due to the IBAD-MgO based template underneath can pin the different portions of vortices irrespective of applied field orientations. This effect could result in improved $J_c(\theta)$ values. Thus, our newly fashioned substrate itself is also a source of increasing $J_c(\theta)$ due to the formation of low-angle grain boundaries within the YBCO matrix, which increases the flux pinning in the wide temperature and angular dependent field ranges.

6. Conclusion

In order to understand the role of the novel IBAD-MgO based template in growth mechanism of YBCO, the BCO and BZO doped YBCO films were prepared by pulsed laser deposition. The crystalline, magnetic and transport properties are thoroughly investigated, especially in terms of the clearly thinner buffer layer architecture that differs from the traditionally used complex buffer layer stack that, within this thickness level, usually has large-angle grain boundaries on the surface. As a conclusion, the both BCO and BZO doped YBCO films grown at 750 °C showed the best superconducting properties as compared to other films grown at 650 °C, 700 °C and 800 °C. The BZO doped films have higher absolute J_c than that in BCO doped ones grown at different T_g. In addition, the angular dependent J_c properties show significant difference in vortex pinning anisotropy and also $J_c(\theta)$ of BZO doped films is higher due to more effective vortex pinning structure as compared to BCO doped films.

Based on the angular dependent J_c data and on the obtained structural properties, the schematic description for the vortex pinning behaviour is proposed for films grown on IBAD-MgO based template and this is compared with the reference films grown on single crystal STO substrates. According to the model, the BCO particles grow in a similar fashion within the YBCO matrix, i.e. as randomly distributed, on

both IBAD-MgO based template and on STO. On the other hand, the BZO nanorods are grown unidirectionally and they are of intermediate sizes in YBCO matrix on IBAD-MgO based template, whereas on STO, the BZO rods are splayed and longer in length. However, the proposed model with reduced anisotropy in BCO and especially in BZO doped films grown on buffered IBAD-MgO based template indicate that the suitable vortex pinning landscape can be utilized with these combinations for great variety of electrical power applications.

Acknowledgements

The Jenny and Antti Wihuri Foundation and Finnish Cultural Foundation is acknowledged for the financial support.

References

[1] D. Larbalestier, A. Gurevich, D.M. Feldmann, A. Polyanskii, High-t_c superconducting materials for electric power applications, Nature 414 (2001) 368–377.
[2] V. Selvamanickam, D.W. Hazelton, L. Motowidlo, F. Krahula, J.H. M. S. Walker Jr., P. Haldar, High-temperature superconductors for electric power and high-energy physics, J. Miner. Metals Mater. Soc. 50 (1998) 27–30.
[3] S.R. Foltyn, L. Civale, J.L. MacManus-Driscoll, Q.X. Jia, B. Maiorov, H. Wang, M. Maley, Materials science challenges for high-temperature superconducting wire, Nat. Mater. 6 (2007) 631–642.
[4] J.L. MacManus-Driscoll, S.R. Foltyn, Q.X. Jia, H. Wang, A. Serquis, L. Civale, B. Maiorov, M.E. Hawley, M.P. Maley, D.E. Peterson, Strongly enhanced current densities in superconducting coated conductors of $YBa_2Cu_3O_{7-x}$ + $BaZrO_3$, Nat. Mater. 3 (2004). 439
[5] H. Yamada, H. Yamasaki, K. Develos-Bagarinao, Y. Nakagawa, Y. Mawatari, J.C. Nie, H. Obara, S. Kosaka, Flux pinning properties of c-axis correlated pinning centres in PLD-YBCO films, Supercond. Sci. Technol. 17 (2004). S25–S29
[6] A. Mahmood, S. Park, B. Jun, J. Youn, Y. Han, T. Sung, C. Kim, Improvement of the superconducting properties of an infiltrated YBCO bulk superconductor by $BaCeO_3$ addition, Physica C 469 (2009). 1165
[7] O.V. Boytsova, A.R. Kaul, S.V. Samoilenkov, I.E. Voloshin, Thin film nanocomposites based on YBCO with defects comprised of self-assembled inclusions, J. Phys. Conf. Ser. 234 (2010). 012008
[8] J.L. MacManus-Driscoll, S.R. Foltyn, Q.X. Jia, H. Wang, A. Serquis, L. Civale, B. Maiorov, M.E. Hawley, M.P. Maley, D.E. Peterson, Strongly enhanced current densities in superconducting coated conductors of $YBa_2Cu_3O_{7-x} + BaZrO_3$, Nat. Mater. 3 (2004) 439–443.
[9] J.Y. Coulter, J.O. Willis, M.M. Mann, P.C. Dowden, S.R. Foltyn, P.N. Arendt, J.R. Groves, R.F. DePaula, M.P. Maley, D.E. Peterson, Magnetic-field anisotropy of high-critical current YBCO coated conductors, IEEE Trans. Appl. Supercond. 9 (1999). 1487
[10] M.Z. Khan, Y. Zhao, X. Wu, M. Malmivirta, H. Huhtinen, P. Paturi, Improved interface growth and enhanced flux pinning in YBCO films deposited on an advanced IBAD-MgO based template, Physica C 545 (2018) 50–57.
[11] C.N.R. Rao, R. Nagarajan, R. Vijayaraghavan, Synthesis of cuprate superconductors, Supercond. Sci. Technol. 6 (1993) 1–22.
[12] M. Malmivirta, L.D. Yao, S. Inkinen, H. Huhtinen, H. Palonen, R. Jha, V.P.S. Awana, S. van Dijken, P. Paturi, The angular dependence of critical current of $BaCeO_3$ doped $YBa_2Cu_3O_{6+x}$ thin films, IEEE Trans. Appl. Supercond. 25 (2015) 1–5. 6603305
[13] M. Irjala, H. Huhtinen, R. Jha, V.P.S. Awana, P. Paturi, Optimization of the $BaCeO_3$ concentration in YBCO films prepared by pulsed laser deposition, IEEE Trans. Appl. Supercond. 21 (2011) 2762–2766.
[14] M. Peurla, P. Paturi, Y.P. Stepanov, H. Huhtinen, Y.Y. Tse, A.C. Bódi, J. Raittila, R. Laiho, Optimization of the $BaZrO_3$ concentration in YBCO films prepared by pulsed laser deposition, Supercond. Sci. Technol. 19 (2006) 767–771.
[15] H. Palonen, H. Huhtinen, M.A. Shakhov, P. Paturi, Electron mass anisotropy of $BaZrO_3$ doped YBCO thin films in pulsed magnetic fields up to 30 T, Supercond. Sci. Technol. 26 (2013) 1–5. 045003
[16] Q.Q. Mu, L.F. Liu, Y.J. Li, Fabrication of IBAD-MgO and PLD CeO_2 layers for YBCO coated conductors, Chin. Phys. Lett. 32 (2015). 078102
[17] H.P. Wiesinger, F.M. Sauerzopf, H.W. Weber, On the calculation of J_c from magnetization measurements on superconductors, Physica C 203 (1992) 121–128.
[18] P. Schweiss, W. Reichardt, M. Braden, G. Collin, G. Heger, H. Claus, A. Erb, Static and dynamic displacements in $RBa_2Cu_3O_{7-\delta}$ (R = Y, Ho; δ = 0.05, 0.5): a neutron-diffraction study on single crystalsStatic and dynamic displacements in $rba_2cu_3o_{7-\delta}$ (r = y, ho; δ = 0.05, 0.5): a neutron-diffraction study on single crystals, Phys. Rev. B 49 (1994) 1387–1396.
[19] H. Huhtinen, M. Irjala, P. Paturi, M. Falter, The effect of BZO doping concentration and thickness dependent properties of YBCO films grown by PLD on buffered NiW substrates, Physica C 472 (2012) 66–74.
[20] H. Huhtinen, M. Irjala, P. Paturi, M. Falter, Optimal BZO doping in YBCO films grown on single crystal STO and buffered NiW substrates, IEEE Trans. Appl. Supercond. 21 (2011). 2753
[21] J. Ye, K. Nakamura, Quantitative structure analyses of YBCO thin films: determination of oxygen content from x-ray-diffraction patterns, Phys. Rev. B 48 (1993) 7554–7564.
[22] P. Paturi, M. Irjala, A.B. Abrahamsen, H. Huhtinen, Defining B_{c_2} B^* and B_ϕ for YBCO thin films, IEEE Trans. Appl. Supercond. 19 (2009) 3431–3434.
[23] L. Krusin-Elbaum, L. Civale, J.R. Thompson, C. Feild, Accommodation of vortices to columnar defects: evidence for large entropic reduction of vortex localization, Phys. Rev. B 53 (1996). 11744
[24] C. Cai, B. Holzapfel, J. Hänisch, L. Fernandez, L. Schultz, Magnetotransport and flux pinning characterictics in RBaCuO (R = Gd,Eu,Nd) and $(Gd_{1/3}Eu_{1/3}Nd_{1/3})BaCuO$ high-T_c superconducting thin films on $SrTiO_3$, Phys. Rev. B 69 (2004). 104531
[25] P. Paturi, M. Malmivirta, H. Palonen, H. Huhtinen, Dopant diameter dependence of $J_c(B)$ in doped YBCO films, IEEE Trans. Appl. Supercond. 26 (2016) 1–5. 8000705
[26] H. Palonen, J. Jäykkä, P. Paturi, Modeling reduced field dependence of critical current density in $YBa_2Cu_3O_{6+x}$ films with nanorods, Phys. Rev. B 85 (2012). 024510
[27] T. Matsushita, Flux Pinning in Superconductors, Springer, Heidelberg, Germany, 2007.
[28] D. Dew-Hughes, The critical current of superconductors: an historical review, Supercond. Sci. Technol. 27 (2001). 713
[29] X. Wang, F.J. Baca, R.L.S. Emergo, J.Z. Wu, T.J. Haugan, P.N. Barnes, Eliminating thickness dependence of critical current density in $YBa_2Cu_3O_{7-x}$ films with aligned $BaZrO_3$ nanorods, J. Appl. Phys. 108 (2010). 113911
[30] M. Malmivirta, L. Yao, H. Huhtinen, H. Palonen, S. van Dijken, P. Paturi, Three ranges of the angular dependence of cirtical current of $BaZrO_3$ doped $YBa_2Cu_3O_{7-\delta}$ thin films grown at different temperatures, Thin Solid Films 562 (2014) 554–560.
[31] F.J. Baca, T.J. Haugan, P.N. Barnes, T.G. Holesinger, B. Maiorov, R. Lu, X. Wang, J.N. Reichart, J.Z. Wu, Interactive growth effects of rare-earth nanoparticles on nanorod formation in $YBa_2Cu_3O_x$ thin films, Adv. Funct. Mater. 23 (2013) 4826–4831.
[32] B. Maiorov, S.A. Baily, H. Zhou, O. Ugurlu, J.A. Kennison, P.C. Dowden, T.G. Holesinger, S.R. Foltyn, L. Civale, Synergetic combination of different types of defect to optimize pinning landscape using $BaZrO_3$-doped $YBa_2Cu_3O_7$, Nat. Mater. 8 (2009) 398–404.
[33] V.F. Solovyov, H.J. Wiesmann, L. Wu, Q. Li, L.D. Cooley, M. Suenaga, B. Maiorov, L. Civale, High critical currents by isotropic magnetic-flux-pinning centres in a 3 um thick YBCO superconducting coated conductor, Supercond. Sci. Technol. 20 (2007). L20
[34] N.J. Long, N.M. Strickland, E.F. Talantsev, Modeling of vortex paths in HTS, IEEE Trans. Appl. Supercond. 17 (2007) 3684–3687.
[35] B. Maiorov, B. Gibbons, S. Kreiskott, V. Matias, Q. Jia, T. Holesinger, L. Civale, Influence of tilted geometries on critical current in superconducting thin films, IEEE Ttans. Appl. Supercond. 15 (2005) 2582–2585.
[36] B. Maiorov, B. Gibbons, S. Kreiskott, V. Matias, T. Holesinger, L. Civale, Effect of the misalignment between the applied and internal magnetic fields on the critical currents of tilted coated conductors, Appl. Phys. Lett. 86 (2005). 132504
[37] S.H. Wee, Y.L. Zuev, C. Cantoni, A. Goyal, Engineering nanocolumnar defect configurations for optimized vortex pinning in high temperature superconducting nanocomposite wires, Sci. Rep. 3 (2013). 23101–9
[38] L. Civale, B. Maiorov, A. Serquis, J.O. Willis, J.Y. Coulter, H. Wang, Q.X. Jia, P.N. Arendt, J.L. MacManus-Driscoll, M.P. Maley, S.R. Foltyn, Angular-dependent vortex pinning mechanisms in $YBa_2Cu_3O_7$ coated conductors and thin films, Appl. Phys. Lett. 84 (2004) 2121–2123.
[39] S. Wimbush, N. Long, The interpretation of the field angle dependence of the critical current in defect-engineered superconductors, New J. Phys. 14 (2012) 1–24. 083017
[40] A.K. Jha, K. Matsumoto, T. Horide, S. Saini, P. Mele, A. Ichinose, Y. Yoshida, S. Awaji, Controlling the critical current anisotropy of YBCO superconducting films by incorporating hybrid artficial pinning centers, IEEE Trans. Appl. Supercond. 26 (2016) 1–4. 8000404
[41] L. Paulius, J.A. Fendrich, W.K. Kwok, A. Koshelev, V. Vinokur, G. Crabtree, B. Glagola, Effects of 1-GeV uranium ion irradiation on vortex pinning in single crystals of the high-temperature superconductor YBCO, Phys. Rev. B 56 (1997). 913

M. Z. Khan & Y. Zhao & X. Wu & R. Jha & V.P.S. Awana & H. Huhtinen & P. Paturi

Improving the flux pinning with artificial BCO nanodots and correlated dislocations in YBCO films grown on IBAD-MgO Based template

III

IEEE transactions on applied superconductivity, 29, 2019, 8002105

Improving the Flux Pinning With Artificial BCO Nanodots and Correlated Dislocations in YBCO Films Grown on IBAD-MgO Based Template

Mukarram Z. Khan, Yue Zhao, X. Wu, Rajveer Jha, Veer P. S. Awana, Hannu Huhtinen, and Petriina Paturi

***Abstract*—To improve the performance of high-temperature superconductors in electrical power systems, a modified IBAD-MgO based template is used as a substrate for the growth of $YBa_2Cu_3O_{6+x}$ (YBCO) doped with various concentrations of $BaCeO_3$ (BCO). The highest critical current density (J_c) in a wide applied field and angular range is realized in the films doped with 2% and 4% BCO content. This is explained to arise from the optimized BCO dopant concentration, which helps to immobilize more vortices both in low and high field ranges. Besides the vortex pinning by randomly distributed BCO nanoparticles, the edge-type dislocations, mainly occurring due to the underlying IBAD-MgO based template, are also a main source of pinning the vortices as seen by the appearance of *c*-axis peak of $J_c(\theta)$ in undoped and 2% doped films. The disappearance of c-peak in films doped with higher concentration can be qualitatively explained by the vortex path model, where the paths of the vortices arising because of high density of BCO particles disguise the columnar type pinning effect coming from the threading dislocations within the films. Therefore, the BCO nanodots can be used for improving the flux pinning besides the threading dislocations in YBCO films on metal substrates.**

***Index Terms*—HTS, YBCO, BCO, flux pinning, angular dependent properties.**

I. Introduction

THE high temperature superconductor $YBa_2Cu_3O_{6+x}$ (YBCO) has already shown its potential in electrical power systems when deposited on flexible buffered metallic substrates [1]. Thinner metallic templates are of immense importance as they reduce the production cost but, on the other hand, a better understanding about YBCO growth on such types of templates is also necessary. As the vortex motion causes dissipation in high temperature superconductors, the pinning of vortices is always desired, especially at high fields where vortex density is quite high [2]. For J_c enhancement in YBCO films grown by pulsed laser deposition (PLD), several non-superconducting phases such as $BaCeO_3$ [3], $BaZrO_3$ [4] or $BaSnO_3$ [5] have been successfully doped as they create pinning sites for the mobile vortices. Based on the lattice mismatch calculations between YBCO matrix and dopant species as well as the elastic constants of the pinning centers, as presented in detail in [6], it is expected that BCO forms non-columnar and spherical particles when grown by PLD. This is also confirmed by TEM analysis, where the point-like BCO particles with a mean diameter of 2.5 nm are observed in 4% BCO doped YBCO films [3].

In this manuscript, our objective is to enhance the J_c in YBCO films when grown on an advanced IBAD-MgO based template by PLD via doping $BaCeO_3$ (BCO). By PLD method, the BCO dopant grows within the YBCO matrix in the form of isotropic and randomly distributed nano-sized particles [3]. For this purpose, the dopant content is optimized within YBCO films deposited on our IBAD-MgO based template. We discuss the structural, magnetic and transport properties of small-scale YBCO films grown at a specific temperature. The main objective is to study the vortex pinning behavior in undoped and BCO doped YBCO films and then to optimize the dopant content for J_c enhancement, when grown on our IBAD-MgO based template.

II. Experimental Details

The YBCO thin films doped with the varying content of non-superconducting phase BCO were prepared by PLD on 5×5 mm^2 IBAD-MgO based templates where the dopant concentration was varied from 0 vol% to 10 vol% with 2 vol% steps. The schematic of IBAD-MgO based template is shown in Fig. 1 and its manufacturing details are explained in [7]. The IBAD-MgO layer not only forms the in-plane grain alignment but is also biaxially textured. Furthermore, the low lattice mismatch, good chemical compatibilty and similar thermal expansion coefficient values between the CeO_2 cap layer and YBCO are important for the optimal growth of YBCO [7]. All the films were deposited at growth temperature $T_g = 750$ °C by using excimer XeCl laser (wavelength = 308 nm, pulse duration = 25 ns and pulse repetition rate = 5 Hz with 1.3 Jcm^{-2} laser fluence). The number of 1500 laser pulses with the growth rate

Manuscript received October 23, 2018; accepted January 31, 2019. Date of publication February 4, 2019; date of current version March 4, 2019. This work was supported in part by the Jenny and Antti Wihuri Foundation and in part by the Finnish Cultural Foundation. *(Corresponding author: Mukarram Z. Khan.)*

M. Z. Khan is with the Wihuri Physical Laboratory, Department of Physics and Astronomy, University of Turku, Turku FI-20014, Finland, and also with the University of Turku Graduate School, University of Turku , Turku FI-20014, Finland (e-mail: mukarram.z.khan@utu.fi).

Y. Zhao is with the Department of Electrical Engineering, Shanghai Jiao Tong University, Shanghai 200240, China.

X. Wu is with the Shanghai Superconductor Technology Company Ltd., Shanghai 200240, China.

R. Jha and V. P. S. Awana are with the Superconductivity Division, National Physical Laboratory (CSIR), New Delhi 110012, India.

H. Huhtinen and P. Paturi are with the Wihuri Physical Laboratory, Department of Physics and Astronomy, University of Turku, Turku FI-20014, Finland.

Color versions of one or more of the figures in this paper are available online at http://ieeexplore.ieee.org.

Digital Object Identifier 10.1109/TASC.2019.2897433

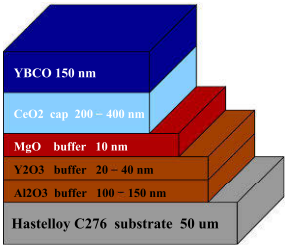

Fig. 1. The schematic structure of IBAD-MgO based polycrystalline metallic substrate, different buffer layers and their thicknesses. The 150 nm thick layer of undoped or BCO doped YBCO was deposited on top of it.

of 0.1 nm/pulse gave us 150 nm film thickness. The detailed PLD deposition conditions are explained elsewhere [8].

The crystallographic properties of films were determined by Philips X'Pert Pro MPD based X-ray diffraction (XRD). The phase purity of films was confirmed by (00l) directional θ-2θ scans whereas the calculations of in-plane and out-of-plane crystallographic textures were made by YBCO (102) (ϕ scans) and (005) (ω scans) peaks, respectively. The Quantum Design physical property measurement system (PPMS) was used for magnetic measurements where critical temperatures T_c of the films were determined by ac magnetization measurements between 10 K−100 K in 0.1 mT ac field. The critical current densities (J_c) were calculated by applying Bean model for films onto the respective hysteresis loops [9]. The accommodation field B*, which is defined as an upper limit of the low-field plateau of J_c(B), is determined by the criterion $J_c(B)/J_c(0) = 0.9$ [10]. On the other hand, the angular dependent transport properties were also done by the use of the horizontal rotator in PPMS. Firstly, all the films were patterned by wet chemical etching to produce 200 μm wide current stripes on each film. Then TPT HBO5 Wire Bonder was used to make electrical contacts on films by aluminium wire. The measurements were made at 40 K and magnetic fields of 0.5 T, 1 T, 2 T, 4 T, 6 T and 8 T with 0° to 360° angular range using 3° of steps.

III. Results and Discussion

A. Structural Properties

All the films are phase pure as shown in Fig. 2 by the relative (00l) peaks of YBCO and other peaks coming from buffer layers of our IBAD-MgO based template. The calculated structural parameters of undoped and BCO doped YBCO are presented in Table I. The c-axis length is nearly the same for all the films and is also very close to the nominal value of YBCO c-parameter i.e. 11.68 Å [11]. However, we observed the increase in $\Delta 2\theta$ values with increasing BCO concentration, which could be linked not only to the strain related variation in c-parameter but also to the out-of-plane lattice coherence length [12].

On the other hand, the in-plane variation of all the films, as depicted by $\Delta\phi$ data, stays approximately the same regardless of the dopant content. The $\Delta\phi$ values are quite large as compared with the STO case which suggests the formation of low-angle grain boundaries along c-direction [13]. Moreover, the intensity

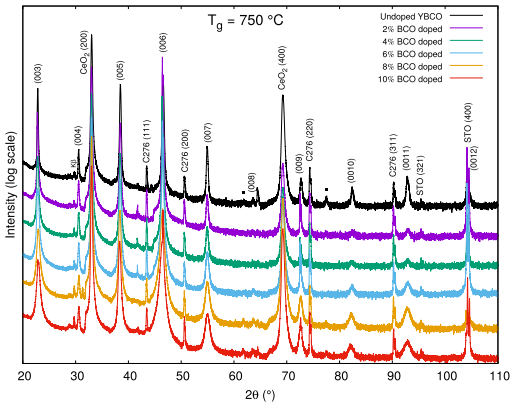

Fig. 2. X-ray diffractograms of undoped and 0% to 10% BCO doped YBCO films grown on a modified IBAD-MgO based template. Labelled peaks, CeO_2 are from cap layer, '·' peaks arose from the buffer layers and C276 peaks reflected from the metal itself. STO peak is also seen due to hastelloy tape glued on it.

TABLE I
Structural Parameters Determined From XRD Measurements of Undoped and Several Concentrations of BCO Doped YBCO Films Grown on IBAD-MgO Based Template

Sample	YBCO lattice c (Å)	$\Delta 2\theta$ (005) (°)	$\Delta\phi$ (102) (°)	I(005)/ I(004)
Undoped	11.69	0.21	4.12	13.12
2% BCO	11.68	0.25	4.16	10.87
4% BCO	11.70	0.30	4.09	11.77
6% BCO	11.69	0.32	4.09	12.86
8% BCO	11.69	0.39	4.09	15.46
10% BCO	11.69	0.39	3.97	15.41

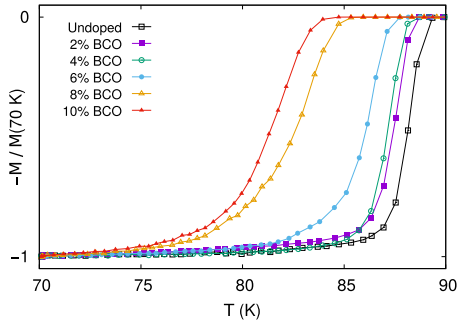

Fig. 3. AC magnetization curves as a function of T for undoped and BCO doped YBCO films grown on an IBAD-MgO based template.

ratio of the (005) and (004) peaks $I(005)/I(004) < 20$ in all the films indicates that the oxygen deficiency is in the range of standard $\delta < 0.1$ [14].

B. Magnetic Analysis

Temperature dependent ac-magnetization curves in Fig. 3 show that the T_c decreases as the BCO dopant concentration increases. It can be observed that the undoped film has the

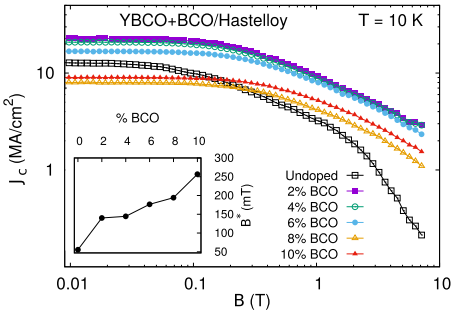

Fig. 4. J_c curves as a function of zero and applied magnetic fields measured at 10 K for undoped and BCO doped YBCO films deposited on an IBAD-MgO based template at $T_g = 750$ °C. The inset shows the accommodation field (B^*) dependence on BCO dopant concentration.

highest T_c and with increasing dopant concentration it starts to decrease which is a typical behavior observed in BCO doped YBCO films [15]. In addition, above 4% dopant content, the width of the transition increases as well as the T_c drops dramatically above 6% dopant concentration. The decrease in T_c with increasing BCO doping can be explained by the formation of non-uniform strain which is directly proportional to the structural deformation of YBCO [3], [16].

J_c s in all the films, depicted in Fig. 4, were calculated using the Bean model [9], [17], [18]. The 2% BCO doped film has the highest J_c whereas the 4% BCO doped has slightly lower J_c in self-field. In high field or above accommodation field B^*, both 2% and 4% doped films have approximately the same J_c s. Above 4% dopant concentration i.e. with 6% BCO doped film, the decrease of self-field J_c is notable while the high field J_c decreases more slowly. This result can be explained by the high density of strong pinning sites due to 6% BCO concentration which pin more number of vortices. Above 6% dopant content the decrease of J_c, both in low and high fields, is remarkable as the film structure gets deteriorated with such a high dopant concentration which affects negatively the superconducting properties. On the other hand, the undoped YBCO has higher self-field J_c than 8% and 10% BCO doped films but lower in high fields. The lower self-field J_c in highly BCO doped YBCO films can be linked to the increased volume of BCO particles and distorted YBCO surroundings with lower T_c, which together decrease the amount of superconducting material [16]. In addition, the inset of Fig. 4 revealing the dependence of B^* on BCO dopant concentration shows that the undoped YBCO film has the lowest B^* and then it jumps three times higher when doped with 2% and 4% BCO. Above 4% dopant content B* increases almost linearly and this behavior is similar as observed in our works [3], [15].

C. Angular Dependent Flux Pinning

Figure 5 shows the angular dependent J_c properties for all the films with respect to different fields. When comparing absolute $J_c(\theta)$ values, we observed that $J_c(\theta)$ increases from undoped to 2% BCO doped film in entire angular range and up to the higher field too. This means that the isotropic BCO nanoparticles pin the vortices effectively especially in high fields with high vortex density. At 4% dopant content, the absolute value of low field $J_c(\theta)$ stays approximately the same as of 2% dopant concentration but high field $J_c(\theta)$ is slightly decreased. Moreover, the c-peak in fields above 2 T decreases slightly, thus showing that the pinning force lacks the local maximum in the c-direction [19] but there is still c-axis oriented pinning. With 6% BCO concentration, the highest $J_c(\theta)$ is observed in low fields among all of our samples, but at the high fields, the $J_c(\theta)$ is even smaller than in the undoped one. Above 6% BCO doped films, the properties start to worsen in the whole field and angular ranges as 10% BCO doped film has even smaller absolute $J_c(\theta)$ than the 8% doped one. The decline of superconducting properties with high dopant concentration is due to excess structural disorder in the film. This matches our structural and magnetic analysis described in previous sections. The c-axis peak arising in undoped or BCO doped films and the slight off position of c-peak from 0° is a typical behavior when YBCO is grown on IBAD-MgO based template [20]–[22]. As YBCO grows c-oriented, the appearance of c-peak in this case is due to threading dislocations which occur because of growth mechanism of underlying IBAD-MgO based template [22]. These dislocations also act as pinning sites and increase $J_c(\theta)$ [13].

The anisotropy in all of our data is related to the density of pinning paths along in-plane and out-of-plane directions. A strong anisotropy is seen when the pinning paths are more populated in one direction than in the other i.e. usually the undoped films have more pinning paths along the ab-plane than the c-direction [23], [24]. Moreover, the effects of the matching field are also responsible for the anisotropic shapes of the curves [25].

The proposed model about the interaction of vortices with threading dislocations and isotropic and randomly distributed BCO particles is presented in Fig. 6. The pronounced appearance of c-peak in undoped and 2% BCO doped films could be due to the trapping of the entire length of vortices by edge-type dislocations, which are formed in the low-angle grain boundaries, caused by the underlying IBAD-MgO based template [13]. When the dopant concentration is 2%, only a few BCO particles in the vicinity of threading dislocations will pin the vortices. However, the isotropic BCO particles are not very effective to pin the vortices in all the angular directions and therefore only the threading dislocations can accomodate the vortices for longer length. Thus, the pinning by BCO nanoparticles together with threading disloacations increases $J_c(\theta)$ as shown by Fig. 5 (b). When the concentration is increased up to 4%, the extra BCO particles will start attracting the vortices, not allowing them to be directly pinned in the threading dislocations. This phenomenon already reduces the c-peak in 4% BCO doped film. In addition, the curves of 4% BCO doped film are the least anisotropic among all of our measured data. This behavior is more pronounced when the BCO concentration is increased to 6%, where the c-peak is already reduced. On the other hand, the 8% and 10% BCO doped films have quite many short vortex pinning paths in between the BCO nanoparticles which not only completely hide the c-peak but, due to the effect of the high

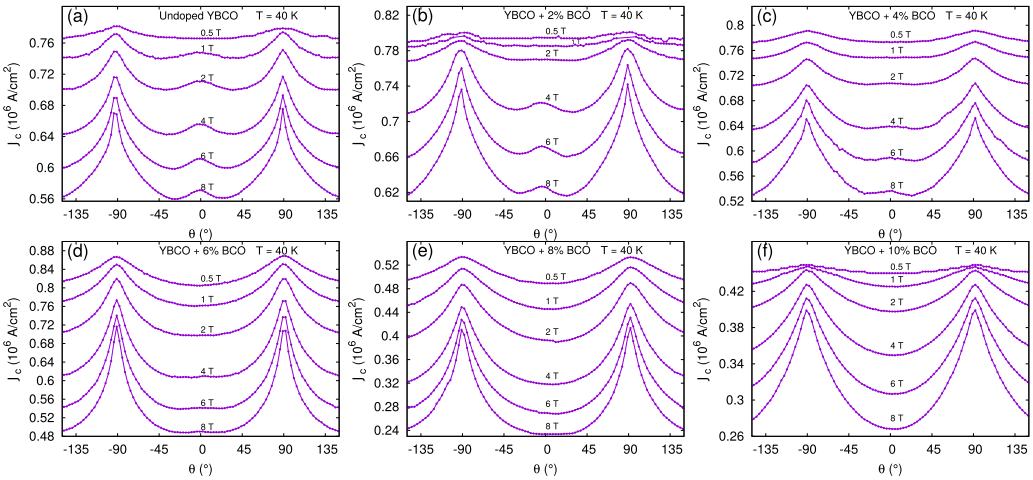

Fig. 5. (a)–(f) The angular dependent J_c plots for undoped and BCO doped YBCO films grown on IBAD-MgO based template measured at 40 K in field range of 0.5 T−8 T. All the graphs were shifted so that 0° always shows the direction of c-axis while −90° and 90° refer to ab-planes in the YBCO structure.

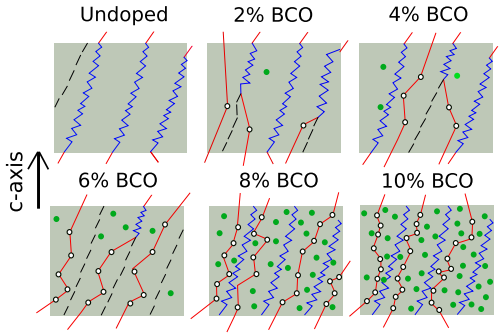

Fig. 6. The schematic of vortex pinning in undoped and 2% to 10% BCO doped YBCO films grown on an IBAD-MgO based template. Black dashed lines correspond to the threading dislocations where no vortex is pinned, whereas blue zig-zag color depicts the pinned vortices within threading dislocations. The green and open circles are BCO produced nanodots where the vortices (red lines) are unpinned and pinned, respectively. In the undoped case, vortices are mobile in between the threading dislocations unlike the BCO doped films where they are trapped by nanodots.

content of dopants, also reduce the absolute $J_c(\theta)$. As the vortices are lengthy, we conclude that the optimized low BCO dopant concentration is the best for making them immobile in between the threading dislocations. However, in the undoped case, not all of the vortices can be pinned by threading dislocations but only some of them, and thus especially at high fields, the great number of vortices move freely within the film which lowers the high field J_c.

IV. Conclusion

An advanced IBAD-MgO based template was used to grow undoped and 2% to 10% BCO doped YBCO films by PLD. The template consists of thinner and modified buffer layers reducing also its production cost. In this work, we optimized the BCO doping concentration in YBCO matrix in terms of vortex pinning. The low-angle grain boundaries, formed due to our IBAD-MgO based template, effectively pin the vortices and increase J_c. According to our results, the 2% and 4% doped films had the best $J_c(\theta)$ in all magnetic fields. These results are significant when optimizing the vortex pinning landscape in wide magnetic field and entire angular ranges and therefore, these structures can be used in future coated conductors for electrical power applications.

References

[1] V. Selvamanickam *et al.*, "High-temperature superconductors for electric power and high-energy physics," *J. Minerals, Metals Mater. Soc.*, vol. 50, pp. 27–30, 1998.

[2] S. R. Foltyn *et al.*, "Materials science challenges for high-temperature superconducting wire," *Nature Mater.*, vol. 6, pp. 631–642, 2007.

[3] M. Malmivirta *et al.*, "The angular dependence of critical current of $BaCeO_3$ doped $YBa_2Cu_3O_{6+x}$ thin films," *IEEE Trans. Appl. Supercond.*, vol. 25, no. 3, Jun. 2015, Art. no. 6603305.

[4] J. L. MacManus-Driscoll *et al.*, "Strongly enhanced current densities in superconducting coated conductors of $YBa_2Cu_3O_{7-x}+BaZrO_3$," *Nature Mater.*, vol. 3, pp. 439–443, 2004.

[5] P. Mele *et al.*, "Systematic study of the $BaSnO_3$ insertion effect on the properties of $YBa_2Cu_3O_{7-x}$ films prepared by pulsed laser ablation," *Supercond. Sci. Technol.*, vol. 21, 2008, Art. no. 125017.

[6] J. Wu and J. Shi, "Inetractive modeling-synthesis-characterization approach towards controllable *in situ* self-assembly of artificial pinning centers in re-123 films," *Supercond. Sci. Technol.*, vol. 30, 2017, Art. no. 103002.

[7] Q.-Q. Mu, L.-F. Liu, and Y.-J. Li, "Fabrication of IBAD-MgO and PLD CeO_2 layers for YBCO coated conductors," *Chin. Phys. Lett.*, vol. 32, 2015, Art. no. 078102.

[8] H. Palonen, H. Huhtinen, M. A. Shakhov, and P. Paturi, "Electron mass anisotropy of $BaZrO_3$ doped YBCO thin films in pulsed magnetic fields up to 30 T," *Supercond. Sci. Technol.*, vol. 26, 2013, Art. no. 045003.

[9] H. P. Wiesinger, F. M. Sauerzopf, and H. W. Weber, "On the calculation of J_c from magnetization measurements on superconductors," *Physica C*, vol. 203, pp. 121–128, 1992.

[10] C. Cai, B. Holzapfel, J. Hänisch, L. Fernandez, and L. Schultz, "Magnetotransport and flux pinning characterictics in RBaCuO (R = Gd, Eu, Nd)

and $(Gd_{1/3}\ Eu_{1/3}\ Nd_{1/3})BaCuO$ high-T_c superconducting thin films on $SrTiO_3$," *Phys. Rev. B*, vol. 69, 2004, Art. no. 104531.

[11] P. Schweiss *et al.*, "Static and dynamic displacements in $RBa_2Cu_3O_{7-\delta}$ ($R = Y, Ho$; $\delta = 0.05, 0.5$): A neutron-diffraction study on single crystals," *Phys. Rev. B*, vol. 49, pp. 1387–1396, 1994.

[12] A. Gauzzi and D. Pavuna, "Quantitative analysis of growth-induced reduction of long range lattice order in ion-beam sputtered $YBa_2Cu_3O_{6.9}$ films," *Appl. Phys. Lett.*, vol. 66, pp. 1836–1838, 1995.

[13] M. Z. Khan, Y. Zhao, X. Wu, M. Malmivirta, H. Huhtinen, and P. Paturi, "Improved interface growth and enhanced flux pinning in YBCO films deposited on an advanced IBAD-MgO based template," *Physica C*, vol. 545, pp. 50–57, 2018.

[14] J. Ye and K. Nakamura, "Quantitative structure analyses of YBCO thin films: Determination of oxygen content from x-ray-diffraction patterns," *Phys. Rev. B*, vol. 48, pp. 7554–7564, 1993.

[15] M. Irjala, H. Huhtinen, R. Jha, V. P. S. Awana, and P. Paturi, "Optimization of the $BaCeO_3$ concentration in YBCO films prepared by pulsed laser deposition," *IEEE Trans. Appl. Supercond.*, vol. 21, no. 3, pp. 2762–2766, Jun. 2011.

[16] M. Peurla *et al.*, "Optimization of the $BaZrO_3$ concentration in YBCO films prepared by pulsed laser deposition," *Supercond. Sci. Technol.*, vol. 19, pp. 767–771, 2006.

[17] C. P. Bean, "Magnetization of high-field superconductors," *Rev. Modern Phys.*, vol. 36, pp. 31–39, 1964.

[18] C. P. Bean and J. D. Livingston, "Surface barrier in type-II superconductors," *Phys. Rev. Lett.*, vol. 12, pp. 14–16, 1964.

[19] L. Civale *et al.*, "Angular-dependent vortex pinning mechanisms in $YBa_2Cu_3O_7$ coated conductors and thin films," *Appl. Phys. Lett.*, vol. 84, pp. 2121–2123, 2004.

[20] B. Maiorov *et al.*, "Influence of tilted geometries on critical current in superconducting thin films," *IEEE Trans. Appl. Supercond.*, vol. 15, no. 2, pp. 2582–2585, Jun. 2005.

[21] B. Maiorov, B. Gibbons, S. Kreiskott, V. Matias, T. Holesinger, and L. Civale, "Effect of the misalignment between the applied and internal magnetic fields on the critical currents of tilted coated conductors," *Appl. Phys. Lett.*, vol. 86, 2005, Art. no. 132504.

[22] S. H. Wee, Y. L. Zuev, C. Cantoni, and A. Goyal, "Engineering nanocolumnar defect configurations for optimized vortex pinning in high temperature superconducting nanocomposite wires," *Sci. Rep.*, vol. 3, pp. 23101–23109, 2013.

[23] N. J. Long, N. M. Strickland, and E. F. Talantsev, "Modeling of vortex paths in HTS," *IEEE Trans. Appl. Supercond.*, vol. 17, no. 2, pp. 3684–3687, Jun. 2007.

[24] N. J. Long, "Model for the angular dependence of critical currents in technical superconductors," *Supercond. Sci. Technol.*, vol. 21, 2008, Art. no. 025007.

[25] S. Wimbush and N. Long, "The interpretation of the field angle dependence of the critical current in defect-engineered superconductors," *New J. Phys.*, vol. 14, 2012, Art. no. 083017.

M. Z. Khan & E. Rivasto & Y. Wu & Y. Zhao & C. Chen & J. Zhu & H. Palonen & J. Tikkanen & H. Huhtinen & P. Paturi
Modifying the critical current anisotropy of YBCO films via buffering layers on IBAD-MgO based templates

Journal of Physics: Conference Series, 1559, 2020, 012037

IV

Modifying the critical current anisotropy of YBCO films via buffering layers on IBAD-MgO based templates

Modifying the critical current anisotropy of YBCO films via buffering layers on IBAD-MgO based templates

M. Z. Khan[1,2], E. Rivasto[1,2], Y. Wu[3], Y. Zhao[3], C. Chen[4], J. Zhu[4], H. Palonen[1], J. Tikkanen[1], H. Huhtinen[1] and P. Paturi[1]

[1] Wihuri Physical Laboratory, Department of Physics and Astronomy, FI-20014 University of Turku, Finland
[2] University of Turku Graduate School (UTUGS), University of Turku, FI-20014 Turku, Finland
[3] School of Electronic Information and Electrical Engineering, Shanghai Jiao Tong University, 200240 Shanghai, Peoples Republic of China
[4] Shanghai Superconductor Technology Co. Ltd., 200240 Shanghai, Peoples Republic of China

E-mail: mukarram.z.khan@utu.fi

Abstract. The role of variations in the buffer layer structure of IBAD-MgO based templates on the critical current anisotropy has been investigated in undoped and $BaZrO_3$ (BZO) doped $YBa_2Cu_3O_{6+x}$ (YBCO) films. Not only do the natural defects grow distinct within the undoped YBCO lattice but also due to the different lengths of BZO induced nanorods within the YBCO matrix, the flux pinning properties are greatly affected by the underlying layers which in turn has a great impact on the angular dependent critical current density $J_c(\theta)$. This has been verified by transport measurements where the shape of the $J_c(\theta)$ varies in accordance with the substrates. Based on our results, the template having a cap layer with the minimum lattice mismatch and a good chemical compatibility with deposited YBCO is proven to be the best for growing both the undoped and BZO doped YBCO films. Furthermore, a model we can present based on the shapes of $J_c(\theta)$ curves depicts how the formation of nanosized defects affects the flux pinning anisotropy.

1. Introduction

Superconductivity is concerned with the very act of cooling down the certain materials to their critical temperatures that brings about the exciting phenomenon of zero resistance. The discovery of high temperature superconductors (HTS) more than three decades ago opened up the gates to electrical power applications which are currently in frequent use [1, 2]. The potential of HTS realized in electrical power systems is arguably thrilling but one has to admit that HTS are complex, difficult to process and expensive to produce which all limit their usability to certain scales.

One of the main obstacles faced in solving these issues is that the structural growth dynamics of HTS restricts the range of suitable deposition substrates to certain flexible but complicated tapes manufactured by several methods [3]. From a laboratory to an industrial scale, the underlying substrate is not just the spectator but it generally plays a critical role on the growth of HTS film. On the other hand, the vortex motion in HTS under the magnetic fields (B)

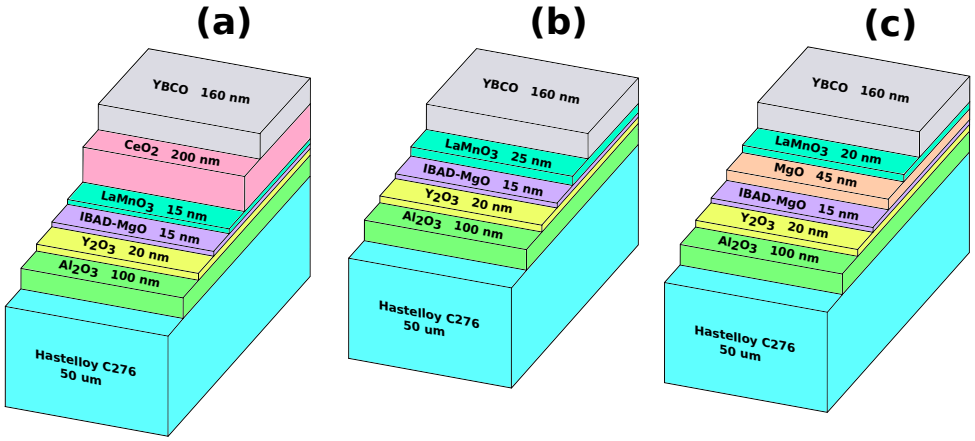

Figure 1. Schematics of IBAD-MgO based templates used for growing YBCO films (a)−(c). The three templates, CeO_2 (a), LMO-MgO (b), and LMO-Epi-MgO (c), differ from each other by the thicknesses and compositions of the buffer layer stacks grown on IBAD-MgO.

needs to be halted for zero resistance which leads to enhanced critical current density J_c and the usual approach for doing so is the introduction of artificial pinning sites within the lattice [2]. Moreover, besides other naturally created defects that appear during the growth process, the self-organized threading dislocations originating from the low-angle grain boundaries also act as strong vortex pinning sites. The out-of-plane threading dislocations are more pronounced when HTS films are grown on technical templates than with those deposited on single crystalline substrates due to larger lattice mismatch in the former [4, 5]. But the films on technical templates exhibit smaller J_c and they are more isotropic in comparison to the films grown on single crystalline substrates. However, thinking about their application, the HTS are required to be flexible so that they can easily be bent and wrapped. Due to these reasons, there is a motivation for developing technical templates that are less complicated, cost effective and sufficiently reliable for the growth of HTS films. Therefore, the fundamental understanding about this issue is a priority, should we want to improve the HTS growth from the substrate surface to the film top in pursuit of high critical currents (I_c) with small anisotropy.

Herein we present the superconducting properties of YBCO films grown on three different ion beam assisted deposition−magnesium oxide (IBAD-MgO) based templates. We investigated the properties of both undoped and artificially BZO doped YBCO films and observed the relative differences in the I_c anisotropies with respect to varying substrate buffer layers architectures. Furthermore, a schematic model of the growth of the natural and artificial defects within the YBCO lattice when grown on these distinct substrates is proposed.

2. Experimental details

Undoped YBCO films and YBCO films doped with 4 % BZO by weight were deposited on three variably structured 5×5 mm^2 IBAD-MgO based templates by the pulsed laser deposition (PLD) method. The schematics of templates are shown in Fig. 1 where the differences in top buffer layers can be seen. From here onwards, the structures in the subfigures (a), (b) and (c) in Fig. 1

Table 1. Structural parameters for undoped and 4 % BZO doped YBCO thin films grown on three different IBAD-MgO based templates.

Template	YBCO lattice c (Å)	$\Delta 2\theta$ (004) (°)	$\Delta\phi$ (102) (°)	$I(005)/I(004)$
undoped YBCO				
CeO_2	11.69	0.12	3.40	14.0
LMO-MgO	11.70	0.15	4.36	13.7
LMO-Epi-MgO	11.70	0.14	3.77	13.5
YBCO + BZO				
CeO_2	11.74	0.19	3.37	13.9
LMO-MgO	11.75	0.21	4.42	12.5
LMO-Epi-MgO	11.73	0.20	4.75	12.9

will be referred as CeO_2 for CeO_2 cap layer, LMO-MgO for $LaMnO_3$ cap layer and LMO-Epi-MgO for $LaMnO_3$-Epi-MgO, templates, respectively. Firstly, three sets of undoped YBCO films were deposited on these templates at temperatures from 625 °C to 850 °C with 25 °C step size to optimize the growth temperature (T_g). The optimized T_g emerged as 775 °C and all the films were deposited at this T_g. A XeCl laser (wavelength λ = 308 nm, pulse duration 25 ns and pulse repetition rate 5 Hz with 1.3 Jcm^{-2} laser fluence) was used as a source for cleaving off the target material and depositing it on the substrate. The applied 1600 laser pulses with a growth rate of $\approx$ 0.1 nm/pulse gave us the films' thicknesses as $\approx$ 160 nm.

The structural properties were characterized using a Panalytical Empyrean X-ray diffractometer (XRD) and performing (00l) directional θ-2θ and ϕ scans to observe the phase purity and in-plane crystallographic texturing of all the films, respectively. A Quantum Design physical property measurement system (PPMS) was utilized for magnetic measurements, where ac magnetization curves were measured from 10 K to 100 K at 0.1 mT ac field for determining the critical temperatures (T_c).

For transport measurements, all the films were patterned by wet chemical etching to obtain 200 μm wide current stripes. The electrical contacts from Quantum Design dc pucks to sample pads were made by using TPT HBO5 Wire bonder with 33 μm thick Al wire. Then the angular dependent J_c anisotropies were measured using a horizontal rotator available in the PPMS. All the measurements were done at the temperature of 40 K under 0.5 T, 1 T, 2 T, 4 T, 6 T and 8 T magnetic fields and 0° to 360° angular range. 40 K was chosen as the measurement temperature as it is far below the T_c and is also a reasonable intermediate temperature when thinking about the low (10 K) and high temperature (77 K) applications.

3. Results and discussion

3.1. Crystallographic and superconducting properties

The most important structural parameters of the grown films are presented in Table 1. The c-axis lengths calculated by the Nelson-Riley method [6] reveal that undoped films have the c-parameters very close to the nominal value (11.68 Å) of YBCO [7] in comparison to all the doped films where relatively long c-axis is observed. This depicts the BZO as a cause of lattice perturbation during the growth process. The $\Delta 2\theta$ shows the undoped films as a winning competitor in terms of better structural growth of YBCO compared to the BZO doped films. Here the notation $\Delta 2\theta$ is the full width at half maximum of the peak. We observe that the films grown on CeO_2 template have the least variation along c-axis among the other templates. For both the undoped and BZO doped films, the $\Delta 2\theta$ values are way smaller than our previously investigated templates [4, 8, 9, 10] showing signs of texture improvement in our current substrates. In addition, the $\Delta\phi$ values for all the films are varying with respect to the

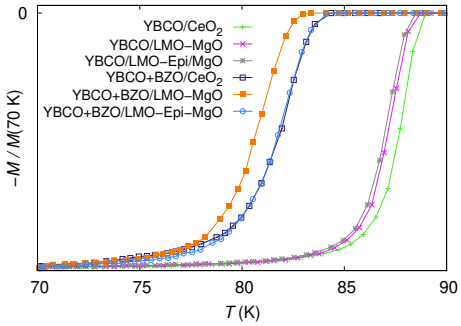

Figure 2. Magnetization curves for the undoped and BZO doped films grown on various templates.

templates, being only half to those reported earlier for YBCO films on NiW substrates [8]. This in-plane $\Delta\phi$ (102) lattice variation is crucial in flux pinning as it correlates positively with the severity of the low-angle grain boundaries which channel the YBCO growth along its *c*-axis and finally leads to the pass through of threading dislocations from the interface to the film surface. Conclusively, the oxygen content for all the films is well in the acceptable range, that is, $\delta < 0.1$ [11].

Fig. 2 displays the temperature dependences of magnetization (deriving the corresponding T_c values) for all the films. The undoped films have higher T_c and sharper transitions than the doped ones which is attributed to the local strain field arising due to the lattice mismatch (∼8 %) between YBCO and BZO and also the possible local oxygen deficiency that can occur around BZO nanocolumns [9, 12, 13]. Comparing the templates, we see that the undoped YBCO grown on CeO_2 has the highest T_c which can be due to less strain caused by the least lattice mismatch between the CeO_2 and YBCO layers. Among the doped films, YBCO deposited on CeO_2 and LMO-Epi-MgO follows the similar T_c curves but LMO-MgO has the lowest T_c and the broadest transition. Our goal is to get as high a J_c as possible at high B so we believe that the importance of the T_c values should be assessed on a per-application basis.

3.2. Angular dependent J_c and anisotropy

In order to compare the $J_c(\theta)$, we shifted the data separately for each constant value of B in such a way that the lowest point for every curve falls at the same level. Moreover, the *c*-peak always occur at 0°, whereas the *ab*-peaks falls at ± 90°. In Fig. 3(a), we display the $J_c(\theta)$ curves for undoped films measured at 0.5 T, 1 T and 2 T. It is observed that, at 0.5 T, both the films grown on CeO_2 and LMO-MgO are almost completely isotropic with the exception of very slight but broad *ab*-peaks. The $J_c(\theta)$ for film on LMO-Epi-MgO is more anisotropic where it shows the wide and pronounced *ab*-peaks. The occurrence of *ab*-peaks in the latter can be due to the more pronounced vortex pinning across the stacking faults. With increasing B from 0.5 T up to 2 T, we see that the shape of $J_c(\theta)$ curves for CeO_2 and LMO-MgO starts to be anisotropic, that is, the appearance of *ab*-peaks and occurrence of *c*-peak for film on CeO_2 is clearly visible. The *c*-peak for film on CeO_2 template should be attributed to the vortex pinning within the threading dislocations formed by the low-angle grain boundaries [14]. It is notable that with increasing B, *ab*-peaks become narrower and sharper for film on LMO-Epi-MgO template. This can be related to the presence of the greater number of pinning paths along *ab*-direction which pin

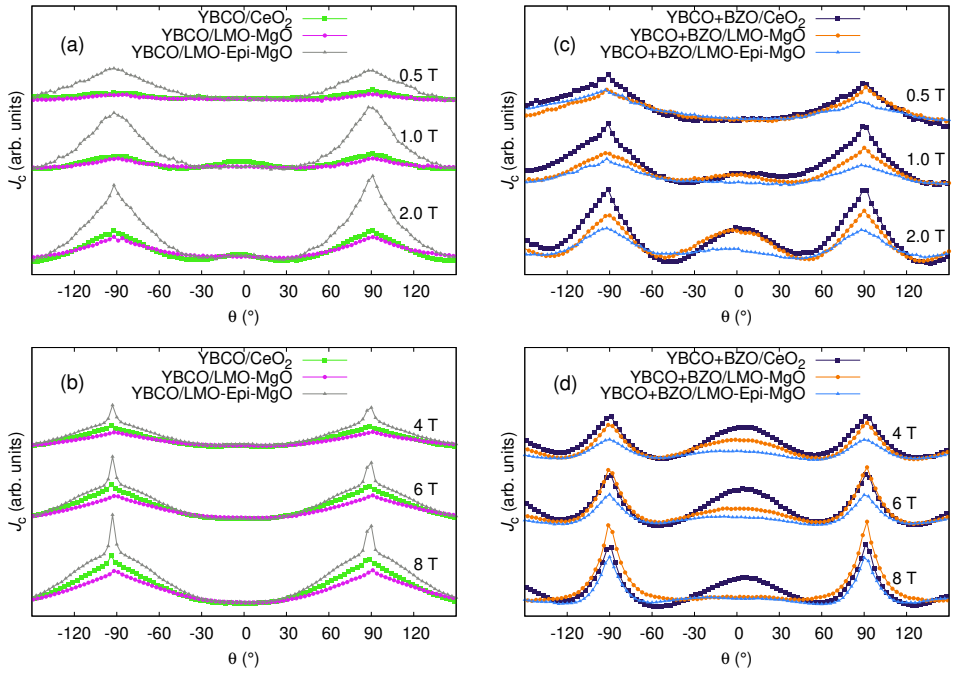

Fig. 3. $J_c(\theta)$ curves for undoped (a)−(b) and BZO doped (c)−(d) YBCO films grown on CeO_2, LMO-MgO and LMO-Epi-MgO templates measured at different B and 40 K.

the increasing number of vortices with respect to higher B [15]. This means that the template governs the YBCO growth and is responsible for the overall $J_c(\theta)$.

Fig. 3(b) displaying the $J_c(\theta)$ graphs for all the undoped films measured at 4 T, 6 T and 8 T reveals the remarkable differences in the shape of the curves when comparing with those measured at 0.5 T−2 T. Firstly, the c-peak for film on CeO_2 template is almost indiscernible at 4 T. As can be seen, that the curves are still somehow isotropic at 4 T for films on CeO_2 and LMO-MgO templates, we observe the subtle and strange behaviour of ab-peaks for film on LMO-Epi-MgO. Earlier we have also reported such a behaviour for the YBCO films grown on single crystalline $SrTiO_3$ (STO) [4]. With increasing B, the ab-peaks are observed to be intense along with the pronounced shoulderings. This means that the film grown on LMO-Epi-MgO template has more pinning paths along ab-direction. Generally, the undoped films have more pinning paths along ab-direction than the c-axis [15]. The shoulders seen beside the ab-peaks can be due to the interplay of in-plane and out-of-plane pinning [16]. Back to the film on CeO_2 template, it is clear that the $J_c(\theta)$ starts to follow anisotropic behaviour from 6 T where relative broad ab-peaks with a wide drop in J_c curve along 0° measured at 8 T can be observed. Finally, in the case of film on LMO-MgO template, the relative isotropic $J_c(\theta)$ is observed even at high B. These results reveal that not only do the natural pinning defects vary in number but they also differ in sizes with respect to the underlying template as can be deduced from an analysis of the differences in the shapes of $J_c(\theta)$ curves (Figs. 3(a) and (b)). Especially, the film on LMO-Epi-MgO template behaves exceptionally in terms of anisotropic $J_c(\theta)$ as compared with

its other two counterparts where $J_c(\theta)$ is seen to be more isotropic.

Figs. 3(c) and (d) display the $J_c(\theta)$ of BZO doped YBCO films on the set of studied templates. In Fig. 3(c), the measured curves at 0.5 T−2 T reveal that $J_c(\theta)$ changes shape with respect to B. At 0.5 T, the shape of $J_c(\theta)$ for BZO doped films on CeO_2 and LMO-MgO templates is quite similar to those of undoped films measured at 2 T. This is related to less c-axis flux pinning at this B and the pinning mostly occurs in-plane which in turn gives us broad ab-peaks. Unlike in the undoped case, more isotropic $J_c(\theta)$ is seen at this B for film on LMO-Epi-MgO template which is due to the pinning of vortices by the dopant thus decreasing the anisotropy. As the BZO grows in the form of nanocolumns along the c-axis in both the single crystalline and buffered metallic templates, it is obvious that they are pinning the vortices effectively [12, 17]. The $J_c(\theta)$ measured at 1 T already reveals the vortex trapping by the induced nanocolumns as we see the c-axis peaks in both the films on CeO_2 and LMO-MgO templates, whereas the film on LMO-Epi-MgO template has not shown any c-peak. This behaviour is related to the lengthened nanorods in films on CeO_2 and LMO-MgO, whereas the shorter nanocolumns in film on LMO-Epi-MgO template are weaker in vortex pinning. The broad and intense c-peaks along with very intense ab-peaks are visible at 2 T for films grown on CeO_2 and LMO-MgO templates. However, the total vortex pinning is not only attributed to the BZO nanocolumns but also to the other naturally created defects during the growth process. This is due to the fact that ab-peaks were seen to become more pronounced with increasing B from 0.5 T−2 T in all the films.

Fig. 3(d) depicting the $J_c(\theta)$ at high B (4 T) indicates a strong flux pinning accross YBCO c-axis for all the films. At 4 T, the film on CeO_2 template again beats its counterparts in terms of isotropic $J_c(\theta)$. A very strong c-peak in this case predicts the nice and elongated growth of BZO nanocolumns within YBCO which are both similar in shape and size to that of vortices [4]. Due to the occurrence of a wide c-peak via enhanced c-axis flux pinning, the ab-peaks tend to be narrow and less intense [16]. A similar tendency is seen for the film grown on LMO-MgO template, whereas with intuitive argument, the c-peak starts to appear in LMO-Epi-MgO substrate due to the growth of shortened and randomly distributed nanocolumns within the film. This result reveals the effect of the substrate on both the YBCO and the dopant induced within it. At 6 T, the c-axis flux pinning gets more pronounced for film on CeO_2 template with the appearance of a very broad and intense c-peak thus telling us that most of the vortices get pinned at this B with maximum pinning force F_p, whereas the c-peaks starts to slightly decrease for the rest of the films. To an end, the film on CeO_2 template still shows a very strong c-peak even at 8 T with pronounced ab-peaks thus revealing the enhanced pinning along both the c-axis and ab-planes. On the other hand, the c-peaks are barely visible for the films on both LMO-MgO and LMO-Epi-MgO templates.

All the $J_c(\theta)$ curves presented in Figs. 3(c) and (d) are asymmetric in the vicinity of 0° which is the typical behaviour for all the films grown on IBAD-MgO based templates being caused by the inclined buffer layer growth during the IBAD process [12, 19, 20]. Furthermore, the low lattice mismatch between the CeO_2 cap layer and the YBCO [21] makes the CeO_2 template the best for growing both undoped and BZO doped YBCO as least anisotropy of $J_c(\theta)$ is revealed when the films were grown on it. To bring forth a comprehensive understanding of this explanation we present a schematic model, in the next section, which illustrates the growth of the defects in both the undoped and doped YBCO films when grown on all of our three templates.

For the detailed anisotropy analysis, the anisotropy of undoped YBCO is best described via the Blatter anisotropy parameter γ, which ultimately represents the electronic mass anisotropy of YBCO [22]. This parameter can be experimentally estimated by plotting the $J_c(\theta, B)$ values (shown in Fig. 3) in the regions where they collapse (between 90° and 180°) as a function of effective magnetic field $B_{\text{eff}} = B\varepsilon(\theta, \gamma)$, where $\varepsilon(\theta, \gamma) = (\cos^2(\theta) + \gamma^{-2}\sin(\theta))^{1/2}$, and finding a value of γ that produces linear B_{eff}-J_c plot [18, 23]. Fig. 4 presents the calculated B_{eff}-I_c curves

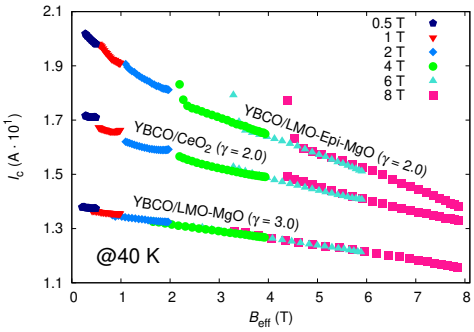

Figure 4. The I_c as a function of effective magntic field B_{eff} along the c-axis of YBCO for all the undoped films. The calculated γ parameters are also given.

and corresponding γ-values which respectively produce the linearity observed in the curves. Our films have the γ values in the range of 2 to 3, which are much lower compared with other YBCO films where γ is always found to be above 5 [18, 24, 25]. In our previous work [24], we calculated the γ values of YBCO films on STO where the films grown by micro- and nanocrystalline sized targets have $\gamma = 5$ and 1.8, respectively. This observed difference is explained by the increased number of correlated pinning sites in n-YBCO (grown from nanocrystalline sized target) that on the other hand, has a lowering effect on γ value. Similarly, Xu *et.al.* [26] compared the anisotropy of two YBCO films, one with Y_2O_3 precipitates and other with stacking faults, where the calculated γ value for the film with Y_2O_3 precipitates is much lower than for the film with stacking faults due to the effective pinning properties of Y_2O_3 precipitates in a wide region around YBCO c-axis. This suggests that in our case, the decreased anisotropy especially in CeO_2 and LMO-Epi-MgO films is due to the increased number of weak point like defects, precipitates or voids. This scaling procedure has not been applied to BZO doped films since the highly correlated BZO nanorods perturb the $J_c(\theta)$ curves in such a way that they do not collapse to a line properly at low temperature and B [24], thus making the anisotropy analysis difficult.

3.3. TEM analysis

Based on our transport properties shown in Fig. 3, we chose the best film (in terms of enhanced isotropy of $J_c(\theta)$) for the TEM analysis. Fig. 5 displays the TEM image of one of the doped films, that is, BZO doped YBCO grown on CeO_2 template. It can be seen that the BZO nanocolumns grow elongated along the c-direction with the presence of short stacking faults (mainly next to the CeO_2/YBCO interface) in between them. Our analysis shows that the BZO nanocolumns are just slightly tilted and are randomly distributed. The lengthened nanorods increase the flux pinning along c-axis, thus reducing the J_c anisotropy, whereas the short stacking faults are the source of pinning the vortices along ab-direction. Moreover, while connecting the microstructure with the angular dependent results (Fig. 3), it can be concluded that the nanorods are very effective in flux pinning as revealed by the most pronounced c-peak of doped film grown on CeO_2 template, especially at high fields from 4 T to 8 T.

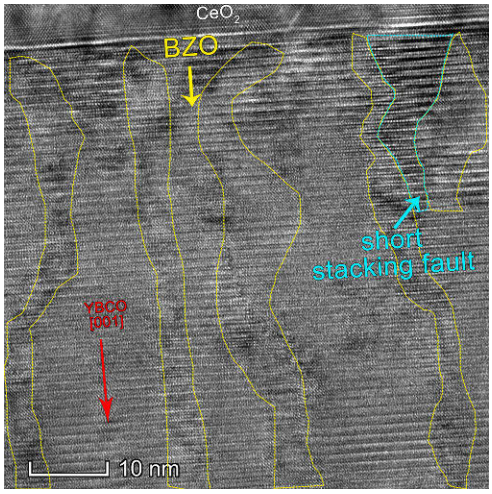

Figure 5. TEM image of BZO doped film grown on CeO_2 template. The yellow boundaries delimit the BZO nanocolumns, whereas the presence of a stacking fault next to the interface is marked by sky blue area.

3.4. Growth model of the defects

According to our schematic shown in Fig. 6 (drawn based on the angular dependent measurements, XRD results and TEM image), one realizes relative differences not only in the number but also in the sizes of both the naturally and artificially induced defects within the films. Comparing the undoped films, we concluded that the growth of long threading dislocations throughout the thickness of the film on CeO_2 template is the source of effective vortex pinning which in turn reveals the *c*-peak (Fig. 3(a)). This is in line with our structural results where the low-angle grain boundaries ($\Delta\phi$) channel the YBCO growth which results in threading dislocations. For LMO-MgO template, the intermediate sized dislocations are still perturbing the vortex motion which increases the isotropic behaviour of the $J_c(\theta)$ especially at low B (Fig. 3(a) and (b)). On the other hand, the same sized stacking faults gave us the similar shapes of $J_c(\theta)$ *ab*-peaks in both the CeO_2 and LMO-MgO templates, whereas more pronounced *ab*-peaks under all the B for film on CeO_2 template is related to the greater number of stacking faults compared with the LMO-MgO template. Thinking about the similarity of *ab*-peaks for film on LMO-Epi-MgO template with that of YBCO grown on single crystalline substrate [4], we see that the growth of long stacking faults makes it energetically preferable to pin a huge number of vortices. Principally, the film on LMO-Epi-MgO template beats the other two in terms of both the number and size of stacking faults and thus has the highest J_c along the *ab*-direction. Moreover, the small-sized threading dislocations in this case are also the source of vortex pinning but do not affect the shape of the *c*-axis peak.

The induced defects in BZO doped films as revealed by Fig. 5 and schematically drawn in Fig. 6, we find in our analysis that the BZO grown nanocolumns are slightly unidirectionally splayed in all the films as this is the cause of anistropic *c*-peaks (Fig. 3(c) and (d)). The main difference among all the films is the length of these nanorods. The nanorods are the longest when film is grown on the CeO_2 template and this is the most effective for strongly enhanced flux pinning thus producing very broad and intense *c*-peak in this case. The length of the

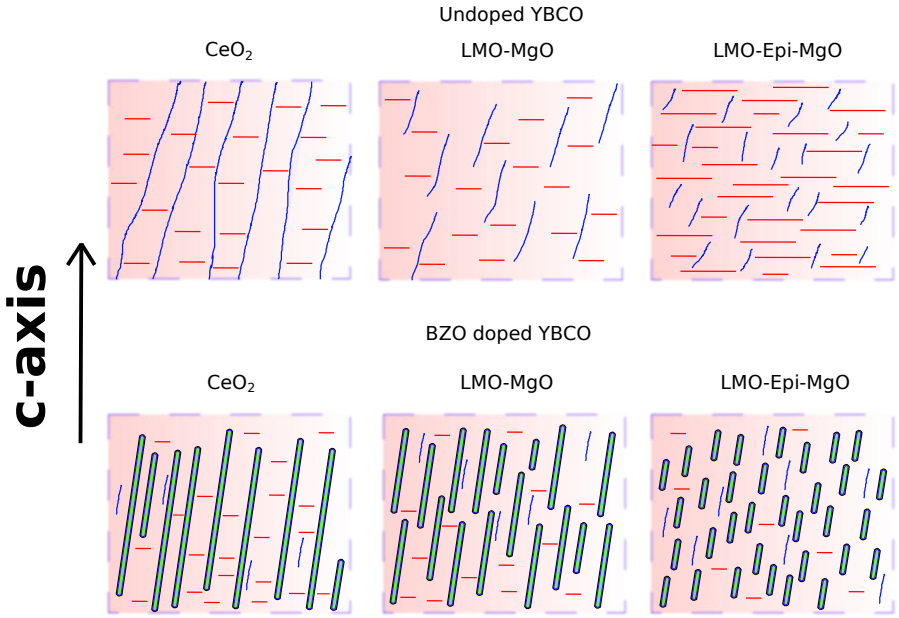

Figure 6. Schematic of some of the induced defects within the (a)−(c) undoped and (d)−(f) BZO doped films grown on different buffered substrates. The red horizontal lines present the stacking faults, whereas the vertically oriented blue threads depict the low-angle grain boundary based threading dislocations. The green filled pipes correspond to the BZO induced nanocolumns.

nanorods is smaller in the film on LMO-MgO template which affects the flux pinning especially at high B as revealed in Fig. 3(d)). The very small sized nanorods grown in the film on LMO-Epi-MgO template cause weakened vortex pinning as a slight c-peak was observed in this case (Fig. 3(c) and (d)). The difference in the shapes of the $J_c(\theta)$ curves of the undoped films from the doped ones can be explained by the Paulius model [27] where J_c is reduced when the inclination angle of the applied field is increased with respect to the c-axis thus decreasing the length of trapped vortex portion. Unlike our undoped films where vortices are only pinned by the natural defects and they can become free and move around at sufficient magnetic field angles, the doped films have the significant edge of firstly pinning the vortices by the nanocoloumns and at certain angles when vortices get untrapped by them the proximate natural defects like threading dislocations and stacking faults can be the cause of their trapping. This effect improves the $J_c(\theta)$ and thus the creation of enhanced natural defects on our templates, especially for film on CeO_2, can be used to help advance fundamental understanding and applied for electrical power applications in wide temperature, field and angular ranges.

4. Conclusion

Three variously buffered IBAD-MgO based templates were used to grow both undoped and BZO doped YBCO films. The analysis of our results showed that the buffer architecture is crucial for growing superconducting films with desired properties. We succeeded in optimizing one of the substrates to achieve the goal of improving the isotropic behaviour of $J_c(\theta)$ on technical

substrates. The optimized CeO_2 template is suitable for the creation of highly effective natural and decorated defects within YBCO films which enhances the pinning of the vortices. Both isotropic and high-valued $J_c(\theta)$ curves are achieved on this template in comparison to other two counterparts. Furthermore, our growth model of the defects gives a basic understanding about the induced defects within all the films deposited on our differently buffered templates. Thus, our results can be utilized in a variety of electrical power applications.

5. Acknowledgments

The Jenny and Antti Wihuri foundation is acknowledged for the financial support.

References

[1] Bednorz J G and Müller K A 1986 *Z. Phys. B* **64** 189–193
[2] Foltyn S R, Civale L, MacManus-Driscoll J L, Jia Q X, Maiorov B, Wang H and Maley M 2007 *Nat. Mater.* **6** 631–642
[3] Paranthaman M P and Izumi T 2004 *Mater. Res. Soc. Bull.* **29** 533–541
[4] Khan M Z, Malmivirta M, Y Zhao X W, Jha R, Awana V, Huhtinen H and Paturi P 2018 *Physica C* **555** 15–23
[5] Khan M Z, Zhao Y, Wu X, Jha R, Awana V, Huhtinen H and Paturi P 2019 *IEEE T. Appl. Supercond.* **29** 8002105
[6] Nelson J B and Riley D P 1945 *Proc. Phys. Soc.* **57** 160
[7] Schweiss P, Reichardt W, Braden M, Collin G, Heger G, Claus H and Erb A 1994 *Phys. Rev. B* **49** 1387–1396
[8] Malmivirta M, Huhtinen H, Zhao Y, Grivel J C and Paturi P 2017 *J. Low Temp. Phys.* **186** 74–83
[9] Huhtinen H, Irjala M, Paturi P and M Falter 2012 *Physica C* **472** 66–74
[10] Khan M Z, Zhao Y, Wu X, Malmivirta M, Huhtinen H and Paturi P 2018 *Physica C* **545** 50–57
[11] Ye J and Nakamura K 1993 *Phys. Rev. B* **48** 7554–7564
[12] Wee S H, Zuev Y L, Cantoni C and Goyal A 2013 *Sci. Rep.* **3** 23101–9
[13] Huhtinen H, Irjala M, Paturi P and Falter M 2011 *IEEE T. Appl. Supercond.* **21** 2753
[14] Kästner G, Hesse D, Scholtz R, Koch H, Ludwig F, Lorenz M and Kittel H 1995 *Physica C* **243** 281
[15] Long N J, Strickland N M and Talantsev E F 2007 *IEEE Trans. Appl. Supercond.* **17** 3684–3687
[16] Wimbush S and Long N 2012 *New J. Phys.* **14** 083017:1–24
[17] Kang S, Leonard K J, Martim P M, Li J and Goyal A 2007 *Supercond. Sci. Technol.* **20** 11
[18] Civale L, Maiorov B, Serquis A, Willis J O, Coulter J Y, Wang H, Jia Q X, Arendt P N, MacManus-Driscoll J L, Maley M P and Foltyn S R 2004 *Appl. Phys. Lett.* **84** 2121–2123
[19] Maiorov B, Gibbons B, Kreiskott S, Matias V, Jia Q, Holesinger T and Civale L 2005 *IEEE T. Appl. Supercond.* **15** 2582–2585
[20] Maiorov B, Gibbons B, Kreiskott S, Matias V, Holesinger T and Civale L 2005 *Appl. Phys. Lett.* **86** 132504
[21] Mu Q Q, Liu L F and Li Y J 2015 *Chin. Phys. Lett.* **32** 078102
[22] Blatter G, Geshkenbein V B and Larkin A I 1992 *Phys. Rev. Lett.* **68** 875
[23] Gutiérrez J, Puig T and Obradors X 2007 *Appl. Phys. Lett.* **90** 162514
[24] Paturi P, Irjala M and Huhtinen H 2008 *J. Appl. Phys.* **103** 123907
[25] Puig T, Gutiérrez J, Pomar A, Llordés A, Gázquez J, Ricart S, Sandiumenge F and Obradors X 2008 *Supercond. Sci. Technol.* **21** 034008
[26] Xu A, Jaroszynski J, Kametani F and Larbalestier D 2015 *Appl. Phys. Lett.* **106** 052603
[27] Paulius L, Fendrich J A, Kwok W K, Koshelev A, Vinokur V, Crabtree G and Glagola B 1997 *Phys. Rev. B* **56** 913

M. Z. Khan & E. Rivasto & J. Tikkanen & H. Rijckaert & M. Malmivirta & M. O. Liedke & M. Butterling & A. Wagner & H. Huhtinen & I. Van Driessche & P. Paturi
Enhanced flux pinning isotropy by tuned nanosized defect network in superconducting $YBa_2Cu_3O_{6+x}$ films

Scientific Reports, 9, 2019, 15425

V

SCIENTIFIC REPORTS
nature research

OPEN

Enhanced flux pinning isotropy by tuned nanosized defect network in superconducting $YBa_2Cu_3O_{6+x}$ films

Mukarram Zaman Khan[1,2*], Elmeri Rivasto[1,2], Jussi Tikkanen[1], Hannes Rijckaert[3], Mika Malmivirta[1], Maciej Oskar Liedke[4], Maik Butterling[4], Andreas Wagner[4], Hannu Huhtinen[1], Isabel Van Driessche[3] & Petriina Paturi[1]

Striving to improve the critical current density *Jc* of superconducting $YBa_2Cu_3O_{6+x}$ (YBCO) thin films via enhanced vortex pinning, the interplay between film growth mechanisms and the formation of nanosized defects, both natural and artificial, is systematically studied in undoped and $BaZrO_3$ (BZO)-doped YBCO thin films. The films were grown via pulsed laser deposition (PLD), varying the crystal grain size of the targets in addition to the dopant content. The microstructure of the PLD target has been observed to have a great impact on that of the deposited thin films, including the formation of vortex pinning centers, which has direct implications on the superconducting performance, especially on the isotropy of flux pinning properties. Based on experimentally measured angular dependencies of *Jc*, coupled with a molecular dynamics (MD) simulation of flux pinning in the YBCO films, we present a quantitative model of how the splay and fragmentation of BZO nanorods artifically introduced into the YBCO film matrix explain the majority of the observed critical current anisotropy.

To obtain the freedom to engineer future high-temperature superconductor (HTS) applications for desired operating magnetic field and temperature ranges, it is necessary to optimize the vortex pinning landscape for an enhanced, isotropic flux pinning performance[1–6]. In addition to naturally formed crystalline defects, which typically have spatial dimensions distinctly below the superconducting coherence length, defect-engineering with artificially produced pinning centers (APCs) with dimensionalities of 1D–3D have been observed to be extremely effective[7–10]. However, the complex nucleation process of YBCO during PLD process, that leads to growth island size variation, and the manner in which this could affect the size and distribution of the nanoscale structural defects is chiefly neglected. Especially, a clear gap exists in the current literature regarding how ordered arrays of nanoscale defects can also influence and regulate the distribution and growth of more effective APCs and thus decrease the anisotropy by allowing vortices to be trapped in a wider angular range[11]. Partly, the clear lack of information on the subject is arguably be due to the rather general assumption that during PLD process, the film growth method of our choice, the target material is largely decomposed on the atomic level, and thus its properties should not have an effect on the formation and nucleation of particles on the substrate surface. This assumption, which our studies have led us to challenge, would precariously force one to downplay the potential importance of target microstructure on the functional properties of derived films.

The angular dependence of the J_c has an excellent physical importance providing an approach to the problem of flux pinning and vortex dynamics anisotropy in HTSs, both from the experimental and theoretical point of view. For instance, in the angular dependent critical current plots, one can easily observe how the various types of pinning centers such as correlated linear, columnar or planar defects and, on the other hand, defects based on growth mechanisms together with YBCO's intrinsic pinning can dramatically alter the angular dependence of $J_c(B)$[4]. For understanding the origin of angular dependent flux pinning $J_c(\theta)$, experimental tools like transmission electron microscopy (TEM) are often exploited to probe the structural properties and features, such as the defects naturally formed during the film growth, as well as the size, shape, orientation and distribution of the artificially produced and self-assembled pinning centers[5,12,13]. However, methods like positron annihilation spectroscopy,

[1]Wihuri Physical Laboratory, Department of Physics and Astronomy, University of Turku, FI-20014, Turku, Finland. [2]University of Turku Graduate School (UTUGS), University of Turku, FI-20014, Turku, Finland. [3]SCRiPTS, Department of Chemistry, Ghent University, Krijgslaan 281 S3, 9000, Ghent, Belgium. [4]Institute of Radiation Physics, Helmholtz-Zentrum Dresden - Rossendorf, Bautzner Landstraße 400, 01328, Dresden, Germany. *email: mukarram.z.khan@utu.fi

which gives information about vacancy-type defects, are only rarely utilized on HTS thin films[14,15]. In addition to experimental scrutiny, simulations offer a way of understanding the roles that different pinning landscapes may have in explaining the angular and magnetic field dependencies of J_c, as well as a method for designing the most effective pinning centers for future applications[16–18].

In this work, we experimentally demonstrate the often downplayed effects of PLD target synthesis method and crystallinity on the growth kinetics and nucleation of particles and the distribution of chemical elements in YBCO thin films. The original used targets for depositing films differ from each other by the average crystal grain size, that is, nanocrystalline (n-YBCO) and microcrystalline (μ-YBCO). The phenomenon is widely investigated structurally, magnetically and resistively, and discussed together with the results of theoretical simulations in order to form a comprehensive picture of how the anisotropies of different kinds of pinning sites result in complicated angular dependent flux pinning behaviour.

Results and Discussion

Microstructure and defect formation. The microstructure and defect formation of the films is investigated by atomic force microscope (AFM) and TEM. Based on the detailed surface microstructure analysis shown in Supplementary Information (SI), we can conclude that the average in-plane surface particle diameter for the undoped n-YBCO is clearly smaller than that for the undoped μ-YBCO films. This indicates a greater number of nucleation sites and smaller growth island size in n-YBCO films which, on the other hand, cause improved flux pinning by defects localized on boudaries between single particles fused together and on the contact points of the growth island network when the film is formed with the Volmer-Weber growth mode[19,20].

As shown in the cross-sectional TEM images in Fig. 1a, the n-YBCO exhibits the presence of long stacking faults in the bottom, middle and top layers along with the twin boundaries, whereas in μ-YBCO (Fig. 1b), the short stacking faults and twin boundaries (see SI) are observed throughout the film. The presence of a large number of short stacking faults throughout the μ-YBCO film could be related to the relaxation of strain, as revealed by decreased inhomogeneous strain ε_{WH} explained in crystallographic properties of SI.

Comparing the BZO doped n- and μ-YBCO, Fig. 1c,d, the stacking faults are only visible in μ-film and they are relatively short and randomly distributed. The diameters of BZO nanorods in the films grown using n- and μ-grain sized targets average at 7.5 nm and 6.5 nm, respectively, whereas the average distances between nanorods are estimated to be 9 nm and 12 nm, respectively. In the n-films, the BZO rods seem to be unbroken and relatively long, with smaller splay (85–203 nm in length and 5–15° tilted) than in the μ-film, where they are short and more tilted (21–45 nm in length and 20–25° tilted) as presented in Fig. 1c,d, respectively. This spacing is calculated over several cross-sectional areas. Since we are using these values in simulations, therefore only the average values are reported here. Moreover, for both undoped and BZO doped films, the n-films are slightly thicker ($\approx$15 nm) than the μ-films. In Table 1, the collection of naturally and artificially created defects within the undoped and BZO doped n- and μ-YBCO films with the details of BZO nanorods are presented.

Regarding our TEM results (see SI for more details), one is naturally led to wonder what exactly has caused the increased splay and fragmentation of the BZO nanorods in the μ-film compared to the n-film. It is known that the tendency of BZO to form long upright nanocolumns is increased as the YBCO unit cell is stretched along its c-axis, since a larger YBCO film c lattice parameter will better match against unstrained BZO (where $a = b = c = 4.193$ nm, to be compared with 1/3 of the YBCO c parameter)[21]. As shown in SI, the c-axis of the doped μ-film is indeed very slightly smaller than that of the doped n-film. Furthermore, the n-film may have provided better local conditions for coherent BZO–YBCO interfaces to develop via improved oxygen diffusion through the larger number of grain boundaries and other defects associated with growth island edges[22]. The increased fragmentation of the μ-film nanorods is likely to stem from similar origins, but may also have been compounded by the lower local availability of BZO during the growth process. As will be later illustrated in growth mechanism section, we propose that relatively large clusters of crystalline material are transferred as such to the film during n-YBCO deposition, whereas μ-YBCO essentially breaks down at the atomic scale, also spreading the BZO components around more evenly and in smaller units.

Variable energy positron annihilation spectroscopy (VEPAS) is used for probing the defect type and concentration in n-YBCO and μ-YBCO films. The low electron momentum fraction, S (valence electrons) as a function of positron implantation energy, E, shown in Fig. 2, is directly proportional to defect concentration and/or defect size. S and W are unitless and are just a ratio of a certain fraction of the annihilation spectrum (a Gaussian; S-in the middle, W-on the spectrum tails) normalized to the total number of annihilation events. It can be clearly seen that the μ-YBCO sample exhibits a larger concentration of vacancy-like defects such as mono-vacancies or bi-vacancies[23]. The S–W plot (right panel) shows a linear relation for the most of the data points, which suggests the same defect type across the films' thickness for both samples and therefore only variations in the defect concentration are expected. Besides this, a sub-surface region, where a line with a slightly different slope can be drawn for a n-YBCO sample, possibly indicates another defect type. In addition, the lower defect concentration in nano-crystalline films is confirmed by the larger positron diffusion length, L_+, which is inversely proportional to the defect concentration. For the analysis of L_+, the VEPFIT code[24] has been utilized, which permits to fit $S(E)$ curves for multilayered systems and to acquire the thickness L_+ and specific S parameters for each layer within a stack. As derived from VEPFIT analysis of the $S(E)$ curve the difference in L_+ is close to a factor of 2, which translates to the μ-YBCO films having approximately twice the amount of defects over their n-YBCO counterparts.

Since the crystallites size for both film types is much larger than L_+, positrons annihilate mostly in defects situated inside the crystals rather than at grain boundaries (or twin boundaries). The positrons cannot reach the grain boundaries, but are trapped by nearby defects almost upon their implantation. Therefore, the overall localized trapping takes place and most likely positrons preferentially annihilate with open volume defects like dislocation loops and vacancy-like defects. In addition, the defect distribution seems to be constant across the films thickness, which is reflected by a presence of a plateau in $S(E)$ for $2\,\text{keV} < E < 6\,\text{keV}$.

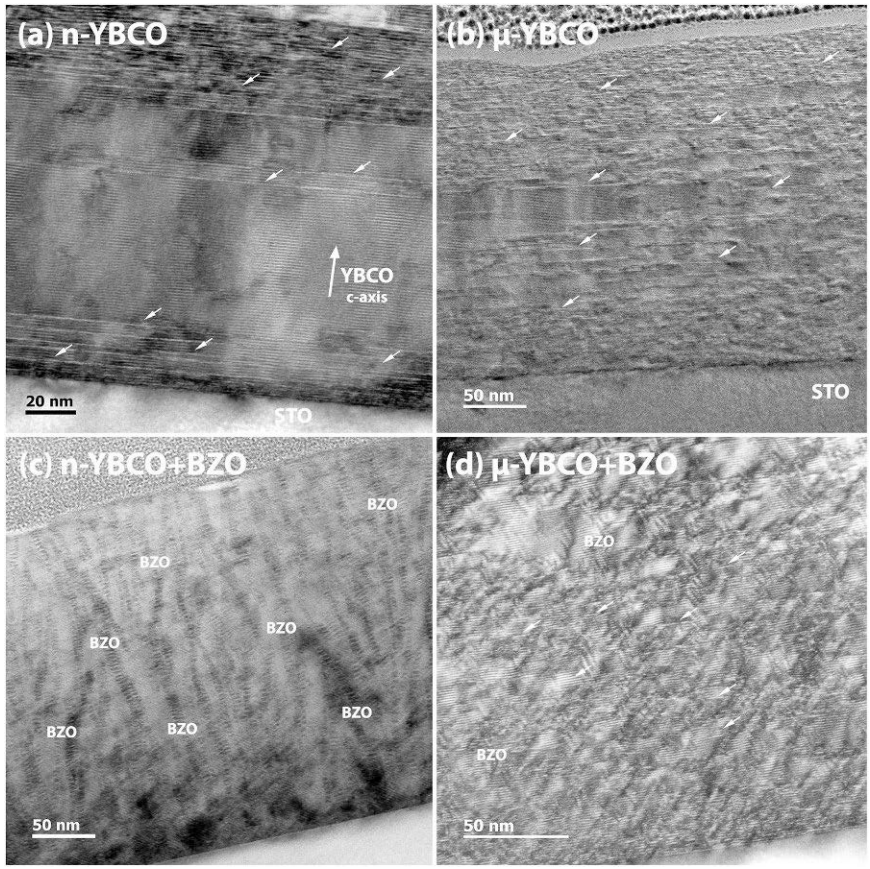

Figure 1. Cross-sectional TEM images of both undoped and BZO doped YBCO films deposited from targets with varying grain sizes (**a**–**d**). The bright vector arrows depict stacking faults. Extended BZO nanocolumns (labeled) are observed in n-YBCO + BZO (**c**), whereas broken BZO nanorods and short stacking faults are seen in μ-YBCO + BZO (**d**).

Samples	Stacking faults	Splay of nanorods (°)	Twin boundaries
n-YBCO	Bottom layer with long stacking faults	—	In bottom layer
μ-YBCO	Randomly distributed short stacking faults	—	Visible (see SI)
n-YBCO + BZO	Few in number	5–15 (unbroken)	Not visible
μ-YBCO + BZO	Randomly distributed short stacking faults	20–25 (often broken)	Not visible

Table 1. A compilation of TEM results depicting the microscopic characterisitics of undoped and BZO doped n- and μ-YBCO films.

Direction dependent superconductivity. Before studying the $J_c(\theta)$ properties at low temperature, the normal state resistivities were measured at 300 K, giving $\rho = 192$, 175, 166 and 151 $\mu\Omega$ cm for μ-YBCO + BZO, μ-YBCO, n-YBCO + BZO and n-YBCO, respectively. This is in agreement with the increased number of vacancy type defects observed by VEPAS in films grown from microcrystalline targets, as well as with lowered T_c values also magnetically obtained for BZO-doped films.

In our $J_c(\theta)$ results, $\pm 90°$ denotes the direction of *ab*-planes of YBCO, whereas 0° the c-axis of YBCO. A comparison between the $J_c(\theta)$ of undoped n-YBCO and undoped μ-YBCO films (Fig. 3a,b) shows that the n-YBCO curve is much flatter and has a sharp peak at the $B \,||\, ab$-direction, whereas the μ-YBCO film clearly has broader *ab*-peaks. This isotropic angular dependence of J_c in n-YBCO is even more pronounced at magnetic fields below 4 T. When looking at the absolute J_c values, we can see that, as observed in magnetic measurements in the

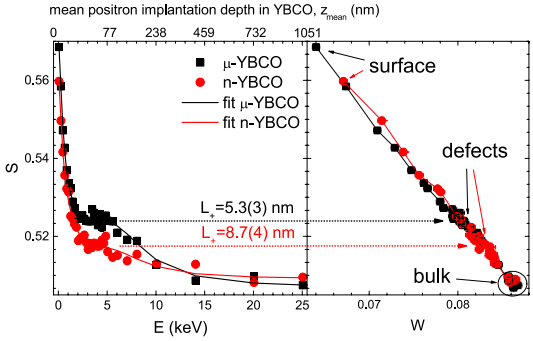

Figure 2. Low electron momentum fraction, *S*, as a function of positron implantation energy, *E* (left panel) and *S* versus the high electron momentum fraction, *W* (right panel). The error bars are about the same size as the symbols. The *S*(*E*) curves have been fitted using VEPFIT code and the thus obtained positron diffusion length, L_+, is given for the μ-YBCO and n-YBCO samples.

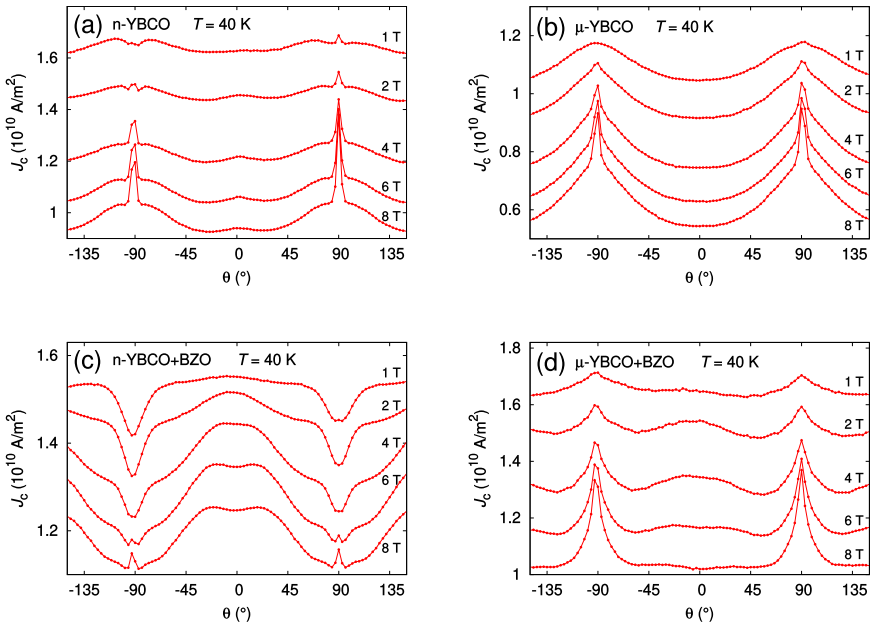

Figure 3. The angular dependencies of J_c measured at 40 K and different magnetic fields for films deposited from undoped nanocrystalline (**a**) and microcrystalline (**b**) as well as from BZO doped nano- and microcrystalline targets, (**c**) and (**d**), respectively.

c-direction, the undoped n-YBCO has higher J_c through the whole angular range and in all magnetic fields up to 8 T when compared to undoped μ-YBCO films. This is in line with structural results, where a smaller island size produced a larger amount of strain-relaxing structural defects in n-YBCO. In addition, we have observed earlier that the twin domain size is smaller in n-YBCO films which again means the presence of greater number of twin boundaries along the YBCO *c*-axis[25]. This increased number of lattice defects in n-YBCO film is in agreement with the small *c*-peak around 0° (Fig. 3a), which is completely missing in the μ-YBCO film. As explained with the vortex path model[26,27], in μ-YBCO film where a great number of short stacking faults occur, vortices have the possibility to be pinned over a shorter distance in the *c*-direction than the standard deviation of the *ab* separation distance of the vortices, in line with the absence of a *c*-axis peak.

In BZO doped YBCO films of Fig. 3c,d, the absolute J_c value is higher and general anisotropy is smaller in μ-YBCO + BZO film measured in fields $B \leq 2$ T, while the strong *c*-axis peak of n-YBCO + BZO starts to

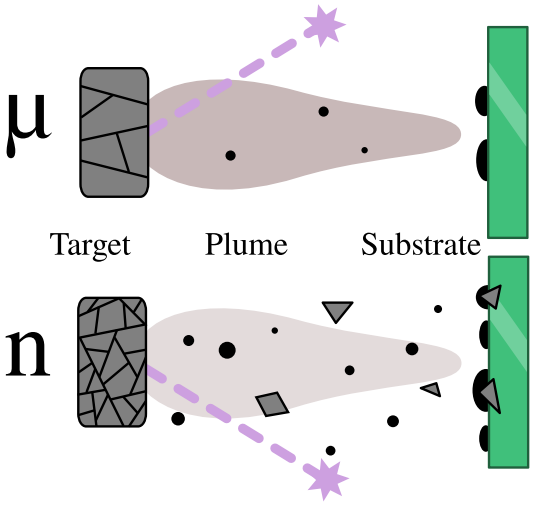

Figure 4. A schematic of the proposed effect of PLD target grain size on the growth process of the deposited film. Upon receiving a laser pulse (stars and dashed lines), the microcrystalline μ-YBCO (top) produces a smooth plume of individual atoms and ions (gray cloud) with very few multi-atom clusters (black dots and gray polygons) in comparison with the nanocrystalline n-YBCO (bottom) which has many more grain boundaries over a given ablation surface. Due to their low mobility on the substrate, the larger fragments will more readily act as individual growth centers, leading to the observed increase in film surface granularity when a n-YBCO target is used instead of μ-YBCO.

dominate at $B > 2$ T, also producing higher J_c within the whole angular range. In μ-YBCO + BZO film, a relatively weak *c*-axis peak in 1 T can be observed, but the *c*-peak is more pronounced in the range $2\,\mathrm{T} \leq B \leq 6\,\mathrm{T}$, almost disappearing again in an 8 T field. When compared to n-YBCO + BZO film, the peak of μ-YBCO + BZO along the *ab*-plane is relatively broad and it increases with increasing magnetic field. This effective pinning along the *ab*-plane leads to weakened *c*-axis pinning, since the great number of in-plane pinning centers such as stacking faults pin the vortices, especially at high magnetic fields. Similar features in the $J_c(\theta)$ curve have earlier been observed in BZO doped YBCO films grown at extremely high temperatures, leading to shortened BZO nanocolumns and an increased number of stacking faults parallel to the *ab*-plane[28]. The weakening of the *c*-axis peak as well as the broad *ab*-peak in the μ-YBCO + BZO film can be explained by the vortex path model in terms of the trapping angle of the Cu–O spacer layers or stacking faults[26]. In the n-YBCO + BZO film, the *ab*-peak first forms a dip that evolves into a sharp peak with increasing magnetic field above 6 T.

Because of the more important vortex–vortex interactions at high magnetic fields, an ever-increasing number of vortices start to pin along the individual BZO nanorods since the long sideways steps along the *ab*-plane are prohibited[26]. Therefore, we can conclude that the field dependence of $J_c(\theta)$ in both BZO doped YBCO films can be explained with the vortex path model where, as confirmed by TEM, besides the BZO nanocolumn network, a clearly different natural vortex pinning landscape occurs in n-YBCO + BZO and μ-YBCO + BZO.

Target grain size based growth mechanism. We have a great variety of parameters, such as energy density of the laser and substrate – target distance in the PLD process that need to be optimized. Previous studies[12,29] showed that these paramters have an impact on the properties of YBCO films but the effect of target grain size has been chiefly neglected. One of the traditional assumptions regarding the PLD process is that the laser breaks down the surface of the target at the atomic level[30]. It is therefore not trivially clear that the grain size of the target should have any effect on the final composition of the deposited film. Our results, in particular the observed angular anisotropy of J_c, do show such a difference, however. We propose to explain this in terms of how the target granularity affects the particle size distribution of the PLD plume. A schematic of the proposed difference between micro- and nanocrystalline YBCO targets is presented in Fig. 4. Due to the larger density of grain boundaries in n-YBCO it seems plausible that the ablation laser could cleave off a proportionally larger number of multi-atom clusters in addition to the single atoms and ions that, on the other hand, dominate the composition of the μ-YBCO plume[30]. The larger clusters coming off n-YBCO will have less mobility than individual adatoms on the substrate, resulting in a larger number of individual film growth centers appearing with n-YBCO. As a consequence, we indeed observe almost twice as many growth islands on the surface of a fully-grown n-YBCO film. On the other hand, judging by the consistency of the final film thicknesses, the total amount of matter passed from the target to the substrate does not significantly depend on the target granularity. It certainly takes less energy to cleave off a large cluster of atoms from the target than the same amount of atoms individually, but this can be balanced by the lower probability that a heavy cluster attains and retains enough kinetic energy to reach

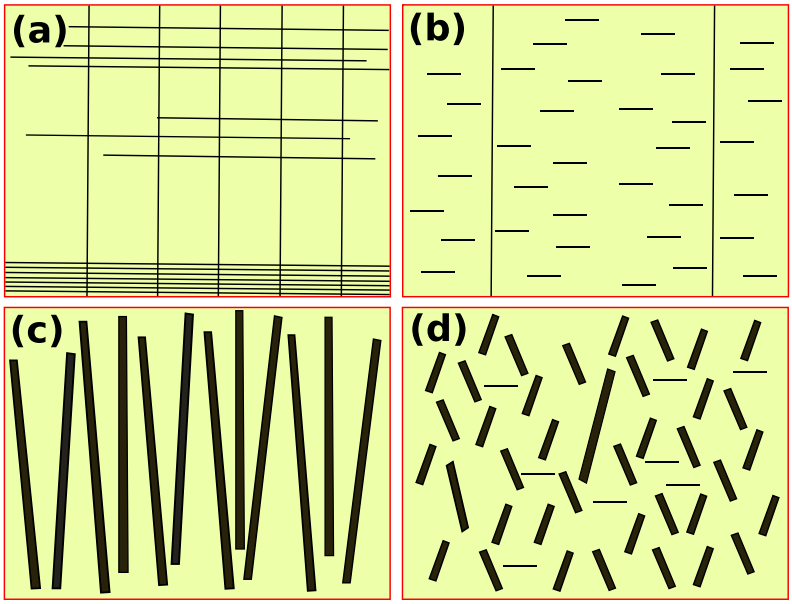

Figure 5. The schematic diagram of the defects grown in undoped n-YBCO (**a**), undoped μ-YBCO (**b**), n-YBCO + BZO (**c**) and μ-YBCO + BZO (**d**) films during the deposition. Long vertical lines refer to threading dislocations along the *c*-axis whereas both short and long horizontal lines to stacking faults along the *ab*-plane. The thick and variously tilted, both short and extended, columns represent the BZO induced nanorods.

the substrate. Thus lighter fragments (or individual atoms) receive a proportionally larger kinetic energy per mass than heavier, more voluminous fragments during the ablation process.

In Fig. 5, we have presented the schematic of distribution of natural and artificial defects based on our structural, microstructural and flux pinning results. Comparing the undoped cases in Fig. 5a,b, the n-YBCO not only has extended stacking faults at the interface but it also has a high density of threading dislocations, related to the smaller growth islands. The n-YBCO also has relatively long stacking faults in the top layer of the film, increasing the *ab*-plane pinning. Due to the growth of larger growth islands in μ-YBCO than in n-YBCO, it turns out that there are not only the short and randomly distributed stacking faults but also it has lesser number of threading dislocations than in n-YBCO as revealed by the c-peak in Fig. 3a. The random growth of short stacking faults is critical, as not only does it hinder the *c*-axis pinning, but also contributes to the broad *ab*-peaks. In the doped cases, as presented in Fig. 5c,d, the stacking faults in n-YBCO + BZO are completely absent, when multidirectionally tilted nanorods were induced. These tilted nanorods can be a source of the double *c*-axis peak shown in Fig. 6b. Moreover, the elongated BZO nanorods passing through the entire film thickness produce a broad and intense *c*-peak because of their both size and shape similarities with the vortices that can effectively pin them even at high fields of 6 T and 8 T as depicted in Fig. 3c. The randomly distributed stacking faults in μ-YBCO + BZO can also cause the BZO rods to grow shorter and strongly splayed with unspecified directions. Both randomly distributed and shortened BZO nanorods and stacking faults reduce the *c*-axis vortex pinning as the vortices could take several steps unlike in n-YBCO + BZO, where the vortices are strongly pinned along the elongated nanorods. The short and randomly distributed nanorods contribute to the relatively weak *c*-axis pinning as shown in Fig. 3d only up to 4 T, and strikingly lose their effect at higher fields.

Nanostructure induced critical current anisotropy. In order to compare the shape and the anisotropy in $J_c(\theta)$ curves, the most important data is plotted at fields of 2 T and 6 T, as shown in Fig. 6. In Fig. 6, the lowest point for both the data measured at 2 T and 6 T was shifted to the same level to make the shape comparison easier. The formation and the shape evolution of the *c*-axis peak with the effect of multi-structured and broadened peak along the YBCO *ab*-plane as well as their link with the in-plane and out-of-plane structural pinning centers will be discussed in the light of MD simulations.

Firstly, comparing the results of undoped films presented in Fig. 6a, the presence of long stacking faults in n-YBCO makes the in-plane vortex pinning more effective which leads to the sharp and narrow *ab*-peaks. The *ab*-peaks are quite small at 2 T but more intense at 6 T which can be explained by the effect of high density of vortices pinned within stacking faults and CuO_2 at high fields[28]. It is notable that at both low and high fields, the *ab*-peaks occured as sharp peaks with shoulders around them. The shoulders in the vicinity of the *ab*-peaks in undoped n-YBCO can be due to the interplay of in-plane and out-of-plane correlated pinning, instead of being a sign of any unorthodox pinning at intermediate angles[17]. As explained earlier, the n-YBCO contains more

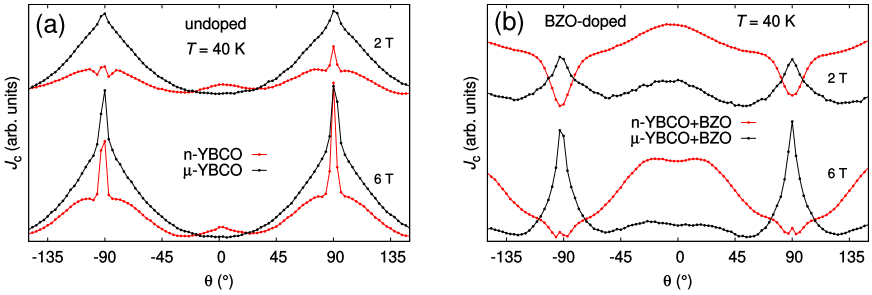

Figure 6. The shape comparison of the angular dependent J_c (40 K: 2 T and 6 T fields) in undoped (**a**) and BZO doped (**b**) YBsCO films deposited from nanocrystalline and microcrystalline targets.

nucleation centers than μ-YBCO leading to smaller growth island sizes, which again creates a large amount of *c*-axis oriented dislocation-type pinning centers. These out-of-plane threading dislocations interact with the long in-plane stacking faults thus acting as a source of occurance of the shoulders. The small *c*-peak, present both at low and high fields in n-YBCO, is directly related to the high density of threading dislocations passing through the film as discussed earlier in detail with Fig. 3. On the other hand, the strong and broad *ab*-peaks observed at 2 T in μ-YBCO arise due to the small and randomly distributed stacking faults within the film. However, the *ab*-peaks are significantly intense at 6 T, thus indicating more effective vortex pinning by the randomly distributed stacking faults at high fields. Considering the absence of a *c*-axis peak in μ-YBCO, the growth of large islands in this case produces a notably smaller number of threading dislocations which, despite pinning the vortices, are not as effective as to show a *c*-axis oriented peak like in n-YBCO, since the occurence of the *c*-peak is only possible when the angular dependent pinning force has a local maximum along the *c*-axis[31]. Although the μ-YBCO has twice the number of vacancy-type defects compared to n-YBCO as shown by our VEPAS measurements, these oxygen vacancy complexes are weak pinning centers and do not contribute to significant correlated pinning unlike defects such as dislocations.

Discussing the angular dependent curves for BZO doped films shown in Fig. 6b, the n-YBCO + BZO has huge dips along the *ab*-plane in a 2 T field but small *ab*-peak seems to arise at 6 T. The absence of *ab*-peaks at 2 T could be related to the high density of elongated and well-ordered, largely *c*-axis oriented nanorods, which worsen the *ab*-plane pinning but improve the *c*-axis pinning in such a way that a broad and immensely strong *c*-peak occurs. This would also suppress the *ab*-peak from arising in its usual direction[32]. At 6 T, the *c*-axis pinning weakens which not only narrows the *c*-peak but also allows the small *ab*-peaks to appear. Here, the elongated and well-ordered BZO rods grow due to the absence of stacking faults, unlike in μ-YBCO + BZO. The slight splay of BZO nanorods is also a source of the broad *c*-axis peak[5,17], whereas the better out-of-plane correlation of the unit cells within n-films and the array of structural defects resulting from the island growth mechanism also contribute to the significant *c*-axis pinning[4]. On the other hand, the smaller number of short and randomly distributed stacking faults in μ-YBCO + BZO produce a less intense but broad *ab*-peak at 2 T which becomes sharp and intense at 6 T. The random distribution of stacking faults could also affect the growth of BZO nanorods, reducing the *c*-axis pinning both at low and high magnetic fields.

In order to support this flux pinning mechanism, we have calculated the effect of the tilt angle and length of the artificially produced BZO nanorods using MD-simulations[18], since the presence of both splay and fragmentation in BZO columnar pinning sites is observed by TEM. In order to study these effects on the critical current angular dependency separately, MD simulation was employed with the pinning site configurations illustrated in Fig. 7. The simulation model is based on a layer structure that restricts the movement of each particle into a specific layer parallel to YBCO's *ab*-plane. This layer structure limits the angular range of simulations to $\pm 60°$, as measured from the YBCO *c*-axis[18]. Columnar pinning sites are modeled by chains of immovable particles spanning several layers, whereas single pinning sites only have one corresponding particle. Vortices are modeled in the same manner, their corresponding particles being allowed to move within their layers. The forces experienced by the vortices in different pinning site configurations, as well as the implementation of the splay and fragmentation of columnar pinning centers are explained in detail in SI.

The $J_c(\theta)$ curves simulated using the different tilting angles of the nanorods are presented in Fig. 8a. The overall widths of the simulated peaks seem to be somewhat independent of the splay of the nanorods. Near $\theta = 0°$, the peak intensity decreases as splay of the nanorods increases. At higher angles $\theta > 30°$, the effect seems to be opposite. Double peaks are observed in every case. Surprisingly, simulations run with 10°-splay produce considerably higher J_c value at $\theta = 0°$ compared with simulations using 0°-splay. At 0°-splay, high intensity double *c*-axis peak is observed with maxima at angles $\theta = \pm 20°$. The reason for observing peak maxima at 20° instead of 0° is that at this angle the vortices are optimally oriented in such a way that, (i) the nanorods pinning force still overcomes the magnetic force thus aligning the vortices along the nanorods and pinning them strongly and, (ii) the nanorods are splayed just enough so that they are more likely to come across a pinning center and even get simultaneously entangled into several different nanorods. So, in conclusiion, at lower angles than the angle where the peak maxima occurs, the nanorods are more strongly pinned, but the probability of a vortex coming across a pinning site is much lower. At higher angles than this, the vortices have high probability to come across a pinning site, but the

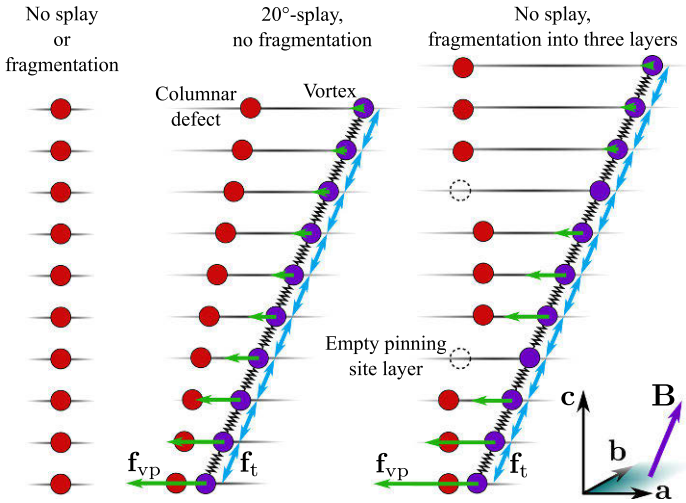

Figure 7. Examples of columnar pinning site models and vortices attracted to them, patterns typically used in the MD simulation of $J_c(\theta)$ for tilted and fragmented columnar pinning sites. On the left, the simplest case is illustrated where no splay or fragmentation takes place. In the middle, a solid columnar pinning site is tilted 20° from YBCOs *c*-axis shown in the diagram. On the right, no splay takes place but the pinning site is fragmented into three fragment layers with a layer free of pinning sites between them. Such fragment layers were positioned randomly, independent of each other. Notice that in order to keep the thicknesses of the fragmented layers constant, the number of pinning site particles may vary by ± 1 as the nanorods are fragmented, shown schematically above. The pinning force $\mathbf{f}_{vp}$, vortex line tension $\mathbf{f}_t$ and vortex line tension experienced by every vortex particle are also presented.

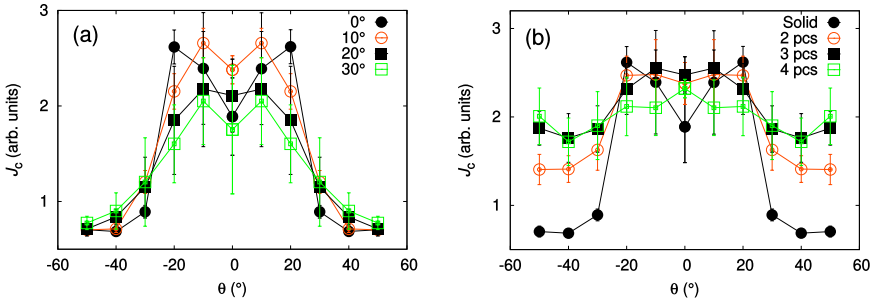

Figure 8. Simulated $J_c(\theta)$ curves for solid nanorods with 0°, 10°, 20° and 30° of splay (**a**) and 0°-splayed nanorods fragmented into 1, 2, 3 and 4 pieces (**b**), as explained in Fig. 7. The absolute values between (**a**,**b**) are comparable with each other.

magnetic force overcomes the pinning force and the vortices get only partly pinned thus weakening the total pinning force significantly. This same effect is also behind other observed double peak structures for other simulated *c*-peaks. The $J_c(\theta)$-curves simulated using different nanorod fragmentation is presented in Fig. 8b. Fragmentation of nanorods clearly widens the *c*-axis peak. A double peak is observed only for unfragmented simulation due to volume maximizing effect presented before. A random positioning of nanorod fragments into their independent layers destroys the double peak as the vortices can easily bend between these fragmentation layers. The intensity of the *c*-axis peak also remains approximately constant until nanorods are fragmented into four pieces. In general, the fragmentation of nanorods into several pieces seems to result in the increased isotropy of the $J_c(\theta)$-curves.

In order to mimic the measured properties of μ-YBCO + BZO and n-YBCO + BZO films, the simulations with both splay and fragmentation were also carried out. The n-YBCO + BZO sample was modelled with solid 20 particle long columnar pinning sites randomly splayed in 10° angle, as measured by TEM. The μ-YBCO + BZO, on the other hand, was modelled with columnar pinning sites that were fragmented into four pieces and using an average splay angle of 22.5°. Figure 9 shows how the *c*-axis peak measured in 4 T and at 40 K fits to the simulated data relatively good. At angles $\theta < \pm 30°$, both simulations reproduce the measured shapes of the peaks indicating

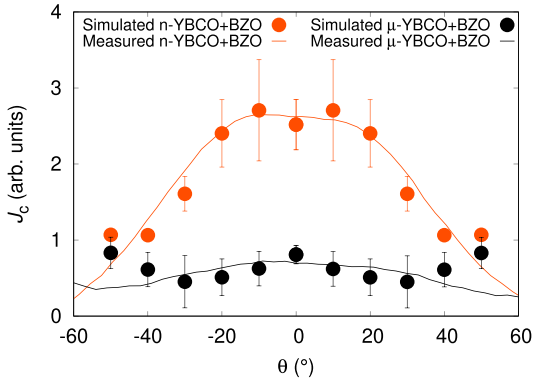

Figure 9. Simulated $J_c(\theta)$ data together with the experimentally determined $J_c(\theta)$ curves for μ-YBCO + BZO and n-YBCO + BZO films measured in 4 T at 40 K.

such a difference in BZO growth within the n-YBCO and μ-YBCO matrices as stated before in the schematic diagram of Fig. 5. However, the experimental data deviates from simulated $J_c(\theta)$ values at angles $\theta > \pm 30°$ due to overly simplified simulation model, where the tilting angles of nanorods and lengths of the fragments are kept constant. Especially, the constant height fragment layers, that are separated by constant distance, create additional symmetry to the system which is definitely not present in reality. The presence of such symmetry might have nebulous effects to the simulated $J_c(\theta)$-curves which indeed can be the reason behind observed deviation between measured and simulated data. The effect of the anisotropy of the surrounding YBCO lattice, which is assumed ideal in the simulation model, should also be noted. As a conclusion, we have gained multiple lines of corroborating evidence that the splay and the fragmentation of the BZO nanorods are mainly responsible for the observed critical current and its anisotropy, at least around the YBCO *c*-axis.

Conclusion

In this work, a great variety of modern techniques in the fields of experimental and computational condensed matter physics were combined to systematically investigate the influence of growth mechanisms and defect formation, both natural and artificial, on the superconducting properties of undoped and BZO doped YBCO thin films. In particular, focus was given to differentiating and modeling how various types of nanosized structural defects can act as vortex pinning centers, enhancing the in-field critical current density and modifying its anisotropy. The results were qualitatively discussed in terms of existing theory, in addition to which the most critical defect types were successfully modeled by a quantitative MD simulation configured based on experimental transmission electron microscopy observations. Collecting the newly obtained critical current anisotropy data and all accessible structural properties of the superconductor materials under our focus, we were able to propose a schematic model that provides a basic framework for vortex pinning landscape engineering. This leads us further closer to the superconducting industrial applications required for the devices needed to be operated within wide temperature, angular and field ranges.

Methods

Target synthesis. Four ceramic YBCO samples were synthesized as precursors to the films studied in this work. The samples differ from each other by the average crystal grain size (being nano- or microcrystalline) or BZO doping (0% or 4% by mass), so that all combinations of the two parameters are manifested in the sample set. In the following text, we will prefix the grain size class and suffix the doping class to each sample identifier, so that μ-YBCO and n-YBCO refer to the undoped micro- and nanocrystalline samples, respectively, and μ-YBCO + BZO and n-YBCO + BZO to the corresponding doped samples. The microcrystalline samples μ-YBCO and μ-YBCO + BZO were manufactured in the form of sintered pellets by the standard solid state ceramic method[33]. We followed the recipe found in ref.[33]. for $YBa_2Cu_3O_7$ with the exception that the sintering temperature was lowered to 920 °C to avoid the observed melting of one of the reagents or intermediate products at the suggested temperature of 950 °C. The BZO doping was implemented simply by adding stoichiometric amounts of $BaCO_3$ and Y_2O_3-stabilized ZrO_2 to the YBCO precursor mix. Heating rates were kept at 100 °C/h and after each burn the furnace was simply switched off to allow passive air cooling back to room temperature. X-ray diffractometry (XRD) and Rietveld refinement showed the samples to be ≥99% phase pure, with crystallite sizes in the order of micrometers (too large for reliable analysis using the Scherrer formula[34]). The relative densities of μ-YBCO and μ-YBCO + BZO were 76% and 80%, respectively, based on mechanical measurements. The citric acid combustion variant of the sol-gel method[35] was used to synthesize the nanocrystalline pellet samples n-YBCO and n-YBCO + BZO. The details of the process have been described in our earlier publications[36,37]. The relative densities of n-YBCO and n-YBCO + BZO in the final pelletized form were 86% and 75%, respectively, and the grain sizes of both were ca. 60 nm based on the Scherrer formula[34]. XRD and Rietveld analysis showed no impurity phases, again indicating purities of ≥99%.

Thin films fabrication. The undoped and BZO doped YBCO films were prepared by pulsed laser deposition (PLD) on (100) $SrTiO_3$ (STO) substrates using a 308 nm XeCl excimer laser with a pulse duration of 25 ns and a repetition rate of 5 Hz with a laser fluence of 1.3 Jcm^{-2}. The flowing oxygen pressure in the chamber was 0.2 torr and the substrate temperature during the deposition was 750 °C. To get the optimized properties of the films, *in situ* post-annealing treatments were carried out at the annealing temperature $T_a = 725$ °C in atmospheric pressure oxygen with heating and cooling rates of 25°/min.

Structural characterization. The crystallographic properties of the films were determined by x-ray diffraction (XRD) measurements with a Philips X'Pert Pro MPD system (Cu K_α radiation). To determine the phase purity of the films, (θ, 2θ) scans in the (00l) direction were made. The lattice parameters were determined from detailed 2D (ϕ, 2θ) texture scans of the YBCO (212)/(122) peaks using 2D Levenberg–Marquardt fitting[38] of Gaussian peaks. The out-of-plane crystallographic texture was determined by XRD rocking curves (RC) of the YBCO (005) peaks (ω scans). The oxygen stoichiometries of the films were estimated from the intensity ratios of the (005)/(007) peaks[39,40]. The correlation length of the lattice was determined from the rocking curve of a (005) peak as $r_c = c/(\pi l \Delta\omega)$, where c is the longest lattice parameter of YBCO and l is the order of the Bragg reflection[41]. The microstrain in c direction was determined with the Williamson–Hall method[41]. The FWHM of the (00l) peaks was used to determine the microstrain, ε_{WH}, which in this case describes the variation of the c parameter throughout the whole film thickness.

Surface microstructure and TEM measurements. The surface microstructure and the thickness of the films ≈260 nm for undoped and ≈240 nm for BZO doped films, respectively, were performed on a Bruker Innova AFM. Bright-field transmission electron microscopy (BF-TEM) was performed using a Cs-corrected JEOL JEM 2200FS instrument, operated at 200 kV. Samples for BF-TEM were prepared by cutting a cross-sectional lamella via the Focused Ion Beam (FIB) technique in a FEI Nova 600 Nanolab Dual Beam FIB-SEM. The lamella were extracted using the *in situ* lift out procedure with an Omniprobe extraction needle[42].

VEPAS measurements. VEPAS measurements have been conducted at the apparatus for *in situ* defect analysis (AIDA)[15] of the slow positron beamline (SPONSOR)[14]. Positrons have been implanted into a sample with discrete kinetic energies E in the range between 0.05 and 35 keV, which allows for depth profiling from the surface down to a few micrometers. A mean positron implantation depth can be approximated by a simple material density dependent formula: $z_{mean} = 5.71 \times E^{1.62}$. Implanted into a solid positrons lose their kinetic energy due to thermalization and after a short diffusion annihilate at delocalized lattice sites or localize in the vacancy like defects and interfaces, usually emitting two anti-collinear 511 keV gamma photons once they meet electrons. Since at the annihilation site thermalized positrons have very small momenta compared to the electrons, a broadening of the 511 keV line is observed mostly due to momentum of the electrons, which is measured with one or two high-purity Ge detectors (energy resolution of of 1.09 ± 0.01 keV at 511 keV). This broadening is characterized by two distinct parameters S and W defined as a fraction of the annihilation line in the middle (511 ± 0.93 keV) and outer regions (508.56 ± 0.35 keV and 513.44 ± 0.35 keV), respectively. The S parameter is a fraction of positrons annihilating with low momentum valence electrons and represents vacancy type defects and their concentration. The W parameter approximates overlap of positron wavefunction with high momentum core electrons. Plotting calculated S as a function of positron implantation energy, $S(E)$, provides depth dependent information, whereas S–W plots are used to examine atomic surrounding of the defect site and its size (type)[43].

Magnetic and transport measurements. Magnetic measurements were made with a Quantum Design physical property measurement (PPMS) system, and the onset critical temperatures, T_c, were determined with ac magnetization measurements in the range of 10–100 K (in ac field of 0.1 mT). The critical current densities, J_c, at 10 K were determined from the hysteresis loops using the Bean model for rectangular films: $Jc = 2\Delta m/[a(1 - a/3b)V]$, where a and b ($b \geq a$) are the width and the length of the sample, V is the sample volume and Δm is the opening of the hysteresis loop[44]. The transport properties of all the films were measured using the horizontal rotator option available for the PPMS. The measurements were done at magnetic fields of 0.5 T, 1 T, 2 T, 4 T, 6 T and 8 T and temperatures at 10 K, 40 K and 77 K with 0° to 360° angular range using 3° of steps. For this purpose, all the films were patterned by wet chemical etching. The etched patterns were 50 μm wide current stripes on each film. The contacts on the films were made by aluminium wire using a TPT HB05 Wire Bonder and without any metal contact pad in-between the bond and surface of YBCO. Based on our earlier studies and on the measurements in this work, the magnetic field dependencies of J_c as well as the shape of the angular dependence of J_c are similar at different measurement temperatures below ≈70 K[10,45]. Although the measurements were carried out in a rather wide temperature range, we decided to concentrate the analysis on measurements at 40 K, which is far enough from T_c and, on the other hand, meets the temperature requirements for power technology applications[1].

MD simulations. The angular dependent MD simulations were used to reproduce the shape of $J_c(\theta)$ around the $B||c$ of YBCO, by simulating the vortices in the superconducting thin films when different kinds of artificially produced pinning centers are available in the YBCO matrix. The details of the MD simulations are presented elsewhere[18].

Received: 11 April 2019; Accepted: 10 October 2019;
Published online: 28 October 2019

References

1. Larbalestier, D., Gurevich, A., Feldmann, D. M. & Polyanskii, A. High-Tc superconducting materials for electric power applications. *Nat.* **414**, 368–377 (2001).
2. MacManus-Driscoll, J. L. *et al*. Strongly enhanced current densities in superconducting coated conductors of $YBa_2Cu_3O_{7-x}$+$BaZrO_3$. *Nat. Mater.* **3**, 439–443 (2004).
3. Yamada, H. *et al*. Flux pinning properties of c-axis correlated pinning centres in PLD-YBCO films. *Supercond. Sci. Technol.* **17**, S25–S29 (2004).
4. Foltyn, S. R. *et al*. Materials science challenges for high-temperature superconducting wire. *Nat. Mater.* **6**, 631–642 (2007).
5. Wee, S. H., Zuev, Y. L., Cantoni, C. & Goyal, A. Engineering nanocolumnar defect configurations for optimized vortex pinning in high temperature superconducting nanocomposite wires. *Sci. Rep.* **3**, 23101–9 (2013).
6. Obradors, X. & Puig, T. Coated conductors for power applications: materials challenges. *Supercond. Sci. Technol.* **27**(044003), 1–17 (2014).
7. Pan, V. *et al*. Supercurrent transport in $YBa_2Cu_3O_{7-d}$ epitaxial thin films in a dc magnetic field. *Phys. Rev. B* **73**, 054508 (2006).
8. Golovchanskiy, I. A., Pan, A. V., Shcherbakova, O. V., Fedoseev, S. A. & Dou, S. X. An all-field-range description of the critical current density in superconducting YBCO films. *Supercond. Sci. Technol.* **24**, 105020 (2011).
9. Golovchanskiy, I. A., Pan, A. V., Shcherbakova, O. V. & Fedoseev, S. A. Rectifying differences in transport, dynamic, and quasi-equilibrium measurements of critical current density. *J. Appl. Phys.* **114**, 163910 (2013).
10. Paturi, P., Irjala, M., Huhtinen, H. & Abrahamsen, A. B. Modeling flux pinning in thin undoped and $BaZrO_3$-doped YBCO films. *J. Appl. Phys.* **105**, 023904 (2009).
11. Huhtinen, H., Järvinen, J., Laiho, R., Paturi, P. & Raittila, J. Laser deposition from a nanostructured YBaCuO target: Analysis of the plume and growth kinetics of particles on $SrTiO_3$. *J. Appl. Phys.* **90**, 1521–1528 (2001).
12. Maiorov, B. *et al*. Synergetic combination of different types of defect to optimize pinning landscape using $BaZrO_3$-doped $YBa_2Cu_3O_7$. *Nat. Mater.* **8**, 398–404 (2009).
13. Matsumoto, K. & Mele, P. Artificial pinning center technology to enhance vortex pinning in YBCO coated conductors. *Supercond. Sci. Technol.* **23**(014001), 1–12 (2010).
14. Anwand, W., Brauer, G., Butterling, M., Kissener, H. R. & Wagner, A. Design and construction of a slow positron beam for solid and surface investigations. *Defect Diffus. Forum* **331**, 25–40 (2012).
15. Liedke, M. O. *et al*. Open volume defects and magnetic phase transition in Fe60Al40 transition metal aluminide. *J. Appl. Phys.* **117**, 163908 (2015).
16. Long, N. J. Model for the angular dependence of critical currents in technical superconductors. *Supercond. Sci. Technol.* **21**(025007), 1–8 (2008).
17. Wimbush, S. & Long, N. The interpretation of the field angle dependence of the critical current in defect-engineered superconductors. *New J. Phys.* **14**(083017), 1–24 (2012).
18. Paturi, P., Malmivirta, M., Hynninen, T. & Huhtinen, H. Angle dependent molecular dynamics simulation of flux pinning in YBCO superconductors with artificial pinning sites. *J. Phys. Cond. Mat.* **30**(315902), 1–7 (2018).
19. Hylton, T. L. & Beasley, M. R. Flux-pinning mechanism in thin films of YBCO. *Phys. Rev. B* **41**, 11669 (1990).
20. Dam, B., Huijbregtse, J. M. & Rector, J. H. Strong pinning linear defects formed at the coherent growth transition of pulsed-laser-deposited $YBa_2Cu_3O_{7-d}$ films. *Phys. Rev. B* **65**, 064528 (2002).
21. Wu, J. & Shi, J. Inetractive modeling-synthesis-characterization approach towards controllable *in situ* self-assembly of artificial pinning centers in RE-123 films. *Supercond. Sci. Technol.* **30**, 103002 (2017).
22. Malik, V. K. *et al*. Pulsed laser deposition growth of heteroepitaxial $YBa_2Cu_3O_7/La_{0.67}Ca_{0.33}MnO_3$ superlattices on $NdGaO_3$ and $Sr_{0.7}La_{0.3}Al_{0.65}Ta_{0.35}O_3$ substrates. *Phys. Rev. B* **85**, 054514 (2012).
23. Tuomisto, F. & Makkonen, I. Defect identification in semiconductors with positron annihilation: Experiment and theory. *Rev. Mod. Phys.* **85**, 1583 (2013).
24. van Veen, A. *et al*. VEPFIT applied to depth profiling problems. *Appl. Surf. Sci.* **85**, 216 (1995).
25. Peurla, M., Huhtinen, H., Tse, Y. Y., Raittila, J. & Paturi, P. Structural properties of YBCO thin films deposited from different kinds of targets. *IEEE T. Appl. Supercond.* **17**, 3608–3611 (2007).
26. Paturi, P. The vortex path model and angular dependence of Jc in thin YBCO films deposited from undoped and $BaZrO_3$-doped targets. *Supercond. Sci. Technol.* **23**(025030), 1–7 (2010).
27. Malmivirta, M. *et al*. Enhanced flux pinning in YBCO multilayer films with BCO nanodots and segmented BZO nanorods. *Sci. Reports* **7**, 14682 (2017).
28. Malmivirta, M. *et al*. Three ranges of the angular dependence of cirtical current of $BaZrO_3$ doped $YBa_2Cu_3O_{7-d}$ thin films grown at different temperatures. *Thin Solid Films* **562**, 554–560 (2014).
29. Pysarenko, S. V., Pan, A. V. & Dou, S. X. Origin of surface morphology variation during pulsed laser deposition of YBCO superconducting films. *IEEE T. Appl. Supercond.* **21**, 3179 (2011).
30. Chrisey, D. B. & Hubler, G. K. *Pulsed Laser Deposition of Thin Films* (John Wiley Sons Inc., 1994).
31. Civale, L. *et al*. Angular-dependent vortex pinning mechanisms in $YBa_2Cu_3O_7$ coated conductors and thin films. *Appl. Phys. Lett.* **84**, 2121–2123 (2004).
32. Wang, X. *et al*. Eliminating thickness dependence of critical current density in $YBa_2Cu_3O_{7-x}$ films with aligned $BaZrO_3$ nanorods. *J. Appl. Phys.* **108**, 113911 (2010).
33. Rao, C. N. R., Nagarajan, R. & Vijayaraghavan, R. Synthesis of cuprate superconductors. *Supercond. Sci. Technol.* **6**, 1–22 (1993).
34. Patterson, A. The scherrer formula for x-ray particle size determination. *Phys. Rev.* **56**, 978 (1939).
35. Kakihana, M. "sol-gel" preparation of high temperature superconducting oxides. *J. Sol-Gel Sci. Technol.* **6**, 7 (1996).
36. Raittila, J., Huhtinen, H., Paturi, P. & Stepanov, Y. P. Preparation of superconducting $YBa_2Cu_3O_{7-d}$ nanopowder by deoxydation in Ar before final oxygenation. *Phys. C* **371**, 90–96 (2002).
37. Paturi, P., Schlesier, K. & Huhtinen, H. Effect of target density on YBCO thin films deposited from nanograined targets. *Phys. C* **469**, 839 (2009).
38. Press, W. H., Flannery, B. P., Teukolsky, S. A. & Vetterling, W. T. *Numerical Recipes in C: The Art of Scientific Computing* (Cambridge University Press, 1990).
39. Ye, J. & Nakamura, K. Quantitative structure analyses of YBCO thin films: Determination of oxygen content from x-ray-diffraction patterns. *Phys. Rev. B* **48**, 7554–7564 (1993).
40. Ye, J. & Nakamura, K. Systematic study of the growth-temperature dependence of structural disorder and superconductivity in $YBa_2Cu_3O_{7-d}$ thin films. *Phys. Rev. B* **50**, 7099–7106 (1994).
41. Birkholz, M. *Thin Film Analysis by X-ray Scattering* (Wiley-VCH, 2006).
42. Rijckaert, H. *et al*. Optimizing nanocomposites through nanocrystal surface chemistry: Superconducting ybco thin films via low fluorine metal organic deposition and preformed metal oxide nanocrystals. Chem. *materials* **29**, 6104–6113 (2017).
43. Clement, M., de Nijs, J. M. M., Balk, P., Schut, H. & van Veen, A. Analysis of positron beam data by the combined use of the shape and wing parameters. *J. Appl. Phys.* **79**, 9029–9036 (1996).
44. Wiesinger, H. P., Sauerzopf, F. M. & Weber, H. W. On the calculation of Jc from magnetization measurements on superconductors. *Phys. C* **203**, 121–128 (1992).
45. Paturi, P., Irjala, M., Abrahamsen, A. B. & Huhtinen, H. Defining B_c, B^* and B_ϕ for YBCO thin films. *IEEE T. Appl. Supercond.* **19**, 3431–3434 (2009).

Acknowledgements
The authors wish to thank the Jenny and Antti Wihuri Foundation, Finland, for financial support. M.Z.K. and E.R. are thankful to University of Turku Graduate School (UTUGS) for general resources. M.Z.K. acknowledges funding from Finnish Cultural Foundation. Finally, the computer resources of the FGCI project (Finland) are greatly acknowledged.

Author contributions
M.Z.K., H.H. and P.P. conceived and designed the project. M.Z.K. deposited all the films, performed XRD, magnetic, surface microstructure, wet chemical etching and angular dependent measurements and also prepared the manuscript. E.R. carried out the simulations and also wrote the simulations part, M.M. coded the simulations program, J.T. synthesized the targets and proposed the PLD growth model. H.R. and I.V.D. carried out the TEM measurements and analyzed their results. M.O.L., M.B. and A.W. performed the VEPAS measurements and did their analysis. All the authors discussed the results and commented on the manuscript.

Competing interests
The authors declare no competing interests.

Additional information
Supplementary information is available for this paper at https://doi.org/10.1038/s41598-019-51978-0.

Correspondence and requests for materials should be addressed to M.Z.K.

Reprints and permissions information is available at www.nature.com/reprints.

Publisher's note Springer Nature remains neutral with regard to jurisdictional claims in published maps and institutional affiliations.

Supplementary Information: Enhanced flux pinning isotropy by tuned nanosized defect network in superconducting $YBa_2Cu_3O_{6+x}$ films

Mukarram Zaman Khan[1,2,*], Elmeri Rivasto[1,2], Jussi Tikkanen[1], Hannes Rijckaert[3], Mika Malmivirta[1], Maciej Oskar Liedke[4], Maik Butterling[4], Andreas Wagner[4], Hannu Huhtinen[1], Isabel Van Driessche[3], and Petriina Paturi[1]

[1]Wihuri Physical Laboratory, Department of Physics and Astronomy, University of Turku, FI-20014 Turku, Finland
[2]University of Turku Graduate School (UTUGS), University of Turku, FI-20014 Turku, Finland
[3]SCRiPTS, Department of Chemistry, Ghent University, Krijgslaan 281 S3, 9000 Ghent, Belgium
[4]Institute of Radiation Physics, Helmholtz-Zentrum Dresden - Rossendorf, Bautzner Landstraße 400, 01328 Dresden, Germany
[*]mukarram.z.khan@utu.fi

Detailed TEM analysis

For making the comprehensive comprasions of the as induced natural and artificial defects in all the films, the TEM images with the resolutions of 20 nm are also presented in Fig. S1. These images are well in line to those in Fig. 1.

Scanning transmission electron microscopy (STEM) was utilized to compare the stacking faults within the undoped n-YBCO and μ-YBCO as presented in Fig. S2. In relation to Fig. 1 in the main manuscript, it can be seen here also (at the resolution level of 100 nm) that the stacking faults are longer in n-YBCO as compared to μ-YBCO where they are observed to be shorter and randomly distributed within the entire film. Moreover, BF-TEM images presented in Fig. S3 clearly reveal the presence of twin boundaries within the undoped n-YBCO and μ-YBCO films.

Crystallographical properties

The 2θ X-ray diffractograms seen in Fig. S4 reflect the good chemical purity and desired growth orientation of the YBCO films. Only YBCO $(00l)$, STO $(h00)$ and, in the samples doped with $BaZrO_3$ (BZO), BZO (200) reflections are observed, i.e. YBCO has grown epitaxially, with its crystallographic *c*-axis normal to the STO substrate as expected, and no impurity phases need to be considered to explain the data. The BZO dopant also shows cube-on-cube orientation alongside the YBCO matrix, an expected feature due to the self-assembled columnar growth mode of BZO in this system[S1]. Granted, the only visible Bragg reflection (200) is among the most intense ones of BZO, but in the powdered sample approximation an even stronger (by a factor of ~ 3) (110) reflection should be visible at $2\theta = 30.08^\circ$ in superposition with YBCO (004), something our relative intensity measurements on the YBCO (400) and (500) reflections (see Table S1) rule out. This favours the topotaxial growth interpretation.

The detailed 2θ–ϕ scans of the YBCO peak group $(212)/(122)$ shown in Fig. S5 give a graphical comparison of the crystal quality between the four film samples. Biaxial twinning, with a/b twin boundaries running along $[110]$ and $[1\bar{1}0]$, is evident in all films, though an increased *ab*-plane splay in the BZO-doped ones somewhat obscures the twin structure. The n-films originating from nanocrystalline PLD targets both show slightly better peak definition than their "μ" counterparts (even disregarding the fact that the μ-YBCO film was accidentally attached to the sample holder at a slight tilt, leading to an artificial correlation between 2θ and ϕ), indicating the crystal structure is coherent over longer distances in the n-films.

That the YBCO crystal structure is more homogeneous in the n-films is corroborated by the findings on the YBCO (005) reflection presented in Table S1. In particular, the FWHM ω values show that n-YBCO has by far the best *c*-axis orientation among the films, whereas n-YBCO+BZO beats μ-YBCO+BZO by a relatively smaller margin in this sense. The FWHM 2θ values reflect a known difference in how the BZO-doped and undoped films handle the elastic stress from the substrate interface: the doped films develop low angle grain boundaries in the *ab*-plane, nucleating these defects at the BZO impurities, whereas the undoped films prefer clean biaxial twinning and also retain a higher inhomogeneous strain (ε_{WH} in Table S1), as determined by Williamson-Hall (WH) plots[S2,S3]. The addition of BZO also seems to reduce the orthorhombicity of YBCO, suggesting that BZO works as a mild reductant in the system and lowers the oxygen content of YBCO when other synthesis parameters are kept constant[S4].

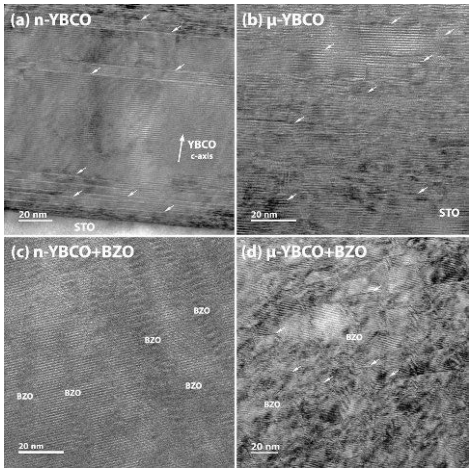

Figure S1. TEM images (20 nm resolution) of the all the films deposited from targets with varying grain sizes (a)−(d). Stacking faults are marked by the bright vectors, whereas the nanorods induced in the doped films are labelled as BZO.

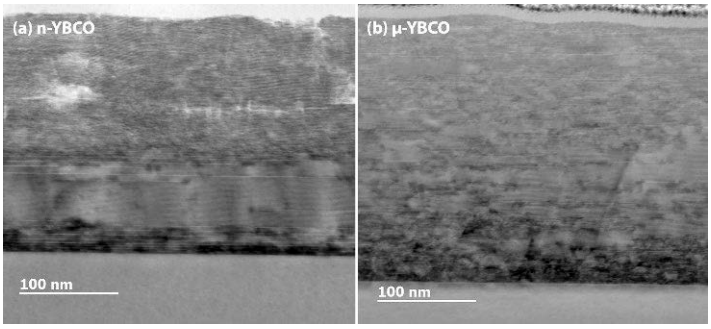

Figure S2. STEM images depicting the comparison of stacking faults with respect to their density and sizes for undoped n-YBCO and μ-YBCO films (a)−(b).

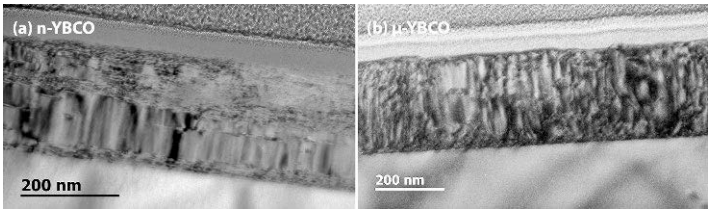

Figure S3. BF-TEM images, displaying the presence of twin boundaries, and taken with a diffraction vector **g** = (100) of undoped n-YBCO and μ-YBCO films (a)−(b).

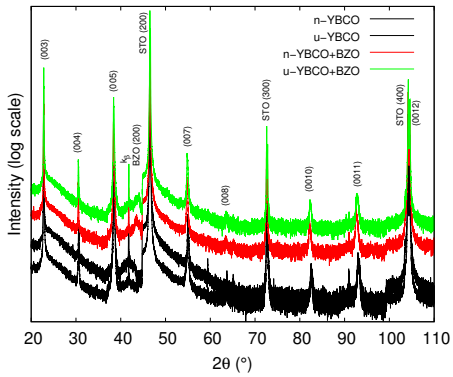

Figure S4. The room temperature X-ray 2θ diffractograms of the undoped and BZO doped YBCO films deposited from nanocrystalline and microcrystalline targets.

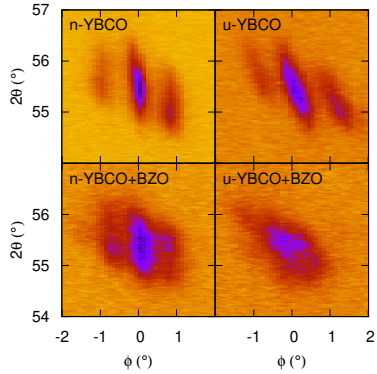

Figure S5. XRD (212)/(122) peaks as a function of 2θ and relative ϕ with normalized intensities for undoped and BZO-doped YBCO films deposited using nanocrystalline and microcrystalline targets.

Table S1. Structural parameters determined from XRD measurements for undoped and BZO doped YBCO films deposited from different kinds of targets.

Samples	YBCO lattice			Orthorhombicity	ε_{WH}	FWHM 2θ	FWHM ϕ	FWHM ω	r_c
	a (Å)	b (Å)	c (Å)	(%)	(%)	(005) (°)	(102) (°)	(005) (°)	(nm)
n-YBCO	3.831	3.897	11.685	1.710	0.013	0.17	1.30	0.21	19.7
μ-YBCO	3.826	3.893	11.678	1.723	0.008	0.14	1.37	0.29	14.3
n-YBCO+BZO	3.843	3.879	11.722	0.949	0.008	0.11	1.59	0.28	14.8
μ-YBCO+BZO	3.851	3.887	11.716	0.934	0.011	0.13	1.11	0.32	13.1

Surface microstructure

As can be seen from the $2 \times 2\,\mu m^2$ AFM images in Fig. S6, the average in-plane surface particle diameter of ≈ 180 nm for the undoped n-YBCO film is clearly smaller than that of ≈ 300 nm for the undoped μ-YBCO film. The higher out-of-plane scale bar in μ-YBCO film also indicates larger growth islands and thus rougher surface, which is confirmed by the root-mean-square roughness values of 3.3 nm for n-YBCO and 4.8 nm for μ-YBCO film, respectively. To further investigate the film growth and thus the epitaxial crystallization of the YBCO film on STO substrate, we applied only fifteen pulses with the normal laser fluence in the PLD process and studied the grouping and nucleation of three dimensional clusters on a substrate in both undoped n-YBCO and μ-YBCO cases. Although the threshold energy for depositing single YBCO particles at the normal deposition distance between the target and the substrate has been observed to be clearly smaller for n-YBCO than for μ-YBCO targets[S5,S6], we could not find a difference in fragment size at the beginning of the growth process when the nucleation of the particles had already started on the surface of the heated substrate. The in-plane fragment size for both targets was on average $120 - 200$ nm, which is roughly the same as the island size in the finished n-YBCO film but only half of that in μ-YBCO film.

Magnetic properties

The normalized magnetizations of all four samples are shown as functions of temperature in the main panel of Fig. S7. It can be seen that in undoped YBCO films T_c is on average 5 K higher than that of BZO doped films. However, the films prepared from nanocrystalline target have approximately 1 K higher T_c although the transitions are slightly broader than in films grown from microcrystalline targets. This is in line with VEPAS measurements, where a greater number of vacancy-type defects, for example oxygen vacancy complexes, have been observed. The J_c curves measured at 10 K and calculated using the Bean model[S7] for all undoped and BZO doped YBCO films are shown in the inset of Fig. S7. In terms of vortex pinning, two completely different $J_c(B)$ curve shapes can be observed in undoped and BZO doped YBCO films. First of all, the low field J_c is clearly higher in undoped YBCO films. This can be understood by the volume of BZO rods as well as by the distorted YBCO with lower T_c around the rods that decreases the amount of superconducting material in doped films[S8]. In undoped YBCO films,

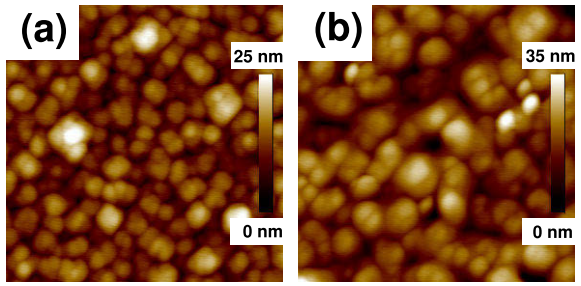

Figure S6. AFM images of the undoped n-YBCO (a) and undoped μ-YBCO (b) films. The scan sizes of the images are $2 \times 2\ \mu m^2$ and the values of the height scale bars are given in subfigures.

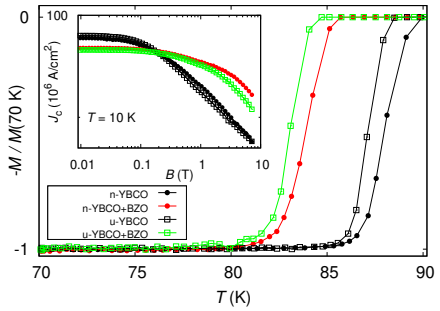

Figure S7. The normalized ac magnetizations as functions of temperature (main panel) and the magnetic field dependencies of J_c determined from the hysteresis loops at 10 K (inset) for undoped and BZO doped YBCO films deposited using nanocrystalline and microcrystalline targets.

the J_c clearly starts to drop below 100 mT while in BZO doped films, before reduction, a longer constant value in J_c curve can be observed. The upper limit of low-field plateau of J_c(B) calculated by criterion $J_c(B)/J_c(0) = 0.9$ is called as accomodation field B^*[S9]. Since the single vortex pinning is important below the B^* and above B^* the collective pinning dominates[S10], we can conclude that the clearly higher J_c above 500 mT is related to columnar network of BZO nanorods formed in the YBCO matrix. In addition to the high density of pinning sites, the characteristic round shape of the J_c curve in BZO doped YBCO is based on the large size of pinning centers. This has been observed to increase the depth of the pinning potential, number of pinned vortices per rod and to suppress the long-range ordering of the vortex lattice[S11]. It is also noteworthy that in both undoped and BZO doped cases, the n-YBCO films have slightly higher J_c above 200 mT when compared with μ-YBCO films, indicating more anisotropic pinning centers and thus the better in-field performance in films grown from nanocrystalline targets.

MD simulations

The MD-simulations, mainly the forces experienced by the vortices in different pinning site configurations as well as the splay and the fragmentation of columnar pinning centers, are implemented as follows. The force between a vortex and pinning site particle depends on the radius of the pinning site, chosen to be 4 nm, which corresponds to measured values presented above. The only force acting across layers is the spring-like line tension force between two vortex particles in adjacent layers, which keeps the vortices structured. Other forces applied in the simulation are the repulsion force between vortices, a drag force, the Lorentz force caused by a current through the sample and an angle dependent magnetic force that acts to align the vortex particles parallel to the external magnetic field. The value of the critical current was solved iteratively by the bisection method where the current was adjusted until certain vortex stability requirements were fulfilled. All the simulations were run on five randomly generated pinning site configurations corresponding to certain splay or fragmentation of the pinning sites

and the external magnetic field was varied between the angles of -50° and 50°, with 10° steps. In every simulation, we used a computationally efficient 200 × 200 unit sized grid with 32 randomly generated columnar pinning sites that had the minimum distance of 26 units from each another. The simulations were run with 14 vortices, corresponding to a magnetic field of 0.75 T. The final $J_c(\theta)$ was determined by the average value of the results of these individual simulations corresponding to the absolute values of a certain angle as well as the standard deviation that is used as an error limit.

The effect of the splay of the columnar pinning sites on the angular dependency of J_c was studied by creating 20-particles-long solid rows of pinning site particles and tilting them to 0°, 10°, 20° and 30° angles. The locations and orientations of the tilted pinning sites were randomly generated. The effect of fragmentation was studied by creating 0°-splay pinning sites that were cut into two, three and four pieces respectively, separated by one completely pinning site particle free layer. The number of particles representing a single pinning site was kept as close to 20 as possible, resulting in 20, 10+10=20, 7+7+7=21 and 5+5+5+5=20 particles per single pinning site, corresponding fragmentation into one, two, three and four pieces, respectively. Pinning site fragments in a single fragment layer, that is fragments confined between layers free of pinning site particles, were randomly positioned into their corresponding layers. Due to empty layers between the fragments, the number of used layers and length of the vortices increased as a number of fragments resulting at worst for three extra layers and vortex particles per vortex. The effect of these extra layers or one extra pinning site particle to $J_c(\theta)$ can be assumed to be negligible, which allows us to compare obtained $J_c(\theta)$ curves between different fragmentations.

References

S1. Baca, F. J. *et al.* Interactive growth effects of rare-earth nanoparticles on nanorod formation in $YBa_2Cu_3O_x$ thin films. *Adv. Funct. Mater.* **23**, 4826–4831 (2013).

S2. Zak, A. K., Majid, W. A., Abrishami, M. & Yousefi, R. X-ray analysis of ZnO nanoparticles by williamson–hall and size–strain plot methods. *Solid State Sci.* **13**, 251 (2011).

S3. Mele, P. *et al.* Ultra-high flux pinning properties of $BaMO_3$-doped $YBa_2Cu_3O_{7-x}$thin films (m = zr, sn). *Supercond. Sci. Technol.* **21**, 032002 (2008).

S4. Farneth, W., Bordia, R., McCarron, E., Crawford, M. & Flippen, R. Influence of oxygen stoichiometry on the structure and superconducting transition temperature of $YBa_2Cu_3O_x$. *Solid State Commun.* **66**, 953 (1988).

S5. Huhtinen, H., Laiho, R. & Paturi, P. Superconductivity in low-dimensional structures. *Phys. Low-Dimensional Struct.* **11/12**, 93 (1998).

S6. Huhtinen, H., Järvinen, J., Laiho, R., Paturi, P. & Raittila, J. Laser deposition from a nanostructured YBaCuO target: Analysis of the plume and growth kinetics of particles on $SrTiO_3$. *J. Appl. Phys.* **90**, 1521–1528 (2001).

S7. Wiesinger, H. P., Sauerzopf, F. M. & Weber, H. W. On the calculation of J_c from magnetization measurements on superconductors. *Phys. C* **203**, 121–128 (1992).

S8. Peurla, M., Huhtinen, H., Tse, Y. Y., Raittila, J. & Paturi, P. Structural properties of YBCO thin films deposited from different kinds of targets. *IEEE T. Appl. Supercond.* **17**, 3608–3611 (2007).

S9. Cai, C., Holzapfel, B., Hänisch, J., Fernandez, L. & Schultz, L. Magnetotransport and flux pinning characterictics in RBaCuO (R=Gd,Eu,Nd) and $(Gd_{1/3}Eu_{1/3}Nd_{1/3})$BaCuO high-$T_c$ superconducting thin films on $SrTiO_3$. *Phys. Rev. B* **69**, 104531 (2004).

S10. Krusin-Elbaum, L., Civale, L., Thompson, J. R. & Feild, C. Accommodation of vortices to columnar defects: Evidence for large entropic reduction of vortex localization. *Phys. Rev. B* **53**, 11744 (1996).

S11. Palonen, H., Jäykkä, J. & Paturi, P. Modeling reduced field dependence of critical current density in $YBa_2Cu_3O_{6+x}$ films with nanorods. *Phys. Rev. B* **85**, 024510 (2012).

M. Z. Khan & E. Rivasto & H. Rijckaert & M. O. Liedke & Y. Zhao & M. Butterling & A. Wagner & I. Van Driessche & H. Huhtinen & P. Paturi

Strongly enhanced critical current densities in YBCO superconductor on buffered metal for coated conductor applications

VI

Submitted to ACS Applied Electronic Materials

Strongly enhanced critical current densities in YBCO superconductor on buffered metal for coated conductor applications

Mukarram Zaman Khan[1,2,*], Elmeri Rivasto[1,2,*], Hannes Rijckaert[3], Maciej Oskar Liedke[5], Yue Zhao[4], Maik Butterling[5], Andreas Wagner[5], Isabel Van Driessche[3], Hannu Huhtinen[1], and Petriina Paturi[1]

[1] *Wihuri Physical Laboratory, Department of Physics and Astronomy, University of Turku, 20014 Turku, Finland*
[2] *University of Turku Graduate School (UTUGS), Univeristy of Turku, 20014 Turku, Finland*
[3] *SCRiPTS, Department of Chemistry, Ghent University, Krijgslaan 281 S3, 9000 Ghent, Belgium*
[4] *School of Electronic Information and Electrical Engineering, Shanghai Jiao Tong University, 200240 Shanghai, People's Republic of China*
[5] *Institute of Radiation Physics, Helmholtz-Zentrum Dresden - Rossendorf, Bautzner Landstraße 400, 01328, Dresden, Germany*
[*] *Correspondence: mukarram.z.khan@utu.fi; elmeri.o.rivasto@utu.fi*

June 13, 2021

Abstract

We demonstrate a straightforward and easily applicable technique for growing the highly improved quality of artificially $BaZrO_3$ doped $YBa_2Cu_3O_{6+x}$ films on a commercially used buffered metallic template by pulsed laser deposition. Our method relies on reducing the grain size of the target material, which completely prevents the transfer of the harmful grain boundaries or weak links from the substrate through the buffer layers on the deposited high temperature superconducting film. An extra benefit, a great improvement in the self-assembly of $BaZrO_3$ dopants is also observed as the critical current density is increased in the high temperature range up to 40% and the

growth rate of the film can be increased by 25%. We discuss our results by providing a universal quantitative theory on the transfer of grain boundaries from the substrate to film. Our results can be considered extremely attractive for the vastly growing coated conductor industry.

1 Introduction

The high temperature superconductors (HTS) have been of interest for various applications ever since their discovery due to the possibility to have dissipation free power transmission at practically accessible temperatures. These applications range from simple power transmission lines to state-of-the-art magnets used in fusion reactors. The exploitation of HTS materials has been limited due to their fragile ceramic structure which complicates the production of wires from them. The usability of HTS materials in various applications depends fully on the possibility to reliably grow them on buffered metallic templates enabling the production of flexible HTS cables for practical usage [1]. A quality film growth on these templates requires good texturization and chemical stability of the substrate surface [2]. In the field of coated conductors, there are two distinct commonly used methods to achieve these requirements. The first method is to deformation-texturize the metal surface by rolling assisted biaxially textured substrate approach (RABiTS), where one utilizes the standard thermomechanical processing in order to obtain smooth biaxially oriented substrates [3, 4]. The introduction of various buffer layers is further required for achieving the well structured surface with high enough chemical stability. Another possibility is to texturize the buffer layer structure during deposition via the ion-beam assisted deposition method (IBAD) [5].

A commonly used deposition method of superconducting thin film on top of the aforementioned substrates among the coated conductor industry is the pulsed laser deposition (PLD), which is actively developed to provide better film growth and to be more cost-effective [6, 7]. The PLD is an attractive growth method of HTS films, since it effectively allows the addition of dopants within the YBCO matrix [8]. These dopants are extremely important, especially for applications that work under high magnetic fields, since they act as pinning centers eliminating the dissipation caused by the movement of the field induced vortices. A huge leap in improving the su-

perconducting critical current at high magnetic fields was the discovery of dopants that self-assemble themselves during the PLD process as YBCO c-axis oriented nanorods [9]. Among a wide range of discovered self-assembled dopants, perhaps the most famous one is $BaZrO_3$ (BZO), which we have also utilized in this work.

Until now, mainly $YBa_2Cu_3O_{6+x}$ (YBCO) and $GdBa_2Cu_3O_{6+x}$ (GdBCO) has been managed to grow on these buffered metallic templates utilizing PLD for the large scale coated conductor manufacturing [10]. However, these non-single crystalline templates are extremely harsh growth environments for the films to be deposited due to presence of the great number of grain boundaries, which are usually transferred on the film deposited on the top of it [11, 12, 13, 14, 15]. This grain boundary transfer significantly diminishes the benefits of the HTS materials, such as liquid nitrogen cooling, as they limit the superconducting critial current more substantially in the high temperature range. The critical current, determined by the grain boundaries, has been observed to decrease linearly in zero field as the temperature is increased according to superconductor-insulator-superconductor (SIS) model [16, 17, 18]. More unfortunately, under applied magnetic fields the critical current is suppressed exponentially as a function of temperature [16] and in some cases the grain boundaries can even become weak links blocking the applied current completely [19, 20].

In this work, we present a new simple and easily accessible method of depositing BZO doped YBCO films on an advanced IBAD-MgO based buffered metallic template that almost completely prevents the substrate-film grain boundary transfer. Amazingly, our method also provides major improvement to the formation of BZO nanorods within the YBCO lattice resulting to 40% increased critical current in the high temperature range and allows 25% faster deposition rate of the film. The presented method is based on increasing the size of the particles emitted from the PLD target by reducing the target material grain-size down to nano-scale via sol-gel synthesis [21, 22]. The details of the target preparation and the PLD process are presented in supporting information (SI). The IBAD-MgO based buffer layer structure of the metallic template used in this work is presented in Fig. 1 and the details of the fabrication process are given in [23].

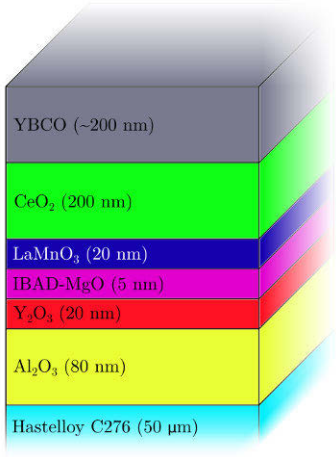

Figure 1: The buffer layer structure of the metallic template that was used as a substrate in this work.

2 Results and discussion

2.1 Grain boundary transfer

The commonly used YBCO targets for the PLD process are produced by the solid-state ceramic method resulting into a pellet formed by micrometer-sized grains (μ-YBCO) [24]. However, the production of a YBCO target with greatly reduced grain size (n-YBCO) is also possible by utilizing the citric acid combustion variant of the sol-gel method, the details of which can be found in our previous works [21, 22]. The morphological properties of both intrinsic n-YBCO and μ-YBCO are presented and extensively studied in [25], where the average grain size for n-YBCO was estimated to be from a few tens to a few hundred nanometers, while for μ-YBCO, it was estimated to be several microns. That is, the grain sizes between the n- and μ-YBCO targets differ by two orders of magnitude.

In this work, films were grown using the aforementioned n-YBCO and μ-YBCO targets doped with 4% BZO on the non-single-crystalline buffered CeO_2-capped IBAD-MgO-based metallic template presented in Fig. 1. The microstructures of the films were studied in detail with bright field scanning transmission electron microscopy (BF-STEM) and variable energy positron

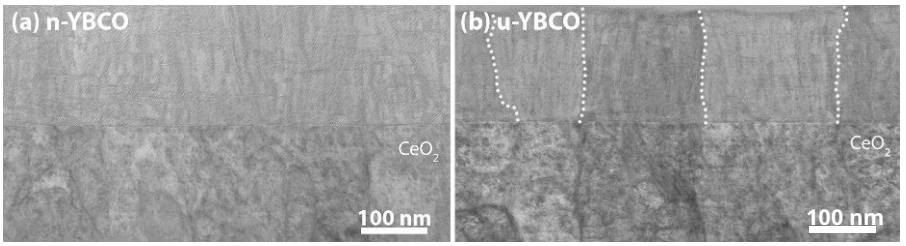

Figure 2: The BF-STEM images of (a) n-film and (b) μ-film. The white dotted lines indicate grain boundaries.

annihilation lifetime spectroscopy (VE-PALS) which provide detailed local and average global information about the microstructures of the samples, respectively. Further details about the measurement techniques are presented in supporting information (SI).

The cross-sectional BF-STEM images of the films deposited from the n-YBCO target (n-film) and the μ-YBCO target (μ-film) are presented in Fig. 2a-b, respectively. The grain boundary transfer from the substrate to the films is clearly observed for the μ-film as expected. Surprisingly, in the case of n-film the grain boundary transfer seems to be completely absent. However, the BF-STEM images of the n-film reveal larger intrinsic lattice defects, in particular stacking faults and threading dislocations, when compared with the μ-film.

In order to further confirm that the grain boundary transfer in the n-films is immensely reduced, we have measured the volumetric positron (e^+) lifetimes (τ_i) and annihilation intensities (I_i) as a function of implantation energy as presented in Fig. 3. The positron implantation energy is proportional to the average distance that the positron can penetrate the sample. If an implanted positron happens to end up inside a void with reduced electron density, such as a lattice defect, the annihilation of the positron is delayed on a time scale of $\sim 0.1-0.5$ ns. This time scale can be further divided into characteristic times representing specific defect types scaling with the available open volume. By measuring the positron annihilation lifetimes one is then able to probe the presence and size of different types of lattice defects ranging from single vacancies to larger voids in the whole sample [26, 27].

The measured e^+ lifetimes revealed two different characteristic times. The measured short positron lifetime τ_1 is in the range typical for single

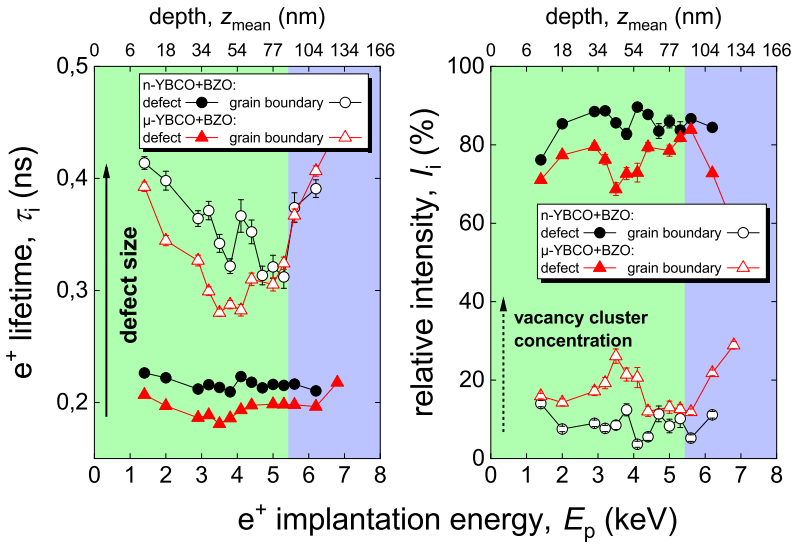

Figure 3: The DB-VEPAS analysis of positron life times as a function of positron implantation energy and mean positron implantation depth for both BZO doped n- and μ-YBCO films. The sub-surface and film bulk are different regions of both the samples as marked by green and blue colors, respectively.

cation vacancy or neutral oxygen vacancy and their complexes [28, 29, 30, 31], while longer lifetime τ_2 represents vacancy complexes situated at grain boundaries or surfaces. As seen in Fig. 3, the n-film has longer positron lifetimes for both intrinsic defects as well as grain boundaries. This is in line with the BF-STEM measurements which indicated the presence of defects with increased size in the n-film. Dislocations without attached vacancies are usually shallow positron traps (weakly bounding positrons), becoming much stronger as a complex with a vacancy [32]. The increased number of threading dislocations in the n-film observed by BF-STEM could be related with a raise of vacancy concentration, considering larger measured τ_1 for the n-film. Fig. 3 also presents the relative intensities of both lifetime components which, very intuitively, are related to the numbers of the associated defects. The relative intensity for grain boundaries is clearly higher for μ-YBCO throughout the film thickness, which is direct evidence that the grain boundary transfer is

globally reduced in the n-film.

In order to comprehensively understand why the grain boundary transfer is absent when the film is deposited from the n-YBCO target we propose a simple 1-dimensional model where the grain boundary of the substrate is assumed to act as a Gaussian potential hill $U(x) = \exp(-x^2/2\sigma^2)$ experienced by the particle emitted from the target as schematically illustrated in Fig. 4a. The full width at half maximum (FWHM) of the potential hill to which, for simplicity, we refer as the Gaussian root mean square width σ, is assumed to be proportional to the width of the grain boundary w by relation $\sigma = w/2$. The maximum force experienced by a particle is obtained when the center of mass of the particle is located at a point where $\partial_x^2 U(x) = 0$, that is at $x = \pm\sigma$. We consider the 1-dimensional particle as a homogeneous rigid body of length $2R$ in order to express the mass of the particle (m) with a simple relation $m \sim R$. With the aforementioned relations the maximum acceleration of the rigid body particle can be calculated by using the simple Newtonian dynamics formula $a(x) = \partial_x U(x)/m$ obtaining

$$a_{\max}(R, \sigma) \sim \frac{1}{R\sigma^2} \int_{\sigma-R}^{\sigma+R} x \mathrm{e}^{-x^2/2\sigma^2} dx, \tag{1}$$

where $\sigma = w/2$. The reasoning of Eq. (1) is illustrated in Fig. 4 while a detailed derivation of Eq. (1) is presented in SI. The calculated $a_{\max}(R)$ curves for various widths of grain boundaries are presented in the main panel of Fig. 4b. In all of the cases, the $a_{\max}$ is readily reduced as the particle size is increased, suggesting that the effect of the grain boundary on the growth of the film is highly reduced by increased particle size. In order to further estimate the effect of a grain boundary of size w to an arbitrary size particle, we have defined the particle critical radius (R_{c}) as the radius above which $a_{\max} < 10^{-5}$. The numerically calculated R_{c} as a function of w are presented in the inset of Fig. 4b. One can observe a clear linear dependency of $R_{\mathrm{c}}(w) = 4.59w + 2.7$ nm. Typical length scale of the grain boundaries is around 2 nm, suggesting that the particle radii emitted from the target would have to be increased only up to 12 nm in order to prevent the grain boundary transfer.

As explained in our previous work [25], a larger grain size of the μ-YBCO target enhances heat diffusion from the laser pulse to the interior of the target as the grain size is inversely proportional to the number of oxygen filled grain boundaries that act as thermal insulators. This limits the energy density on the surface of the target enabling the emission of mainly single atoms

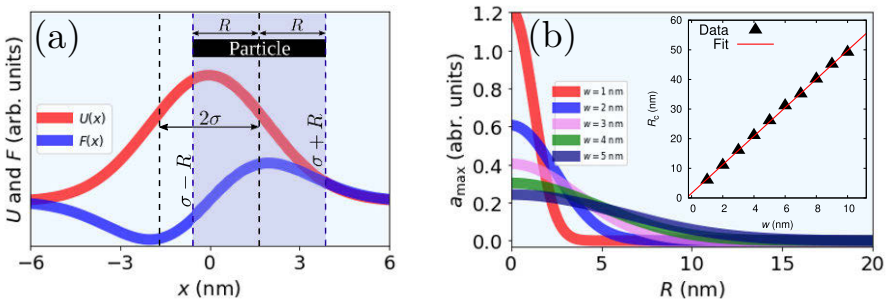

Figure 4: (a) The Gaussian potential $U(x)$ centered at $x = 0$ and the force $F(x) = \partial_x U(x)$. The black dashed lines present the σ of the Gaussian potential at which the center of the mass of the particle of radius R (indicated in the figure) is located. The blue dashed lines delimit the region of integration. (b) Main: The maximum acceleration experienced by a nucleation particle size of radius R in the vicinity of a grain boundary of width w. Inset: Calculated critical particle radii, above which the $a_{\max} < 10^{-5}$, as a function of grain boundary width.

of unit cells that interact strongly with the grain boundaries of the substrate, according to arguments presented above. In the case of the n-YBCO target, that is filled with the insulating grain boundaries, one can achieve greatly enhanced energy density on the surface of the target allowing the emission of large clusters for which the grain boundary interaction is highly reduced. The 12 nm critical particle radius proposed by the introduced theory is certainly in the plausible range to be emitted from the n-YBCO target. The fact that the n-film was observed to have larger and greater number of intrinsic lattice defects is also in line with the proposed theory as the increased size of emitted particles is associated with highly increased formation of individual growth islands on the substrate, as suggested by molecular dynamic simulations presented in [25]. The differences of the proposed PLD processes using different grain sized targets are illustrated in Fig. 5.

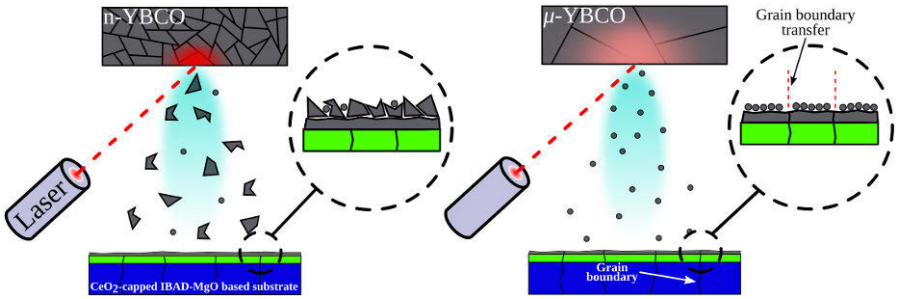

Figure 5: A schematic illustration of the PLD process for n- and μ-grain sized YBCO targets on a non-single-crystalline buffered CeO_2-capped IBAD-MgO-based metallic template.

3 The effect of grain boundaries

The deteriorating effect of the grain boundaries on superconductivity in the high temperature range is dramatically manifested as the critical current density (J_c) was determined by measuring the magnetic hysteresis loop of the n- and μ-films and then calculating the J_c from the openings of the measured loops as suggested by the Bean model [33]. The magnetically measured J_cs as functions of applied magnetic fields at 10 K and 77 K are presented in Fig. 6a. At 10 K, the n-film is observed to have on average 1.7 times higher J_c when compared with the μ-film. However, at 77 K the J_c of the n-film is observed to become over 100 times greater when compared with the μ-film as the field is increased over 2 T. This overwhelming improvement of J_c in the n-film demonstrates the effectiveness of the grain boundaries in resisting passage of Cooper pairs through them in the high temperature range as the magnetic field induced weak eddy currents are unable to pass the grain boundaries in the μ-film. Thus the different grains in the μ-film act more or less as individual superconducting films as illustrated in Fig. 6b. Thus the J_c calculated by the Bean model gives very low values for the μ-film.

The fact that the grain boundaries become more resistive for the supercurrent as the temperature is increased is a well known phenomenon explained by the quantum mechanical SIS-model that is usually applied to Josephson junctions [16, 17, 18]. Here, we present an alternative Ginzburg-Landau (GL) theory based approach that provides much more simple and intuitive

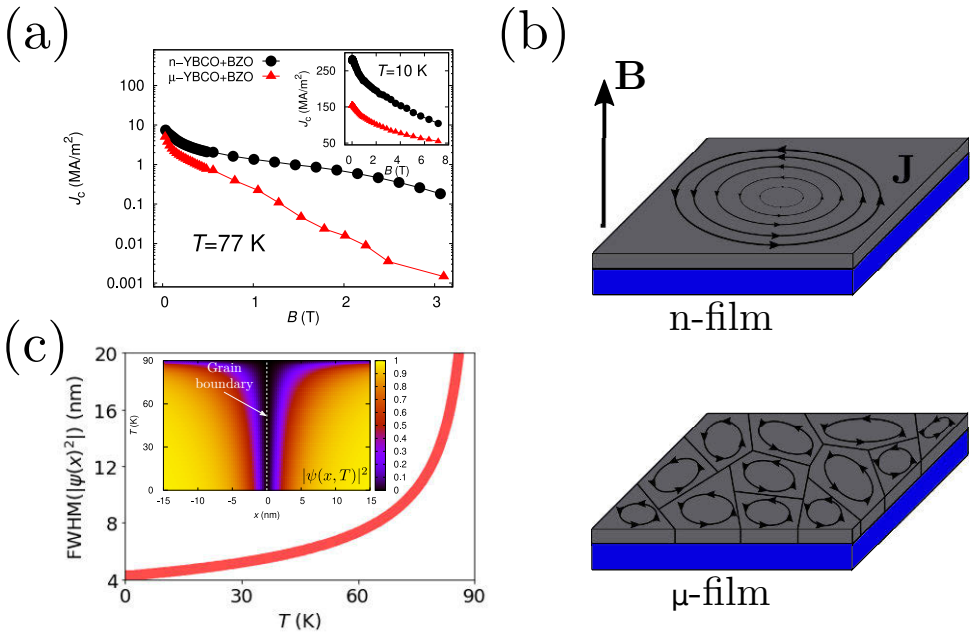

Figure 6: (a) The magnetically measured J_c at 10 K and 77 K as a function of the magnetic field for n- and μ-films. (b) A schematic illustration of the magnetic field induced shielding current circulation in the n- and μ-films. (c) Main: The full width half maximum (FWHM) of the function $|\psi(x,T)|^2$ (Eq. (2)) as a function of temperature. Inset: The shape of the of the function $|\psi(x,T)|^2$ as a function of distance and temperature.

understanding for this rather fundamental effect. We assume that the superconducting order parameter ψ in the vicinity of a grain boundary located at $x = 0$ can be described by a function

$$\psi(x) = \frac{x}{\sqrt{x^2 + 2\xi^2}} e^{i\theta}, \tag{2}$$

where ξ is the superconducting coherence length and θ is the phase of the superconducting wave function. Eq. (2) is also used to describe the order parameter of an Abrikosov vortex [34, 35] and was chosen because we are interested in the high field range where the vortices get pinned in the grain

boundaries giving the order parameter the form expressed by Eq. 2. According to the GL theory ξ can be expressed in terms of the GL phenomenological parameter a as $\xi = \sqrt{\hbar^2/2ma}$, where $\hbar$ is the Planck's constant divided by 2π and m is the mass of the electron pair. The parameter a, on the other hand, has a temperature dependency of $a(T) = (T/T_c - 1)^{-1/2}$, where $T_c \approx 90$ K is the critical temperature of YBCO [36]. Inserting these expressions into Eq. (2) one can deduce the temperature dependency of the shape of $\psi(x)$ in the vicinity of the grain boundary as illustrated in the inset of Fig. 6c, where the non-superconducting area ($|\psi| = 0$) clearly broadens as a function of temperature. The main panel of Fig. 6c illustrates the exponential increase of the full width half maximum (FWHM) of the $|\psi(x)|^2$ as a function of temperature. The FWHM of the $|\psi(x)|^2$ can be intuitively related to the effective resistivity of the grain boundary analogically to the thickness of insulating layer in Josephson junctions that is inversely proportional to the critical current of the junction [37]. We thus conclude that the exponential suppression of the critical current accross a grain boundary as a function of temperature is simply due to broadening of the area of reduced superconductivity in the vicinity of the grain boundary.

3.1 Nanorod formation and transport properties

Another significant difference between the deposited n- and μ-films is the formation of the BZO nanorods as seen in Figs. 7a-b. The effect of the nanorods, when it comes to flux pinning, is highly determined by their fragmentation as more solid nanorods enable greater critical current densities [38, 39]. In the case of n-YBCO, the length of the nanorods varies between 75–150 nm, while for μ-film the length is only 25–45 nm. That is, the nanorods in the n-film are on average over 3 times longer suggesting superior transport properties of the n-film under high magnetic fields when compared to the μ-film. Interestingly, the nanorods are are also splayed twice as much in the n-film when compared with the μ-film. Such a huge difference in the length of the nanorods was also observed in our previous work [39], where n- and μ-films were grown on single crystalline substrate. We conclude that the improved formation of the nanorods is directly related to the reduced grain size of the target and is not due to the substrate. The n-film can also be observed to grow on average 40 nm thicker when compared with the μ-film with the same number of pulses in the PLD process. This is obviously due to the larger particle sizes emitted from the n-YBCO target. The almost 25% faster film

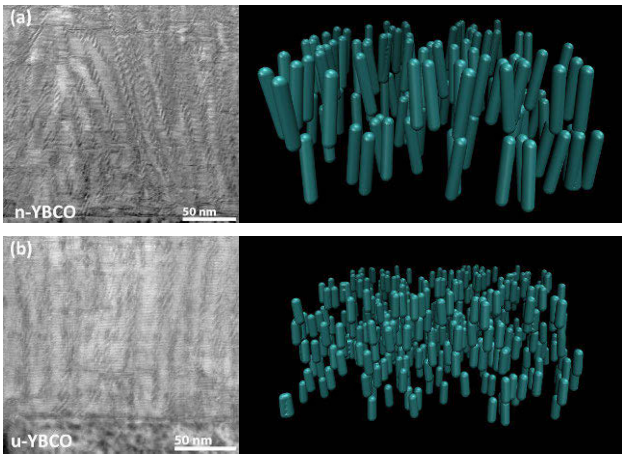

Figure 7: The BF-STEM images and 3D schematic illustrations of the observed distributions of the BZO nanorods for (a) n-film and (b) μ-film.

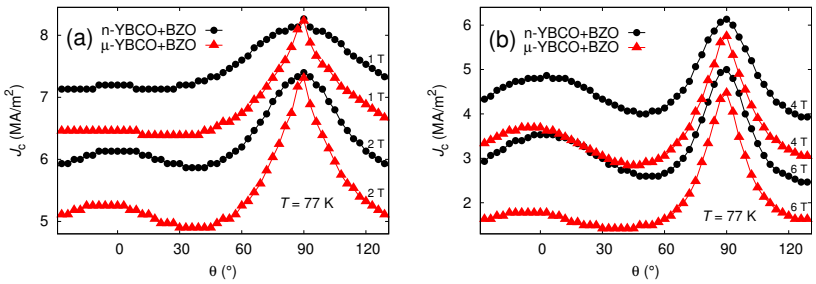

Figure 8: The angular dependency of the J_c in (a) low magnetic field and (b) high magnetic field, ranges. The 0° angle is along the YBCO c-axis.

growth with highly improved film quality should attract the coated conductor industry into using the nano-sized YBCO targets. A summary of all the measured nanorod parameters are presented in Table 1.

In order to study whether the absence of grain boundaries and the improved nanorod growth actually make the transport properties on the n-film superior when compared with the μ-film, the magnetic field angle (θ) dependency of the J_c was resistively measured in a wide field range. The $J_c(\theta)$

curves measured at high temperature are presented in Fig. 8. The shapes of the $J_c(\theta)$ are very similar between the n- and μ-films and above 1 T, a clear improvement of J_c can be seen around $\theta = 0$ indicating the direction along the YBCO c-axis. This so called c-peak arises due to improved vortex pinning along the c-axis and is the fingerprint of c-axis oriented lattice defects, which in this case are mainly the BZO nanorods. The absolute values of J_c show an impressive 40% improvement of J_c in the n-film along the YBCO c-axis when compared with the μ-film. Interestingly, the J_c along the YBCO ab-axis is approximately the same for both films, suggesting that the improved J_c at $\theta < 90^{\circ}$ is in particular due to increased vortex pinning performance of the n-film.

Finally, in order to study how much the nanorods contol on the anisotropy of the critical current ($J_c(\theta)$), the $J_c(\theta)$ curves were simulated using the molecular dynamics method at 1 T for pinning landscapes resembling the observations of the structures of the BZO nanorods in the BF-STEM images presented in Table 1 for n- and μ-films, respectively. Detailed information about the utilized simulation model is provided in the SI. The used pinning landscapes for n- and μ-films are illustrated in Fig. 7 and the simulated critical current anisotropies are presented in Fig. 9. The simulations are in line with the experimental measurements as the c-peak is absent for both of the films at 1 T and the difference of the absolute values of J_c for the n- and μ-films is clearly reduced at higher angles. This suggests that the pinscape for formed by the BZO nanorods mainly determines the critical current anisotropy of the associated film, despite the substantial differences in the grain boundaries and other defects between the films.

Table 1: A compilation of microscopic results measured by BF-STEM for BZO doped YBCO grown by different grain sized targets.

Parameter	n-film	μ-film
Film thickness (nm)	200–210	160–170
Stacking fault length (nm)	22.8±8.5	21.9±5.0
Nanorod diameter (nm)	7.8±1.4	6.1±1.0
Nanorod length (nm)	75–150	25–45
Nanorod spacing (nm)	12.3±3.6	10.3±2.8
Nanorod splay (°)	15.2±3.3	7.5±1.7

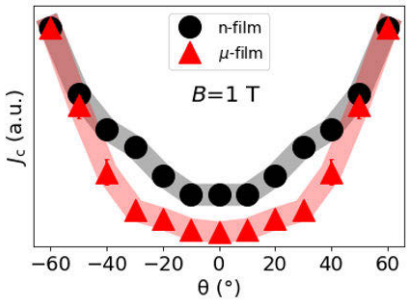

Figure 9: The normalized shapes of the simulated critical current density anisotropies under 1 T applied field concidering only the effect of nanorods. The zero angle corresponds to a field parallel to the YBCO c-axis.

4 Conclusions

We have introduced a new method of using the target with nanosized grains to highly improve the quality of PLD deposited BZO doped YBCO films on buffered metallic templates via elimination of grain boundaries and improved self-assembly of nanorods. The improved film quality is manifested in particular by the 40% improved J_c along the YBCO c-axis. Furthermore, we have provided a widely applicable theory for the grain boundary transfer from substrate to film, which could be of great interest also in research outside the HTS coated conductors. Also, the usage of the target material with nanosized grains in the PLD process may be of great interest in other fields of materials science.

5 Acknowledgements

The Jenny and Antti Wihuri Foundation, Finland, is acknowledged for financial support. M.Z.K. and E.R. are grateful to University of Turku Graduate School (UTUGS) for providing general resources. M.Z.K. also thanks to the University of Turku Foundation for financial support. H.R. acknowledges support and funding as postdoctoral fellow fundamental research of the Research Foundation - Flanders (FWO) under grant number 1273621N. We would like to thank Ahmed G. Attallah and Eric Hirschmann from

Helmholtz-Zentrum Dresden-Rossendorf for assistance. This work was partially supported by the Impulse und Net-working fund of the Helmholtz Association (FKZ VH-VI-442 Memriox) and the Helmholtz Energy Materials Characterization Platform (03ET7015). The computer resources of the Finnish IT Center for Science (CSC) and the FGCI project (Finland) are also acknowledged.

6 Experimental details

The n- and μ-grain size targets were synthesized via a citric acid combustion variant of the sol-gel method and solid-state ceramic method, respectively. The films were deposited via PLD at 775 °C with 308 nm laser pulse of 65 mJ at 5 Hz frequency under 0.175 Torr oxygen circulation. The films were given *in-situ* post-annealing treatment of 1 atm oxygen for 10 min at 750 °C.

Both magnetic and transport measurements were carried out by the Quantum Design physical property measurement system (PPMS). For transport measurements, 200 μm wide stripes were patterned on the surface of the film via photolithography and wet chemical etching. The stripes were connected to the PPMS sample holder with a wire bonder using 50 μm wide aluminium wire.

The samples were prepared for the BF-STEM measurements by cutting and milling a cross-sectional lamella via focused ion beam technique. The lamella were extracted using an *in-situ* lift-out procedure after which the STEM was carried out with BF detector on operating voltage of 200 kV.

The VEPALS measurements were performed at the mono-energetic positron spectroscopy beamline, which is the end station of the radiation source ELBE at HZDR, Germany.

Further details about sample preparation and measurements are provided in SI.

7 Author contribution

M.Z.K. conceived and designed the project. M.Z.K. prepared the samples and performed the magnetic and the transport measurements. E.R. is solely credited for conceiving the mathematical modelings and carrying out simulations. M.Z.K. and E.R. together analyzed the results and wrote the manuscript.

Y.Z. provided the metallic template. M.O.L., M.B. and A.W. conducted the VEPAS measurements and analyzed their results. H.R. performed BF-STEM measurements and did the analysis together with I.V.D. H.H. and P.P. supervised the project. All the authors reviewed and commented on the manuscript.

References

[1] V. Selvamanickam, D. Hazelton, L. Motowidlo, F. Krahula, J. Hoehn, M. Walker, and P. Haldar, "High-temperature superconductors for electric power and high-energy physics," *Journal of Minerals, Metals and Materials Society*, vol. 50, no. 10, pp. 27–30, 1998.

[2] X. Obradors and T. Puig, "Coated conductors for power applications: materials challenges," *Superconductor Science and Technology*, vol. 27, no. 4, p. 044003, 2014.

[3] A. Goyal, D. Norton, D. a. Christen, E. Specht, M. Paranthaman, D. Kroeger, J. Budai, Q. He, F. List, R. Feenstra, *et al.*, "Epitaxial superconductors on rolling-assisted biaxially-textured substrates (RA-BiTS): A route towards high critical current density wire," *Applied superconductivity*, vol. 4, no. 10-11, pp. 403–427, 1996.

[4] A. Goyal, D. Lee, F. List, E. Specht, R. Feenstra, M. Paranthaman, X. Cui, S. Lu, P. Martin, D. Kroeger, *et al.*, "Recent progress in the fabrication of high-j_c tapes by epitaxial deposition of YBCO on RA-BiTS," *Physica C: Superconductivity*, vol. 357, pp. 903–913, 2001.

[5] Y. Iijima, K. Kakimoto, M. Kimura, K. Takeda, and T. Saitoh, "Reel to reel continuous formation of Y-123 coated conductors by IBAD and PLD method," *IEEE transactions on applied superconductivity*, vol. 11, no. 1, pp. 2816–2821, 2001.

[6] Y. Wu, G. Jiang, J. Zhu, D. Wu, X. Quan, J. Shi, H. Suo, and Y. Zhao, "Ultra-fast growth (up to 100 nm s-1) of heavily doped $EuBa_2cu_3o_7$ film with highly aligned $BaHfO_3$ nanocolumn structure," *Superconductor Science and Technology*, vol. 34, no. 5, p. 05LT01, 2021.

[7] Y. Wu, Y. Zhao, X. Han, G. Jiang, J. Shi, P. Liu, M. Z. Khan, H. Huhtinen, J. Zhu, Z. Jin, and Y. Yamada, "Ultra-fast growth of cuprate superconducting films: dual-phase liquid assisted epitaxy and strong flux pinning," *Materials Today Physics*, p. 100400, 2021.

[8] J. MacManus-Driscoll, S. Foltyn, Q. Jia, H. Wang, A. Serquis, L. Civale, B. Maiorov, M. Hawley, M. Maley, and D. Peterson, "Strongly enhanced current densities in superconducting coated conductors of $YBa_2Cu_3O_{7-x}$+$BaZrO_3$," *Nature materials*, vol. 3, no. 7, pp. 439–443, 2004.

[9] B. Maiorov, S. Baily, H. Zhou, O. Ugurlu, J. Kennison, P. Dowden, T. Holesinger, S. Foltyn, and L. Civale, "Synergetic combination of different types of defect to optimize pinning landscape using $BaZrO_3$-doped $YBa_2Cu_3O_7$," *Nature materials*, vol. 8, no. 5, pp. 398–404, 2009.

[10] Y. Yamada, A. Ibi, H. Fukushima, K. Takahashi, S. Miyata, R. Kuriki, H. Kobayashi, M. Konishi, T. Kato, T. Hirayama, and Y. Shiohara, "GdBaCuO and YBaCuO long coated conductors by IBAD-PLD method—enhancement of production speed and critical current in a magnetic field," *IEEE Transactions on Applied Superconductivity*, vol. 17, no. 2, pp. 3371–3374, 2007.

[11] D. M. Feldmann, J. L. Reeves, A. Polyanskii, G. Kozlowski, R. R. Biggers, R. M. Nekkanti, I. Maartense, M. Tomsic, P. Barnes, C. E. Oberly, *et al.*, "Influence of nickel substrate grain structure on $YBa_2Cu_3O_{7-x}$ supercurrent connectivity in deformation-textured coated conductors," *Applied Physics Letters*, vol. 77, no. 18, pp. 2906–2908, 2000.

[12] Y. Zhao, L. Ma, W. Wu, H.-L. Suo, and J.-C. Grivel, "Study on advanced $Ce_{0.9}La_{0.1}O_2/Gd_2Zr_2O_7$ buffer layers architecture towards all chemical solution processed coated conductors," *Journal of Materials Chemistry A*, vol. 3, no. 25, pp. 13275–13282, 2015.

[13] M. Lao, J. Hecher, P. Pahlke, M. Sieger, R. Hühne, and M. Eisterer, "Magnetic granularity in pulsed laser deposited YBCO films on technical templates at 5 k," *Superconductor Science and Technology*, vol. 30, no. 10, p. 104003, 2017.

[14] Y. Wang, L. Zhou, C. Li, Z. Yu, J. Li, L. Jin, P. Wang, and Y. Lu, "Texture transfer mechanism of buffer layer in coated conductors," *Journal*

of superconductivity and novel magnetism, vol. 25, no. 4, pp. 811–816, 2012.

[15] V. Mihalache, N. Stefan, I. Enculescu, I. Mihailescu, M. Socol, and M. Miroi, "The influence of the microstructure and morphology of CeO_2 buffer layer on the properties of YBCO films PLD grown on Ni tape," *Journal of Superconductivity and Novel Magnetism*, vol. 27, no. 11, pp. 2475–2485, 2014.

[16] J. Mannhart, P. Chaudhari, D. Dimos, C. C. Tsuei, and T. R. McGuire, "Critical currents in [001] grains and across their tilt boundaries in $YBa_2Cu_3O_7$ films," *Phys. Rev. Lett.*, vol. 61, pp. 2476–2479, Nov 1988.

[17] H. Hilgenkamp and J. Mannhart, "Grain boundaries in high-T_c superconductors," *Reviews of Modern Physics*, vol. 74, no. 2, p. 485, 2002.

[18] D. G. Steel, J. D. Hettinger, F. Yuan, D. J. Miller, K. E. Gray, J. H. Kang, and J. Talvacchio, "Electrical transport properties of [001] tilt bicrystal grain boundaries in $YBa_2Cu_3O_7$," *Applied Physics Letters*, vol. 68, no. 1, pp. 120–122, 1996.

[19] D. Dimos, P. Chaudhari, and J. Mannhart, "Superconducting transport properties of grain boundaries in $YBa_2Cu_3O_7$ bicrystals," *Phys. Rev. B*, vol. 41, pp. 4038–4049, Mar 1990.

[20] S. E. Babcock, "High-temperature superconductors from the grain boundary perspective," *MRS Bulletin*, vol. 17, pp. 20–26, 1992.

[21] J. Raittila, H. Huhtinen, P. Paturi, and Y. P. Stepanov, "Preparation of superconducting $YBa_2Cu_3O_{7-\delta}$ nanopowder by deoxydation in ar before final oxygenation," *Physica C: Superconductivity*, vol. 371, no. 2, pp. 90–96, 2002.

[22] P. Paturi, K. Schlesier, and H. Huhtinen, "Effect of target density on YBCO thin films deposited from nanograined targets," *Physica C: Superconductivity*, vol. 469, no. 14, pp. 839–842, 2009.

[23] Y. Zhao, J.-M. Zhu, G.-Y. Jiang, C.-S. Chen, W. Wu, Z.-W. Zhang, S. K. Chen, Y. M. Hong, Z.-Y. Hong, Z.-J. Jin, and Y. Yamada, "Progress in fabrication of second generation high temperature superconducting tape

at Shanghai Superconductor Technology," *Superconductor Science and Technology*, vol. 32, no. 4, p. 044004, 2019.

[24] C. Rao, R. Nagarajan, and R. Vijayaraghaven, "Synthesis of cuprate superconductors," *Superconductor Science and Technology*, vol. 6, no. 1, p. 1, 1993.

[25] M. M. Aye, E. Rivasto, M. Z. Khan, H. Rijckaert, E. Salojärvi, C. Haalisto, E. Mäkilä, H. Palonen, H. Huhtinen, I. Van Driessche, *et al.*, "Control of the nanosized defect network in superconducting thin films by target grain size," *Scientific Reports*, vol. 11, no. 1, pp. 1–11, 2021.

[26] R. Krause-Rehberg and H. S. Leipner, "Positron annihilation in semiconductors: defect studies," 1999.

[27] F. Tuomisto and I. Makkonen, "Defect identification in semiconductors with positron annihilation: Experiment and theory," *Rev. Mod. Phys.*, vol. 85, pp. 1583–1631, Nov 2013.

[28] M. J. Puska and R. M. Nieminen, "Theory of positrons in solids and on solid surfaces," *Rev. Mod. Phys.*, vol. 66, pp. 841–897, Jul 1994.

[29] K. O. Jenson, R. M. Nieminen, and M. J. Puska, "Positron states in $YBa_2Cu_3O_{7-x}$," *J. Phys.: Condens. Matter*, vol. 1, 1989.

[30] T. McMullen, P. Jena, S. N. Khanna, Y. Li, and K. O. Jensen, "Positron trapping at defects in copper oxide superconductors," *Phys. Rev. B*, vol. 43, pp. 10422–10430, May 1991.

[31] L. Smedskjaer, B. Veal, D. Legnini, A. Paulikas, and L. Nowicki, "Positron trapping in the superconductor $YBa_2Cu_3O_x$: $Ba_2Cu_3O_x$," *Physica B+C*, vol. 150, no. 1, pp. 56–60, 1988.

[32] S. Assali, M. Elsayed, J. Nicolas, M. O. Liedke, A. Wagner, M. Butterling, R. Krause-Rehberg, and O. Moutanabbir, "Vacancy complexes in nonequilibrium germanium-tin semiconductors," *Applied Physics Letters*, vol. 114, no. 25, p. 251907, 2019.

[33] H. Wiesinger, F. M. Sauerzopf, and H. W. Weber, "On the calculation of J_c from magnetization measurements on superconductors," *Physica C: Superconductivity*, vol. 203, no. 1-2, pp. 121–128, 1992.

[34] H. Palonen, J. Jäykkä, and P. Paturi, "Giant vortex states in type I superconductors simulated by Ginzburg–Landau equations," *Journal of Physics: Condensed Matter*, vol. 25, no. 38, p. 385702, 2013.

[35] G. Blatter, M. V. Feigel'man, V. B. Geshkenbein, A. I. Larkin, and V. M. Vinokur, "Vortices in high-temperature superconductors," *Reviews of Modern Physics*, vol. 66, no. 4, p. 1125, 1994.

[36] C. Poole, H. A. Farach, R. J. Creswick, and R. Prozorov, "Superconductivity, 2nd edition," 2007.

[37] P. Dubos, H. Courtois, B. Pannetier, F. K. Wilhelm, A. D. Zaikin, and G. Schön, "Josephson critical current in a long mesoscopic S-N-S junction," *Physical Review B*, vol. 63, no. 064502, p. 1, 2001.

[38] E. Rivasto, M. Z. Khan, M. Malmivirta, H. Rijckaert, M. M. Aye, T. Hynninen, H. Huhtinen, I. Van Driessche, and P. Paturi, "Self-assembled nanorods in YBCO matrix–a computational study of their effects on critical current anisotropy," *Scientific reports*, vol. 10, no. 1, pp. 1–14, 2020.

[39] M. Z. Khan, E. Rivasto, J. Tikkanen, H. Rijckaert, M. Malmivirta, M. O. Liedke, M. Butterling, A. Wagner, H. Huhtinen, I. Van Driessche, *et al.*, "Enhanced flux pinning isotropy by tuned nanosized defect network in superconducting $YBa_2Cu_3O_{6+x}$ films," *Scientific reports*, vol. 9, no. 1, pp. 1–12, 2019.

Supporting Information: Strongly enhanced critical current densities in YBCO superconductor on buffered metal for coated conductor applications

Mukarram Zaman Khan, Elmeri Rivasto, Hannes Rijckaert, Maciej Oskar Liedke, Yue Zhao, Maik Butterling, Andreas Wagner, Hannu Huhtinen, Isabel Van Driessche, Petriina Paturi

June 13, 2021

1 Experimental details

1.1 Target preparation

In order to synthesize the target with nanometer grain size (n-YBCO+4%BZO), we utilized the citric acid combustion variant of the sol-gel method. The detailed description of the synthesis procedure can be found in our previous works [1, 2]. For synthesizing a pellet with micro gain size (μ-YBCO+4%BZO) we used the solid-state ceramic method as explained in [3]. The synthesis procedure was slightly tuned in terms of sintering temperature which was lowered to 920 °C from the original value of 950 °C in ref. [3]. This was done to avoid the melting of intermediate products. Both of the targets were $\geq$99% pure as verified by X-ray diffraction and Rietveld analysis.

The morphological properties of both intrinsic n-YBCO and μ-YBCO are presented and extensively studied in [4]. These results also apply to the doped targets. As a summary, the width of YBCO (005) peak was measured by XRD and Scherrer formula was used to calculate the average crystallite sizes of the targets, which sets boundaries for the actual grain sizes. As a result, the average grain size for n-YBCO was estimated to be from a few

tens to a few hundred nanometers, while for μ-YBCO, it was estimated to be several microns. That is, the grain sizes between μ- and n-targets differ by two orders of magnitude.

1.2 Pulsed laser deposition

The *in-situ* films were epitaxially grown by the PLD method. Both of the films were deposited while using the same optimized parameters but by just utilizing different targets with varying target grain size. The buffered metallic template, provided by Shanghai Superconductor Technology Ltd. in the form of tape, was firstly mechanically cut into 5×5 mm^2 substrates and then glued on same sized $SrTiO_3$ (STO) crystals via silver paste for reliable deposition and measurement purposes. Both films were deposited at 775 °C and the heating rate of 25 °C/min was in action to reach the deposition temperature. 308 nm XeCl excimer laser was used with the energy of 65 mJ, 25 ns of pulse duration and 5 Hz of repetition rate with a laser fluence of 1.3 J/cm^2. 0.175 Torr oxygen circulation was applied during the depositions. After the depositions, the films were given an *in-situ* post-annealing treatment under atmospheric oxygen pressure at 750 °C for 10 minutes. Finally, the temperature of the substrate was lowered back to room temperature with a cooling rate of 25 °C/min.

1.3 BF-STEM measurements

In order to perform the Bright-Field Transmission Electron Microscopy (BF-TEM) measurements, the samples were prepared by cutting a cross-sectional lamella via the Focused Ion Beam (FIB) technique in a FEI Nova 600 Nanolab Dual Beam FIB-SEM. The lamella were extracted using the *in-situ* lift out procedure with an Omniprobe extraction needle. BF-STEM was performed using a Cs-corrected JEOL JEM 2200FS instrument operated at 200 kV.

1.4 VEPALS measurements

The positron annihilation lifetime experiments were performed at the monoenergetic positron spectroscopy (MePS) beamline, which is the end station of the radiation source ELBE (Electron Linac for beams with high Brilliance and low Emittance) at HZDR (Germany) [5, 6], by using a digital lifetime $CrBr_3$ scintillator detector coupled to a Hamamatsu R13089-100 PMT.

SPDevices ADQ14DC-2X digitizer with 14 bit vertical resolution and 2 GS/s horizontal resolution and with a time resolution function down to about 0.205 ns was utilized. The resolution function required for spectrum analysis uses two Gaussian functions with distinct intensities depending on the positron implantation energy, E_p, and appropriate relative shifts. All the spectra contained at least 10^7 counts.

In general, positron lifetime is directly proportional to defects size, hence the larger is the trapping open volume longer it takes for positrons to find and annihilate with electrons [7, 8]. Typical lifetime spectrum $N(t)$ is described by $N(t) = \sum(I_i/t_i)\exp(-t/t_i)$, where t_i and I_i are the positron lifetimes and relative intensity of the i-th component, respectively ($\sum I_i = 1$). The specific lifetime components represent characteristic defect sizes and their relative intensity can be in certain cases related to concentration of the i-th defect size. A mean positron implantation depth was approximated using a simple material density (ρ) dependent formula: $z_{\mathrm{mean}} = 36/(\rho E_{\mathrm{p}}^{1.62})$.

1.5 Magnetic and transport measurements

Both the magnetic and transport measurements were done with the Quantum Design physical property measurement system (PPMS). The J_{c} at 10 K and 77 K was calculated from the hysteresis loops using the Bean model for rectangular films, that is, $J_{\mathrm{c}} = 2\Delta m/[a(1 - a/3b)V]$, where a is the width and b the length of the sample with $b \geq a$, V as the volume of the film and Δm is the opening of the hysteresis loop [9]. To perform the angular dependent measurements, 200 μm wide bridges were made on each of the film by standard photolithography, wet chemical etching and the electrical contacts from the surfaces of the films to puck pads were made by using Al wire installed in TPT HB05 Wire Bonder. The $J_{\mathrm{c}}(\theta)$ curves were measured by installing the sample on an horizontal rotator and measuring J_{c} at different angles between the film surface and the applied field.

2 Vortex dynamics simulations

A detailed technical description and validation of the simulation model have been given in [10]. The simulation model has also been used very successfully in our previous works [11, 12], thus further enhancing the validity and applicability of our model. Here, we only summarize the most important

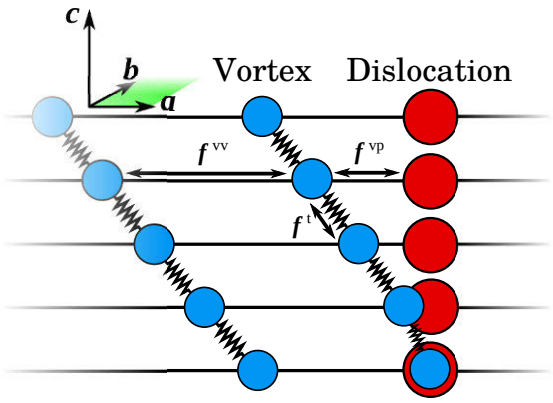

Figure 1: A schematic illustration of the simulation model.

features of our simulation model, as they are presented in the supplementary material of [13].

The simulation model is based on a layer structure schematically illustrated in Fig. 1, in which the vortices are modeled as the chains of particles connected to each other via spring-like line tension force f^{t} acting between two vortex particles of the individual vortex located in adjacent layers. The vortex is also affected by the magnetic force f^{m} that strives to align the individual vortex particles along its angle θ. Furthermore, the vortex particles are also affected by Lorentz force f^{L} that strives to keep the vortices moving and a drag force f^{d} that slows the movement of the vortices. The attractive pinning force f^{vp} acts between a vortex particle and a nanorod particle that are located in the same layers while the vortex-vortex interaction repels the vortex particles of the same layer away from each another. The total force acting on the particle i (in the layer i) of vortex n can thus be calculated from

$$\mathbf{F}^{\mathrm{tot}}_{i,n} = \sum_{j=i\pm1} \mathbf{f}^{\mathrm{t}}_{(i,n),(j,n)} + \sum_{j=i\pm1} \mathbf{f}^{\mathrm{m}}_{(i,n),(j,n)} + \sum_{m\neq n} \mathbf{f}^{\mathrm{vv}}_{(i,n),(i,m)} + \sum_{k} \mathbf{f}^{\mathrm{vp}}_{(i,n),(i,k)} + \mathbf{f}^{\mathrm{L}}_{(i,n)} + \mathbf{L}^{\mathrm{d}}_{(i,n)}. \quad (1)$$

The value of the critical current at certain angle was obtained iteratively by using the bisection method, where the absolute value of the current was adjusted until a certain stability of the vortex system was achieved. In order

to get good statistics for a certain simulation, five different pinning site configurations were randomly generated for which $J_c(\theta)$ curves were calculated separately. The simulations were run in a 100x100x20 nm^3 grid (20 layers) with periodic boundary conditions. The final $J_c(\theta)$ was then calculated as the average value, with standard errors, of the previously mentioned simulations. The parameters used for nanorods, which mimic pinning landscapes observed in the BF-STEM images of the real systems, are presented in Table 1 for n- and μ-film, respectively.

As all molecular dynamics simulations, the efficiency of our computational model is highly affected by the number of particles n present in the simulation as the runtime scales by $O(n^2)$. Accurate simulation of $J_c(\theta)$ based on TEM images requires a lot of pinning site particles, which limits the highest field (proportional to the number of vortices) in our simulation to around 1 T, above which the simulation runtime becomes too long for the purpose of this work. Reducing the grid size was not considered as an option since it would limit the effect of vortex-vortex-interactions.

Due to the layer structure of the simulation model, $J_c(\theta)$ curves can only be simulated reliably up to $\pm 60°$, since above this angle, the layer structure itself induces fictitious forces striving to align the vortex along the YBCO c-axis. Also, at high angles, the repulsion forces between the vortex particles located in different layers should be taken into account which is not the case in this simulation model.

Table 1: The parameters for the nanorods used in the $J_c(\theta)$ simulations for n- and μ-films.

	Number	Diameter (nm)	Splay (∘)	Fragments
n-film	66	7.8	15.2	2
μ-film	94	6.1	7.5	5

3 Theory for grain boundary transfer

We model the grain boundary as a Gaussian shaped potential well

$$U(x) = \mathrm{e}^{-x^2/2\sigma^2}, \tag{2}$$

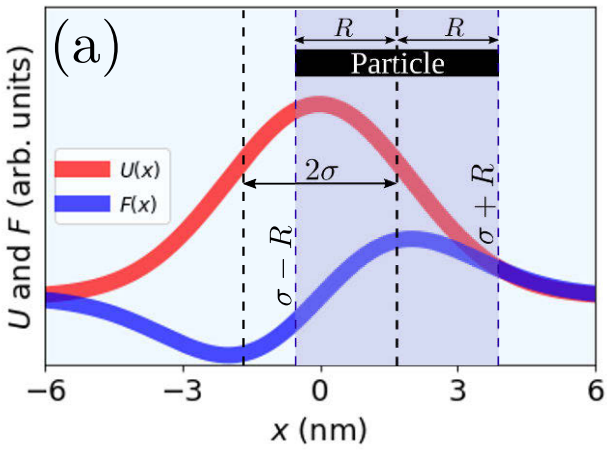

Figure 2: The Gaussian potential $U(x)$ centered at $x = 0$ and the force $F(x) = \partial_x U(x)$. The black dashed lines present the σ of the Gaussian potential at which the center of the mass of the particle of radius R (indicated in the figure) is located. The blue dashed lines delimit the region of integration.

as experienced by the nucleating particle, where we assume that σ is proportional to the width of the grain boundary. The force experienced by a point like particle located at x is then

$$F(x) = -\frac{\partial U(x)}{\partial x} = \frac{x}{\sigma^2} \mathrm{e}^{-x^2/2\sigma^2}. \tag{3}$$

We are interested in the maximum force that can be experienced by the particle. The location x, at which the pointlike particle experiences this maximum force $F_{\max}$ is found at the zero points of $\partial_x F(x)$. That is,

$$\frac{\partial_x F(x)}{\partial x} = 0 \Longleftrightarrow \frac{(x^2 - \sigma^2)\mathrm{e}^{-x^2/2\sigma^2}}{\sigma^4} = 0 \Longleftrightarrow x = \sigma. \tag{4}$$

Since we are interested in how particles of different sizes behave under the influence of force field described by Eq. (3), we are concidering a rigid and homogeneous 1-dimensional particle of length $2R$ as illustrated in Fig. 2. Since we are interested in the maximum possible force, we choose that the center of the mass of the particle to be located at $x = \sigma$. Since the particle is

concidered as a rigid body, the total force on the particle is simply the sum of the forces experienced by different parts of the body, that is

$$F_{\max}(x) = \int_{\sigma-R}^{\sigma+R} F(x)dx. \tag{5}$$

The quantity to be concidered here is, however, the acceleration of the particle. Since the particle is concidered homogeneous, the mass of the particle is directly proportional the radius, that is $m \sim R$. Thus, the maximum acceleration experienced by the particle is

$$a_{\max}(x) = \frac{F_{\max}(x)}{m} \sim \frac{F_{\max}(x)}{R}. \tag{6}$$

Inserting Eqs. (5) and (3) into Eq. (6), one obtains the final result

$$a_{\max}(x) \sim \frac{1}{R\sigma^2} \int_{\sigma-R}^{\sigma+R} x\mathrm{e}^{-x^2/2\sigma^2} dx, \tag{7}$$

which can be analytically evaluated for different σ and R.

References

[1] J. Raittila, H. Huhtinen, P. Paturi, and Y. P. Stepanov, "Preparation of superconducting $YBa_2Cu_3O_{7-\delta}$ nanopowder by deoxydation in ar before final oxygenation," *Physica C: Superconductivity*, vol. 371, no. 2, pp. 90–96, 2002.

[2] P. Paturi, K. Schlesier, and H. Huhtinen, "Effect of target density on YBCO thin films deposited from nanograined targets," *Physica C: Superconductivity*, vol. 469, no. 14, pp. 839–842, 2009.

[3] C. Rao, R. Nagarajan, and R. Vijayaraghaven, "Synthesis of cuprate superconductors," *Superconductor Science and Technology*, vol. 6, no. 1, p. 1, 1993.

[4] M. M. Aye, E. Rivasto, M. Z. Khan, H. Rijckaert, E. Salojärvi, C. Haalisto, E. Mäkilä, H. Palonen, H. Huhtinen, I. Van Driessche, *et al.*, "Control of the nanosized defect network in superconducting thin films by target grain size," *Scientific Reports*, vol. 11, no. 1, pp. 1–11, 2021.

[5] A. Wagner, W. Anwand, A. Attallah, G. Dornberg, M. Elsayed, D. Enke, A. Hussein, R. Krause-Rehberg, M. Liedke, K. Potzger, *et al.*, "Positron annihilation lifetime spectroscopy at a superconducting electron accelerator," in *Journal of Physics: Conference Series*, vol. 791, p. 012004, IOP Publishing, 2017.

[6] A. Wagner, M. Butterling, M. O. Liedke, K. Potzger, and R. Krause-Rehberg, "Positron annihilation lifetime and doppler broadening spectroscopy at the ELBE facility," in *AIP Conference Proceedings*, vol. 1970, p. 040003, AIP Publishing LLC, 2018.

[7] R. Krause-Rehberg and H. S. Leipner, "Positron annihilation in semiconductors: defect studies," 1999.

[8] F. Tuomisto and I. Makkonen, "Defect identification in semiconductors with positron annihilation: Experiment and theory," *Rev. Mod. Phys.*, vol. 85, pp. 1583–1631, Nov 2013.

[9] H. Wiesinger, F. M. Sauerzopf, and H. W. Weber, "On the calculation of J_c from magnetization measurements on superconductors," *Physica C: Superconductivity*, vol. 203, no. 1-2, pp. 121–128, 1992.

[10] P. Paturi, M. Malmivirta, T. Hynninen, and H. Huhtinen, "Angle dependent molecular dynamics simulation of flux pinning in YBCO superconductors with artificial pinning sites," *Journal of Physics: Condensed Matter*, vol. 30, no. 31, p. 315902, 2018.

[11] M. Z. Khan, E. Rivasto, J. Tikkanen, H. Rijckaert, M. Malmivirta, M. O. Liedke, M. Butterling, A. Wagner, H. Huhtinen, I. Van Driessche, *et al.*, "Enhanced flux pinning isotropy by tuned nanosized defect network in superconducting $YBa_2Cu_3O_{6+x}$ films," *Scientific reports*, vol. 9, no. 1, pp. 1–12, 2019.

[12] E. Rivasto, M. Khan, Y. Wu, Y. Zhao, C. Chen, J. Zhu, H. Huhtinen, and P. Paturi, "Lattice defect induced nanorod growth in YBCO films deposited on an advanced IBAD-MgO template," *Superconductor Science and Technology*, vol. 33, no. 7, p. 075008, 2020.

[13] E. Rivasto, M. Z. Khan, M. Malmivirta, H. Rijckaert, M. M. Aye, T. Hynninen, H. Huhtinen, I. Van Driessche, and P. Paturi, "Self-assembled nanorods in YBCO matrix–a computational study of their effects on critical current anisotropy," *Scientific reports*, vol. 10, no. 1, pp. 1–14, 2020.

TURUN
YLIOPISTO
UNIVERSITY
OF TURKU

Painosalama, Turku, Finland 2021

ISBN 978-951-29-8594-4 (PRINT)
ISBN 978-951-29-8595-1 (PDF)
ISSN 0082-7002 (PRINT)
ISSN 2343-3175 (ONLINE)